MINISTÉRIO DA EDUCAÇÃO

UNIVERSIDADE FEDERAL DO RIO GRANDE DO SUL

Escola de Engenharia

Programa de Pós-Graduação em Engenharia de Minas, Metalúrgica e de Materiais – PPGE3M

DEVELOPMENT OF AN OXIDE CERAMIC MATRIX COMPOSITE MANUFACTURED VIA THE COMBINATION OF FILAMENT WINDING AND FREEZE GELATION PROCESS

Eng. Thays Machry

Tese de Doutorado

Porto Alegre - RS
2018

MINISTÉRIO DA EDUCAÇÃO

UNIVERSIDADE FEDERAL DO RIO GRANDE DO SUL

Escola de Engenharia

Programa de Pós-Graduação em Engenharia de Minas, Metalúrgica e de Materiais – PPGE3M

DEVELOPMENT OF AN OXIDE CERAMIC MATRIX COMPOSITE MANUFACTURED VIA THE COMBINATION OF FILAMENT WINDING AND FREEZE GELATION PROCESS

Eng. Thays Machry

Engenheiro de Materiais

Tese de doutorado apresentada ao programa de Pós-Graduação em de Engenharia de Minas, Metalúrgica e de Materiais – PPGE3M, como parte dos requisitos para a obtenção do título de Doutor em Engenharia.

Área de Concentração: Ciência e Tecnologia de Materiais

Porto Alegre - RS
2018

Esta tese foi julgada para a obtenção do título de Doutor em Engenharia, na área de concentração Ciências e Tecnologia dos Materiais e aprovada em sua forma final pelo Orientador e pela Banca Examinadora.

Orientador: Prof. Dr. -Ing. Carlos Pérez Bergmann
Co-orientador: Prof. Dr. -Ing Hazim Ali Al-Qureshi

Banca Examinadora:

Profa. Dra. Annelise Kopp Alves
Dra. Sabrina Arcaro
Prof. Dr. Neftalí Lenin Villarreal Carreño

Prof. Dr. Carlos Pérez Bergmann
Coordenador do PPGE3M

ACKNOWLEDGMENT

I am grateful and honored to have developed this work at Airbus Group Innovations at the Metallic Technologies and Surface Engineering Department lead by Dr.-Ing. Claudio Dalle-Donne, in the Team Materials and Processes lead by Dipl.-Ing. Achim Schoberth. A special thanks to my supervisor and office colleague, Dipl.-Ing. Christian Wilhelmi. Also, I would like to thank Dr.-Ing. Dietmar Koch.

I would like to thank Prof. Carlos Bergmann and the Federal University of Rio Grande do Sul for the great opportunity to supervise and guide the work in its final stage. I would like to thank also Prof. Dr.-Ing. Hazim Ali Al-Qureshi for being a father and a mentor in life and professionally during the past years.

My greatest knowledge and personal growth during these last years was possible because of your trust and encouragement.

In addition, I would like to thank my colleagues from the Advanced Ceramics group from the University of Bremen and my colleagues from Airbus Group Innovations who helped directly and indirectly in the development of this work.

Finally, I dedicate this work to my family: Thiago Medeiros Araujo, Cleusa Regina Oliveira Vivian and Renato Machry. This opportunity would have never come true without all of your unconditional support.

Thank you very much!

TABLE OF CONTENTS

LIST OF ABBREVIATIONS

2D	Two Dimensional
3D	Three Dimensional
BoR	Ball on Ring
CMC	Ceramic Matrix Composite
CMCs	Ceramic Matrix Composites
CSI	Ceramic Slurry Infiltration
CTE	Thermal Expansion Coefficient
CVD	Chemical Vapor Deposition
CVI	Chemical Vapor Infiltration
D	with Dolapix
den	Denier
DLR	German Aerospace Center (Deutsche Luft und Raumfahrt)
DTA	Differential Thermal Analysis
EADS	European Aeronautic Defense and Space Company
EAM	European Apogee Motor
EDX	Energy Dispersive X-Ray
EELS	Electron Energy Loss Spectroscopy
EFD	Edge-defined film-fed technique
F-CVI	Thermal gradient forced flow Chemical Vapor Infiltration
HS	Hot Structure
HT	High Temperature
I-CVI	Isothermal/ isobaric Chemical Vapor Infiltration
IEP	Isoelectric Point
IF-CVI	Isothermal forced flow Chemical Vapor Infiltration
ILS	Interlaminar Shear
ILSS	Interlaminar Shear Strength
LPI	Liquid Polymer Infiltration
LSI	Liquid Silicon Infiltration
MTS	Methyltrichlorosilane
OXIPOL™	Oxide CMC based on Polymers
PAN	Polyacrylonitrile
P-CVI	Pressure flow Chemical Vapor Infiltration
PIP	Polymer Infiltration and Pyrolysis
PVA	Polyvinyl Acrylic
PyC	Pyrolytic carbon
QI	Quasi-isotropic
RMI	Reactive Melt Infiltration
RPM	Rotations per Minute
RT	Room Temperature
RTM	Resin Transfer Molding
RVL	Reusable Launch Vehicle
SEM	Scanning Electron Microscope
SENB	Single Edge Notched Beam
STA	Simultaneously Thermal Analysis
TEM	Transmission Electron Microscope
TG	Thermogravimetry
TG-CVI	Temperature gradient Chemical Vapor Infiltration

TLF	Thermal conductibility (Thermal Leitfähigkeit)
TPS	Thermal Protection System
UD	Uni-directional
Vol. %	Volume percent
wD	without Dolapix
WHIPOX^{TM}	Wound Highly Porous Oxide CMC
WIC	Weak Interface Composite
WMC	Weak Matrix Composite
Wt. %	Weight percent
XRD	X-Ray Diffraction

LIST OF SYMBOLS

F	Force
K_{IC}	Fracture Toughness
t	Time (second)
T	Temperature (°C)
V_{PK}	Volume Pycnometer
V_{Ref}	Volume Reference
P	Pressure
ρ	Density
P_{op}	Porosity
S	Strength
ν	Poisson's Ratio
α	Radius of the circles in support point from ball on ring test
τ	Interlaminar Shear Strength Transversal Tensile Test
σ	Strength
E_{bend}	Elastic Modulus
ε	Strain

SUMMARY

Oxide ceramic matrix composites (CMCs) are promising materials for extreme application environments where high temperatures combined with mechanical loads under oxidative and/ or corrosive conditions are required. Such applications are, e.g., gas turbines, thermal protection systems and high speed missiles. In order to fulfill these requirements oxide ceramic matrices must be developed and combined with ceramic fibers in order to build composites.

In this work, oxide based CMCs are developed by combining the advantages of the colloidal approach to manufacture oxide ceramic matrix with the advantages of the filament winding technique to infiltrate the ceramic fibers into sol gel matrix and consolidate the composite via freeze gelation.

Using the sol gel technique and the freeze gelation process, mullite and alumina based ceramic matrices are developed and oxide ceramic fibers (Nextel^{TM} 610, 3000 denier, organic sized) are infiltrated via the filament winding technique. Directly after fiber infiltration and lay-up, the material is frozen and consolidated due to the sol gel transition from the silica nanoparticles dispersed in the sol gel. After consolidation, the material is dried and the ice crystals formed during freezing are evaporated, finally the material is sintered in normal atmosphere. The resulting porosity corresponds to the space occupied by the former ice crystals.

It is found that for the development of such ceramic matrices, homogenization of the suspension and particle size of ceramic fillers is fundamental to guarantee the stability of the suspension during filament winding and to control growth of ice crystals during freezing. Composites are then manufactured and their physical, thermo-physical and mechanical properties are tested with focus on interlaminar properties. The combination of filament winding with freeze gelation is successfully demonstrated. Homogeneous impregnation of fiber filaments is achieved when mullite or alumina are used as fillers, nevertheless a better mechanical performance of the composites manufactured with alumina matrix is observed. As mullite matrix composites need higher temperatures for mullite formation their mechanical strength, especially under interlaminar loadings, is reduced.

RESUMO

Compósitos de cerâmica oxida são materiais promissores para aplicações em ambientes de aplicações extremas onde resistência a altas temperaturas combinadas a cargas mecânicas sob oxidação e/ ou corrosão são necessárias. Tais aplicações são, por exemplo, turbinas a gás, sistemas de proteção térmica e mísseis de alta velocidade. A fim de cumprir esses requisitos, matrizes de cerâmica oxida devem ser desenvolvidos para a manufatura de compósitos com fibras cerâmicas.

Neste trabalho, compósitos de cerâmica oxida foram desenvolvidos através da combinação das vantagens do processo coloidal para a fabricação de uma matriz cerâmica oxida com as vantagens de uma técnica robotizada (filament winding) para infiltração da suspensão coloidal (sol gel) nas fibras cerâmicas. O compósito é consolidado através da gelificação da suspensão por congelamento.

Usando a técnica do sol gel e o processo de gelificação por congelamento, matrizes cerâmicas com mulita ou alumina como carga foram desenvolvidas e infiltradas em fibras cerâmicas oxidas (Nextel^{TM} 610, 3000 denier, proteção orgânica) usando uma técnica para infiltração de filamentos chamada “filament winding”. Diretamente após infiltração e montagem, o compósito é congelado e consolidado devido a transição da solução em gel. Depois de consolidado, o material é secado e os cristais de gelo formados durante o congelamento do material são evaporados, por fim o compósito é sinterizado em atmosfera normal. A porosidade resultante no compósito corresponde ao espaço ocupado pelos antigos cristais de gelo.

Verificou-se que, para o desenvolvimento de tais matrizes cerâmicas, homogeneização da suspensão e tamanho de partícula dos elementos de carga é fundamental para garantir a estabilidade da suspensão cerâmica durante seu processamento. Os compósitos fabricados e suas propriedades físicas, termomecânicas e mecânicas são testadas com ênfase nas propriedades interlaminares do compósito. A combinação do processo de gelificação com o “filament winding” foi demonstrada com sucesso. Impregnação homogênea dos filamentos de fibras é alcançado independentemente da matriz cerâmica usada, no entanto, um melhor desempenho mecânico dos compósitos com carga de alumina é observado. Isso ocorre, pois, os compósitos com mulita necessitam de temperaturas de sinterização mais elevadas para elevar sua resistência e propriedades interlaminares, dadas ao compósito pela matriz cerâmica.

1 INTRODUCTION

1.1 Context of Work

Monolithic ceramics are materials well known due to their resistance to high temperatures, their chemical and oxidative stability, elevated hardness and compressive strength. Monolithic ceramics find applications in different fields, such as cutting tools, furnace components, medical implants and bearings. In comparison with metals they present lower density and intrinsic oxidation resistance. On the other hand, monolithic ceramics present higher brittleness and low fracture toughness, which is their main drawback (Newman, Schäfer 2001).

In order to improve ceramic brittleness and fracture toughness, fibers are used as reinforcement. Fiber reinforced ceramic matrix composites (CMC) started being significantly studied in the early 1980s (Cox, Zok 1996; Meyer, Waas 2018). These materials, specially oxide based CMC, provide high strength, toughness, notch insensitivity, refractoriness and environmental stability at high temperature applications where metals are usually limited by their melting temperature and monolithic ceramics are limited by their low damage tolerance. Furthermore, this class of materials can be designed to induce macroscopic inelastic deformation mechanisms in either tension or shear (Simon, Danzer 2006; Simon 2005). These characteristics make them promising materials for applications such as thermal protection systems for reusable spacecraft, hyper sound missiles, combustion chamber, diffusor and exhaust from aircraft engines and stationary gas turbines (Figure 1-1).

(a) (b) (c)

Figure 1-1 – Ceramic matrix composites (CMC) possible applications: thermal protection systems for spacecraft (a) (Braun, Weihs 2012), combustion chamber for aircraft engines and stationary gas turbines (b) and hyper sound missiles (c).

The reinforcement provided by the fibers and consequently the material fracture toughness shall be adjusted by crack deflection and energy dissipation of the material. In CMC, the crack propagation is achieved along the fiber matrix interface leading to the pull-out effect. The pull-out effect can be designed either by using weak interface composites (WIC) or weak matrix composites (WMC). The WMC concept is characterized as a fiber dominant behavior, while the fiber interface is not particularly conditioned to allow debonding and the crack propagation is accompanied by energy dissipation through a porous matrix. The WIC concept is governed by a weak fiber-matrix interface, in which the energy dissipation occurs from a gap or weak fiber-matrix interface generating the fiber pull-out (Simon, Danzer 2006; Koch et al. 2008, Ramdane et al. 2017).

Within the class of ceramic matrix composites C/C (carbon matrix reinforced with carbon fiber), C/SiC (silicon carbide matrix reinforced with carbon fiber), SiC/SiC (silicon carbide matrix reinforced with silicon carbide fiber) are most commonly found. Carbide based composites have already achieved a high manufacturing and design level and are already being industrially produced due to their very good mechanical properties. They can be found regularly in air and space applications as thermal protection systems for spacecraft, missiles and brake pads. Nevertheless, this class of CMC presents a strong disadvantage which is their low oxidation stability at temperatures higher than approximately 500°C, leading consequently to loss of mechanical performance due to embrittlement, limiting their use in air and oxidative environments (Shi et al. 2018). In order to use these materials at high temperature applications, expensive oxidation coatings are needed. This drawback contributed significantly to the development of oxide based CMC.

Among the promising applications for oxide based ceramic matrix composites, the use in aircraft engine and stationary gas turbines has been intensively developed in the past decades due to the demand for materials with improved performance, availability, maintainability, durability and reduced emissions of NO_x and CO (Meyer, Waas 2018). The contributing factors are raising fuel costs, the need to minimize operating and maintenance costs and increasingly strict emission regulations. Ceramic materials have the potential to provide 30.000 hours of trouble free operation that industrial gas turbine operators expect. Ceramic matrix composites are of interest for gas turbine hot section components because of their superior high temperature durability compared to metals, which enables higher component operating temperatures, and, consequently, improves fuel efficiency. Additionally, the air saved due to the reduced demand for hot section component cooling could be redirected to lean out the combustor primary zone and reduce the formation of NO_x (Roode et al., 2005). The reduction in cooling air also enables higher firing temperatures, improving engine efficiency, and the incorporation of a combustor liner made of CMC would then prevent the formation of CO (Roode et al. 2005).

With this background, continuous development of oxide based CMC manufactured with different matrix systems and processing routes has been made mostly in Germany and in the United States. Nowadays oxide based CMC are manufactured e.g. at Airbus Group Innovations (UMOX™), German Aerospace Center (WHIPOX™ and OXIPOL™), at Walter E.C. Pritzkow Special Ceramics (Keramikblech®), at the Air Force Research Laboratory (AFRL), COI Ceramics and at the University of Santa Barbara. These materials are mainly produced with oxide fibers Nextel™ from 3M™ Company (USA), made of alumina (Nextel™ 610) or mullite (Nextel™ 720). The ceramic matrices developed for these materials are manufactured using polymer based slurries, water based slurries or via sol based slurries. The fiber infiltration and composite lay-up takes place either by filament winding when continuous fibers are used or by hand lamination when fiber cloths are used.

All these developments with different combinations of manufacturing routes result in ceramic composites with different microstructures and properties. The high requirements in long term applications could, with today's development state, not yet be fulfilled. The progress achieved in the CMC field during the last 15 to 20 years has not led yet to broader application and has been mostly realized in laboratory scale or

at research institutes where industrial manufacturing processes are not applicable. Regardless of the manufacturing route used until now, all these materials have still not yet achieved high performance mechanical properties in respect to their interlaminar properties and present often long processing times which reflects directly in high manufacturing costs. Additionally, some of these composites contain low amounts of silicon carbide being more susceptible to oxidation.

This way, the necessity for alternative manufacturing routes to develop CMC and fulfill the requirements for these promising applications, overcoming the drawbacks of the actual state of the art of CMC materials is given.

Filament winding and freeze gelation are chosen as manufacturing methods to develop the oxide CMC. In the freeze gelation technique manufacturing time and costs are relatively low. Due to the suspension stability and the small particle sizes from the materials in the ceramic suspension, pores formed are homogeneously distributed in the material and the ceramic can be sintered at temperatures that correspond to the maximum sintering temperature of the ceramic fibers. Filament winding is a well-known technique for matrix infiltration among fiber filaments and composite lay-up. It guarantees production reproducibility and homogeneous fiber impregnation throughout the composite.

The topics discussed in this Thesis were researched using mainly Science Direct, along with websites and books. At Science Direct, the number of publications related to the topics is shown by year in Figure 1-2. It is noticeable the great amount of publications in the field of freeze gelation due to its high application for manufacturing of oxide ceramics and ceramic foams. On the other hand, near to none publications are found when oxide CMC is researched in combination with Freeze Gelation.

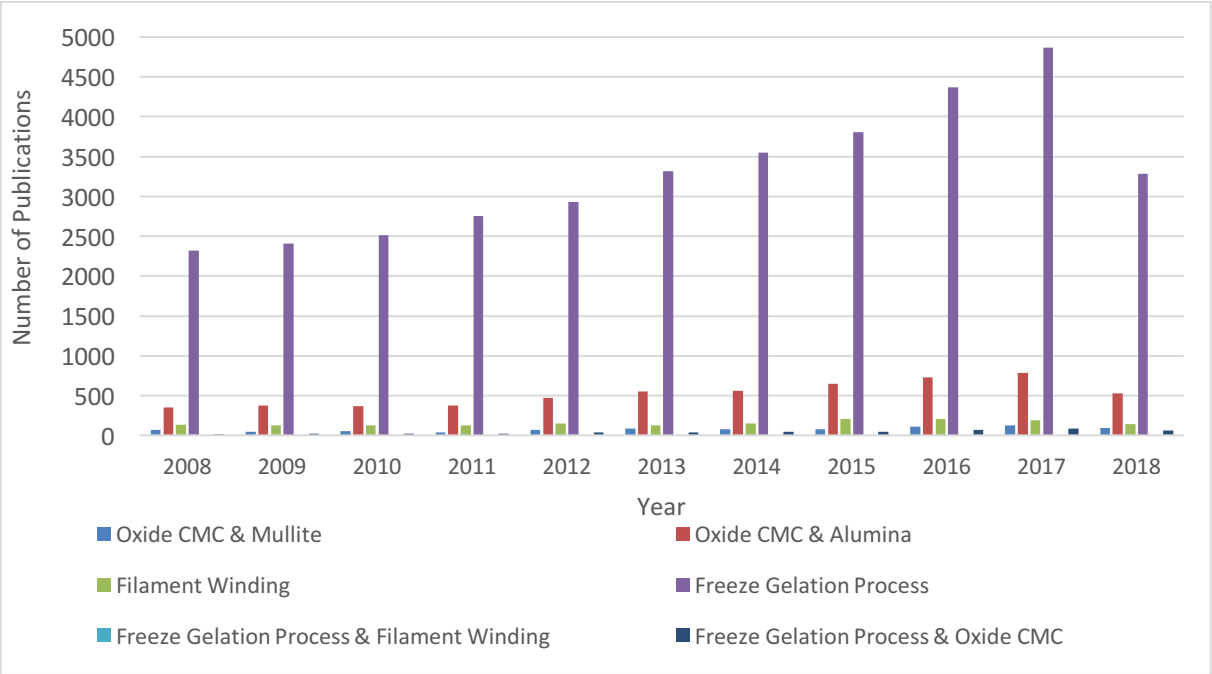

Figure 1-2 – Results from bibliographic research conducted using Science Direct data repository.

1.2 Objectives and Motivation

In order to fulfill the requirements for the use of oxide based CMC in applications such as combustion chambers for gas turbines, ceramic composites have been constantly developed and, with this, alternative cost-efficient processing techniques are emerging. In order to improve interlaminar properties and to enhance the production of cost-efficient manufacturing routes, freeze gelation and filament winding, are combined for the manufacture of an oxide based CMC.

The combination of the freeze gelation and the filament winding processes for the production of oxide based ceramic matrix composites is the objective of the work. Verification of the final developed process to manufacture rotation symmetric components is also aimed.

For the composite development several topics are studied and investigated, such as:

- ⇨ different mullite and alumina fillers varying in particle size and surface area as well as the silica sol to be used are studied;
- ⇨ a homogeneous and stable ceramic suspension is developed;
- ⇨ the filament winding equipment and parameters are adapted to sol gel suspensions for homogenous infiltration of the fibers;

- ⇨ freeze gelation is investigated for achievement of homogeneous pore formation within the composite;
- ⇨ manufacturing parameters from the beginning of the production route up to composite sintering are investigated and adapted for improvement of mechanical performance.

2 FUNDAMENTAL ASPECTS

2.1 Colloidal Technology

Ceramics have been processed by colloidal routes for several hundreds of years although the colloidal processing of ceramics has emerged more recently as a field of research. The interest in this processing technology has increased over the years due to its attractive advantages such as near-net-shape potential, high reliability and flexibility, short processing times and low-cost.

The term “colloid” is used to describe particles that have at least one dimension with size ranging from 10^{-3} to 1 μm. In colloidal systems, the contact area between particles and the dispersing media is very large which results in a strong influence of the interparticle forces on the suspension behavior. The interaction of the particles determines the flow behavior before green body formation as well as the structure and properties of the green body. Therefore, it is important to understand the role of particle interactions in determining the slurry rheology, so that parameters such as pH, electrolyte concentration and/ or adsorbed/ unabsorbed polymer can be controlled. The solid loading of the suspension is also of great importance since it has a strong effect on the mechanical properties of the green body (Bergström 2001; Aksay 1991; Sharma et al. 2003).

Through careful control of interparticle forces, colloidal suspensions can be prepared in the dispersed, weakly flocculated or strongly aggregated state (Figure 2-1). In the dispersed state the particles that are in the suspension repulse one another. In the weakly flocculated state, particles agglomerate as clusters or flocks in suspension at solid volume fractions below the gel point. In the strongly aggregated state particle agglomeration is formed either as particle network or by individual clusters in the suspension. The dominating interparticle forces in most ceramic systems are the van der Waals, electrostactic, and steric (polymeric) forces (Lewis 2001; Bergström 2001; Shaw 1992).

The van der Waals forces are interactions always existing in ceramic systems and they are attractive between similar particles. This force is electrodynamic since it results from the interactions between oscillating or rotating dipoles within the interacting media. For a colloidal system to be created some type of interparticle

repulsion, such as electrostatic or steric has to exist in order to overcome the van der Waals attraction (Shaw 1992; Liang et al. 2007).

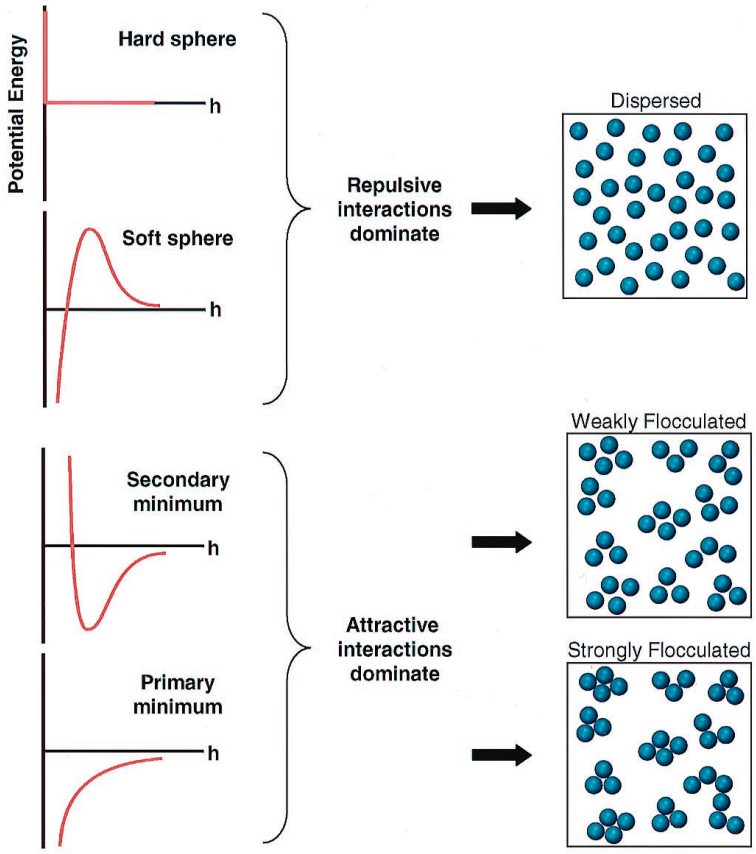

Figure 2-1 - Schematic illustration of the interparticle forces and the resulting suspension structure (Lewis 2001).

Electrostatic forces are only present where charged particles are interacting through a polar medium. Therefore, electrostatic forces are particularly important for ceramic materials in polar medium such as water or ethanol. The electrostatic forces are in general stronger and in longer range than all other surface forces. Thus, they often dominate the properties of a colloidal suspension.

In this kind of force the net charge is controlled by pH (potential of Hydrogen ions) and the reaction constant for the respective dissociation reaction (Figure 2-2A). The isoelectric point (IEP) is the pH value where the surface concentrations of positive and negative ions are the same. Ions of opposite charge are attracted to the charged surface and form a diffuse ion “cloud”, the electrical double layer. The thickness of this electrical double layer is a very important parameter since it controls the range of the double layer repulsion. The thickness is controlled by the

concentration and valence of ions in solution, a high concentration of ions results in a thin double layer (Sigmund et al. 2000).

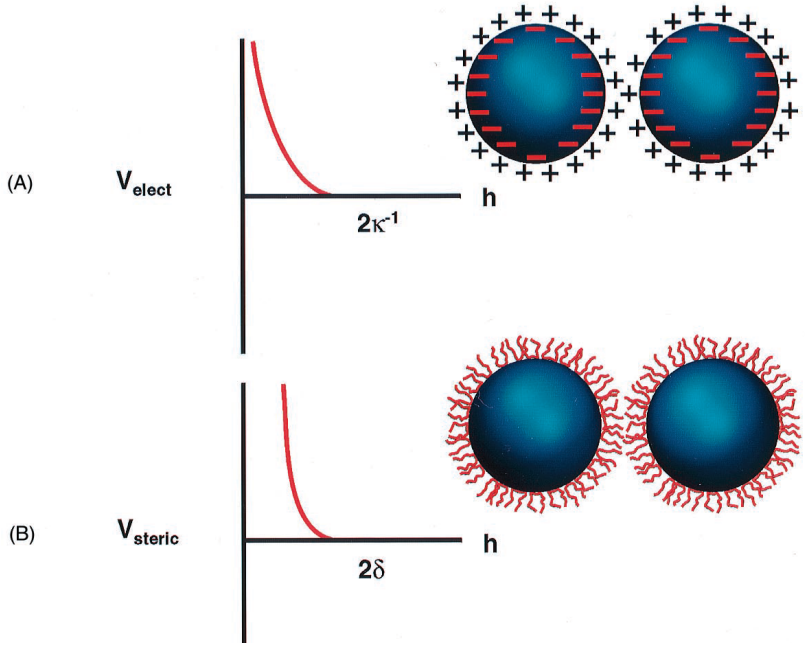

Figure 2-2 - Schematic illustration of the interaction potential energy for (A) electrostatic and (B) steric forces, where κ^{-1} is double layer thickness and δ is adsorbed layer thickness (Lewis 2001).

In some ceramic systems, creating a stable suspension simply by controlling pH is not possible since large additions of acid or base can result in dissolution of the particles or an excessive ionic strength. This way, addition of suitable polymeric dispersants is commonly used to create colloidal stable suspensions. In this approach, when two particles are covered with adsorbed polymer layers the interpenetration of the polymer layers results in a repulsive force or steric stabilization (Figure 2-2B). Thus, these polymeric additives can prevent coagulation due to this interparticle repulsion. In order to be effective, the polymer layer must be thick and dense enough to overcome the van der Waals attraction between particles and to prevent bridging flocculation (Lewis 2001).

2.1.1 Sol Gel

Sol gel processing has brought a new view in the domain of glass and ceramics fabrication (Russel-Floyd et al. 1993a; Pierre 1998). Among several ways of

ceramic matrix composite (CMC) production, this promising technique has proved to be viable and has gained its place in the field along the recent years.

Several near-net-shape forming techniques for ceramic components have been developed in which fluid slurries can be transformed into rigid bodies without liquid removal, called sol gel. These direct consolidation forming techniques include, among others, gel casting. Direct consolidation routes have the potential to transfer the high degree of homogeneity achieved in the slurry to the green state. Depending on the technique used, ceramic powders and/ or colloidal suspensions can be aqueous or nonaqueous, electrostatically or sterically stabilized (Tari 2003, Rodeghiero et al. 1998).

A colloidal suspension of solid ceramic particles (sol) may be converted to a non-crystalline gel through controlled interruption of the small interparticle forces that control sol stability. The interruption of the interparticle forces in order to achieve consolidation or gelation of the sol may take place by modification of the suspension pH or change in temperature or even pressure. The gel maybe then dried and sintered. (Russel-Floyd et al. 1993a; Chant et al. 1995a; Chant et al. 1995b; Harris et al. 1998; Hench, West 1990).

It is important to study the zeta potential and isoelectric point (IEP) of the particles to be used in the sol gel suspension in order to know the pH range in which the suspension can be manufactured, avoiding flocculation or coagulation. Zeta potential corresponds to the electro kinetic potential of particles in colloidal systems. Its value is related with the stability of the colloidal suspension, by indicating the degree of repulsion or attraction of the charged particles in suspension. If the zeta potential is zero, attraction exceeds repulsion, meaning that the particles will flocculate or coagulate. Higher zeta potential values (negative or positive) means that the particles are stable in a suspension. The isoelectric point corresponds to the pH value at which the particles are zero charged, i.e. the zeta potential is zero. At this point, the particles attract each other and coagulate due to the lack of charging and a stable suspension is no longer achieved.

Advantages of sol gel methods over conventional ceramic processing routes include high matrix homogeneity since the fine ceramic particles are intimately mixed in the colloidal state, the ability to prepare compositions which are difficult to achieve by conventional methods, and relatively low sintering temperatures as a consequence of the high reactivity from the very high surface area of the gel (Chant

et al. 1995; Statham et al. 1998; Sigmund et al. 2000; Rodeghiero et al. 1998; Tari 2003). However, its major drawback is the inherently shrinkage of the gel which occurs as the gel dries out during evaporation of the original solvent and during subsequent sintering. Non-reactive fillers and reinforcing fibers reduce the volume shrinkage to levels as low as 7% from typically 20-25% (Chant et al. 1995a; Statham et al. 1998; Chant et al. 1995b).

2.1.2 Freeze Gelation

The freeze gelation process is applied when sol gel suspensions are gelled by submitting them to subzero temperatures. The use of freeze gelation overcomes many of the limitations of sol gel processing, permitting the formation of low-cost, crack-free, typically zero-shrinkage ceramics even in the presence of high loadings of reinforcing fibers (Statham et al. 1998; Harris et al. 1998).

The freeze gelation route can be divided in four steps: preparation of the slurry, freezing, removal of solvent and sintering.

Ceramic suspensions are prepared as water-based sol and ceramic filler is added in order to improve mechanical stability and reduce shrinkage. In the homogenization step, it is very important to assure the stability of the sol gel suspension in order to avoid any segregation, which could yield in density and porosity gradients in the final material microstructure. In the case of composites, the slurry is first infiltrated into fibers and then submitted to sub-zero temperatures to force gelation. In the case of monolithic ceramics, the slurry is submitted to sub-zero temperatures directly after homogenization and shaping (Chant et al. 1995a; Statham et al. 1998; Deville 2008; Scotti, Dunand 2018).

During freezing, ice crystals are formed from the aqueous solvent of the sol with a small increase in volume caused by the transformation of water to ice. A gel is formed in the regions between the ice crystals. As freezing occurs, the particles in the slurry are rejected from the moving freezing front and piled up between the growing ice crystals. Subsequently, the frozen material is dried at temperatures slightly above ambient temperature for water removal. This step results in bulk shrinkage often below 1%, owing to low capillary stresses associated with the relatively large and open porosity, typically 1-10 μm in diameter, which results from the nucleation and growth of ice crystals during freezing. The green body is relatively weak and must,

therefore, be sintered to achieve sufficient strength. Mostly, the macro pores will be a replica of these ice crystals, while the micro pores will be a result of sintering densification of the matrix (Chant et al. 1995a; Deville 2008; Scotti, Dunand 2018).

In order to consolidate and to prevent the gel from melting during reheating to ambient temperature, it is necessary to use a freeze sensitive sol, i.e., an irreversible sol gel transformation. There are a variety of colloidal sols that are irreversible after freezing; the majority of those are silica-based sols (Statham et al. 1998; Brinker, Scherer 1990). The silica sol is consolidated by compaction of particles and formation of a three-dimensional network. Two mechanisms can promote this consolidation: gelation or coagulation. The first involves the collision of two particles and the formation of siloxane bonds (Si-O-Si) under the release of water (H_2O). In the second, a clotting agent, usually an electrolyte, acts as a "bridge" between two silica particles connecting them.

The consolidation of the sol, either by gelation or coagulation, can be influenced by factors such as pH, size and concentration of particles, presence of electrolytes and organic liquids as well as temperature (Iler 1979). With this property the silica sol can be used as a binder, avoiding the use of other hydraulic binders. The strength and consolidation of the green body is, therefore, achieved by the formation of a three-dimensional network of siloxane bonds particles and not by hydration of a binder additive (Ismael et al. 2006).

Several aspects and process parameters influence directly the freeze gelation process and the final material structure and properties. These aspects are associated with the colloidal silica sol, fillers, solidification and sintering parameters.

For the sol gel transformation, it is crucial that the particles present in the suspension are sufficiently small to remain stable in suspension and capable of relatively close packing as the growing ice crystals concentrate the colloidal particles into inter-dendritic areas during freezing. The filler that is added to the sol influences the stability and final physical characteristics of the ceramic such as its porosity. This way, filler particle size and weight fraction must be adjusted in order to achieve an optimum viscosity for infiltration of fibers or casting and for the desired porosity and mechanical strength to be achieved (Russel-Floyd et al. 1993a; Russel-Floyd et al. 1993b; Russel-Floyd et al. 1990). The study of each component pH and isoelectric point when adding ceramic fillers to the silica sol is also of importance in order to

avoid particle aggregation during suspension preparation and to optimize slurry stabilization.

A critical stage of this process is the solidification, i.e. freezing, since the characteristics of the future porosity will be determined at this step. During the formation and growth of ice crystals, ceramic particles in suspension are rejected by the moving solidification front and entrapped between the ice crystals. The pore structure is influenced then, additionally to the solvent used, by the freezing rate and the freezing direction applied (Deville 2008; Scotti, Dunand 2018).

The freeze gelation process results in a porosity gradient in the monolithic ceramic microstructure (Koch et al. 2003; Waschkies et al. 2009; Deville et al. 2010; Deville et al. 2007; Deville 2006). As the freezing front proceeds from the cooled surface to the interior of the slurry a strong gradient in the porosity is observed. An uniform and texture free microstructure with formation of ultra-fine ice crystals in the range of a few nanometers is observed in the surface close to the freezing front. With increasing distance from the cooled surface the pore size increases.

During freezing, the velocity of the liquid front decreases rapidly as the distance from the freezing front deceases until it reaches a steady state with an approximate constant value (Figure 2-3). Consequently, the first frozen zone reveals a planar ice front where the filler particles are entrapped. The ice crystals then move progressively to a columnar and eventually lamellar morphology, with a progressive ordering of the lamella. A steady state is eventually reached and ice crystals become continuous, running through the entire sample with a constant thickness (Waschkies et al. 2009). Figure 2-3 shows an example of an alumina suspension frozen at -10°C, the spacing between the former ice crystals increases dramatically as the ice crystal grow inside the ceramic material stepping away from the cooled side.

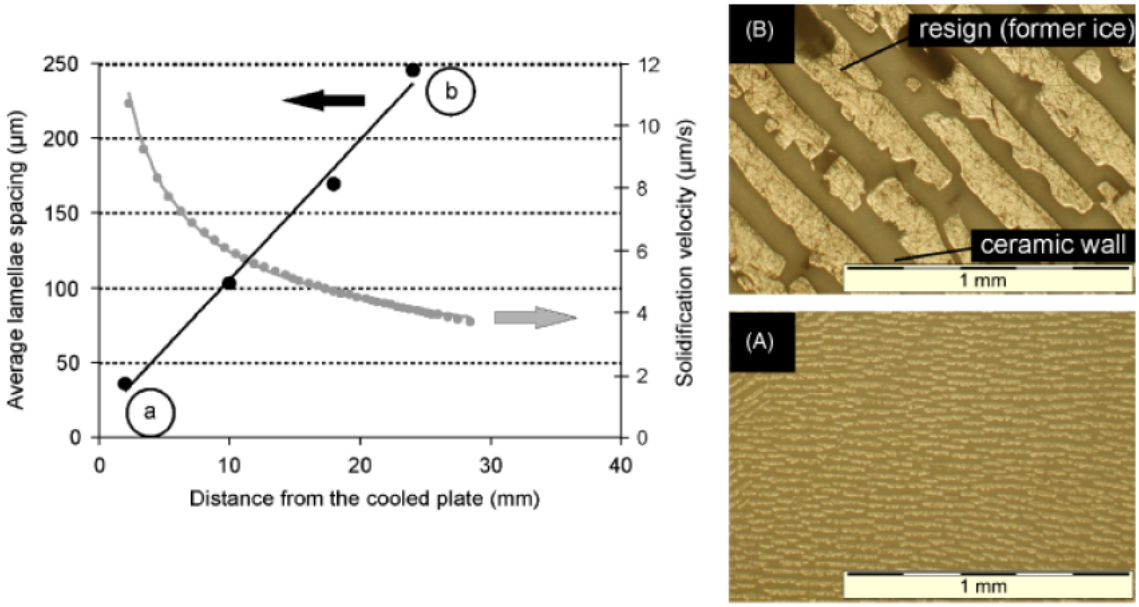

Figure 2-3 – Lamella spacing development during solidification (22 vol. % solids loading) under constant freezing conditions of -10°C (Waschkies et al. 2009).

Additionally, the size of the particles in suspension influences the ice crystals size and, consequently, the final porosity (Liu et al 2016). Figure 2-4 shows the porosity of an aqueous alumina suspension frozen with a constant cooling rate of 5K/ min until complete solidification is achieved. The smaller the filler particle size the more nucleation sites for ice crystals will be available and so several pores with smaller size will be formed (Deville et al. 2010, Liu et al 2016).

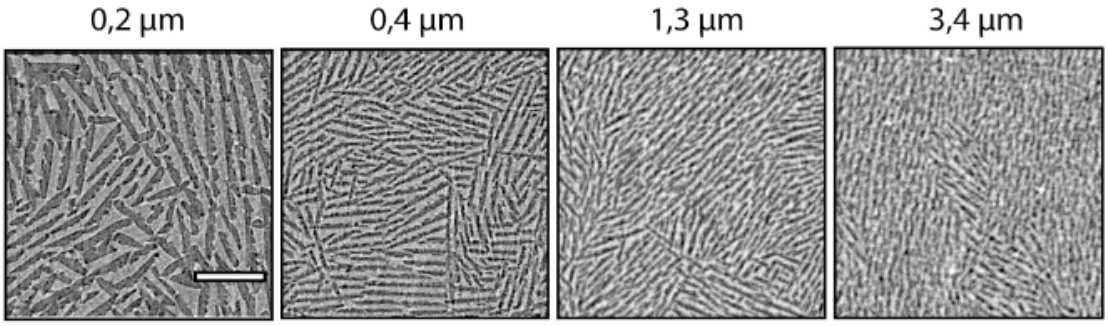

Figure 2-4 - Influence of particle size in structure porosity of aqueous alumina suspensions. Scale bar indicate 150 µm (Deville et al. 2010).

The main advantage of the freeze gelation process is the ability to form large or small complex-shaped near-to-net-shape components with multidirectional fiber reinforcement either by simple casting for short fiber reinforcement, by filament

winding for continuous fiber reinforcement or by hand lay-up for fabric weaves (Deville 2008; Glissen et al. 2000; Russel-Floyd et al. 1990; Naskar et al. 2009).

2.2 Ceramic Matrix Composites

Ceramic matrix composites (CMC) present their behavior highly dependent on its components, i.e. the combination of fiber reinforcement, fiber-matrix interface and matrix material determines the composites characteristics and performance. CMC are able to provide high strength, toughness, notch insensitivity, light weight, refractoriness and environmental stability at high temperatures. For these fields, the use of metals is commonly limited due to their low melting temperature and high density, and the use of monolithic ceramics is limited due to their very low damage tolerance. In contrast to monolithic ceramics, the ceramic matrix composites can exhibit “metal-like” or “quasi-ductile” behavior, which enables extensive stress redistribution at holes and notches. Therefore, these materials are most attractive concerning the anticipated needs of many high temperature applications (Chant et al. 1995a; Keller et al. 2005).

In this chapter, fibers and processes used for manufacture of oxide based CMCs are going to be described, as well as existent fiber-matrix designs and application fields for these materials.

2.2.1 Fibers for CMC

The fiber, the matrix, the fiber-matrix interface, the microstructure and the reinforcement orientation define the mechanical properties of ceramic matrix composites. When a suitable combination is generated using adequate manufacturing processes it is possible to obtain enhanced strength and toughness. Nevertheless, choosing the adequate fiber is important since they are the component responsible for the material reinforcement, i.e. they determine the maximum properties achievable in a composite. Fibers are characterized by their highest individual strength and stiffness properties and therefore dictate the potential of the CMC.

Furthermore, the type of fiber selected influences the manufacturing process to be used and the fiber-matrix interface to be selected. Other factors such as fiber type,

grain size, number of filaments per roving, fiber architecture and volume ratio will also influence strongly the final characteristics of the composite.

Composites can be generally reinforced with continuous fibers, short fibers, fiber mats or whiskers. For the manufacture of high-performance CMC, continuous fibers are generally used. The fiber flexibility is one of their most important characteristics once it enables their workability such as for handling matters or in the case of textile fabrication process for pre-form manufacture (such as fiber deposition, weaving, braiding and stitching) (Koch 2008). Conventionally, fibers are classified based on their composition and structure as shown in Figure 2-5.

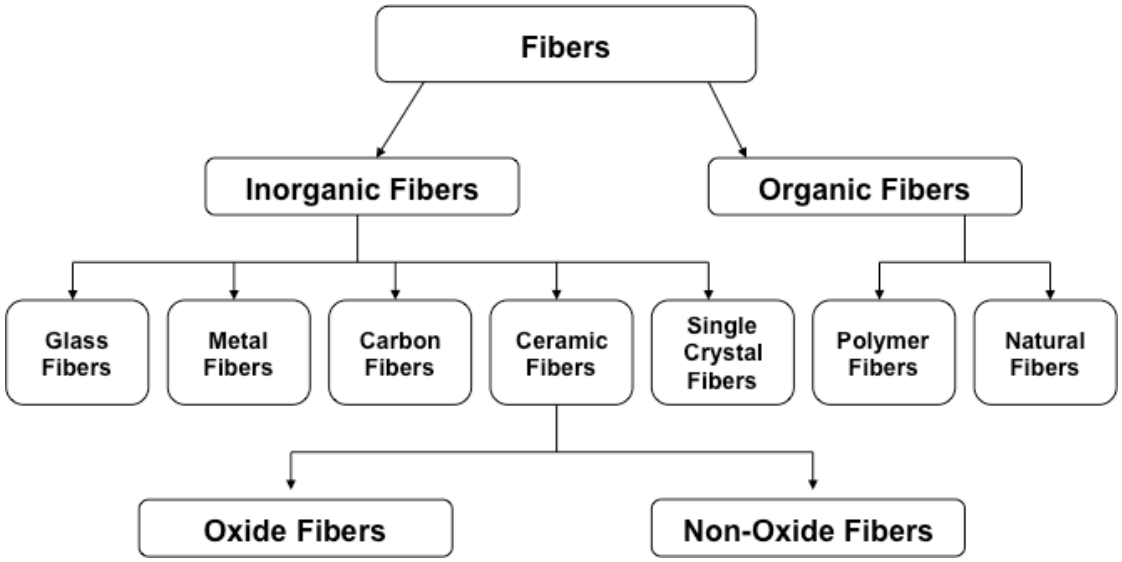

Figure 2-5 - The classification of fibers (Koch 2008).

The fibers are divided in inorganic and organic. The manufacturing process of inorganic fibers can be subdivided into direct and indirect routes.

In the indirect process the fibers are not obtained by a spinning process, instead, precursors are used to impregnate fiber shaped preforms.

In the direct process, inorganic precursors (salt solutions, sols, or precursor melts) are directly spun to form fibers. In this process, stabilization of the fibers during spinning includes progressive condensation reactions and the formation of chemical bonds in the fibers. At the end, the residual amounts of solvents and organic additives are removed via pyrolysis treatment (Wilson 2006; Clauß 2008).

Carbon fibers were the first high-performance fibers to be developed. Nowadays they provide significantly high strength, high stiffness, low density, and low

thermal expansion to the composite. In addition, carbon fibers have high thermal and electrical conductivity which make them suitable for specialized applications where thermal energy and electrical current need to be specifically controlled. They are, nevertheless, prone to oxidation.

Ceramic fibers are further classified in oxide and non-oxide fibers. Non-oxide Si-based fibers are produced by Si organic polymer precursors via melt spinning and cross-linking, the fibers are finally submitted to pyrolysis treatment for conversion to ceramic fibers.

Oxide fibers will be described in more detailed once they were used in the development of this work. Figure 2-6 shows the sol gel process used mainly in the manufacture of oxide fibers from 3M™. In this process, a sol is first formulated and concentrated in order to form a viscous gel. A precursor fiber is then spun from the gel and dried in order to remove water and increase the fiber solids content. The fiber is then transformed into ceramic fiber via pyrolysis. Coating is performed for protection, improvement of fiber stability and workability. At the end of the process the fiber is wound into a fiber roving (3M™ Ceramic Textiles and Composites; Chawla 1998).

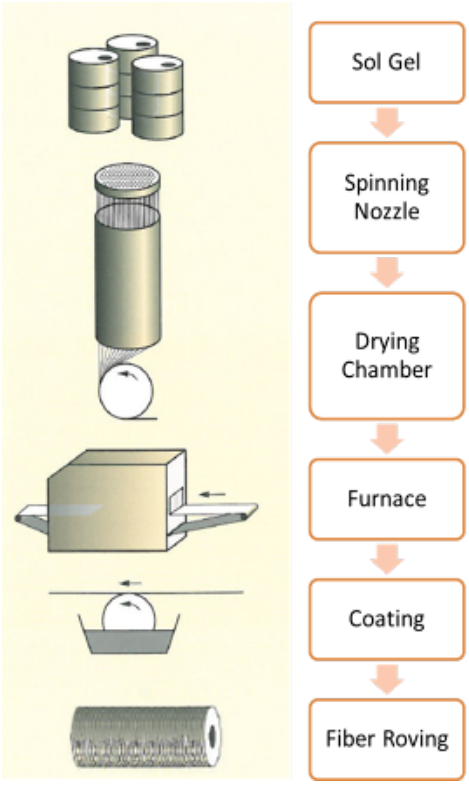

Figure 2-6 – Sol gel process to fabricate oxide based ceramic fibers (Adapted from 3M™ Ceramic Textiles and Composites).

Current commercially available oxide fibers are mainly produced with alumina (α-Al_2O_3), silica (SiO_2) or mullite ($3Al_2O_32SiO_2$). These fibers present high tensile strength and Young's modulus values and, due to their oxide nature, these fibers are stable against oxidation at high temperatures.

Pure α-Al_2O_3 fibers when exposed to temperatures above 1100°C show grain growth and pore formation. Addition of silica to the fiber composition and formation of mullite was found to decrease grain growth. Mullite located at the grain boundaries of the α-Al_2O_3 phase significantly lowers grain growth (Clauß 2008, Bunsell 2005). A negative point of oxide fibers is that they tend to form larger grains when kept at high temperatures over long time periods. The larger grains tend to grow at the expense of smaller grains because of diffusion processes at grain boundaries, leading to fiber embrittlement. Above 1200°C, the use of ceramic fibers in CMCs for long time applications is limited.

Oxide ceramic fibers are commercially available mainly from 3M™ (USA) under the commercial name of Nextel™. A variety of different fibers with different compositions and properties are available under the names Nextel™ 312, 440, 550, 650, 610 and 720 (Table 2-1). The "denier" (or "den") is a measurement unit for the linear mass density of fibers. It is defined as the mass in grams per 9000 meters of fibers. In the International System of Units, the "dtex" is used instead, which corresponds to the mass in grams per 10000 meters of fibers. Since the fibers have different densities, the denier does not indicate directly the number of filaments. For example, Nextel™ 720 fiber with 3000 den has about 900 filaments per fiber bundle, Nextel™ 610 fiber with 3000 den has about 800 filaments per fiber bundle.

In CMC, Nextel™ 610 and 720 fibers are most commonly used due to their higher strength and creep resistance in comparison to other oxide fibers. Nextel™ 610 is a pure α-Al_2O_3 fiber and it is noted for its outstanding single filament strength properties of 2600 MPa and Young's modulus of 370 GPa. The addition of small quantities of Fe_2O_3 and SiO_2 leads to very small grain sizes of about 100 nm and high strengths, however, at temperatures beyond 1000°C the fine-grained microstructure shows poor creep resistance due to grain boundary sliding. Nextel™ 720 has the highest thermal stability leading to higher creep resistance but lower strength. This fiber presents small needle like Al_2O_3 grains (70-100 nm) distributed between mullite grains (300-500 nm). Its tensile strength is of 2100 MPa and its

Young's modulus is 260 GPa (3M™ Ceramic Textiles and Composites; Wilson 2006; Wilson, Visser 2001). Since the successful creation of Nextel™ 610 and 720 fibers, no further oxide ceramic fiber has been developed by 3M™.

In Figure 2-7 a graph comparing the strength of single filaments of these two fiber types when submitted to different temperatures evidences the higher thermal stability of Nextel™ 720 in comparison with Nextel™ 610. The last, shows rapidly strength decrease after exposure to temperatures above 1000°C.

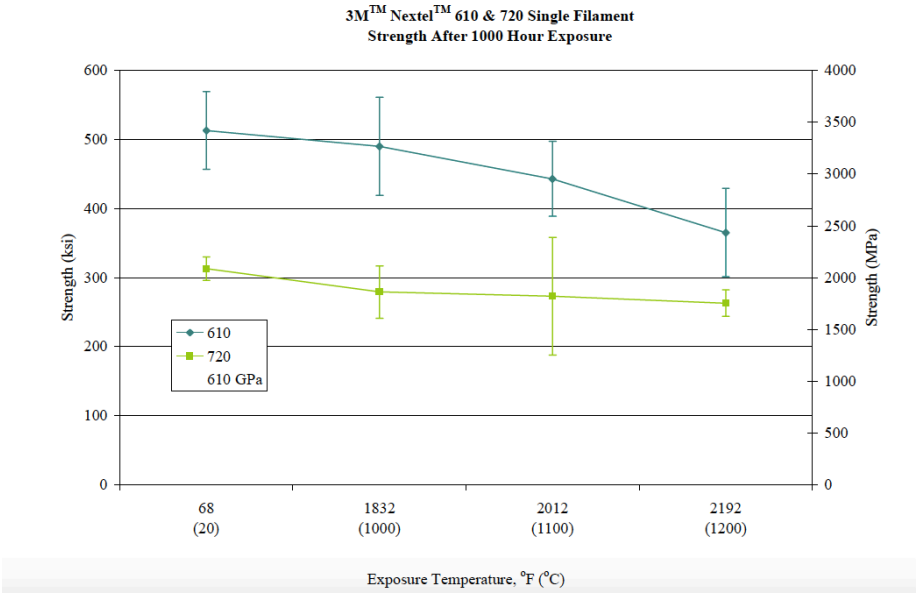

Figure 2-7 - Strength retention of Nextel™ 610 and Nextel™ 720 after exposure to temperature (3M™ Ceramic Textiles and Composites).

Besides Nextel™ fibers, single crystal alumina fibers known as *Saphikon* were also developed. These fibers are grown from molten aluminum in the edge-defined film-fed technique (EFD). They present strength of 3,5 GPa and fiber filaments with diameter of ca. 125 µm. The anisotropy and reduction in strength at lower temperatures of single crystals alumina fibers lead the company Saphikon to produce directionally solidified YAG-alumina fibers by the edge defined film method. YAG-alumina filaments do not show the reduction in strength observed at single crystal alumina fibers. At room temperature these fibers present values of Youg's modulus of 344 GPa and values of strength ranging from 1350 to 2400 MPa with short term strength retention up to 1500°C (Bansal 2005).

CeraFib GmbH is a company founded in 2006 in Germany that produces alumina and mullite fiber filaments. Their fibers called CeraFib 75 (mullite) and

CeraFib 99 (alumina) are available commercially and offer properties (Table 2-1) comparable to the Nextel™ fibers. No study on the creep resistance of this fiber has been done yet. CeraFib is improving their fibers to enhance its spin-ability, i.e., reduce filament breakage during coiling of fiber bundle (Petzold et al. 2011). Since 2011 no further developments of this fiber have been reported.

Table 2-1 - Important properties of selected oxide ceramic fibers (3M™ Ceramic Textiles and Composites; Bansal 2005; Petzold et al. 2011).

Fiber Trademark (Producer)	Composition (wt. %)	Diameter (µm)	Density (g/cm³)	Tensile Strength (MPa)	Young's modulus (GPa)
Nextel™ 720 (3M™)	85% Al_2O_3 15% SiO_2	10-12	3,4	2100	260
Nextel™ 610 (3M™)	99% Al_2O_3	10-12	3,9	3100	380
Nextel™ 550 (3M™)	73% Al_2O_3 27% SiO_2	10-12	3,03	2000	193
Nextel™ 440 (3M™)	70% Al_2O_3 28% SiO_2 2% B_2O_3	10-12	3,05	2000	190
Nextel™ 312 (3M™)	62,5% Al_2O_3 24,5% SiO_2 13% B_2O_3	10-12	2,7	1700	150
Saphikon (Saphikon)	$Y_3Al_5O_{12}$-Al_2O_3	125	-	1350-2400	344
CeraFib 75 (CeraFib GmbH)	75% Al_2O_3 25% SiO_2	10-12	3,1	2200	200
CeraFib 99 (CeraFib GmbH)	99% Al_2O_3	10-12	3,8	2900	370

2.2.2 Processes to Fabricate Ceramic Matrix Composites

In this chapter, methods of fiber preform fabrication and matrix infiltration will be reported. Special attention will be given to the filament winding technique and the ceramic slurry infiltration (CSI) method once these processes were used for the manufacture of composite materials in this work.

Fiber Preform Fabrication

Fiber preform can be classified into 2- or 3- dimensional preforms. According to the various textile techniques available, the fibers can be processed and classified through different techniques such as weaving, braiding, winding or stitching.

The 2D woven fabrics are more commonly used where good in-plane properties, drapability, and large area coverage are required. Two-dimensional fabrics are commonly used in fabrication of engine nozzle structure, thermal protection systems, and other relatively non-complex hardware with relatively low out-of-plane loading requirements. The 3D structure has excellent damage tolerance, improved shear property performance and designed specific strength and stiffness. The fabrics can be divided into different bond types, each with a different weaving sequence between weft and warp thread (Figure 2-8). Generally, when the fiber deflection is increased the form stability and the handling of fabrics are improved but, on the other hand, the mechanical properties of composites are decreased (Knoche 2010).

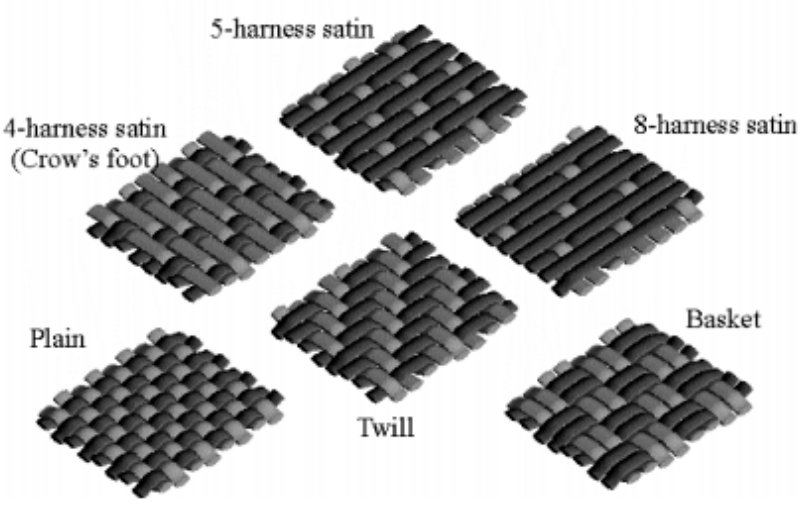

Figure 2-8 - Different weave architectures available for fiber preforms manufacture (Department of Defense 2002).

Another way to produce fiber preforms is via braiding. Its advantage is based on the ability to fabricate textile preforms with different lengths, diameters and different fiber architectures. Braiding has been more commonly used with carbon fibers although research developments with ceramic fibers have already been done (Stobbe 2010, Türk 2011). In Figure 2-9 a circular braiding machine from Herzog

Machine Factory GmbH & Co KG, Germany is shown. It has 144 bobbins and a fully automated handling robot from KUKA Robots GmbH, Germany.

Figure 2-9 – Robot-assisted circular braiding machine at Airbus Group Innovations, Germany.

The filament winding technique is characterized for producing preforms with different geometries, with considerable geometrical accuracy, reproducibility and generally high fiber volume fractions. Additionally, this technique allows the fabrication of rotation symmetric products such as pressure vessels, shafts, containers, pipelines, radomes, turbine thrusters, and combustion chambers. Differently to other techniques, in filament winding, slurry infiltration is done simultaneously to fiber lay-up.

The filament winding process consists basically in the infiltration of fiber bundles through immersion into a matrix suspension bath. The fiber bundles are conducted under controlled tension through an eye and wound onto a rotating mold (mandrel) in a prescribed path. More sophisticated machines allow winding of up to three fiber bundles simultaneously, as well as the use of two infiltration baths for more homogeneous slurry infiltration into the fiber inner filaments (Figure 2-10).

For better performance and quality of the final winded component several aspects during filament winding must be brought in attention. Some of these aspects are:

- the control of the tension in the fiber bundle must be maintained constant throughout the process;
- the fiber alignment has to be assured;
- the rollers leading the fiber to the mandrel and infiltration rollers must roll constantly and equally for homogeneous slurry infiltration;

- the distance between fiber bundles after lay-up must be adjusted to fiber type, slurry system and tool geometry to avoid fiber gap or overlapping.

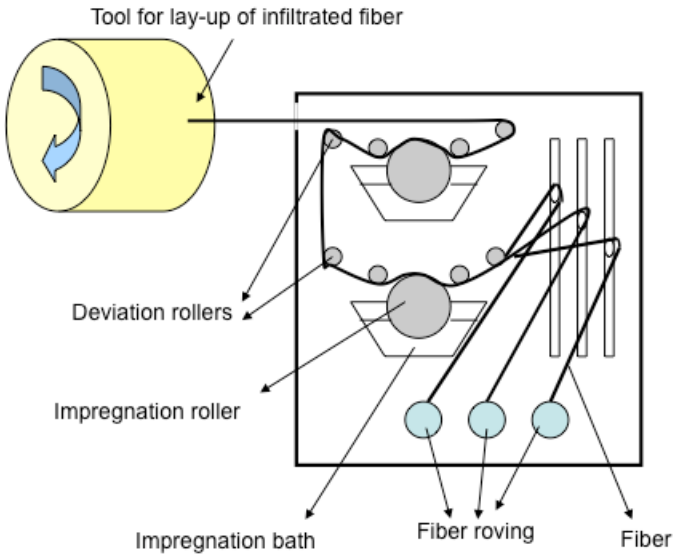

Figure 2-10 - Filament winding process schema exemplifying the fiber roving infiltration and lay-up at a rotating mandrel.

Filament winding machines are often equipped with a computer-aid positioning sequencer. On Figure 2-11 a fully automated robot assisted with 6+2-axis winding machine is shown. With this machine ceramic matrix composites in this work are manufactured at Airbus Group Innovations in Germany.

Figure 2-11 - Robot assisted 6+2-axis filament winding machine at Airbus Group Innovations.

Three-dimensional structures can be manufactured by expanding 2D preforming techniques via the stitching process (Figure 2-12). The process enables high flexibility for example of fiber volume ratio, arrangement, insertion and loop

formation. Additionally, different fiber types can be used, but more often carbon fibers are used. The loop formation is of particular influence on CMCs properties such as interlaminar or tensile strength. Furthermore, the use of this process influences the infiltration behavior since additional channels for matrix incorporation are obtained.

Figure 2-12 - Robot assisted stitching machine for CMC preforming available at Airbus Group Innovations.

Matrix Infiltration Methods

The composite matrix, as well as the fibers used are very important when determining the type and properties of the composite. The matrix has a fundamental function as load distribution by internal friction mechanisms between fiber and matrix, likewise it enables quasi-plastic and the damage tolerant behavior of the composite. The fabrication method used to bring the matrix together with the fibers influences the final material properties since the infiltration degree and the ceramic yield varies with the infiltration route used.

The processing routes for matrix infiltration can be divided into polymer infiltration pyrolysis (PIP), chemical vapor infiltration (CVI), liquid silicon infiltration (LSI) and ceramic slurry infiltration (CSI). These processes as well as their advantages and disadvantages are described in this section.

Polymer Infiltration Pyrolysis (PIP)

The polymer infiltration and pyrolysis (PIP) method comprises the infiltration of a low viscosity polymer into the fiber structure followed by pyrolysis. Under pyrolysis, the polymer precursor is heated under inert atmosphere and transformed into ceramic due to decomposition.

The infiltration of the fiber with the polymer precursor can be done either by resin transfer molding (RTM) or via filament winding technique. On the RTM process the fiber preform is placed into a mold with the form of the component. Once the mold is closed, the polymer is injected into the cavity. The infiltration process is driven by capillary forces and is therefore commonly conducted at normal pressure but it may also be vacuum or pressure assisted. When the filament winding technique is used one layer of fibers in UD direction (prepreg) can be manufactured. The final material can be obtained by cutting the prepreg with the desired geometry, the prepreg is then laminated by stacking them with the desired fiber architecture (Figure 2-13).

After infiltration of the fiber preform via RTM or fiber filaments via filament winding, the material is submitted to thermal treatment during which polymer cross-linking takes place. Alternatively to thermal treatment, the cross-linking can also be initiated by radiation (γ-rays or electronic beam). Laminated prepregs are cured under vacuum in an autoclave, the cross-linking temperature normally varies from 100°C to 200°C under pressures from 5 to 20 bars. For cross-linking in the RTM process similar temperatures are used but depending on the mold lower pressures are applied (Knoche 2010; Koch et al. 2008a; Schmidt et al. 2008).

Following, the material is pyrolysed under inert atmosphere for decomposition of the organic based polymer at temperatures between 800°C to 1300°C. Volatile products such as CO, Hydrogen (H_2), CO_2, CH_2, H_2O are released as a result of pyrolysis, forming a porous structure of the emerging ceramic matrix. The ceramic yield is determined by the composite weight loss. The density of the porous ceramic formed can be further increased by subsequent re-infiltration cycles. The number of necessary infiltrations to reduce porosity and increase density can be reduced when ceramic fillers are added to the matrix composition.

This process offers several advantages such as prevention of fiber damage due to low processing temperatures, it allows good control of the matrix composition and the microstructure, fabrication of near-net-shape parts and matrices of various compositions (silicon carbide, silicon nitride, silicon carbonitride) may be obtained. On the other hand, the process has relatively high production costs and time due to the multiple re-infiltration pyrolysis cycles applied (Kopeliovich 2010, Kopeliovich 2018). Also, residual silicon is found in the matrix after pyrolysis.

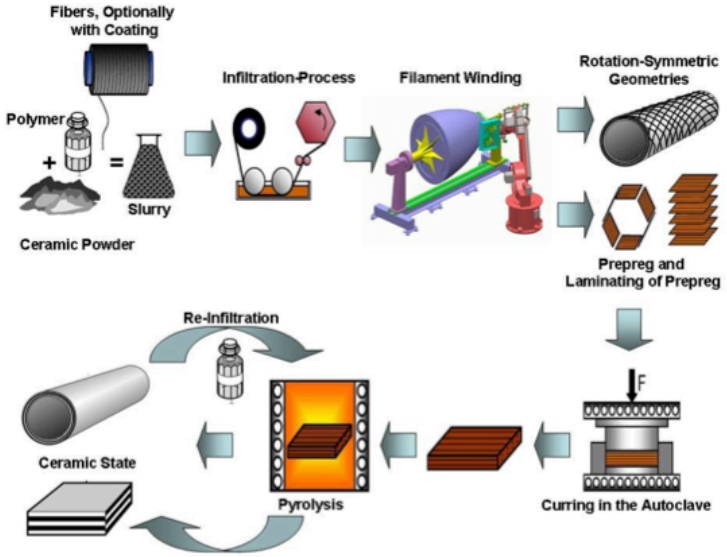

Figure 2-13 - Process steps of the PIP route for the fabrication of CMC.

Chemical Vapor Infiltration (CVI)

Chemical vapor infiltration (CVI) is a process in which reactant gases diffuse into a heated fibrous preform and react to solid phase on the fiber surface. The infiltration of the gaseous precursor into the reinforcing fiber structure (preform) is driven either by diffusion or an imposed external pressure. The deposition fills the space between the fibers, forming a composite material in which the matrix is the deposited material and the dispersed phase is the fiber preform (Figure 2-14). Chemical vapor infiltration is similar to chemical vapor deposition (CVD), by which a deposit is formed when the reactant gases react on the outer substrate surface.

Modified CVI processes have been developed with the aim of reducing the time needed for infiltration and to achieve progress in near-net shaping and tailoring the matrices and interphases. These modified processes include radio- or microwave-frequency assisted CVI, pressure-pulsed CVI, forced-flow CVI and rapid CVI (Knoche 2010).

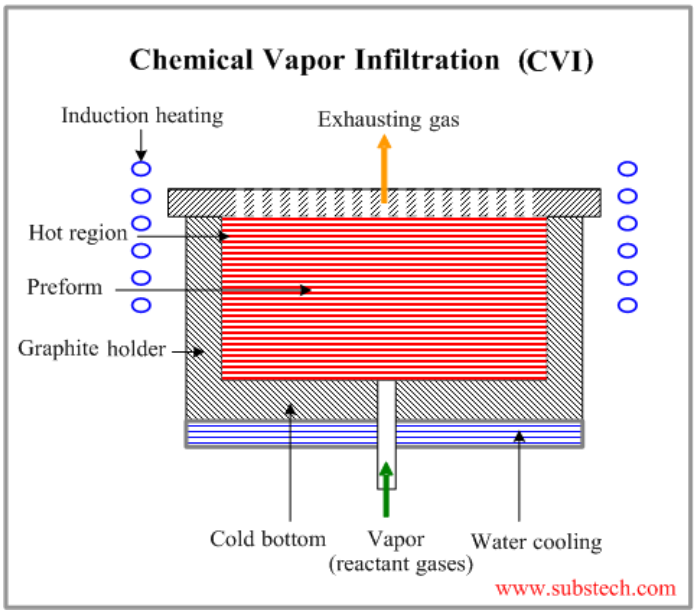

Figure 2-14 – Illustration of a chemical vapor infiltration (CVI) reactor (Kopeliovich 2010).

The CVI process offers advantages such as low fiber damage due to relatively low infiltration temperatures, fabrication of matrices of high purity, generation of low residual stresses due to low infiltration temperatures, materials with enhanced mechanical properties (strength, elongation, toughness), good thermal shock resistance and possibility of matrices fabrication with various compositions (SiC, C, Si_3N_4, BN, B_4C, ZrC, etc.). Nevertheless, due to the slow processing rate, very long process times have to be stated (may continue up to several weeks depending on the material thickness) and the process involves high initial capital and production costs (Kopeliovich 2010b, Kopeliovich 2018).

Liquid Silicon Infiltration (LSI)

In this process a green body is firstly made by infiltrating high-carbon precursors into a fiber preform. Using roving infiltration and subsequent winding techniques or CFRP methods such as RTM enables near-net shaping. After precursor curing, the material is pyrolysed under nitrogen atmospheres or vacuum at temperatures between 800°C and 1200°C. During the process, volatile products are released and a porous carbon structure is formed.

Subsequently, the preform is infiltrated with molten silicon or silicon alloys. The melted silicon enters into the porous structure driven by capillary forces. The melt reacts with carbon forming silicon carbide according to the reaction: Si (liquid) + C

(solid) → SiC (solid). SiC produced by this reaction fills the preform pores and forms the ceramic matrix.

In contrast to the composites fabricated by PIP and CVI, ceramic matrices formed by liquid silicon infiltration are fully dense (have zero or low residual porosity). Additionally, it is a low cost technique with short production times, which allows the fabrication of complex and near-net-shape composites with thermal and electrical conductivity.

Ceramic Slurry Infiltration (CSI)

In the ceramic slurry infiltration (CSI) technique liquid slurry is used to infiltrate fiber preform or fiber roving via filament winding. Capillary forces drive the infiltration process and water and/ or sol gel based slurries may be used.

Water based slurries contain dispersed ceramic fillers, binder, dispersing and/ or wetting agents. Ceramic fillers normally used are alumina (Al_2O_3), silica (SiO_2), glass, mullite ($3Al_2O_32SiO_2$), silicon carbide (SiC) or silicon nitride (Si_3N_4). These slurries are, after infiltration within the fibers, consolidated via hot pressing. Hot pressing is performed at high temperature and increased pressure, which enhances the intrusion of the ceramic material into the fibers structure. The particles consolidate resulting in low porosity densified composites with good mechanical properties. The reinforcing fibers may be, however, damaged by the high pressure applied in the hot pressing stage. In addition, hot pressing requires relatively expensive equipment and allows the fabrication of only small and simple parts.

Alternatively, sol gel based suspensions can be used for the fabrication of CMC. Colloidal suspensions containing fine ceramic particles of up to 100 nm are dispersed into water or organic solvent. Ceramic fillers such as alumina and mullite may be added to the suspension in order to increase the material strength and reduce porosity and shrinkage. The suspension is infiltrated into the fibers using, for example, filament winding technique and consolidated via gelation.

At elevated temperatures, sols containing organometallic compounds (e.g. alkoxides) undergo cross-linking (polymerization) by either the polycondensation or hydrolysis mechanism. Polymerization converts sol into gel and the gels may be transformed into ceramics at relatively low sintering temperatures, which reduces the probability of fiber damage. After gelation, the material must be dried for removal of

water or the organic component. Re-infiltration with sol followed by drying and sintering may be conducted if higher densification of the material is desired.

The gelation or consolidation of the ceramic suspension takes place, nevertheless, not only by elevating temperature but also, for example, by application of pressure, pH change or submission of the material to temperatures below zero degree, i.e. the freeze gelation technique (Chapter 2.1.2).

2.2.3 Mechanical Fracture Behavior

High performance ceramic matrix composites are known for their good mechanical performance and oxidation resistance at high temperatures and oxidative environments. Nevertheless, in order to achieve high fracture toughness and damage tolerance, the fiber/ matrix interaction can be optimized.

The ceramic fibers are responsible for reinforcing the component since they represent the highest strength achievable in the composite. The matrix, on the other hand, is responsible for holding the fibers together. The main defects that lead to crack initiation are found in the composite matrix. These defects, such as microcracks, pores and inhomogeneities, are often generated as a consequence of the fabrication process.

The basic requirement to obtain tough composites is that cracks initiated in the matrix do not propagate into fibers, but bypass them by deflecting into fiber-matrix debonding cracks. This requires a fiber/matrix interface sufficiently weak to fail before the fiber. The most common approach is the use of fiber coating to promote crack deflection and frictional sliding along the fiber-matrix interface (Figure 2-15a), these materials are termed weak interface composites (WIC). In a second approach the fiber and the matrix have strong bonds but the matrix is weak and susceptible to multiple cracking while the fibers maintain their high stiffness and strength to assure the composite crack tolerance (Figure 2-15b). These materials are termed weak matrix composites (WMC) (Naslain et al. 2001; Zok, Levi 2001, Ramdane et al. 2017).

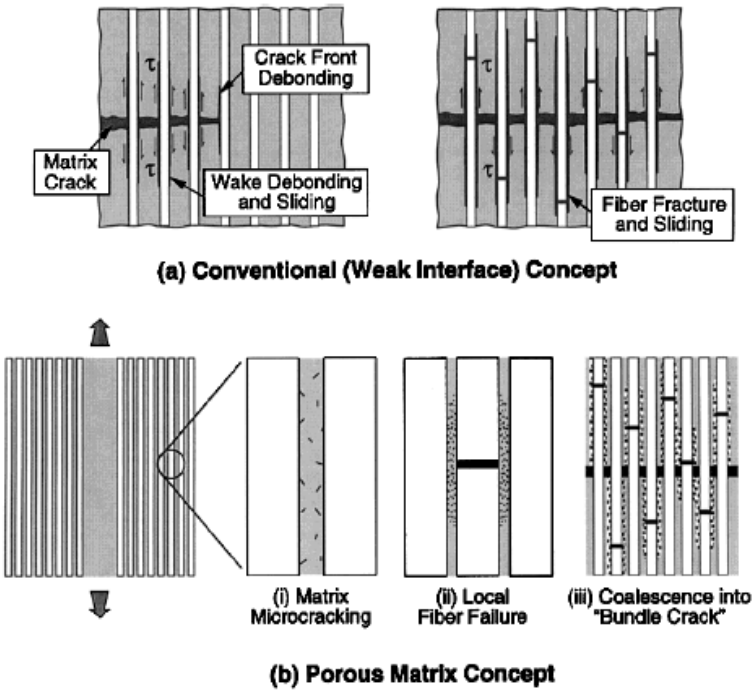

Figure 2-15 - Schematic of the damage processes that enable damage tolerance, weak interface concept (a) and weak matrix concept (b) (Zok, Levi 2001).

In any case, the fracture energy (Γ) between interface (i) and fiber (F) has to be controlled, as showed by He and Hutchinson (Figure 2-16). In this model, brittle failure occurs when the fracture energy ratio of interface and fiber exceeds a limit. For non-brittle behavior a ratio $\Gamma_i/\ \Gamma_F \leq 0.25$ must not be exceeded if the fiber and matrix have similar Young's modulus. As an example, for a CVI derived CMC, where the Young's moduli of the fiber and the matrix are similar, a fiber coating is required to lower its relative fracture energy $\Gamma_i/\ \Gamma_F$ for a non-brittle behavior, being this composite characterized as WIC (Knoche 2010; Koch et al. 2008c; He, Hutchinson 1989).

The two approaches to achieve high fracture toughness in CMC are further described in the following.

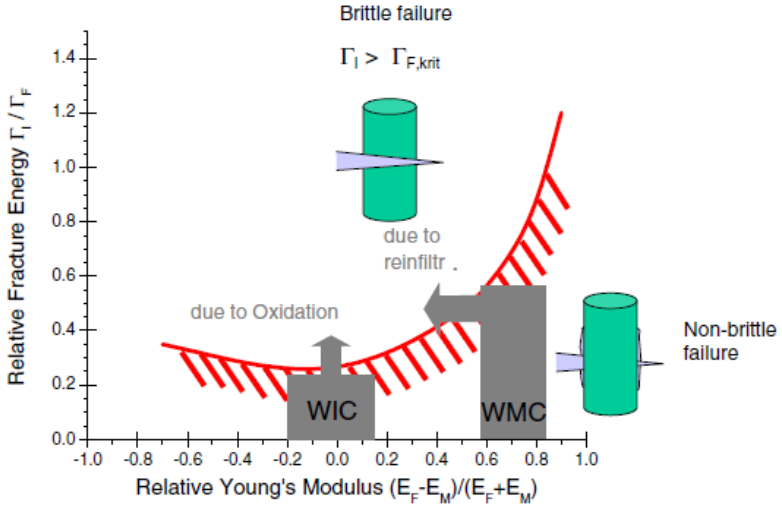

Figure 2-16- He & Hutchinson plot indicating the fracture energy required for non-brittle failure (He, Hutchinson 1989), modified (Knoche 2010).

Weak Interface Composites (WIC)

In this approach, when the composite is loaded in tensile mode, the initial crack propagates first in the matrix and through the composite, being bridged by the strong fibers which remain intact as the stress concentration at the interface does not induce fiber failure but rather initial fiber-matrix debonding. In the debonding area the stresses are carried by the fibers across the crack surface and, as a consequence, shear stresses are induced in the fiber-matrix interface promoting progressive debonding. These stresses are partly transferred to the matrix by friction between fiber and matrix. Beyond the matrix cracking strength, the composite is still able to resist load until the fibers begin to fail, the composite maximum strength is reached when about 15 to 30% of the fibers have failed. As a consequence of the energy dissipation in the fiber-matrix interface, fiber pull-out and bridging are formed in contrast to brittle materials where fibers are directly sheared in the plane of the matrix leaving no hint for energy dissipation mechanisms and damage tolerance (Figure 2-17) (Koch 2008; Knoche 2010; Koch et al. 2008a).

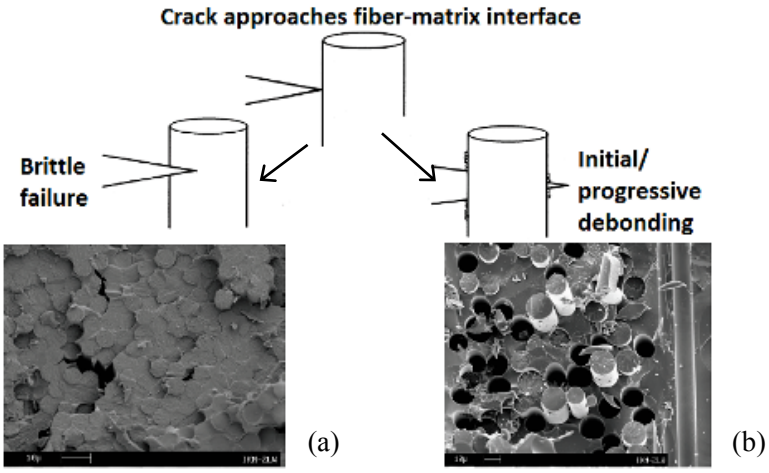

Figure 2-17 - Microstructures of a WIC composites showing brittle failure (a) and fiber pull-out after fracture (b) (Koch 2008).

Ideally, the micro-mechanical mechanism will determine the macro-scale behavior of the composite. Figure 2-18 shows a tensile testing curve of idealized WIC as well as its mechanical failure sketches corresponding to each stage of the test. In the beginning of the process, within the linear-elastic stage (1) the fiber and matrix are equally strained. In this stage microcracks in the matrix may occur but they are stopped by the fibers and do not affect the original stiffness of the composite. Beyond a critical stress level, inelastic contributions to the curve appear from further debonding and cracking bridging (2a and 2b). The load is increasingly transferred to fibers and, after fiber failure is initiated, a continuous decrease of the Young's modulus of the composite is observed (3). The failure of most fibers (4) is then reached leading to a drop in the load. Small residual strength is observed in form of fiber pull-out, although this is a minor effect compared to the composite strength and regarding practical applications (Koch 2008; Knoche 2010).

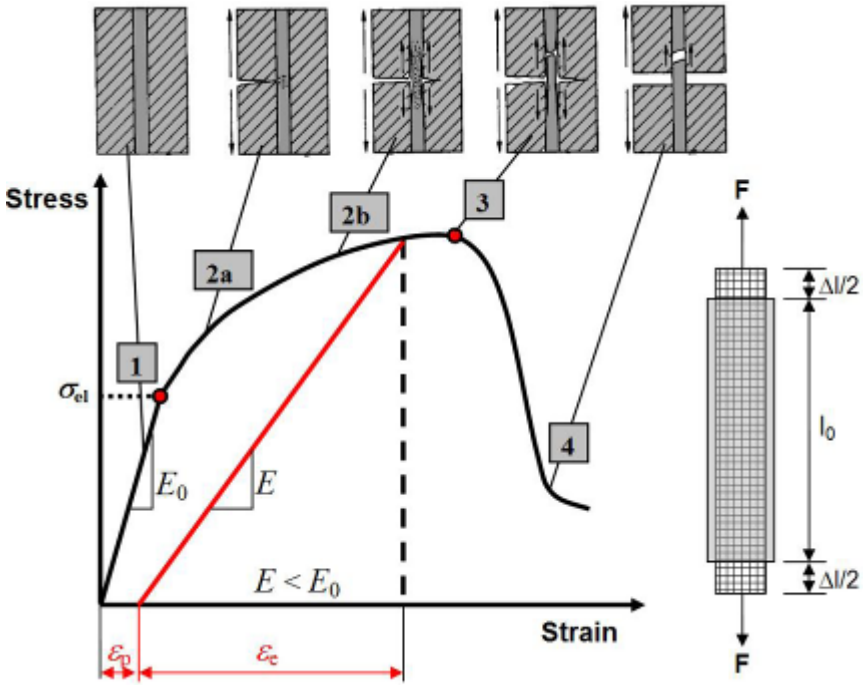

Figure 2-18 - Idealized stress-strain behavior of a WIC during tensile testing related to the correspondent micro-mechanical damage mechanism (Knoche 2010).

In weak interface composites fiber coating is used to promote debonding. The interface coatings should be chemically and microstructurally stable at the desired operational conditions. The coating should also be thermodynamically stable with the fiber substrate and the surrounding matrix, resisting solid-state reactions. Also, it should be resistant to oxidation, corrosion and steam. As coating composition, mainly pyrocarbon is used as fugitive coating.

These coatings are applied to the fiber and are burned-out after processing leaving a gap between fiber and matrix, then the crack kinks along the matrix and the gap. Fugitive carbon coating in dense composites with calcium aluminosilicate matrix manufactured with Nextel^{TM} fibers has been shown to be useful once the composite retains approximately 80% of their as processed strength after long-term heat treatment (in air at 1000°C for 500 h) (Keller et al. 2000). Studies in oxide based composites have shown as well that under notched tensile test the strength of a composite with fiber coating was approximately 25% higher than the strength from the same composite without fiber coating (Weaver et al. 2008).

In the last ten years weak interphases made of e.g. boron nitride, barium zirconate and monazite have been investigated in CMCs (Chawla 2008; Venkatesh 2002; Chen et al. 2002; Boakye et al. 2011; Davis et al. 2000; Keller et al. 2003). In composites with Nextel^{TM} fibers and alumina matrix, application of monazite ($LaPO_4$)

coatings presented strength of ca. 230 MPa in un-notched and notched specimens and extensive fiber pull-out was observed at each side of the notch (Davis et al. 2000).

Materials used in porous interphases must be chemically compatible with fibers and matrix. Porous interphases fracture in the same way as weak interphases. Zirconia, mullite and alumina have been demonstrated as suitable porous interphases for composites (Haslam et al. 2000; Nubian et al. 2000; Lewis et al. 2000; Holmquist et al. 2000; Weaver et al. 2008). Within these materials, zirconia is of particular interest, as it does not sinter to alumina based fibers and matrix as it is the case for an alumina or mullite interface (Newman 2002).

Weak Matrix Composites (WMC)

In the absence of fiber coating, the matrix must be sufficiently weak to enable damage tolerance under loading and still retain adequate strength. This way, crack deflection is controlled using fine scale porosity in the matrix and the fiber/ matrix interface does not need to be specified in a particular way. Since the porous matrix is not able to carry significant high loads, the mechanical performance of these materials is strongly dominated by the fiber and by the composite fiber architecture. Therefore, mechanical performance depends on loading direction, being the highest strength manifested in axial direction (0°/90° fiber orientation) and low strength in off axis direction, for example in ± 45° fiber orientation (Figure 2-19) (Knoche 2010; Zok, Levi 2001).

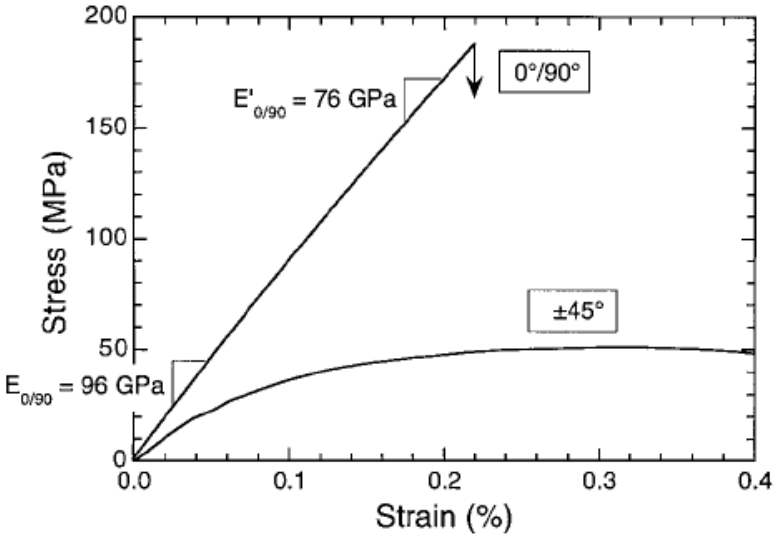

Figure 2-19 - Typical tensile properties of a porous mullite-alumina matrix carbon fiber reinforced composite in 0°/90° and ±45° orientarion (Zok, Levi 2001).

In porous matrix composites, fiber pull-out occurs in a different manner compared to composites with adjusted fiber coating. Differently to WIC, where fiber pull-out phenomena can be easily recognized, in porous composites these events are often not as obvious. Instead, most of the matrix between the fibers can be missing or still attached to the fiber, demonstrating that the matrix has fragmented during loading. Figure 2-20a shows a fracture surface area where only fibers and matrix fragments still bonded to the fibers can be seen. In Figure 2-20b, a different area from the same specimen shows a relatively brittle fracture mode where fibers and matrix fractured at the same plane, indicating that the crack energy dissipated in both the matrix and the fiber (Lange 2010).

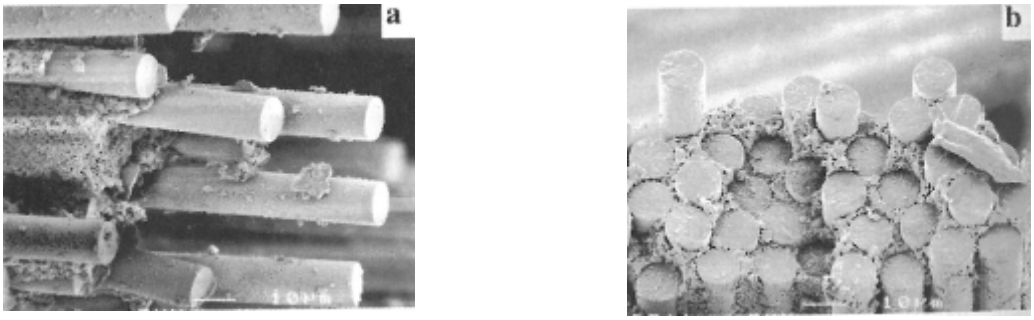

Figure 2-20 - Porous matrix CMC showing a region with fiber pull-out (a) and a region where fiber and matrix fractured at the same plane (b) (Lange 2010).

Improvements in the interlaminar properties of WMC can be obtained by reducing the matrix porosity by re-infiltrating the composite. This would consequently lead to a reduction of damage tolerance of the composite under fiber-dominated loadings. It was shown (Lange 2010) that the tensile strength of 0°/90° cloth laminate CMC continuously decreased with increasing density. At the same time, the length of the fiber pull-out became smaller and disappeared as the matrix became sufficiently dense and was not able to separate the fibers from the matrix by cracks, as the WMC area in Figure 2-16 demonstrates.

The amount of matrix porosity necessary to promote crack dissipation is an important matter. The optimum porosity where the matrix is still capable to transfer load to the fibers, thus retaining a suitable ILS and off-axis in-plane strength, remains still to be established. This value of matrix porosity has been suggested in several literatures to be approximately 30 vol. % (Levi et al. 1999; Davis et al. 2000; Kerans R.J. et al. 1999).

2.2.4 Applications

Oxide and non-oxide ceramic matrix composites can be found in several applications such as friction elements as bearings, brakes for automotive and aerospace sector, furnace and burner components, propulsion systems, thermal protection systems and combustion chambers for gas turbines.

In propulsion systems, carbon reinforced silicon carbide (C/SiC) manufactured via the polymer infiltration and pyrolysis process are mostly used. In rocket nozzle extension they offer simplified cooling design, reduction of component mass, potential to increase payload capabilities, substitution of metal materials to expand the operation temperature, increased performance and reliability. At Airbus Defense and Space (former EADS-Astrium), a C/SiC subscale nozzle extension on the ratio 1:5 for Ariane 5 main engine “Vulcain” was manufactured (Figure 2-21a). Figure 2-21b shows a “Vulcain” subscale nozzle extension during hot test at temperatures up to 2300 K with extreme thermal gradients (Schmidt et al. 2004, Schmidt et al. 2005).

Another example of propulsion applications is the small thruster (Figure 2-22) from Airbus Defense and Space, manufactured with C/SiC composite via the PIP route for the development of the European Apogee Motor (EAM).

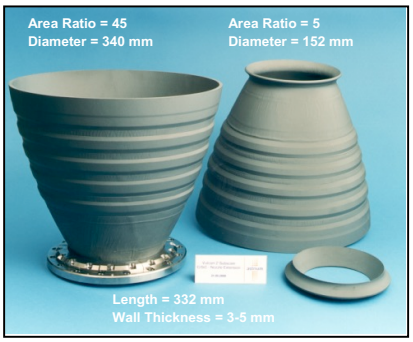

(a)
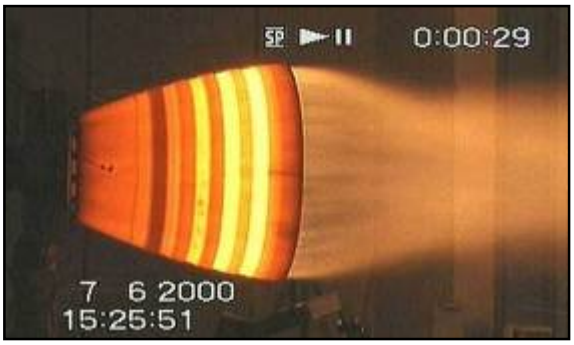

(b)

Figure 2-21 - Vulcain subscale PIP-C/SiC test nozzle extension in ratio 1:5 (a) and test nozzle under hot test (b).

Figure 2-22 - European Apogee Motor (EAM) production model manufactured via the PIP route at Airbus Defense and Space.

Additionally, C/SiC composites as well as oxide based composites can be applied in hot structures (HS) and thermal protection systems (TPS). The main objective of TPS and HS is to protect space vehicles from harsh environments during operation, especially at re-entry. Thermal protection systems are responsible for protecting the vehicle's main structure against overheating and transfer a limited amount of mechanical loads only. Hot structures have to accomplish both thermal protection and mechanical functions. Reusable TPS and HS structures have to fulfill current requirements from different European and German programs such as robust design with high structural and functional reliability for all mission relevant phases, stability against oxidation within the required lifetime, withstand rain erosion and moisture absorption, provide lightweight structures and allow easy inspection and low maintenance effort. In reusable launch vehicles (RVL) different composites are used for various applications as shown in Figure 2-23. Highest loaded areas as leading and trailing edges and nose caps demand the use of carbon reinforced CMCs, in

other regions oxide CMCs, metallic TPS or even fibrous insulations can be implemented.

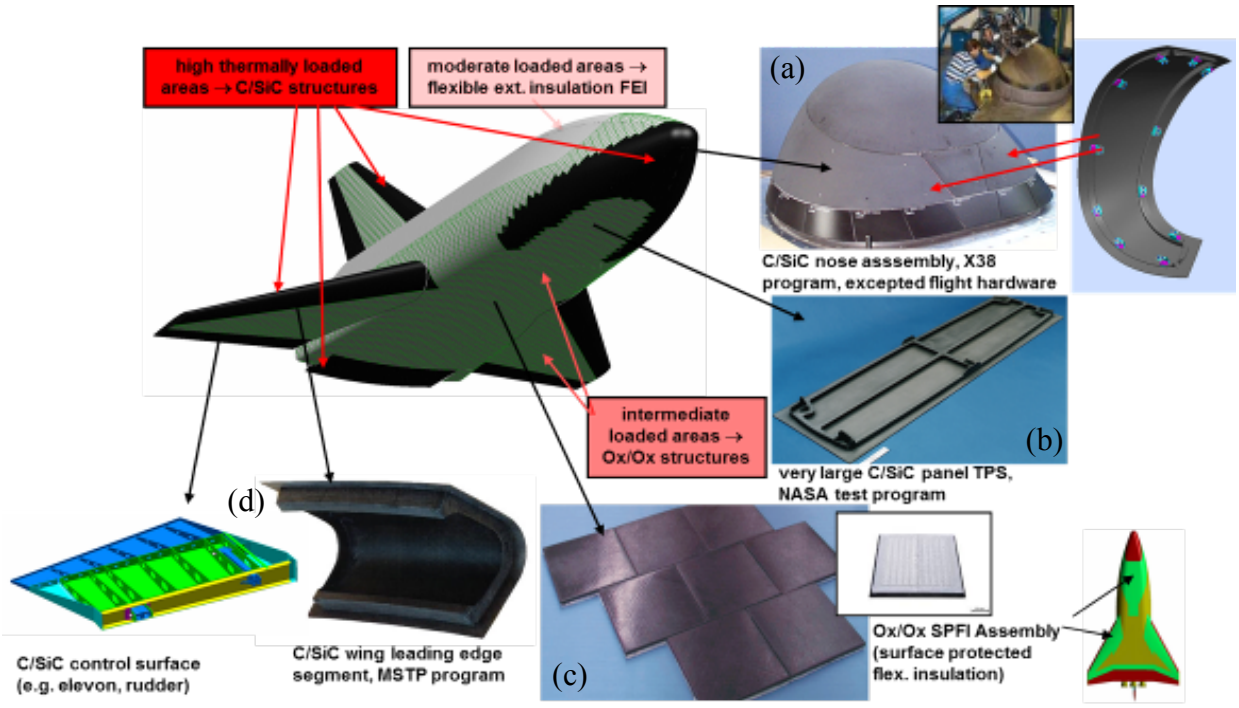

Figure 2-23 - Reusable launch vehicle concept with indicated application areas for TPS and HS and potential CMC solutions, (a) X-38 C/SiC Nose Assembly, (b) C/SiC large panel TPS, (c) oxide CMC TPS and (d) C/SiC wing leading segment (Trabandt et al, 2005; Behrens, Müller 2004).

Due to the high temperature stability of oxide CMCs, compared to conventional metals, higher component operating temperatures are possible leading to improved fuel efficiency. The cooling air saved because of a reduced demand for hot section component cooling could be redirected to lean out the combustor prime zone and reduce the formation of NO_x. The reduction in cooling air enables higher firing temperatures improving engine efficiency and CO_2 emissions are significantly reduced (Gerendas et al. 2011; Roode et al. 2005, Meyer, Waas 2018).

Mainly, fiber reinforced ceramics are likely to be used in static components such as turbine seal segments and combustor liners. In the early 1990s, Rolls-Royce has already started evaluating fiber reinforced ceramics for seal segment in a Trent 800 engine, although a metallic solution was chosen for production.

During the last 20 years at the former Dornier GmbH and now Airbus Group Innovations an oxide based composite named UMOX^{TM} has been developed. This

composite was already successfully flight tested with a Do 228 aircraft jet engine equipped with exhaust components, as shown in Figure 2-24.

Figure 2-24 - Do 228 aircraft jet engine (left) equipped with exhaust cone and nozzels manufactured with UMOX^{TM} (right).

In aerospace applications such as gas turbines intensive developments have been made. Two oxide composites named UMOX^{TM} and WHIPOX^{TM} where developed, instrumented and tested in the high pressure single test facility at DLR – Cologne. Both composites are manufactured with Nextel^{TM} 610 fibers 3000 denier (details to matrix and manufacturing route are given in Chapter 2.3). The CMC combustors were tested under pressure, temperature and air-fuel ratio being representative for an aero-engine on a regional airplane. Figure 2-25 shows the UMOX^{TM} combustor after testing. The test was conducted at temperatures above 2000K and aborted when pressure inside the chamber significantly increased, the relevant test parameters represent around 90% of the maximum take-off thrust of the performance cycles (Gerendas et al. 2013).

Figure 2-25 – Combustion chamber manufactured with UMOX^{TM} after high temperature test.

Oxide ceramic composites find applications also in the thermal treatment industry in furnaces, heat exchangers, hot gas valves, insulators and burners. Keramikblech® (Figure 2-26) and WHIPOX™ (Figure 2-27) are widely applied. Keramikblech® is manufactured with Nextel™ 610 fiber mats and sol gel or water based ceramic slurries and it has recently been successfully used to manufacture a component from an unmanned aircraft Jetoptera J55 that took the skies (Pritzkow 2018). WHIPOX™ use was demonstrated to build a flight recorder protector fitted on the spacecraft ATV-5 that, during re-entry into the earth's athmosphere, burned up with exception of the flight recorder protector (WPX Faserkeramik GmbH, 2016).

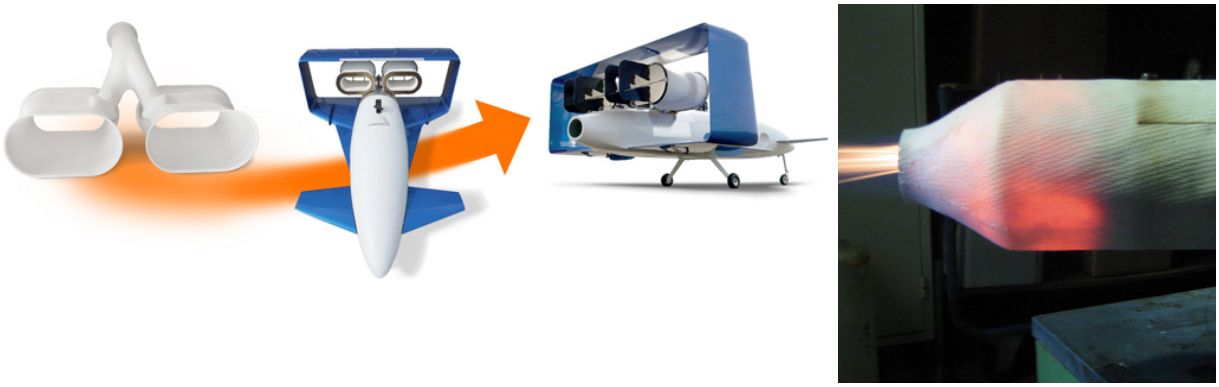

(a) (b)

Figure 2-26 – Unmanned aircraft component manufactured with oxide composite Keramikblech® (a) and as flame tube during operation (b) (Pritzkow 2018, Pritzkow 2008).

Figure 2-27 – Flight recorder protector made with WHIPOX™ (WPX Faserkeramik GmbH, 2016).

2.3 State-of-the-Art Ceramic Matrix Composites

It is mainly within Germany and United States where the main achievements in the field of CMC have been accomplished so far using different manufacturing techniques to approach the same goals: the manufacture of near-net-shape CMCs with good mechanical performance. In this chapter the major developments are described according to the matrix system used: pre-ceramic, water and/ or sol gel based matrices.

2.3.1 Pre-ceramic Based Ceramic Matrix Composites

UMOX™ – European Aeronautic Defence and Space Company (EADS)

UMOX™ matrix is based on a commercial mullite powder and a polysiloxane precursor. Continuous alumina fibers Nextel™ 610 or mullite fibers Nextel™ 720 (3M™, USA) are used as reinforcement. In UMOX™, organic fiber coating is used as fugitive interface (Clauß 2008; Newman, Schäfer 2001).

This composite is manufactured using the PIP (Polymer Infiltration Pyrolysis) process. A fully automated 6+2 axis robot controlled filament winding process is used to lay-up unidirectional layer (prepreg) of impregnated fiber bundles or rotation symmetric components. The basics of the PIP process are explained in Chapter 2.2.2.

The CMC presents fiber volume content from 48-50 vol. % with 10-12 vol. % porosity and density of 2.4-2.5 g/cm^3. When configured with Nextel™ 610, 3000 denier, fiber architecture of 0°/90°, the material presents a tensile strength of 180 MPa, flexural strength of 257 MPa and interlaminar shear strength (ILSS) of 11 MPa (Volkmann et al. 2014, Volkmann et al. 2015). When manufactured with Nextel™ 720, 3000 denier, the composite with the same configurations presents tensile strength of 96 MPa and ILSS of 9 MPa. Interlaminar shear strength values are from four-point short bending measurement.

No further developments of this composite have been published after 2015.

OXIPOL™ – German Aerospace Center (DLR)

OXIPOL™ is an Oxide CMC based on polymers. This composite is manufactured using the PIP route with a polymer based matrix. It is manufactured via RTM (resin transfer molding) and subsequently pyrolyzed under inert atmosphere. This composite was traditionally manufactured with Nitivy weave fabric 2626P. During the last years it has been further developed with Nextel™ fiber mats (3M™) typically Nextel™ 610 and 720.

Mechanical characterization of OXIPOL™ manufactured with Nextel™ 610 shows tensile strength of 135 MPa, flexural strength of 201 MPa, shear strength of 43,5 MPa, interlaminar shear strength (four-point short bending) of 5,6 MPa, density of 2,58 g/cm³ and porosity of 8,58 vol.% (Gerendas et al. 2011, Volkmann et al. 2014, Volkmann et al. 2015).

After 2015, no further developments of this material have been published.

2.3.2 Water and/ or Sol Based Ceramic Matrix Composite

WHIPOX™ – German Aerospace Center (DLR)

WHIPOX™ (Wound Highly Porous Oxide CMC) is manufactured with a highly porous mullite or alumina matrix and Nextel™ fiber bundles (Nextel™ 610 and 720) using the filament winding technique.

Mullite or alumina powder is dispersed in a de-ionized water based solution containing binder, surfactant, emulsifier and liquefying agent. The suspension has a solids content of 30-45 wt. %, viscosity lower than 0.07 Pa.s and pH higher than 6,6 (Göring et al. 2007).

The infiltration of the fiber bundles with the water-based slurry takes place during the filament winding process. In this process, the fiber sizing is first burned-off in a tube furnace. Fiber bundles are then mechanically spread apart and infiltrated with the slurry. Afterwards the bundles pass through a microwave furnace to partially dry the water based slurry and consequently increase the overall matrix content. The fiber is subsequently wound on a rotating mandrel (see Figure 2-28). The green body is dried and pressure-less sintered at ca. 1300°C in air resulting in composites with a

fiber content of around 50 vol. % (Kanka, Schneider 2000; Schneider et al.; Gerendas et al. 2011, Vaseschko, Flucht 2018).

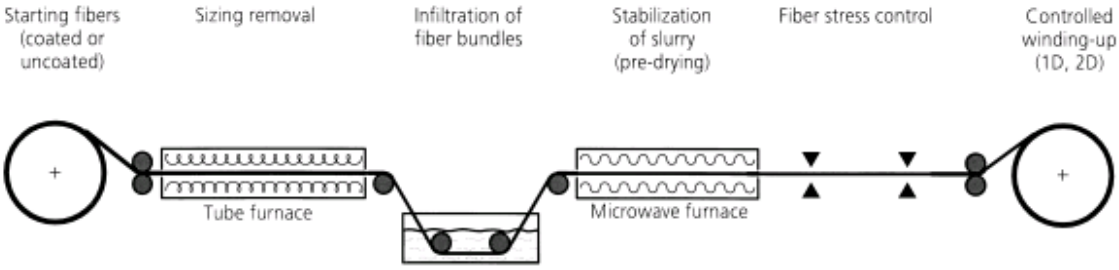

Figure 2-28 - Schema of the filament winding route used to fabricate WHIPOX™ (Kanka, Schneider 2000).

Mechanical properties of WHIPOX™ with Nextel™ 610 and Nextel™ 720, both with 3000 denier in different fiber orientations are summarized in Table 2-2. Both composites present a fiber volume content of approximately 37 vol. % and density of 2,82 g/cm³. Interlaminar shear strength was measured under four-point short bending.

Nowadays, WHIPOX™ is commercially available via the German company WPX Faserkeramik GmbH.

Table 2-1 - Main properties of WHIPOX™ fabricated with different Nextel™ fibers, alumina matrix and different fiber architecture (Gerendas et al. 2011, Volkmann et al. 2015).

Fiber/ Matrix	Fiber Architecture	Tensile Strength (MPa)	Flexural Strength (MPa)	ILSS (MPa)
Nextel™ 610/	0°/90°	110	-	12
Nextel™ 610/	±30°	170,5	284	15
Nextel™ 720/	0°/90°	50	-	12

University of California - Santa Barbara

At the University of California in Santa Barbara, USA, continuous fiber ceramic composites were developed using Nextel™ 610 and Nextel™ 720 fiber mats. The matrix is water based with mullite particles (average particle size 1 µm) packed between and within the fibers. Alumina particles (particle size ca. 200 nm) are then added to fit into the voids of this network. (Levi et al. 1998; Carelli et al. 2002; Heathcote et al. 1999).

Intensive investigations concerning filler effects on microstructure, porosity, in plane mechanical performance, interlaminar properties, creep resistance, effects of thermal aging and performance of un-notched and notched specimens have been done in this composite (Levi et al. 1998; Carelli et al. 2002; Heathcote et al. 1999; Mattoni et al. 2001; Lange et al. 1995; Fujita et al. 2004; Zok 2006; Cox, Zok 1996).

Tensile strength of a composite infiltrated 4 times with 0°/90° fiber orientation is approximately 240 MPa and 130 MPa for Nextel™ 610 and 720, respectively. Interlaminar properties tested under three point bending on specimens in 0°/90° orientation (with Nextel™ 610) shows first nonlinearity at 8 MPa. Delamination occurs mainly through the matrix regions between the fiber layers and the peak stresses can be seen between 8-10 MPa. Similar behavior is observed at samples with Nextel™ 720 where nonlinearity occurs at low stresses but the ultimate shear strength is approximately 8 MPa (Levi et al. 1998).

COI Ceramics

COI Ceramics is a company located in San Diego, California, United States collaborating mainly with Air Force, NASA and Boeing. It provides a series of advanced ceramic products that meet the needs of high temperature applications in both aerospace and industrial markets. Their CMC products are based on sol gel derived matrices and Nextel™ fiber products. COI composites belong to the very few commercially available oxide based ceramic matrix composites.

It can be manufactured through two different routes and using fiber fabrics or continuous fibers, usually Nextel™ (Figure 2-29). The matrix is fabricated from an aqueous sol and filler particles from the Al_2O_3/ SiO_2 system. When ceramic fabrics are used the material is impregnated with the ceramic slurry and laminated in a mold with the desired number of layers and fiber architecture. Fiber bundles are infiltrated and wound into the desired shape and fiber architectures via filament winding. The laminated or wound part is consolidated in the autoclave with application of temperature and pressure ($T < 150$ °C, $p < 6{,}8$ bar) and is further de-molded and sintered at temperatures between 990 and 1150 °C. If desired the component can be further mechanically finished (COI Ceramics).

Mechanical properties of these composites with different configurations (fiber and matrix) are shown in Table 2-3. A standard COI composite presents 0°/90° fiber orientation, 10 layers of an eight hardness satin weave, aluminosilicate matrix and no

re-infiltration. The higher tensile strength (365 MPa) and interlaminar shear (15 MPa) properties are observed when aluminosilicate matrix and Nextel™ 610 fiber is used. With Nextel™ 720 fiber the aluminosilicate matrix presents tensile strength of 220 MPa and ILSS of 14,3 MPa (COI Ceramics). No further developments of this oxide CMC could be found in the literature.

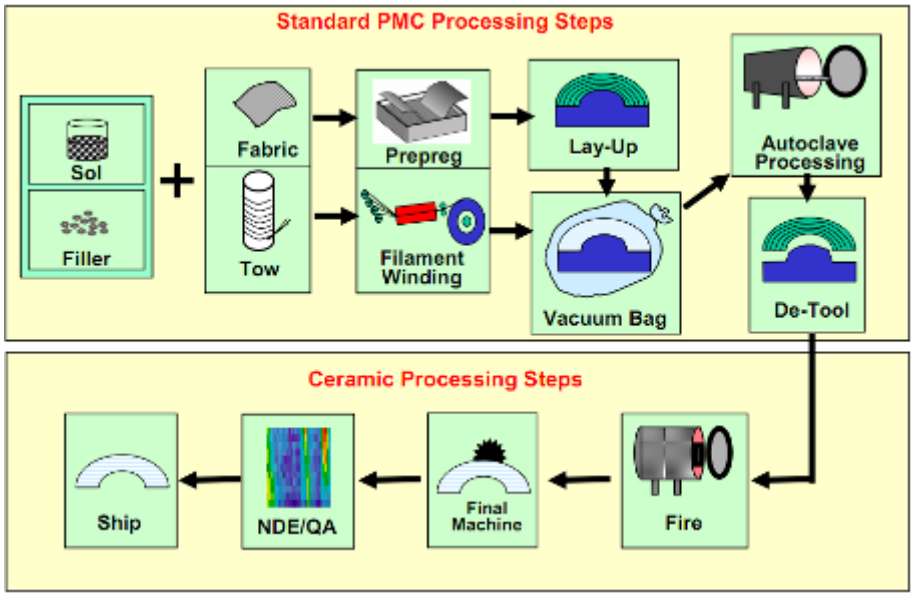

Figure 2-29 - Oxide CMC manufacturing process scheme from COI Ceramic (COI Ceramics).

Table 2-2 - Typical properties of oxide CMCs from COI Ceramics (COI Ceramics). AS indicates aluminosilicate matrix and A alumina matrix. N represents Nextel™ fiber and the subsequent number indicates the fiber type.

Property	AS-	AS-	A-	AS-	AS-
Composite Density (g/cm^3)	2,30	2,60	2,73	2,80	2,83
Nominal Fiber Volume (%)	48	45	45	39	51
Open Porosity (%)	24	25	25	25	25
Young's Modulus (GPa)	31	76	70	96	124
Tensile Strength (MPa)	124	220	169	261	365
Short Beam Shear Stregth(MPa)	9,0	14,3	12,5	-	15,0
Thermal Expansion (10^{-6}/K)	4,8	6,3	6,0	8,0	8,0
Maximum Application Temperature	650	1100	1200	1000	1000

Keramikblech – Walter E. C. Pritzkow Special Ceramics

"Keramikblech" or "sheet ceramic" is the material based on oxide fabrics and oxide matrix manufactured at Walter E.C. Pritzkow Special Ceramics, Germany.

In Figure 2-30 the fabrication process of this CMC is presented. The matrices are first manufactured based on aqueous slurries from the Al_2O_3/ SiO_2 system or on organic sols (Al_2O_3/ SiO_2/ mullite/ 8YSZ) and filler powders (Al_2O_3/ SiO_2). The fibers used are mainly Nextel^{TM} fabrics. After hand infiltration and lamination of the fiber fabrics, the material is dried, de-molded and subsequently sintered at temperatures between 1000°C and 1300°C. Re-infiltration with aqueous or organic sols is provided if required. After each re-infiltration step sintering must be conducted (Pritzkow 2001; Pritzkow 2008; Pritzkow et al. 2005, Tushtev 2016).

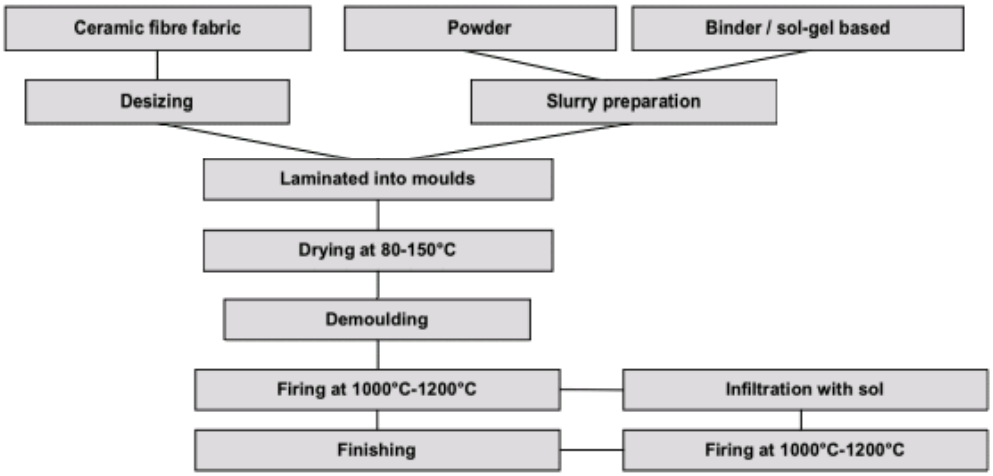

Figure 2-30 - Schema of the fabrication process of “sheet ceramic” from Walter E. C. Pritzkow Special Ceramics (Pritzkow 2008).

Initially, this composite when made with 4 layers of Nextel^{TM} 610 fabrics and a mullite based sol gel ceramic matrix, a tensile strength of 152 MPa was achieved, as well as bending strength from 260-300 MPa and interlaminar shear strength of 4 MPa (Pritzkow et el. 2005).

In further materials development, a composite with its ceramic matrix based on mullite as the main component (particle size less than 2 µm) and alumina with smaller particle sizes (0,2 µm) was produced and called AvM1415N. A second composite with alumina as the main matrix component (particle size from 0,5 to 0,8 µm) and zircon oxide containing particle sizes lower than 0,1 µm was also developed and called FVV12. Under four-point bending an ultimate strength slightly higher than 300 MPa for FVV12 and approximately 150 MPa for AvM1415N was determined.

Recently, further developments in water based alumina ceramic matrices have been done in a collaborative work together with the Fraunhofer Institute ISC,

Germany. In this work several ceramic powders with different particle sizes were investigated as well as their influence on the porosity, shrinkage and interlaminar properties of the composites. In this study it was stated that a matrix with Al_2O_3 and ZrO_2 provide higher interlaminar shear strength than only Al_2O_3 based matrices. Additionally, these composites did not require further re-infiltration steps. Table 2-4 summarizes the mechanical performance achieved by these CMCs throughout its development. Interlaminar strength was measured via three-point bending test (Rüdinger, Pritzkow 2012; Pritzkow et al. 2015).

After 2016, no further developments of this material have been published.

Table 2-3 - Mechanical properties of oxide CMC from Walter E. C. Pritzkow Special Ceramics made with Nextel™ 610 fiber fabrics (Rüdinger, Pritzkow 2012*; Pritzkow et al. 2015**, Tushtev 2015**).

Matrix	Fiber Volume %	Bending Strength (MPa)	Young's Modulus (GPa)	ILSS (MPa)
Al_2O_3/SiO_2 **	35-40	150-200	-	12
Al_2O_3/ZrO_2 **	35-45	300-500	-	20
Al_2O_3- ZrO_2-type I*	-	410	80	25
Al_2O_3- ZrO_2-type II*	-	370	90	30
Al_2O_3 *	-	350	80	10

Daimler Chrysler AG

At the Daimler Chrysler AG an oxide CMC started to be developed in 2001 using colloidal processing to manufacture its ceramic matrix. This technique uses the inherent properties of the colloidal suspensions to transform a fluid suspension into a solid green body.

As reinforcement Nextel™ 610 and Nextel™ 720 fiber fabrics are used and no fiber coating is needed since the damage tolerance is obtained by the porous-matrix approach. Figure 2-31 shows a flow chart from this manufacturing route. At first the mullite powder with average particle size of 1 µm is added to water and additives together with a nano powder (d_{50} > 100 nm). The addition of acid or base allows the development of electric double layer repulsion between the oxide particles. After lamination of the fiber bundles the component is formed using hand lay-up and vacuum bagging. The material is dried at ambient temperature and sintered in air at temperatures higher than 1200°C (Simon, Danzer 2006; Simon 2005).

The consolidation of the suspension is achieved by changing its pH. At the beginning the suspension has pH 4. With addition of AlN powder at the end of suspension preparation (step 1 in Figure 2-31), pH is shifted slowly to 9,5. The pH change occurs in approximately 4 hours, leaving time for material lamination (Simon 2005).

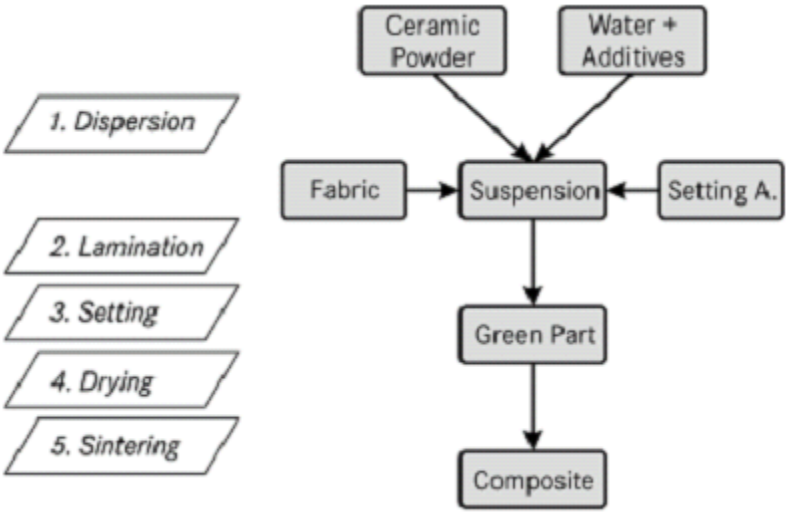

Figure 2-31 - The colloidal route used to manufacture oxide/ oxide composite samples at Daimler Chrysler AG (Simon 2005). Setting A. stands for setting agent.

This process was conducted with both Nextel^{TM} 610 and 720 fiber woven resulting in good mechanical properties, but only laboratory composites were manufactured. Table 2-5 shows the main properties for both composites produced with this technique, where N610/M means use of Nextel^{TM} 610 fiber and a mullite matrix and N720/M uses Nextel^{TM} 720 fiber and mullite matrix. Interlaminar shear strength was measured under three-point bending.

Table 2-4- Main properties from the composite manufactured using colloidal technique and fiber woven at Daimler Chrysler AG (Simon 2005).

Composite	Density (g/cm³)	Fiber Fraction (vol. %)	Porosity (vol. %)	Tensile Strength (MPa)	ILSS (MPa)
N610/ M	2,7 ± 0,05	48 ± 1	23 ± 1	290 – 310	12,5 – 14
N720/ M	2,4 ± 0,05	45 ± 1	25 ± 1	195 – 205	10 – 11,5

University of Bath, United Kingdom

In the early 90's the manufacture of ceramic matrix composites using the freeze gelation technology was investigated. Early studies report the use of colloidal suspensions for the preparation of monolithic ceramics by a freeze casting route where different sols with different particle sizes (without addition of ceramic filler) were investigated (Statham et al. 1998; Laurie et al. 1992). Freeze gelation was then used to manufacture ceramic matrix composites. Primarily, studies evolved the use of different fibers such as glass, carbon, Si-based and Al_2O_3 fibers that were infiltrated via different techniques, such as filament winding, resin transfer molding, hot pressing, casting or injection molding (Figure 2-32) (Russel-Floyd et al. 1990; Harris et al. 1998).

Moreover, extensive work in analyzing the freeze gelation process parameters and their influence on the final composite properties were conducted leading to a substantial knowledge on the gelation of colloidal sols, influence of fillers amount and particle sizes, as well as on sintering and infiltration process steps (Russel-Floyd et al. 1990; Russel-Floyd et al. 1993b; Russel-Floyd et al. 1993a).

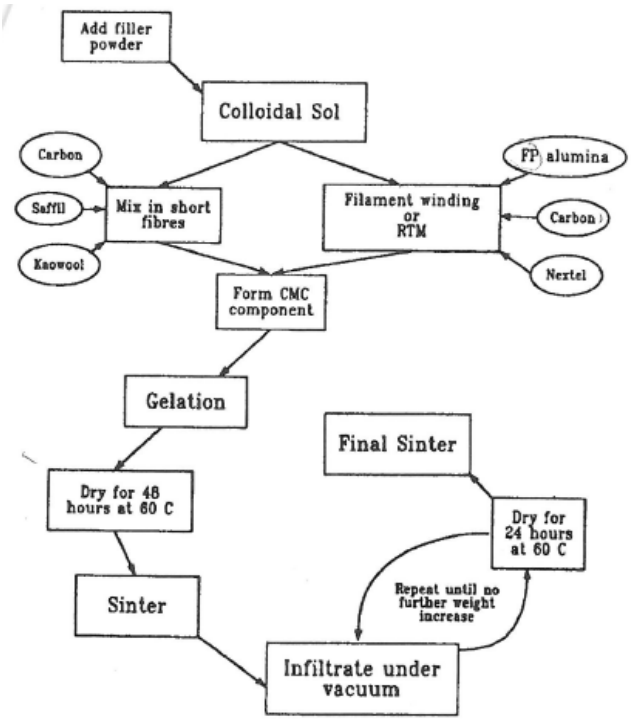

Figure 2-32 - Schematic of possible manufacturing processes of CMC with sol gel matrix system (Russel-Floyd et al. 1990).

The matrix was first developed using colloidal silica sol systems with average particle size of 125 nm with dried amorphous silica and glass fillers and/ or colloidal silica sol with average particle size of 25 nm with dried amorphous silica and quartz fillers. The suspensions were used to impregnate carbon fiber T300 via filament winding and produce unidirectional composites (Figure 2-33). After winding in a hexagonal mandrel, liquid nitrogen was poured into the mandrel to cause freeze gelation of the matrix. After thawing to room temperature and drying at 40°C, test specimens were cut and infiltrated under pressure with colloidal silica with particle size of approximately 7 nm and sintered at 600°C in argon. Samples were infiltrated seven times and sintered after each time at temperatures of 600°C, 750°C, 900°C, 1100°C and 1400°C (Chant et al. 1995a; Chant et al. 1995b).

Unidirectional composites made with amorphous silica and glass ceramic filler showed bending strength of approximately 150 MPa. In the composites made with amorphous silica and quartz filler bending strength of up to 200 MPa was observed (Chant et al. 1995a).

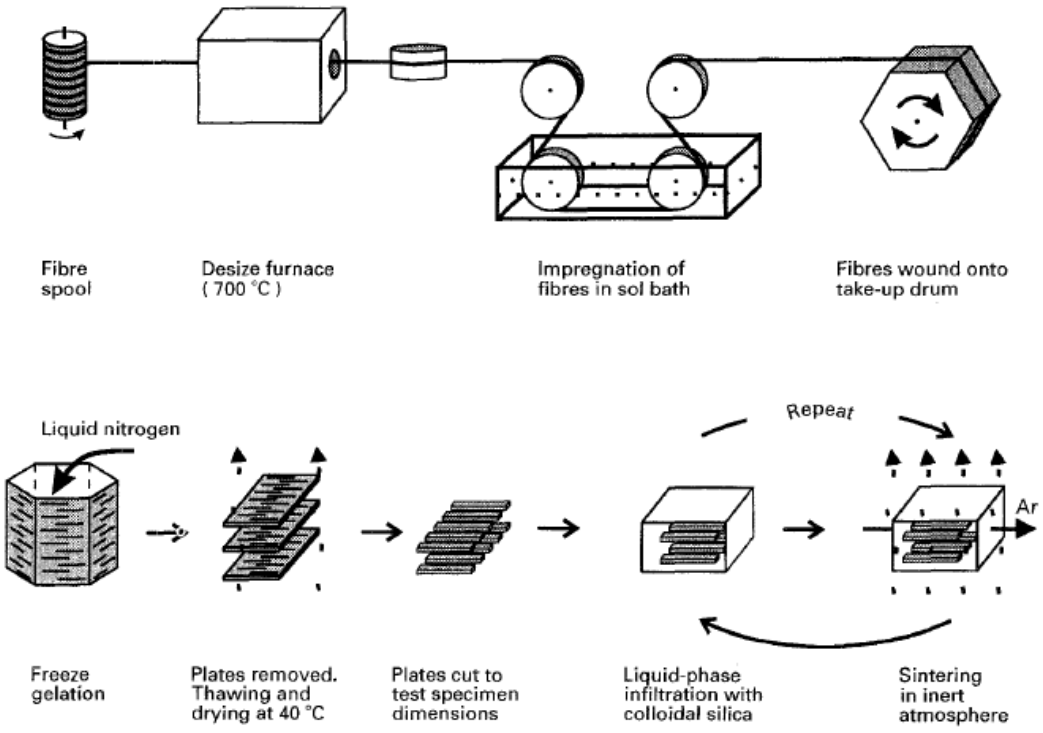

Figure 2-33 - Filament winding route used to fabricate samples with sol gel matrix system at the University of Bath (Chant et al. 1995a).

Composites using oxide fibers, Nextel^{TM} 440, have also been reported (Twitty et al. 1995). Ceramic matrix was manufactured with aqueous sol (50 wt. % SiO_2, 50

wt. % water) and 61 wt. % of ZrO_2 as filler. Unidirectional prepregs were produced via filament winding. These sheets were wet-pressed between stainless steel plates to produce 100x100x5 mm^3 plates. The pressed plates were frozen with liquid nitrogen. After drying, the plates were re-infiltrated three times with Syton D30 silica sol, dried between infiltration steps and then sintered at 950°C for one hour. The sintered plates were infiltrated two more times. Finally, the samples were infiltrated three times and sintered at 500°C for 90 minutes. Final composite fiber volume was between 23 vol.% and 28 vol.% and porosity of 30 vol. %. Table 2-6 resumes the properties of the composites manufactured with Nextel™ 440 and silica-zirconia matrix. No information on these materials interlaminar properties is given in the literature.

Table 2-5 – Mechanical properties of unidirectional composites manufactured with Nextel™ 440 and silica-zirconia matrix at the University of Bath (Twitty et al. 1995).

Batch	Fiber Content (Vol. %)	Flexural Modulus (GPa)	Flexural Strength (MPa)	Work of Fracture (Jm^{-2})
1	26 ± 1	31 ± 6	79 ± 18	477 ± 155
2	23 ± 1	36 ± 2	84 ± 14	502 ± 111
3	28 ± 1	41 ± 4	83 ± 13	871 ± 256

2.3.3 Overview CMC

Different combinations of matrix, fiber, fiber coating, fiber infiltration technique and consolidation method can be used to manufacture ceramic composites. Each combination leads consequently to differences in the mechanical performance of the material.

Figure 2-34 compares the interlaminar properties of some of the composites described along this chapter. The materials presented in this graphic are all manufactured with Nextel™ 610 fiber, 3000 denier. Amongst the composites with higher interlaminar strength are UMOX™ and WHIPOX™, both manufactured using filament winding technique. The composite from COI that uses water based suspension and vacuum for consolidation of the ceramic matrix and from Daimler Chrysler AG, which uses colloidal suspensions to consolidate the ceramic matrix also present high interlaminar strength. One of the latest development from Pritzkow Special Ceramic published in 2015, with interlaminar shear strength of 30 MPa, uses water based suspension and hand lay-up of ceramic fabrics.

The use of an automated technique such as filament winding confers to the composite reproducibility, homogenous infiltration of ceramic fibers and short manufacturing times, reflecting in better mechanical performance of the composite manufactured. From both composites using the filament winding technique, the disadvantage of UMOX^{TM} is the silicon present in the matrix after pyrolysis due to its polymer matrix. The drawback of WHIPOX^{TM} relates to the water based suspensions that can, without controlled drying, develop inhomogeneous pore distribution in the material what may lead to earlier failure of the composite.

The combination of water based suspension with application of vacuum provided good interlaminar strengths in the composite from COI. During the vacuum process, as the water evaporates due to the increase of temperature, the reduced pressure allows smaller pores to close. Reducing the porosity between composite single layers contributes to an increase in the interlaminar strength.

In the Daimler Chrysler AG development, the use of colloidal suspension in combination with hand lay-up allowed the manufacture of composites with interlaminar strength up to 15 MPa. Colloidal routes are a simple, cost-efficient and lean manufacturing technique. The process was limited by the use of the hand lay-up technique, which does not allow control and reproducibility of the infiltration and lay-up parameters. Also, consolidation of suspensions was achieved by pH modification due to the addition of AlN. The shift of the suspension pH was limited to a maximum time of 4 hours. For production of thicker or larger components, production time cannot be limited to only a few hours.

Colloidal processing of ceramics can be used in combination with different gelation methods. The freeze gelation process is highlighted due to its versatility, simplicity and at the same time allows a cost-efficient way to manufacture ceramic bodies. The suspension is, in this case, consolidated by freezing at temperatures below 0 °C. More than that, due to rapid freezing of stable suspensions, porosity is homogeneously distributed in the matrix enhancing the material performance.

In this work, for the development of oxide ceramic matrix composites the advantages of the filament winding technique and freeze gelation process are combined. With the main target of developing a manufacturing route for a cost-efficient and reliable oxide/ oxide composite which good mechanical properties are a result from a homogeneous distribution of pores, successfully infiltration of fiber filaments and the right matrix composition with suitable sintering parameters.

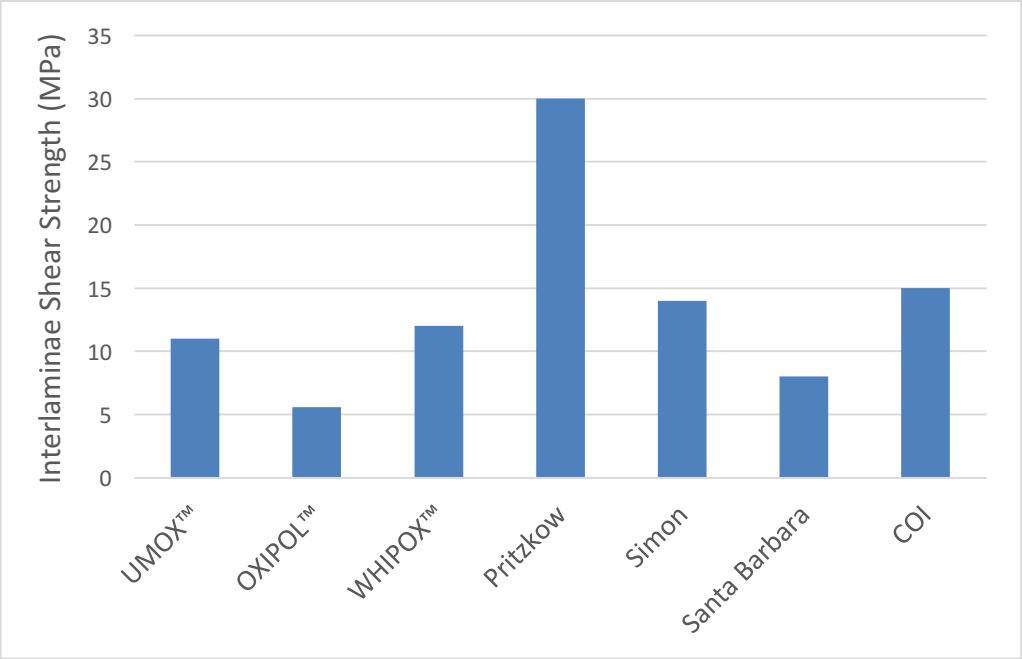

Figure 2-34 – Interlaminar shear strength (ILSS) of state of the art oxide CMC's.

3 MATERIALS AND METHODS

In this chapter the materials, the composite processing route and the characterization methods used during the work are described.

3.1 Materials

To produce the ceramic matrix several silica sols as well as ceramic fillers are investigated regarding their physical properties, pH and isoelectric point. Table 3-1 and 3-2 summarize all the components investigated and their main properties. Dolapix CE64 (referred in the work as Dolapix) from the company Zschimmer & Schwarz GmbH was used as deflocculating agent. Dolapix is an anionic polyethlylol, i.e., an aqueous solution containing 30% of Polymethacrylate of Ammonia. Its effect is a result of the interaction between its bivalent functional groups and the surface charge of the ceramic particles. Associated to the absorption on the particles, a decrease in the slurry viscosity takes place. In chapter 4.1 and 4.2 the characterization and tests conducted for the determination of the ceramic matrix composition are described.

Sols with dispersed silica nanoparticles are chosen due to their irreversible characteristic (chapter 2.1.2), i.e., after freezing followed by drying at ambient temperatures the sol does not melt again and a material with relative good green strength is achieved. Table 3-1 shows the main characteristics of the 4 sols selected for this study with their differences in silica content and particle size.

Table 3-1 - Characteristics of the silica sols investigated for the manufacture of oxide ceramic matrix (CWK Bad Köstritz, Nyacol).

Name/ Manufacturer	Ref. Number	Particle size (nm)	Wt. % Silica	Surface Area (m^2/g)	Density (g/cm^3)	pH at 25 °C	Particle Charge
Kostrosol/ CWK Bad Köstritz	3550	40	50	60-100	1,39	9,2-10	Negative
	1540	15	40	160-210	1,30	9,5-10,3	Negative
	0830	8	30	270-330	1,20	9,5-10,5	Negative
Nexsil/ Nyacol	20	20	40	135	1,20	10	Negative

Mullite is primarily investigated as filler due to its high thermal stability, low thermal expansion and high creep resistance (Schneider et al. 2008; Kanzaki et al. 1985; Schneider et al. 2005). Aluminum oxide powder is also investigated in the sol gel system due to its higher mechanical strength (Antaga 2013) and similar thermal expansion with the fiber (Nextel^{TM} 610) used for composite manufacture. This fiber is chosen for the development of the composite due to its higher strength over Nextel^{TM} 720. The mechanical properties and characteristics of Nextel^{TM} 610 is presented on Table 2-1 in Chapter 2.2.1.

Mullite and alumina fillers are chosen based on their different particle sizes and surface area (Table 3-2) as these characteristics are expected to influence in the ice crystal growth, i.e. matrix porosity, and sinter reactivity. In Table 3-3 some thermo-mechanical properties of mullite in comparison with α-alumina are presented.

Table 3-2 - Characteristics of mullite and alumina ceramic fillers investigated for the manufacture of oxide ceramic matrix (n.a.= not available) (Values taken from each material Data Sheet).

Commercial Name	Manufacturer	Particle Size (μm)	Surface Area (m^2/g)	Chemical (wt. %)	Bulk Density (g/cm^3)
Symulox M72 MC	Nabaltec	3,0 – 5,0	1,8	26,5% SiO_2 72% Al_2O_3	3,13
21113 – 10A	Reimbold & Strick	3,0	1,6	24,2% SiO_2 75,2% Al_2O_3	3,21
KM101	KCM Corporation	0,8	7,7	27,8% SiO_2 72,2% Al_2O_3	3,17
A16SG	Almatis	0,5	8,9	99% Al_2O_3	3,88
TM-Dahr	Krahn-Chemie	0,1	14,5	99% Al_2O_3	3.96
CT3000SG	Almatis	0,5	7,5	99% Al_2O_3	3,90
Ceralox APA-	Sasol	0,3	8,0	99% Al_2O_3	3,94

Table 3-3 - Thermo-mechanical properties of α-alumina and mullite ceramics (Schneider et al. 2008).

Ceramic Filler	Thermal Expansion Coefficient (10^{-6} °C^{-1})	Thermal conductivity ($Kcalm^{-1}h^{-1}$ °C^{-1})	Theoretical Density (g/cm^3)
Alumina	8	26 (20°C) 4 (1400°C)	3,96
Mullite	4,5	6 (20°C) 3 (1400°C)	3,20

3.2 Composite Manufacturing Process

The composites are manufactured by the combination of filament winding with freeze gelation technique (Figure 3-1). Due to the weak matrix concept followed in this study, fiber coating and re-infiltration cycles are not necessary.

For the preparation of the sol gel suspension with mullite a mechanical mixer from IKA electronics is used. The dispersing agent is added to the silica sol and both are mixed at the slowest velocity of the mixer. Then, the ceramic powder is added slowly (in a rate of 10 wt. % at each 3 minutes) to the silica sol being stirred. During this process the velocity of the mixer is increased. After all the powder is added, the slurry is poured into a plastic bottle with ZrO_2 balls of 1 mm diameter and left in a mechanical rotator for 9 hours. Suspensions have solids content of 75 wt. % (56,2 vol. %), from which 17 wt. % is SiO_2 from silica sol, 58 wt. % is ceramic filler and 25 wt. % water prevenient from silica sol.

Since the alumina particles present lower particles sizes, the suspensions are prepared the Ultra TURRAX® mixer also from IKA electronics as it presents higher shear rates and is, consequently, capable of breaking any agglomerates in the suspension.

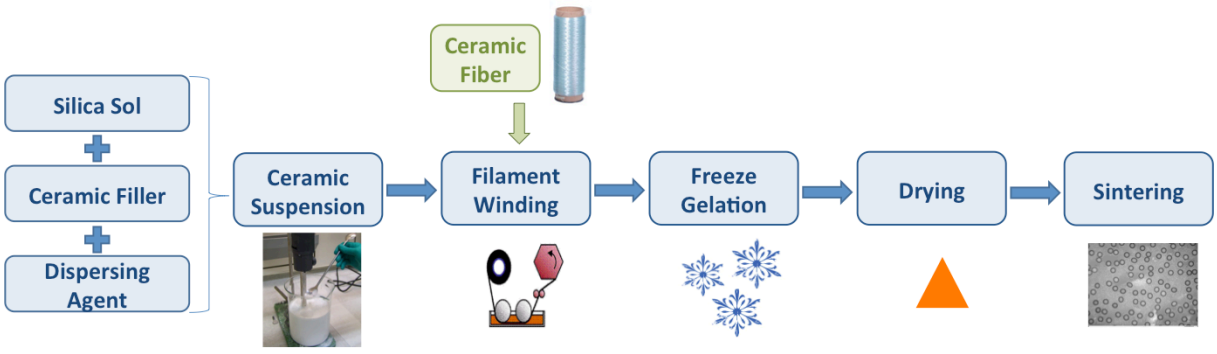

Figure 3-1 - Schematic flowchart showing the concept for the manufacturing process of CMC via freeze gelation and filament winding technique.

The fiber type used is Nextel™ 610, 3000 denier, with PVA sizing from 3M™, USA. The composites are manufactured with 0°/90° fiber architecture and built up in 8 layers resulting in a composite with approximately 3 mm thickness. Figure 3-2 shows the composite after winding and freezing.

Figure 3-2 - Nextel™ 610 fibers with sol gel based suspension composite after filament winding and freeze gelation.

After lay-up, the plate is immediately frozen in order to force sol gel transition. Freezing takes place in a freezer at -18°C for 3 hours. The sol is converted to a rigid matrix without significant shrinkage. In this step, the structure of the material is formed and the characteristics of the porosity are determined once the ice crystals of the solvent are formed and grow in the slurry. In this step, the consolidation of the sol gel suspension takes place due to the formation of a three-dimensional network of siloxane bonds. This network confers to the material enough green strength even after it is submitted again to temperatures above 0°C. The direction of the ice crystal growth is shown exemplarily when monolithic ceramic plates (Figure 3-3a) and composites are frozen (Figure 3-3b). No directed freezing front is applied, molds are placed inside a freezer and freezing takes place from outside to the inside of the samples. Both molds used during ceramic (Figure 3-3a) and composite development (Figure 3-3b) are made with aluminum.

Subsequent drying slightly above room temperature (50-60°C) is conducted during 24 hours in ambient air. This step results in bulk shrinkage often below 1%, owing to low capillary stresses associated with the relatively large and open porosity, typically 1-10 μm in diameter, which results from the nucleation and growth of ice crystals during freezing. Matrix densification is achieved during sintering. Sintering parameters used are described in Chapter 4. Samples for mechanical characterization are prepared using a cutting machine with diamond disc.

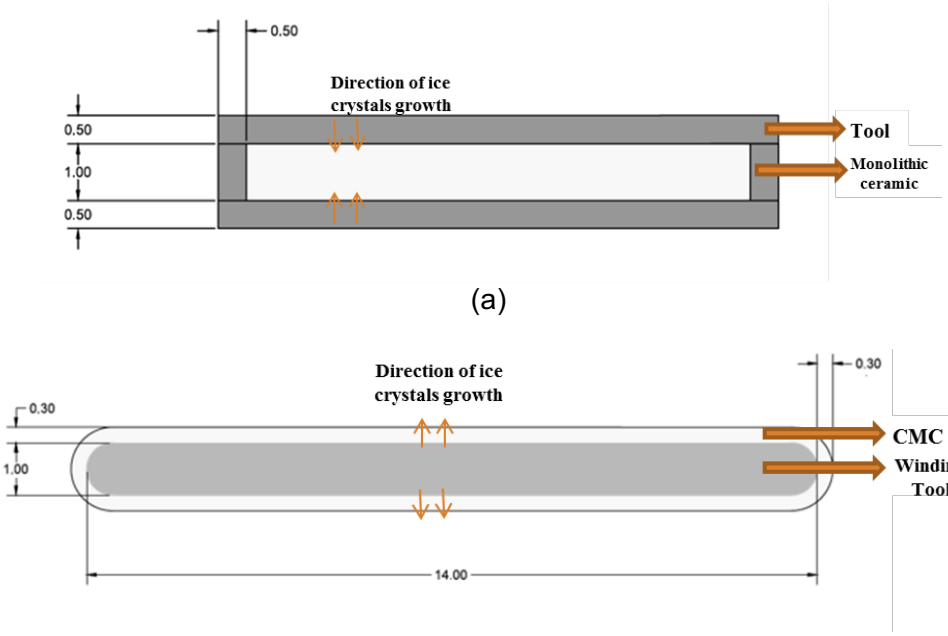

Figure 3-3 – Direction of ice crystals growth during freezing of a (a) monolithic ceramic plate and (b) ceramic matrix composite (CMC) after filament winding technique. Values are given in cm.

In Chapter 4.1.2, for the verification of the consolidation route to manufacture the oxide CMC, composites are impregnated with the sol gel matrix named MF_B. After matrix impregnation and fiber lay-up one tool is taken directly after filament winding to freezing at -18°C for 3 hours, another is submitted to autoclave process and a third one is pressure-less dried at ambient temperature. For the composite submitted to autoclave process a vacuum bag is made, vacuum is pulled and pressure is increased to 7 bar. At the same time that pressure is applied the temperature increases to 120°C. Pressure and temperature are kept constant for 3 hours. All composites are sintered at 1200°C for 3 hours using the same heating and cooling parameters.

In Chapter 4.1.3, sintering temperature of the composites is investigated. Four oxide ceramic matrix composites are manufactured using the process parameters referred above. They are subsequently frozen, dried and sintered in air with the following temperatures:

- Heating with 2°C/ min until 1200°C, dwelling time of 3h;
- Heating with 2°C/ min until 1150°C, dwelling time of 3h;
- Heating with 2°C/ min until 1000°C, dwelling time of 3h, heating with 5°C/min until 1150°C, dwelling time of 1 hour;

- Heating with 2°C/ min until 1000°C, dwelling time of 3h.

It is known that sintering mullite fillers at 1000°C will not be enough for particle diffusion and material densification (Wang et al. 2018). This temperature is chosen to compare the influence of the other sintering parameters in the composite fracture toughness once reaction or adhesion between fiber and matrix is not expected at 1000°C.

For the development of the alumina matrix and alumina matrix composites described in Chapter 4.2 sintering temperature of 1000°C, dwelling time of 3h, heating with 5°C/min until 1150°C, dwelling time of 1 hour is used. Composites are manufactured with fiber architecture of 0°/90° disposed in 8 symmetric layers $[0/90]_{2S}$ (winding tool with 140x140 mm). Same filament winding parameters used to manufacture composite MF_B_40 are used for the composites fabrication.

This process differs from the development performed at the University of Bath in several aspects. The ceramic fillers are added directly to the sol prior to gelation with the aim to reduce the matrix porosity and to avoid additional re-infiltration steps. Additionally, re-infiltration is not performed. The composites are winded using two infiltration baths (guarantying infiltration of the suspension on both sides of the fiber) and laid-up with the desired geometry and amount of layers avoiding the lamination step with the aim to increase the interlaminar performance. Also, composites are frozen at temperatures slightly below 0 °C in a freezer instead of with liquid nitrogen and sintered in air.

3.3 Characterization Methods for Ceramic Matrices and Ceramic Matrix Composites

Optical Microscope and Scanning Electron Microscopy (SEM)

Optical microscope Polyvar SC from Leica is used for microstructural investigations. The samples are embedded with epoxy resin, grinded and polished.

Fracture surfaces from the Single Edge Notched Beam test are studied using a scanning Electron Microscope Model JSM 6320F from the company JEOL. These samples are coated before the investigation with a thin gold layer.

Fracture surfaces from all other mechanical tests are photographed using a photographic camera, no sample preparation is required.

Transmission Electron Microscopy (TEM)

Samples for transmission Electron Microscope studied are prepared using a Focused Ion Beam (FEI ALTURA 865 dual-beam FIB) with 30 keV and 5 keV Ga+ Ion. Before the preparation, the sample is infiltrated with epoxy and a cross section is cut perpendicularly to the fiber direction. The TEM lamella is in particular used to analyse the fiber-matrix interface. For TEM studies the microscope Jeol2012 with Gatan imaging filter (GIF863) is used; EDX analysis is conducted with the Oxford Instruments EDX-System.

Viscosimetry

The viscosity of the ceramic suspensions is measured using a Brookfield Viscometer, model LVDV-E, from Brookfield Engineering Laboratories, USA. The experiments are conducted with spindle number 4 throughout a velocity range of 1 to 100 RPM. The spindle is chosen according to the size of the container in which the suspension is poured into for conducting the test. Viscosity results are given in centipoises (cP).

Hg Porosimetry

The mercury intrusion technique is used to evaluate the open porosity and the pore size distribution using Pascal 140 and 440 from Fisons Instruments. The pressures applied during the experiment are first limited from 0,0001 to 4 bar; the samples are then exposed in a high pressure device to pressures from 1 to 400 bars.

The registered equilibrated pressure (P) is inversely proportional to the diameter (D) of the pores, according to the Washburn equation (Equation 3-1) where γ is surface tension (480 mN/m) and φ is contact angle (141,3°).

$$D = -\frac{4}{P}\gamma \cos \varphi \qquad \text{Equation 3-1}$$

Helium Pycnometry

A Helium pycnometer from Micromeritics USA, model AccuPyc 1330 is used to determine the density of ceramics and composites. The equipment works based on the principle of gas displacement from a pre-defined volume (chamber) by placing a solid volume in the chamber. The size of the helium atoms enables the filling of pores up to a minimum size of approximately 0,1 nm.

The main components of a Pycnometer are a sample chamber and a reference chamber with defined volumes (V_{PK}, V_{REF}). These chambers are connected to each other via a valve system. High sensitivity pressure sensors determine the pressure inside the chambers. For the density determination, the sample is placed into the sample chamber and sealed. After evacuation, the sample chamber is filled with a defined helium gas pressure (P_1). Afterwards, the connection between the chambers is opened and the total pressure (P_2) is measured. From the known chamber volume and the measured gas pressures, the inserted sample volume (V_{PR}) can be calculated according to Equation 3-2. With the known mass of the sample the apparent density can be calculated (Glover 2012).

$$V_{Pr=V_{PK}-V_{Ref}\times\frac{P_2}{P_1-P_2}}$$ Equation 3-2

Archimedes Method

The determination of porosity and apparent density of ceramic matrices and composites can also be conducted following the DIN EN 623 - 2. According to this principle a porous body increases its apparent mass when its pores are filled with a fluid. Similarly, the material buoyancy changes in respect to the theoretical density of the material when closed pores are present. In order to calculate the porosity, the dry mass (m_1), the buoyant mass (m_2) and the wet mass (m_3) have to be determined with a precision balance.

The apparent density is calculated using Equation 3-3, where ρ_w is the density of the liquid in which the material is immersed (usually water) (DIN EN 623). The porosity of the material is calculated using Equation 3-4.

$$\rho_{sch} = \frac{m_1}{V_{sch}} = \rho_w \frac{m_1}{(m_1-m_2)}$$ Equation 3-3

$$P_{op} = \frac{V_{op}}{V_k} = \frac{(m_3-m_1)}{(m_3-m_2)}$$ Equation 3-4

Dilatometry

Dilatometer tests are carried out in order to evaluate the thermal expansion of the different matrices and the composites manufactured. The equipment used is TMA801S from the company Bähr.

With this instrument the difference in length between the specimen to be investigated and a reference sample is measured, measurement resolution is ± 0,01 µm. Specimens have usually the diameter 5 mm and the length 10 mm. The dilatometer performs length-change measurements at constant heating and cooling rates. The linear thermal expansion coefficient can be obtained with an accuracy of ± $0{,}01 \times 10^{-6}$ K^{-1}. On the basis of the measured length changes, which are directly correlated to volume changes, kinetic properties of solid state phase transformations can also be determinate using the dilatometer.

Thermogravimetry (TG) and Differential Thermal Analysis (DTA)

Simultaneous Differential Thermal Analysis (DTA) and Thermogravimetry (TG) are carried out in the STA503 device from the company Bähr.

In DTA, the temperature of a sample is compared with an inert reference material during a programmed change of temperature. Using this technique, the temperature in which thermal events such as phase transformations, melting, decomposition or crystalizations occur can be recognized. If an endothermic event takes place, the temperature of the sample will lag behind that of the reference and a minimum (endothermic) peak will be observed on the curve. On the contrary, if an exothermal event takes place, then the temperature of the sample will exceed that of the reference and a maximum (exothermic) peak will be observed on the curve. The area under the endotherm or exotherm peaks is related to the enthalpy of the thermal event. TG analysis shows changes in mass of the material as a function of temperature or time under a controlled atmosphere.

X-Ray Diffractometry (XRD)

X-Ray diffraction is conducted using the C3000 equipment from Seifert. With this technique diffraction patterns are recorded in the 2D range 10-100° using $Cu_{K\alpha}$ radiation (wave length λ= 0,1542 mm) with Ni filter. Using Bragg's law (Equation 3-5) the lattice parameter of crystalline phases can be determined with θ= angle between the diffracted and the emergent ray and n= order of the diffracted ray. The positions and the intensities of the peaks are used for identifying the underlying phases of the material.

$$n\lambda = 2d \sin\theta$$ Equation 3-5

Zeta Potential Measurement

An AcoustoSizer model II from the company Colloidal Dynamics is used to measure the zeta potential of the particles in suspension. The electroacoustic technique used here involves the measurement of sound waves generated by the particles in suspension. In order to generate the sound waves a high frequency electric field is applied causing the charged particles to move. It is the motion of the particles that generates the sound waves. This effect is called electrokinetic sonic amplitude.

The electrokinetic sonic amplitude is used to determine the amplitude and phase of the particle velocity, relative to the voltage applied for moving the particles. These properties are then used to define the dynamic mobility of the particle, which is used for the determination of the zeta potential.

By titration of acid and/ or base in the suspension, measurement of zeta potential trough a pH a range from 1,0 to 10 is possible. Within this range there will be a pH value at which the particle zeta potential will be zero, i.e., the particles shows zero net charge. This pH value is identified as the isoelectric point of the particle.

Thermal Conductibility

Thermal conductibility of the matrix is measured using a thermo-optical measurement facility. In this measurement, material diffusivity is measured with a CO_2 laser flash. A laser pulse is shot on one side of the sample and the temperature response on the other side of the sample is measured using a pyrometer. Depending on the time and the temperature response the material thermal conductibility is measured. Simultaneously, geometrical change during heating is also measured using an optical dilatometer. The measurement is conducted from 20°C until 1300°C with a heating rate of 2°C/ min. At each 100°C a dwelling time of 20 minutes is applied for temperature homogenization.

Mechanical experiments

For each mechanical test, 10 specimens of the composite are tested.

Ball on Ring Test

In this test, the material is cut into cylinders of 11 mm diameter and is pressed in the center with a ball with a velocity of 1 mm/ min. The material strengths is calculated with Equation 3-6, where *P* is the force in Newton (N), *v* is the Poisson's ratio, *t* is sample thickness (typically 5 mm), *α* is radius of the circles in the support point (7,7 mm), *b* is radius of the region at the center (0,546 mm) and *R* is radius of sample (11 mm) (With, Wagemans 1989).

$$S = \left[3P\ \frac{(1+\nu)}{4\pi t^2}\right] \times \left\{1 + 2\left[ln\left({}^{a}/_{b}\right)\right] + \left[\frac{(1-\nu)a^2}{(1+\nu)R^2}\right]\left[1 - \left(\frac{b^2}{2a^2}\right)\right]\right\} \qquad \text{Equation 3-6}$$

Compression Shear Test

Compression shear tests are performed following DIN EN 658-4 (May 2003). The thickness of the specimens is identical to the original thickness of the composite plate (approximately 3 mm), and the specimens have a length l=27 mm and a width b= 10 mm. This test and all following mechanical tests are conducted in an universal test machine Zwick / Roell Z005 (Zwick, Ulm, Germany) using a load cell of 5 kN, with a crosshead speed of 0,5 mm/min. With this test the interlaminar shear strength of composites can be determined. For this purpose two notches are introduced in the specimen with a distance from each other of 10 mm as illustrated in Figure 3-4. The sample is compressed as indicated by the arrows and the sample is forced to fail by shear between the notches.

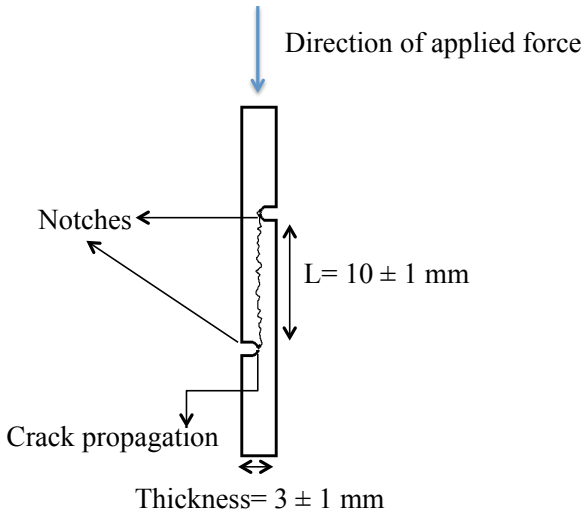

Figure 3-4 – Sketch of a compression shear test specimen with indication of the direction the shear is induced.

The interlaminar shear strength ($ILSS_C$) is calculated using Equation 3-7 (DIN EN 658-4). F is the fracture force; *b* is the sample width and *L* is the distance between notches.

$$ILSS_C = \frac{F}{bL}$$ Equation 3-7

Transversal Tensile Test

The transversal tensile test followed an internal standard from the Advanced Ceramics Institute at the University of Bremen. This method also evaluates the interlaminar strength of composites. In the test, composites samples with dimensions of 10 x 10 x material thickness mm3 are adhered between two metal screws using cyanoacrylate glue. After the glue is cured (20 minutes in room temperature) the sample is submitted to tensile traction. The test consists of applying tensile force in the direction of the arrow indicated in Figure 3-5 and forces the sample to fracture in the transversal direction of the composite sample.

The tests are conducted with an universal test machine Zwick / Roell Z005 (Zwick, Ulm, Germany) using a load cell of 5 kN, with a crosshead speed of 0,5 mm/min.

Figure 3-5 - Tensile test from an oxide ceramic matrix composite sample manufactured with Nextel™ 610 fiber, 3000 denier and sol gel suspension via filament winding and freeze gelation.

The interlaminar shear strength (τ) is calculated using Equation 3-8 in which, τ is the interlaminar shear strength in megapascal (MPa), F is the shear fracture force in Newton (N) and A is the average sample area in square millimeters (mm²).

$$\tau = \frac{F}{A} \quad \text{Equation 3-8}$$

Short Bending Test

The short bending test also determines the interlaminar shear strength (ILSS) of composites. The samples are tested in four-point bending with shorter supports. The stress applied in normal direction to the layers and the test specimen dimensions must be set so that interlaminar failure occurs (DIN EN 658-5).

The short bending tests are made in the universal test machine Zwick / Roell Z005 (Zwick, Ulm, Germany) using a load cell of 5 kN, with a crosshead speed of 0,5 mm/min and a test design with 50 mm length between the lower rollers and 20 mm between the upper ones.

The interlaminar shear strength is calculated according to Equation 3-9 where $ILSS_B$ is the interlaminar shear strength in megapascal (MPa), F is the shear fracture force in Newton (N), b is the average sample width in millimeters (mm) and h is the average sample thickness in millimeters (mm).

$$ILSS_b = \frac{3F}{4bh} \quad \text{Equation 3-9}$$

Bending Test

Bending strength of the sintered ceramic matrices is tested using 3 point bending test (DIN EN 843-1). Bending tests are made using an universal test machine Zwick / Roell Z005 (Zwick, Ulm, Germany) with a load cell of 5 kN, crosshead speed of 0,5 mm/ min and 40 mm length between rollers.

Composites are tested using four-point bending tests. This test is used to evaluate the composite strength in fiber direction. Tests are conducted in an universal test machine Zwick / Roell Z005 (Zwick, Ulm, Germany) using a load cell of 5 kN, with a crosshead speed of 0,5 mm/min and a test design with 80 mm length between the lower rollers and 20 mm between the upper ones.

To measure deflection of the sample a sensor from Solartron Metrology (Bognor Regis, UK) AX5 (±1 mm) Linear Variable Differential Transformer (LVDT) is used.

Through deflection measurement it is also possible to calculate the elastic modulus of the composite.

For the bending strength and elastic modulus calculation, equations 3-10 and 3-11 are used (DIN EN 658-3) in which σ is the bending strength in megapascal (MPa), E is the flexural elastic modulus in gigapascal (GPa), L is the length of the support outer span in millimeters (mm), L_i is the length of the support inner span in millimeters (mm), F is the fracture force in Newton (N), b is the average sample width in millimeters (mm), t is the average sample thickness in millimeters (mm), h is the average sample height in millimeters (mm) and d is the deflection due to the load applied, in millimeters (mm).

$$\sigma = \frac{3F(L - L_i)}{2bt^2} \qquad \text{Equation 3-10}$$

$$E_{bend} = \frac{L^3 F}{4bh^3 d} \qquad \text{Equation 3-11}$$

Single Edge Notched Bending (SENB) Test

Single edge notched bending (SENB) test is conducted according to DIN EN ISO 15732. The test evaluates the fracture toughness of the material. A parameter called the stress intensity factor (K) is used to determine the fracture toughness of most materials. The fracture is the condition in which the crack plane is normal to the direction of largest tensile loading, which is considered as mode I of fracture, called K_I.

Specimens having standard proportions but different absolute sizes produce different values for K_I. This happens because the stress states adjacent to the flaw changes with the specimen thickness until the thickness exceeds some critical dimension. Once the thickness exceeds the critical dimension, the value of K_I becomes relatively constant and this value, K_{IC}, is a true material property called the plane-strain fracture toughness.

The tests are conducted in an universal test machine Zwick / Roell Z005 (Zwick, Ulm, Germany) using a load cell of 5 kN, with a crosshead speed of 0,5 mm/min. In Figure 3-6 an example of an oxide based CMC during test is shown.

The mean value for the fracture toughness is calculated using Equation 3-10 (DIN EN ISO 15732). In Equation 3-12 σ is the strength in megpascal (MPa), c is the maximum crack admitted in meters (m), F is the shear fracture force in Newton (N), B

is the average sample width in millimeters (mm) and *W* is the average sample length in millimeters (mm).

$$K_{IC} = \sigma\sqrt{cY} = \frac{F}{B\sqrt{W}}\frac{L-l}{W}\frac{3\sqrt{\alpha}}{2(1-\alpha)^{1,5}}Y \qquad \text{Equation 3-12}$$

When four point bending test is applied, Y is obtained according to Equation 3-13 (DIN EN ISO 15732).

$$Y = 1{,}9887 - 1{,}326\alpha - \frac{(3{,}49 - 0{,}68\alpha + 1{,}35\alpha^{2)})\alpha(1-\alpha)}{(1-\alpha)^2} \qquad \text{Equation 3-13}$$

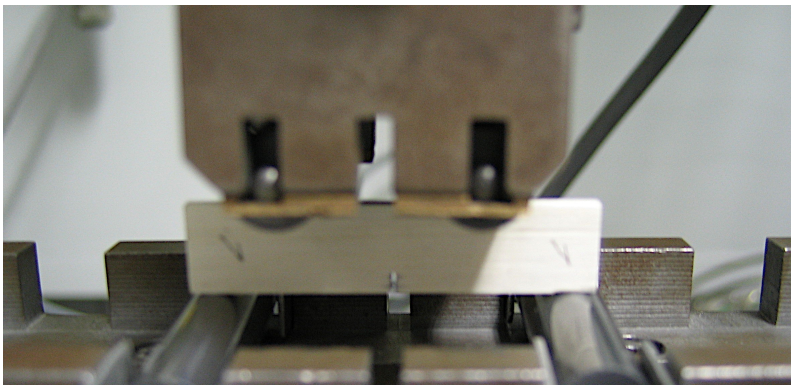

Figure 3-6 - SENB test running with a sample manufactured via the combination of filament winding with freeze gelation process in the test.

Tensile Test

Tensile test is conducted according to DIN V ENV 658. In this test the material is subjected to uniaxial tension until failure. As result the material ultimate strength, elongation, Young's Modulus, Poisson's ratio and yield strength can be obtained (DIN V ENV 658).

The test specimens have normally two shoulders and a gauge (section) in between (Figure 3-7). The shoulders are large so that they can be readily gripped in the machine during the test. The gauge section has a smaller cross-section so that the deformation and failure can occur in this area.

The tests are conducted in an universal test machine Zwick / 1465 Universal Machine (Zwick, Ulm, Germany) using a load cell of 50 kN and a crosshead speed of 1 mm/min. Laser extensometer P50 and clip-on extensometer from MTS model 632.85 F-05 is used.

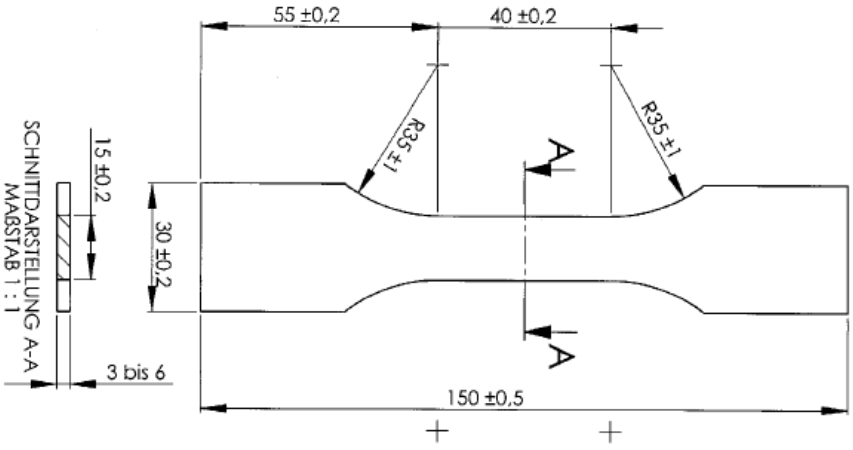

Figure 3-7 - Typical geometry for an oxide based CMC tensile test specimen.

The strain to failure and tensile strength are calculated according to Equation 3-14 and 3-15, respectively (DIN V ENV 658) where ε is the elongation in %, L is the initial sample length in millimeter (mm), L_0 is the sample length after test in millimeters (mm), σ is the tensile strength in megapascal (MPa), F is the fracture force in Newton (N) and A is the average sample area in square millimeters (mm²).

$$\varepsilon = \frac{\Delta L}{L_0} = \frac{L - L_0}{L_0}$$ Equation 3-14

$$\sigma = \frac{F_n}{A}$$ Equation 3-15

Fiber Push-in

Fiber push-in is used to measure the strength to displace the fiber from the ceramic matrix. Tests are performed in an indenter build in the Advanced Composites Center at the University of Bremen.

The indenter tip used for the push-in is normally sharp so that the fiber undergoes plastic deformation during test. In the case of composites in which porous matrix with low modulus is used, the surrounding matrix undergoes an indeterminate amount of elastic shear displacement during fiber push-in (Weaver et al. 2006). Therefore, a rounded conical indenter (Figure 3-8) is used for the measurements.

In this test, a single fiber filament is pushed using an instrumented indenter that measures the resulting force vs. displacement response of the fiber. For testing, samples from the composites are embedded in epoxy resin, grinded and polished.

The test is performed under a microscope for accurate test of the single fiber filament.

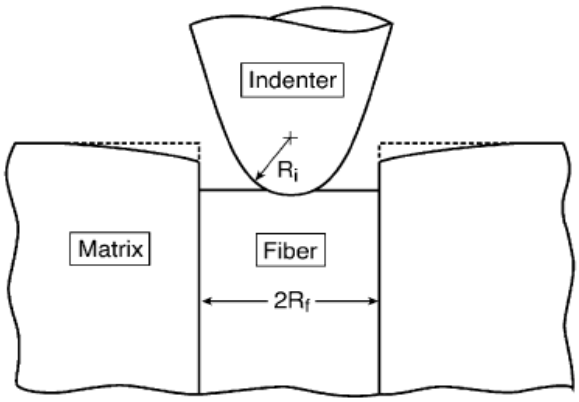

Figure 3-8 - Schematic of the push-in test for porous matrix CMC using a rounded conical indenter (Weaver et al. 2006).

4 RESULTS AND DISCUSSIONS

The combination of filament winding and freeze gelation route using ceramic matrices with different fillers to manufacture oxide ceramic matrix composites is presented in this chapter. This chapter describes, the development of the oxide Ceramic Matrix Composites using mullite as filler (Chapter 4.1), the development of the oxide CMC using alumina as filler (Chapter 4.2), a comparison between both composites (Chapter 4.3) and the verification of the developed composite and process to manufacture a rotation symmetric part (Chapter 4.4).

Mullite is used as ceramic filler in the matrix system due to its high creep and thermal resistance. Chapter 4.1.1 describes the development of mullite as filler for the ceramic matrix, three ceramic matrix compositions are manufactured and characterized. A final composition for the mullite matrix is chosen based on the properties achieved. In Chapter 4.1.2, the freeze gelation process is verified as the consolidation route for the ceramic matrix in comparison to two other methods, consolidation by application of pressure together with temperature and pressure-less drying at ambient temperature. Additionally, in order to enhance the composite mechanical performance, the effect of different sintering temperatures on composite fracture toughness is investigated (Chapter 4.1.3). A correlation between composites with different fiber volume contents and their interlaminar strength is given (Chapter 4.1.4).

For the development of ceramic suspension using alumina as filler, composites are manufactured using the parameters developed throughout the study performed with mullite based composites. Alumina is used as filler due to its high strength and low diffusion rates. Different alumina fillers are evaluated as well as their influence in thermo properties and interlaminar strength of composites (Chapter 4.2).

At the end of the work, a comparison between two composites with mullite or alumina based matrix is given (Chapter 4.3) and the process developed to manufacture oxide ceramic matrix composites is verified to build rotation symmetric and complex structures (Chapter 4.4).

The experimental work developed in this work, is summarized in the flow chart shown below.

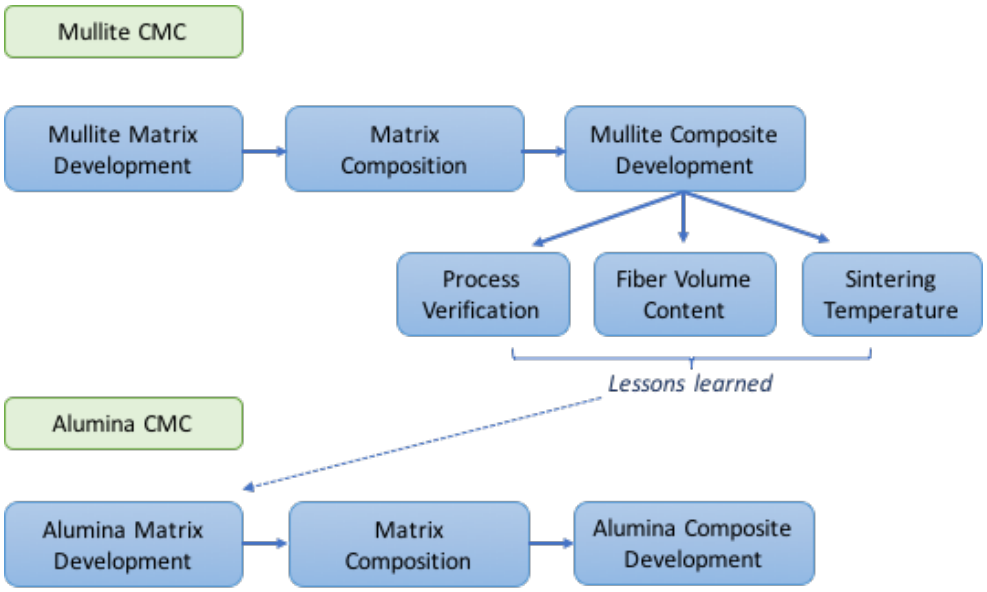

Figure 4-1 – Experimental flow chart applied for the development of the oxide CMCs.

4.1 Development of Oxide Ceramic Matrix Composites with Mullite Matrix

4.1.1 Development of Ceramic Matrix with Mullite Filler

For the development of the Ceramic Matrix Composites, it is necessary to better understand the ceramic fillers used to reinforce the ceramic matrix. This chapter describes the progress made to develop the ceramic matrix with mullite as a filler. This progress is built upon the developments described in the literature (Machry, 2008).

The matrices are developed by testing different ceramic fillers and silica sols. For the selection of the ceramic matrix components the zeta potential and isoelectric point (IEP) of the silica sol and mullite fillers is measured with an Acoustosizer. Zeta potential is used to determine the electrical charge of the sol and mullite filler. With the Acoustosizer it is possible to analyze the zeta potential change regarding the suspension pH. The point in which zeta potential is zero corresponds to the pH the particles in suspension are not charged and will, therefore, precipitate. The pH in which the zeta potential is highly charged (positively or negatively) is when the particles in suspension repeal each other and stay stable in suspension.

Four silica sols are analyzed, Köstrosol 0830, Köstrosol 3550, Köstrosol 1540 from CWK Bad Köstritz, Germany and Nexsil 20 from Nyacol Nano Technologies,

USA. The difference between the analyzed silica sols is their silica particle size and silica percentage (Table 3-1 in Chapter 3.1). Each material is tested without addition of Dolapix (referred as wD) and with addition of 0,5 wt. % of Dolapix (referred as 0,5D) through a pH range from 1.5 to 10. Dolapix is, as mentioned in Chapter 3.1, used as a dispersing agent.

All silica sols presented isoelectric point near to pH 2, similar zeta potential value and curves showing the same tendency (Figure 4-2). Addition of Dolapix did not influence significantly the silica zeta potential. In general, it can be noticed that Dolapix slightly changes the negative values from the zeta potential but it does not influence the isoelectric point. Table 4-1 summarizes the results from the sols with 0,5 wt.% once values for the sols without Dolapix are nearly the same. The addition of Dolapix in the amount of 0,5 wt.% is chosen based on previous internal work conducted at Airbus.

Table 4-1 - Zeta Potential and isoelectric points found for the silica sols Köstrosol 0830, Köstrosol 3550, Köstrosol 1540 and Nexsil 20.

Silica Sol	Dolapix	Highest Zeta Potential (mV)	pH at Highest Zeta Potential	pH at IEP (for wD and 0,5D)
Köstrosol 0830	0,5D	-50,7	9.7	2.0 – 2.2
Köstrosol 3550	0,5D	-63,0	9.2	2.0
Köstrosol 1540	0,5D	-52,3	10.1	1.9
Nexsil 20	0,5D	-59,0	9.0	2.0

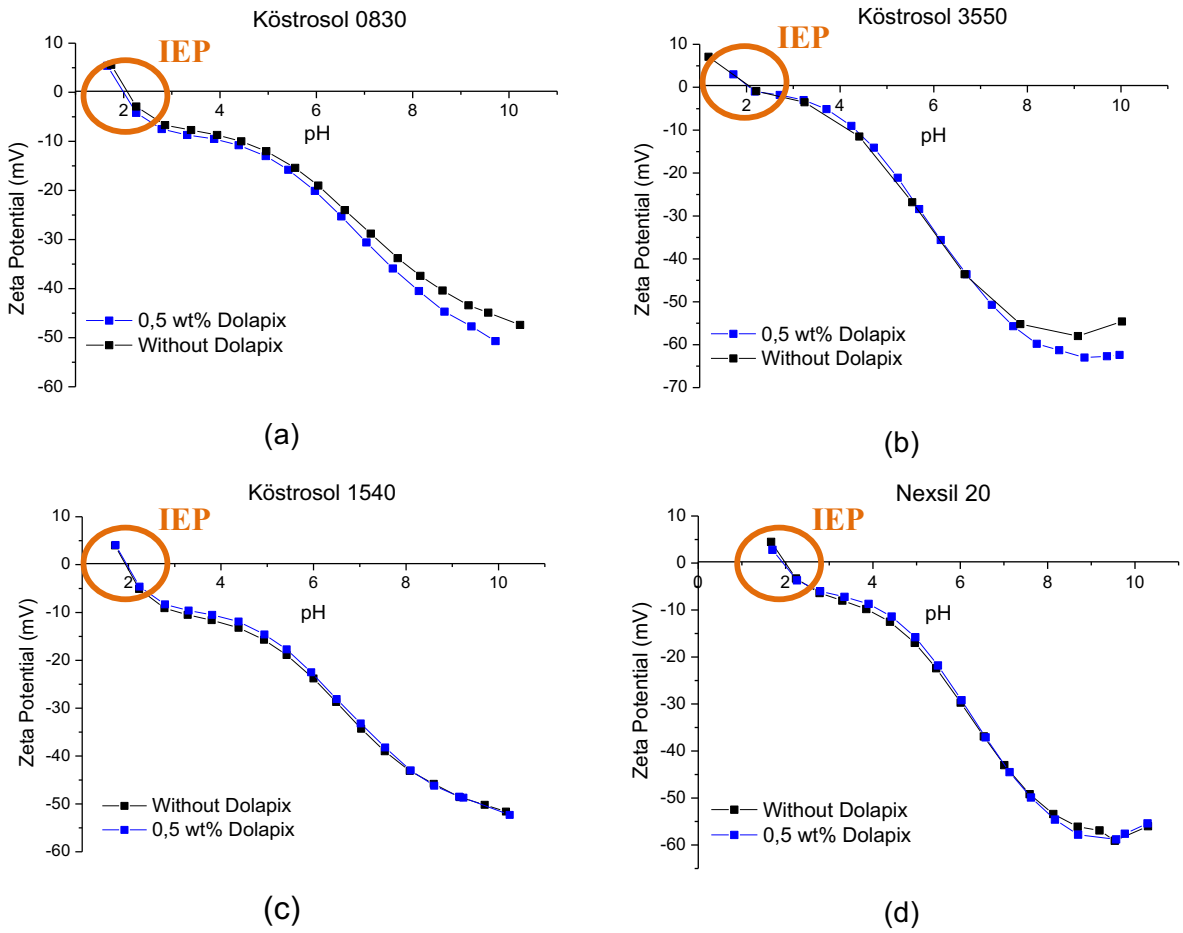

Figure 4-2 - Zeta potential curves from silica sols Köstrosol 0830 (a), Köstrosol 3550 (b), Köstrosol 1540 (c) and Nexsil 20 (d) without and with addition of 0,5 wt. % Dolapix.

Three different types of mullite powders are analyzed through a pH range from 1,5 to 10. The fillers differ in their particle size and composition (Table 3-2 in Chapter 3.1).

Higher zeta potential values from all mullite fillers are observed in the pH between 9.0 and 10.0 (Table 4-2). With mullite in suspension the use of Dolapix changed considerably the IEP (Figure 4-3). The IEP from all mullite fillers without Dolapix are approximately pH 7.0. When Dolapix is added the IEP shifts to pH between 3.0 and 5.0.

Table 4-2 - Zeta Potential and isoelectric points found for ceramic fillers Mullite 21113, Symulox M72 and KM101.

Silica Sol	Dolapix	Highest Zeta Potential (mV)	pH at Highest Zeta Potential	pH at IEP
Mullite 21113	wD	-131,3	9.7	7.3
	0,5D	-124,4	8.9	3.3
Symulox M72	wD	-117,96	9,79	7.1
	0,5D	-118,4	9.8	3.9
KM101	wD	-110,42	9,99	6.4
	0,5D	-113,31	9,68	4.8

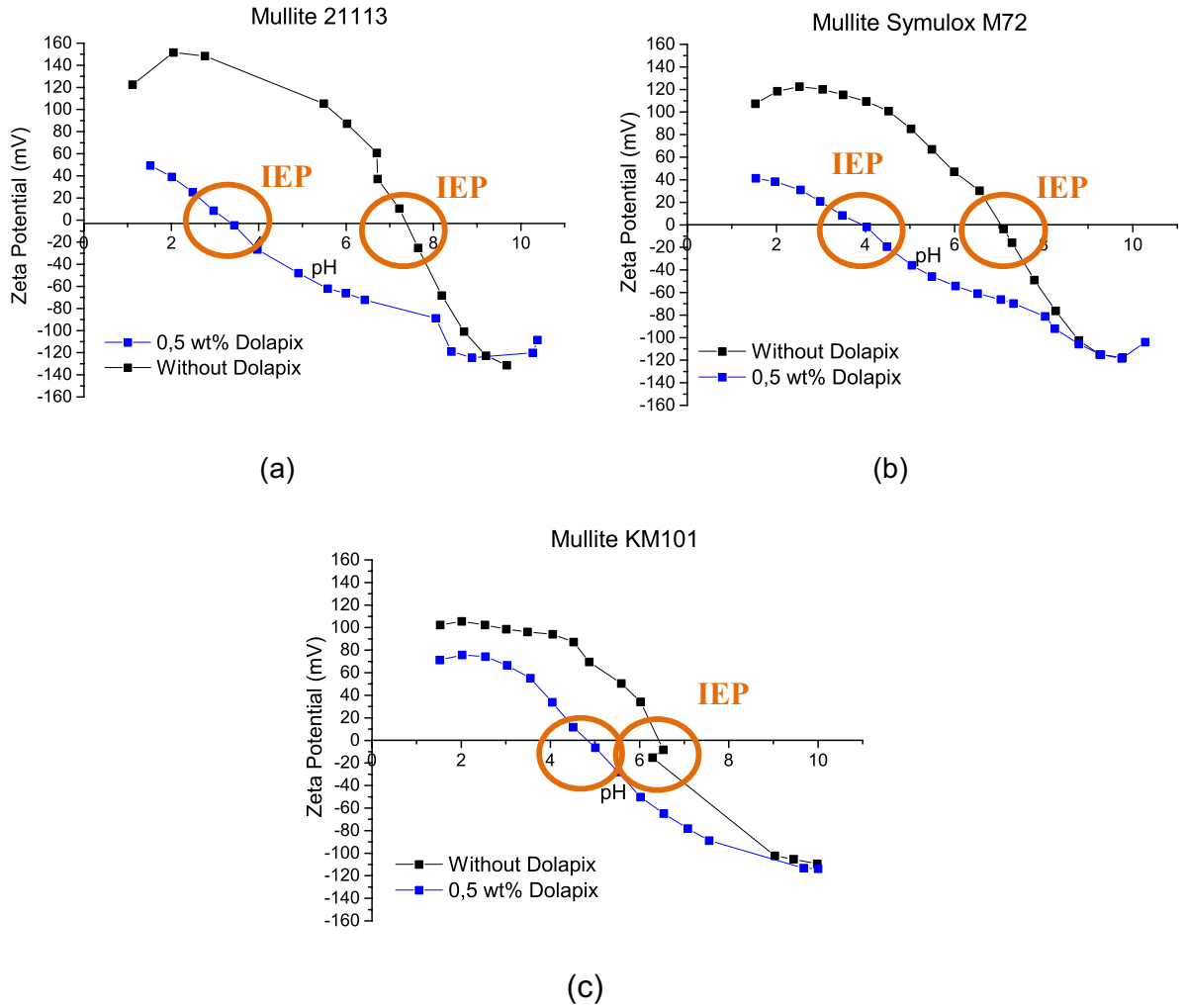

Figure 4-3 – Zeta potential curves from filler particles of Mullite 21113 (a), Symulox M72 (b) and KM101 (c) without and with addition of 0,5 wt. % Dolapix.

As previously indicated in the literature (Sigmund et al. 2000), in order to obtain ceramic suspensions with particles in suspension the pH from the suspension must be in the range in which its components are highly charged (higher zeta

potential). To avoid particle precipitation, the suspension pH must never be close to its components IEP.

From the zeta potential and IEP values from the silica sols and mullite fillers analyzed, the suspension should be developed between pH 9.0 and 10.0. Therefore, manufacturing suspensions within this pH range will guarantee that silica particles from silica sol and mullite particles will be stable in suspension.

Amongst the silica sols tested the ones which presented higher zeta potential values in the suggested pH range are Köstrosol 3550 and Nexsil 20 with 0,5 wt. % Dolapix. These are also the sols with higher silica concentration, which, according to the literature, helps to improve the mechanical strength of the final matrix, and lower the gel porosity (Russel-Floyd et al. 1993; Russel-Floyd et al. 1990).

The use of Dolapix is important with mullite fillers not only because it helps in the suspension stability (higher zeta potential) but also because it shifts the isoelectric point to lower pH values, reducing the chance of precipitation of particles in suspension. This happens as Dolapix promotes repulsive forces, i.e., steric stabilization between the particles in suspension.

When choosing the filler to be used it is important to consider, additionally to the zeta potential, that a material with fine particle size can be easier infiltrated in between the fiber filaments for the composite manufacture. From the mullite powders analyzed, KM101 followed by mullite 21113 present finer grains.

As a consequence, three matrix compositions are chosen for ceramic matrix manufacture and characterizations. MF means that the matrix is made with mullite filler and the letters A, B and C are used to differentiate the compositions.

- ⇨ MF_A = Köstrosol 3550 and mullite 21113 (0,5 wt. % D)
- ⇨ MF_B = Nexsil 20 and mullite 21113 (0,5 wt. % D)
- ⇨ MF_C = Köstrosol 3550 and mullite KM101 (0,5 wt. % D)

Ceramic suspensions are manufactured according to the procedure described in Chapter 3.2. The matrix composition has a total of 75 wt. % (56,2 vol. %) solids content, from which 17 wt. % SiO_2 from silica sol and 58 wt. % mullite; 25 wt. % is water from silica sol. After freezing and drying, monolithic ceramics are sintered up to 1200°C with a heating rate of 2°C/ min and dwelling time of 3 hours.

The viscosity of the suspension is a very important parameter to be adjusted once the matrix must infiltrate the inner fiber filaments during filament winding. Therefore, it is necessary that the suspension present sufficiently low viscosity for

complete fiber infiltration. Figure 4-4 shows the viscosity in centipoises (cP) from the ceramic slurries. Suspensions have a non-Newtonian behavior, i.e., with the increase of velocity or shear rate, the viscosity deceases.

MF_A and MF_B have similar viscosity values once they are manufactured with the same mullite powder (d_{50}= 3 µm). MF_C, on the other hand, is produced using a mullite powder with smaller particle size (d_{50}= 0,8 µm) resulting in significant higher viscosity due to the higher surface area. The filament winding velocity applied during composite manufacturing is between 25 to 40 RPM because it corresponds to static behavior of the suspensions, providing a better infiltration. At this velocity MF_C is 5 to 6 times more viscous than matrix A and B and shows no-Newtonian behavior, demonstrating the poor potential of this suspension for homogeneous fiber infiltration.

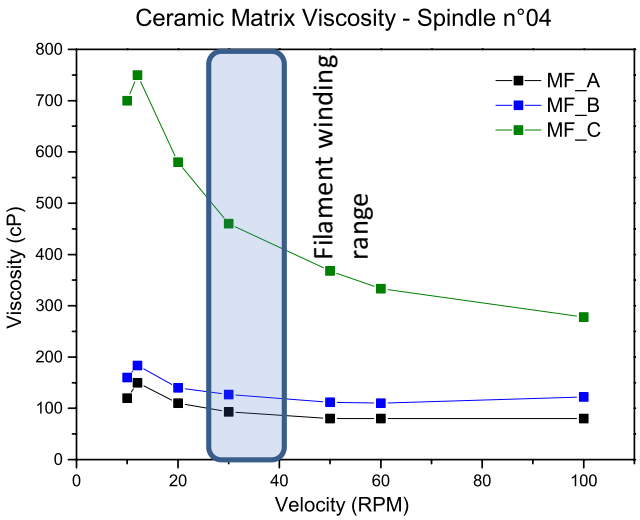

Figure 4-4 - Viscosity from sol gel based suspensions manufactured using different sol gel and mullite powders.

Density of the sintered ceramics is measured using Helium Pycnometer. Porosity and pore size distribution is measured via Mercury Intrusion (Table 4-3). MF_A presents slightly higher porosity (43,29 vol. %) than MF_B (39,90 vol. %). Due to the smaller particle size of the mullite and its more homogeneous distribution amongst the silica particles, a lower volume of porosity is observed in MF_C (32,23 vol. %).

Pore size distribution (Figure 4-5) of MF_A shows a homogeneous monomodal pore distribution with most of the pores ranging from 1 to 10 µm, corresponding to the pores formed by the ice crystals (Deville 2008; Scotti, Dunand

2018). MF_B pores are found mostly in the range from 10 to 100 µm, which can be explained by the long lamellar porosity formed in this matrix after freezing (Figure 4-6b). Also in MF_B, a porosity ranging from 0,1 to 1 µm is observed and indicates remaining nano porosity of the ceramic after sintering. Matrix MF_ C porosity is homogeneously distributed in the range from 1 to 100 µm and a high concentration of pores with a diameter around 0,1 µm is observed. The porosity of 0,1 µm are a consequence of the homogeneous distribution of the mullite particles amongst the silica particles and are formed in between the necks formed during diffusion sintering (Deville 2008).

Table 4-3 - Density and porosity of matrix MF_A, MF_B and MF_C after sintering manufactured with different mullite and silica sols via freeze gelation.

Material	Density (g/cm³)	Porosity (vol. %)
MF_A	2,76	43,29
MF_B	3,01	39,90
MF_C	2,82	32,23

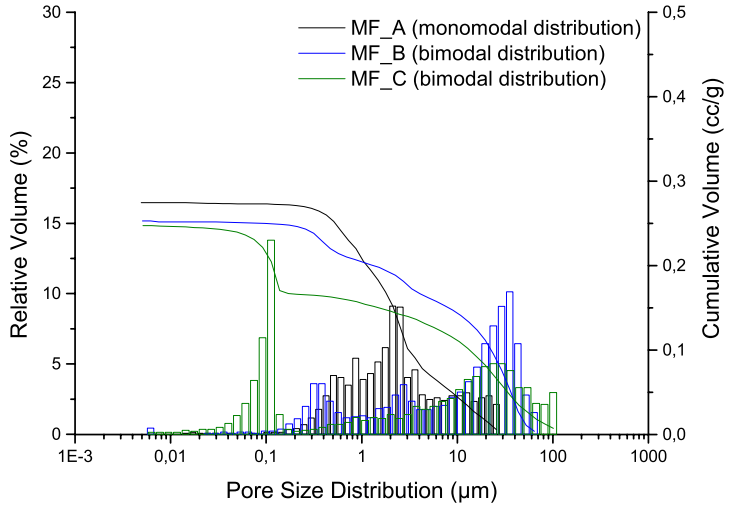

Figure 4-5 - Pore size distribution from matrix MF_A, MF_B and MF_C manufactured via freeze gelation using different sol gel and mullite powders. Total porosity of the matrices are 43,49 vol. %, 39,90 vol. % and 32,23 vol. % respectively for A, B and C.

Microstructures of the matrices are shown in Figure 4-6. Pores and matrix are indicated with arrows. Pores have lighter grey intensity when infiltrated with epoxy resin during sample preparation. The pores in dark grey are not infiltrated with resin.

Matrix MF_A (Figure 4-6a) show higher porosity with formation of some short lamellar pores and pores with different geometries. Lamellar pores are formed in

MF_B (Figure 4-6b). In MF_C (Figure 4-6c), the pores have also a lamellar shape but are shorter than in MF_B; this matrix is denser (image resolution does not show the porosity at 0,1 μm) and cracks between the pores are observed.

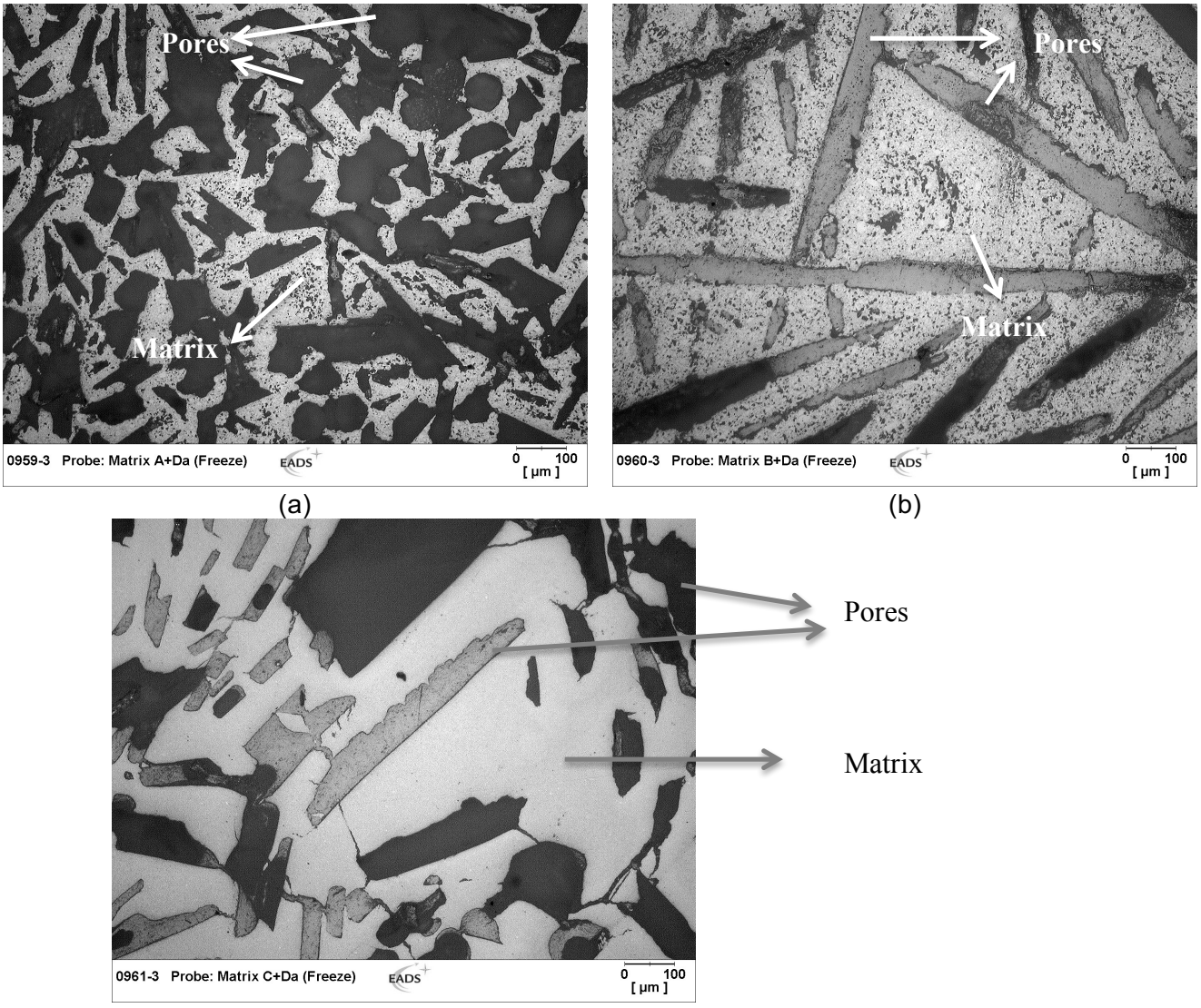

Figure 4-6 - Microstructure of sintered ceramic matrices MF_A (a), MF_B (b) and MF_C (c) manufactured via freeze gelation using different sol gel and mullite powders.

Figure 4-7 shows the curves correspondent to the relative length change of the ceramic matrices. Measurement is performed in samples after freezing and drying, without sintering. Matrix MF_A and MF_B present short expansion until 900 °C, after this temperature they start to shrink. The relative length change at 900 °C for MF_A is of 1,33% and of MF_B is 1,59%. MF_C does not show any shrinkage or expansion until 900°C. After this temperature shrinkage is also observed. The relative length

change of MF_C at 900°C is 3,31%. The on-set temperature of the matrices is 985°C and 961°C, respectively for MF_A, MF_B and MF_C.

The similar behavior of MF_A and MF_B can be correlated to the fact that both matrices are manufactured using the same mullite. During sintering the material normally suffer an expansion due to rearrangement of atoms via diffusion, followed by densification of the component, and consequently by net shrinkage (Antaga 2013, Kim et al. 2016).

Due to the homogeneous distribution of the smaller mullite particles in between the silica particles it is believed that the silica particles have more interstices to rearrange during heating reflecting in no expansion, as shown in Figure 4-7. Contraction is observed on all matrices but a higher shrinkage is noted on matrix MF_C, this can explain the cracks observed in this matrix (Figure 4-6c).

The is Thermal Expansion Coefficient measured in samples previously sintered at 1200°C, dwelling time of 3 hours. CTE values found for each matrix in the temperature range of 100°C to 1200°C are 1,87 $x10^{-6}$/K, 1,85 $x10^{-6}$/K and -1,26 $x10^{-6}$/K for MF_A, MF_B and MF_C respectively.

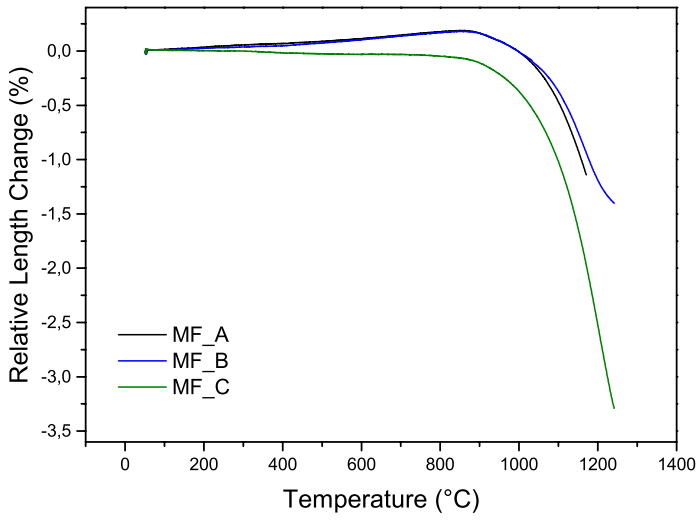

Figure 4-7 – Relative length change of matrices manufactured with different silica sols and mullite fillers via freeze gelation.

Simultaneously thermogravimetric analysis is conducted on the samples (Figure 4-8). Thermogravimetry (TG) shows loss of water from the matrices during heating. In the TG analysis of the matrices it is observed that, from 0°C to 150°C, desorption of physically adsorbed water happens. From 150°C to 900°C concurrent

weight loss is attributed primarily to removal of organics, structural relaxation of silica and loss of chemically bonded water.

In a sole silica system, transformation of silica into β-quartz takes place between 570-870°C, β-quartz is transformed into β-tridymite from 870-1470°C and β-tridymite is transformed into β-cristobalite from 1470-1705°C; these transformations are accompanied by slightly expansion due to accommodation of atoms followed by contractions in the material (Antaga 2013, Kim et al. 2016). These findings support the expansion and shrinkage of the matrices as reported in the matrices relative length change (Figure 4-7).

Since the system presented contain mullite and silica, the transformations are influenced by the presence of the fillers, their particle sizes and distribution among the silica particles. Differential Thermo Analyses (DTA) from all matrices show in Figure 4-8 evidences an endothermic peak between 400°C and 900°C, this peak corresponds to the initial phase transformation of the silica. It is believed that, for this system, crystallization of silica in the cristobalite phase starts to happen at approximately at 900°C. During the cooling phase, no evidences of reactions are observed.

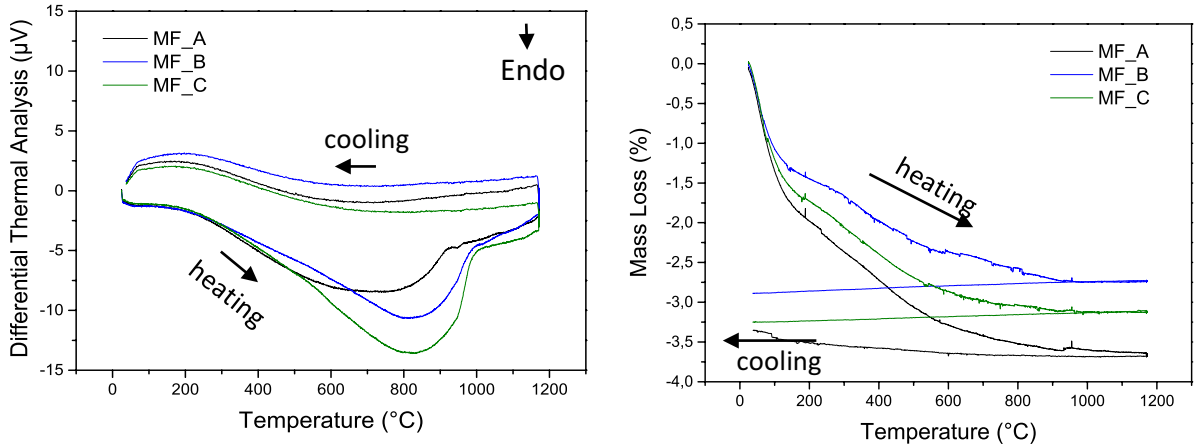

(a) (b)

Figure 4-8 – Differential Thermal Analysis (a) and Thermogravimetry (b) curves from matrix MF_A, MF_B and MF_C heated with 2°C/ min. until 1200°C with dwelling time of 3 hours.

X-Ray diffraction is conducted in MF_A (Figure 4-9) and MF_B (Figure 4-10) sintered at 1200°C, dwelling time of 3 hours. The SiO_2 phase (represented by S) corresponds to high cristobalite cubic face centered and mullite in the orthorhombic

phase (represented by M). This supports the DTA results that the reactions observed correspond to the formation of silica in the form of cristobalite. X-Ray diffraction card number for SiO_2 is 00-027-0605 and for mullite is 00-015-0776.

The difference between MF_A and MF_B is the amount of SiO_2 present after sintering. As it can be seen in Figure 4-10, matrix MF_A (a) presents a higher intensity of reflection on the X-Ray diffraction of silica than in MF_B (b). This can be explained because the silica sol used for matrix A has 10 wt. % more SiO_2 particles than the silica sol used for matrix MF_B, therefore a higher amount of silica crystallizes in MF_A after sintering.

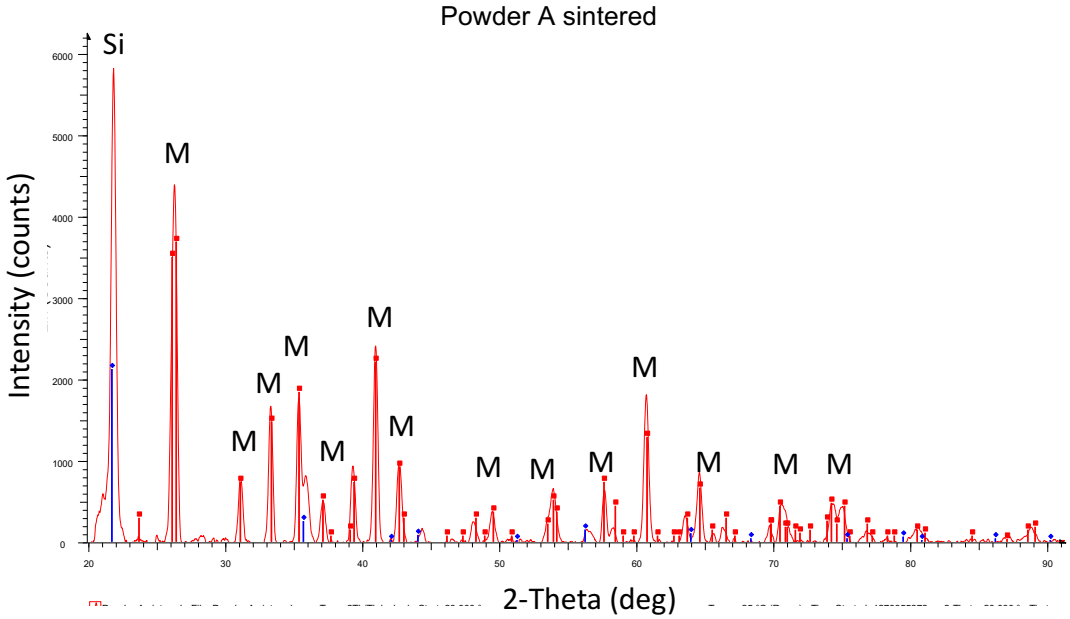

Figure 4-9 – X-Ray diffraction of matrix MF_A after sintering with 2°C/ min until 1200°C and dwelling time of 3 hours.

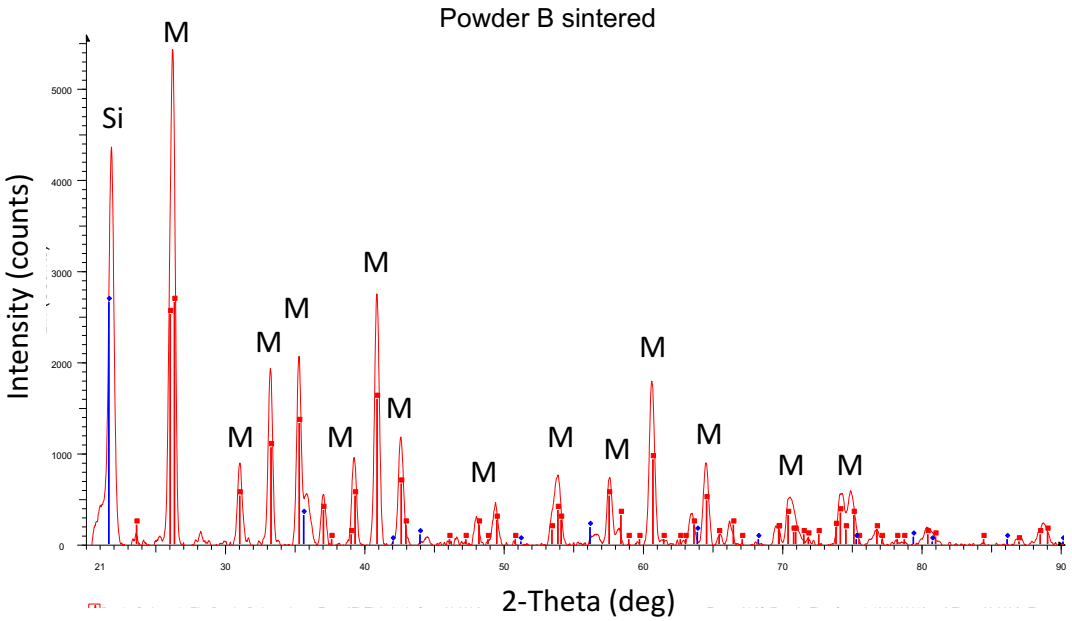

Figure 4-10 – X-Ray diffraction of matrix MF_B after sintering with 2°C/ min until 1200°C and dwelling time of 3 hours.

Figure 4-11 show the bending strength of the matrices. Matrices MF_A and MF_B show higher strength and similar fracture behavior indicating a brittle material. MF_B bending strength is 10,62 ± 0,92 MPa and MF_A is 5,91 ± 0,48 MPa. It has been reported in the literature (Liang et al. 2016) that as the amount of cristobalite increases in a material, its strength is reduced due to the formation of tensile stresses on the cooling phase, leading to a lower mechanical performance. This, together with the pore formation in the material, can explain why MF_A presents lower strength than MF_B. Matrix MF_C shows strength of 2,03 ± 0,34 MPa and deformation; this deformation is a result of the cracks observed in the matrix microstructure.

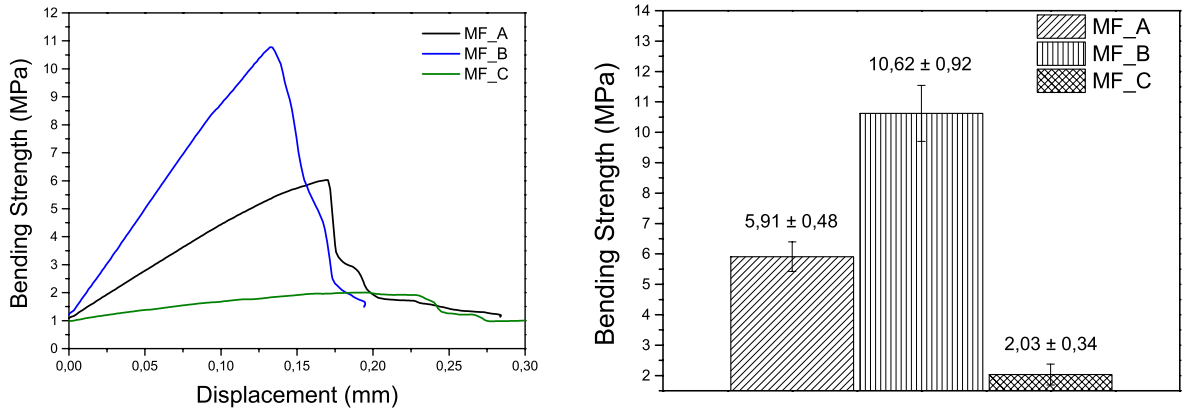

Figure 4-11 - Representative strength vs. displacement curves (a) and bending strength (b) of the different sintered ceramic matrices manufactured with different silica sols and mullite using the freeze gelation technique.

Chapter Summary

Silica sols and mullite fillers are investigated as components to manufacture ceramic matrices using the freeze gelation process. Four different silica sols and three mullite powders are studied regarding their pH and isoelectric point. It is seen that for the manufacture of suspensions with silica sol and mullite fillers the pH in which the suspension must be manufactured is between 9.0 and 10.0 due to the higher zeta potential of the particles at this pH range. Based on zeta potential, IEP and other physical aspects (such as sol content and filler particle size), three ceramic matrix compositions are proposed.

Matrix MF_A and MF_B are manufactured with the same mullite (Mullit 21113) and different silica sols (Köstrosol 3550 and Nexsil 20 respectively). The silica sol from MF_A has particle size of 40 nm and 50 wt. % of silica while MF_B has particle size of 20 nm and 40 wt. % of silica. Viscosity and thermal behavior of A and B showed to be similar as a result of the same mullite used. Matrix MF_B is, however, stronger than MF_A as a result of the pore formation in the matrix and of the smaller amount of silica present in its silica sol which consequently forms lower amount of silica in the form of cristobalite in this matrix.

Higher porosity is observed in MF_A with thicker pores and with different sizes and geometries. In some regions a thin matrix wall separates the pores. This porosity structure probably contributed to an earlier failure of MF_A under bending load since the path for crack dissipation before ultimate failure is shorter than in MF_B.

Microstructure of matrix MF_B shows long and fine pores, characteristic from the growth of lamellar ice crystals in the matrix during the freeze gelation process.

Matrix MF_C is manufactured with the same silica sol as MF_A (Köstrosol 3550) and a mullite filler with finer particle size (KM101). The smaller filler particle size of matrix MF_C (0,8 μm) in comparison to the mullite filler used in MF_A and MF_B (3,0 μm) lead to presence on smaller sized porosity. The smaller filler particle size contributed also to a viscosity 5 to 6 times higher than MF_A and MF_B. The matrix thermal behavior shows a higher shrinkage which consequently lead to the formation of cracks in the material structure. As a consequence from the cracks formed, the bending properties from this matrix are reduced and deformation is observed.

Among the matrices manufactured, matrix MF_B presents better physical and mechanical properties. The composition used to manufacture this matrix is chosen for the further development of oxide ceramic composites to be manufactured with the combination of filament winding with the freeze gelation technique.

4.1.2 Development of Ceramic Composites with Mullite Matrix – Process Verification

In order to assure that the freeze gelation is the most suitable route to manufacture ceramic matrix composites using sol gel systems, composites materials are manufactured using filament winding and three different consolidation routes: freeze gelation, pressure and temperature (autoclave process shown in Figure 4-12) and pressure-less drying at ambient temperature.

Autoclave process is chosen aiming to verify the influence of the application of pressure during matrix consolidation in the composite interlaminar strength. Pressure-less drying is chosen with the aim to ease future process industrialization since, with long manufacturing times, the water from the suspension may dry leaving no time for the suspension to freeze gel.

The routes are evaluated regarding the final composite porosity, porosity distribution and interlaminar strength.

(a) (b)

Figure 4-12 - Oxide based CMC manufactured via filament winding with Nextel™ 610, 3000 denier and sol gel matrix MF_B before (a) and after (b) autoclave process at 7 bar and 120°C.

Experimental Results

The microstructures from the composites are presented in Figure 4-13 and 4-14. The dark grey or black areas correspond to pores. In Figure 4-13a the 8 composite layers in 0°/90° orientation are numbered for better visualization. Figure 4-13 shows the same materials with higher resolution. Arrows indicate the fiber, matrix and pores in the matrix.

Composites microstructure reveals a very good and homogenous infiltration within the fiber filaments where nearly no regions with agglomerated filaments are observed. No evidence of delamination between composite layers can be seen. In Figure 4-13b, higher porosity represented by darker regions in the composite consolidated under pressure and temperature can be seen. Fiber volume content of the CMC samples are calculated in 28,3 ± 0,57 vol. %, 28,8 ± 2,35 vol. % and 24,7 ± 1,35 vol. % respectively to frozen, pressure and temperature and pressure-less drying. The fiber volume calculation is made based on image analysis (see Appendix A.1).

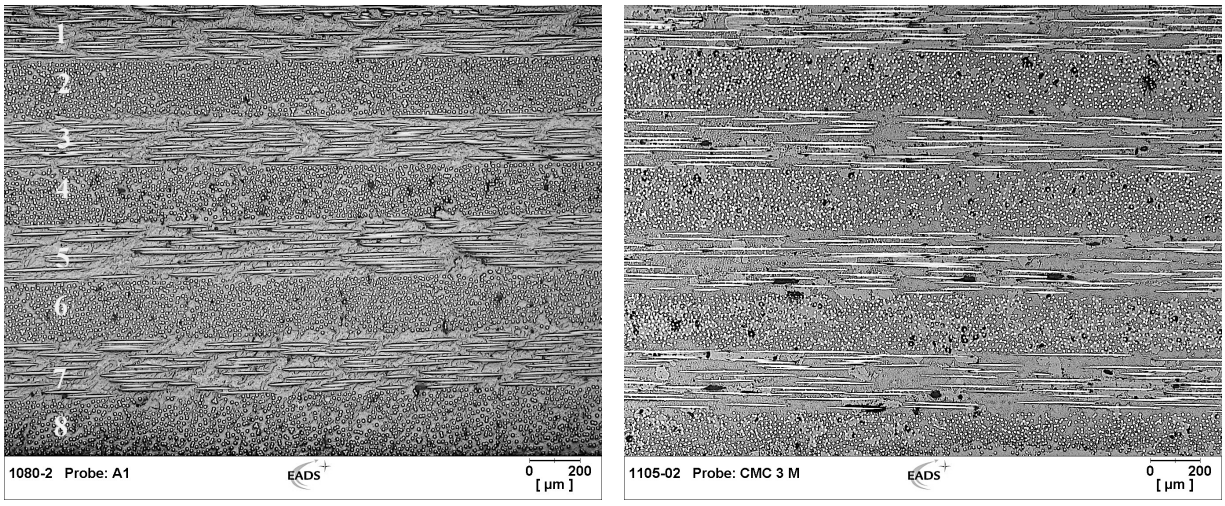

(a) (b)

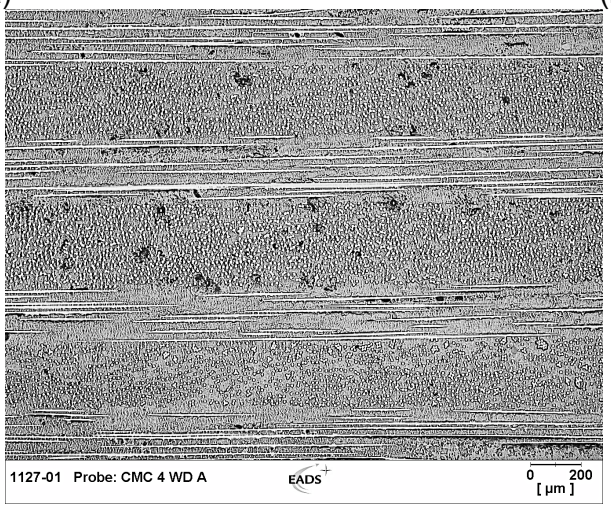

(c)

Figure 4-13 - Microstructure of CMCs manufactured by impregnation of Nextel^{TM} 610 fibers, 3000 denier with sol gel matrix MF_B via filament winding consolidated (a) via freeze gelation, (b) pressure and temperature (autoclave) and (c) pressure-less drying after sintering.

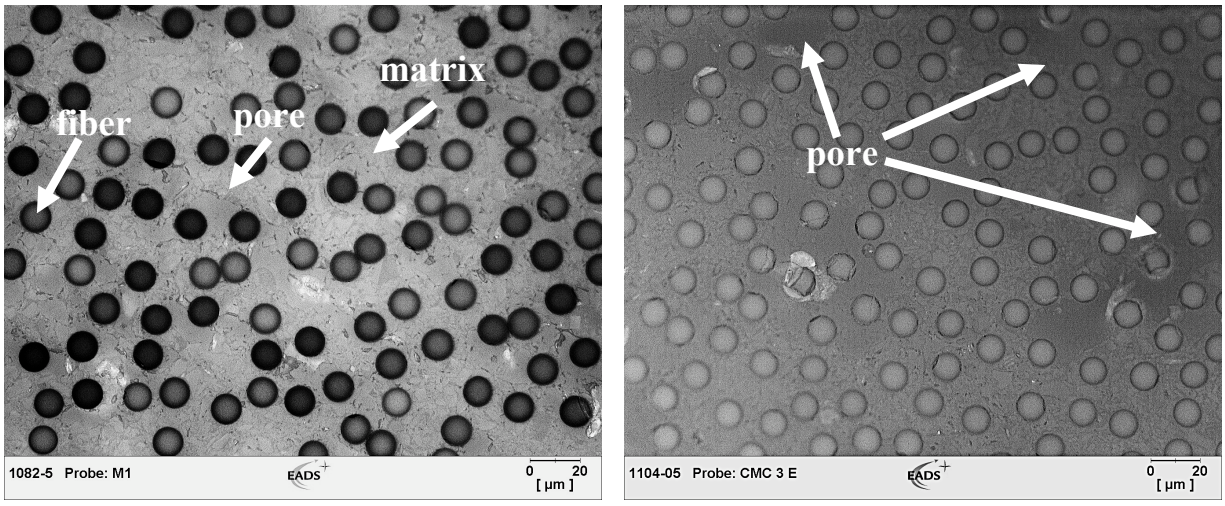

(a) (b)

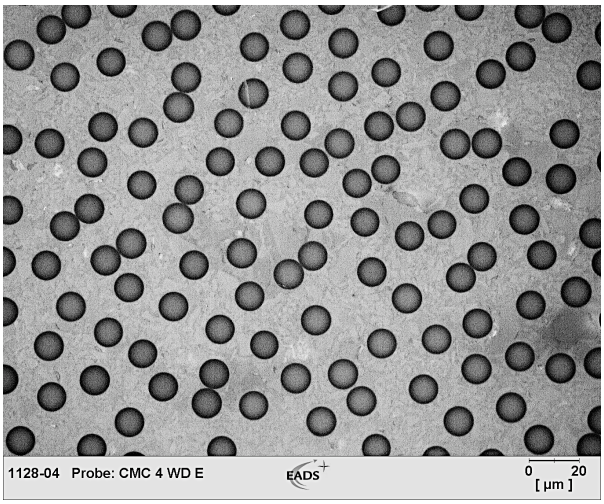

(c)

Figure 4-14 - Impregnation of fiber bundles with ceramic matrix in CMCs manufactured by infiltration of Nextel™ 610 fibers, 3000 denier with sol gel matrix MF_B via filament winding consolidated (a) via freeze gelation, (b) pressure and temperature (autoclave) and (c) pressure-less drying.

A total porosity between 30 and 40 vol. % (Table 4-4) is measured using He Pycnometer. Higher porosity (39,4 vol. %) is found when pressure and temperature is applied, while the composite dried in air presented lower porosity (29,6 vol. %).

Table 4-4 – Total porosity and apparent density values of the different (sintered) oxide CMCs consolidated via freeze gelation, pressure and temperature (autoclave) and pressure-less drying.

Consolidation Route	Fiber	Total Porosity (vol. %)	Apparent density (g/cm³)
Freeze Gelation	Nextel™ 610	33,5	3,23
Pressure and Temperature	Nextel™ 610	39,4	3,31
Pressure less Drying	Nextel™ 610	29,6	3,20

In Figure 4-15 the pore size distributions of the three different materials is shown. The total porosity and the pore distribution results can be correlated to microstructure pictures from the samples, shown in Figure 4-16. In this Figure, all materials are disposed so that the first winded composite layer is in the bottom and the last winded layer at the top of the image.

The CMC consolidated under pressure and temperature (autoclave) showed larger pore sizes and a mono-modal distribution, the application of pressure in the composite may have caused the water from the suspension to move to the bottom of

the material before the component is dried, leading to regions with higher porosity and to an increased total porosity. This theory is corroborated in the literature by Iler 1979. The pore size distribution for the composite frozen show that ice crystal growth is uniformly distributed leading to a mono-modal homogeneous distribution of pores along the composite. In contrast, in the pressure-less dried composite, until the sample is completely dry the water from the matrix slowly deposited in the bottom of the material, leading to an inhomogeneous pore distribution where most of the porosity is found in the first 5 layers of the composite (Figure 4-16).

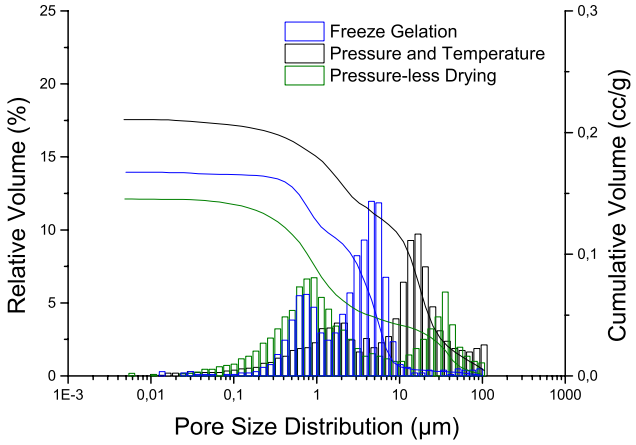

Figure 4-15 - Pore size distribution of sintered CMCs manufactured by impregnation of Nextel^{TM} 610 fibers, 3000 denier with sol gel matrix MF_B via filament winding and consolidated via freeze gelation, pressure and temperature (autoclave) and pressure-less drying.

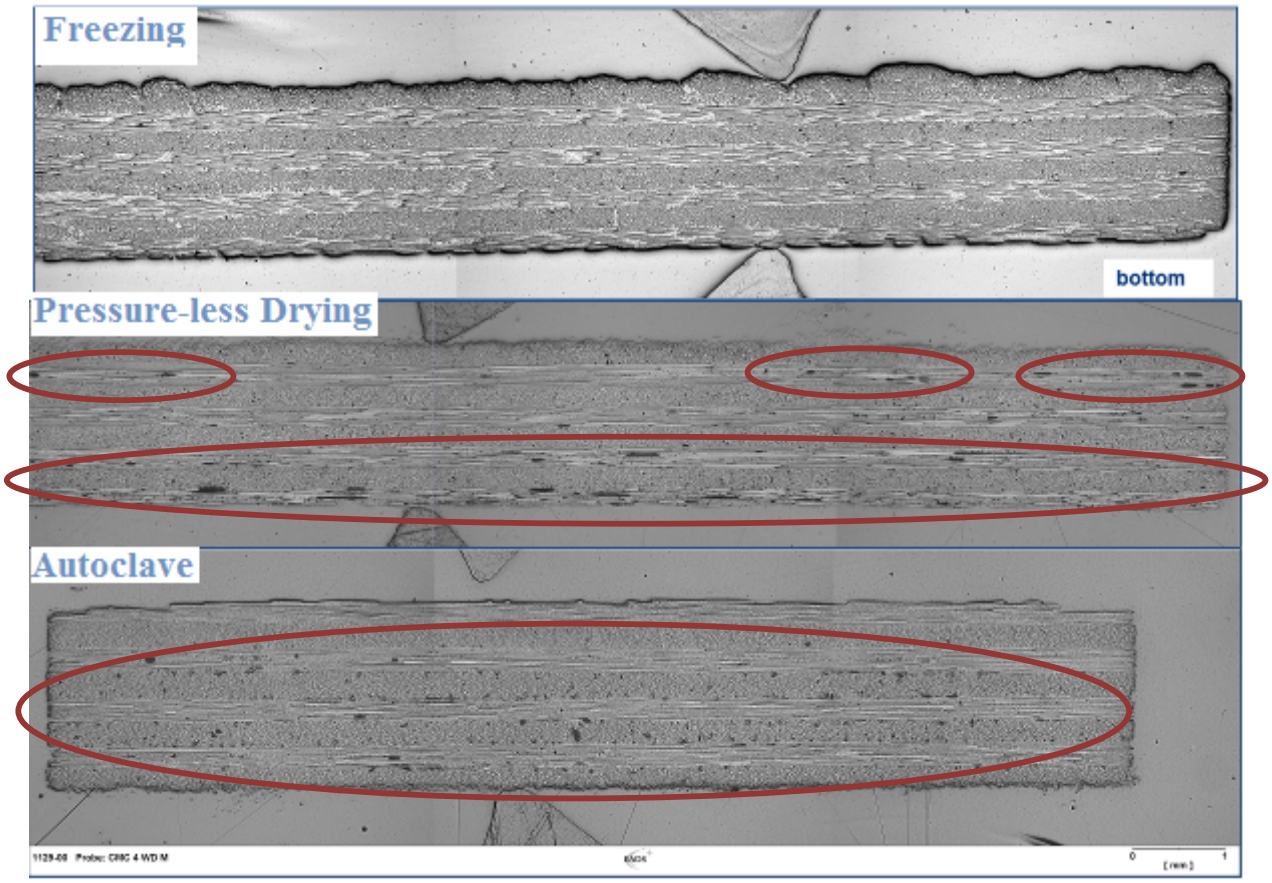

Figure 4-16 - Microstructure of the CMCs manufactured by impregnation of Nextel^{TM} 610 fibers, 3000 denier with sol gel matrix MF_B via filament winding and consolidated via freeze gelation, pressure-less drying and under pressure and temperature (autoclave).

In order to investigate the interlaminar properties of the composites, compressive shear test and transversal tensile test are conducted.

Figure 4-17 presents results from compression shear test. Composite manufactured using the autoclave process presented the lowest compression shear strength, 5,20 ± 2,90 MPa, as a result of the porosity observed in its microstructure. After freezing or drying at ambient temperature compression shear strength of 8,10 ± 1,50 MPa and 7,20 ± 2,20 MPa are respectively measured. Although the strength values are similar, their fracture mode is different. When frozen, all samples failed in the middle layers having the fracture energy dissipated from one layer to the next one (interlaminar failure), while the dried samples showed pure intralaminar failure (Figure 4-18). Intralaminar failure is normally present in weaker composites, where the crack propagates easily in the same layer as it started, in contrast to the interlaminar failure where bonding between layers is higher and the crack dissipates through different layers of the composite in order to find a weaker path to propagate

(Parthasarathy, Kerans, 2016). The high strength deviation is attributed to inhomogeneous pore distribution of the samples consolidated under pressure and temperature (autoclave) and pressure-less drying as shown in Figure 4-16.

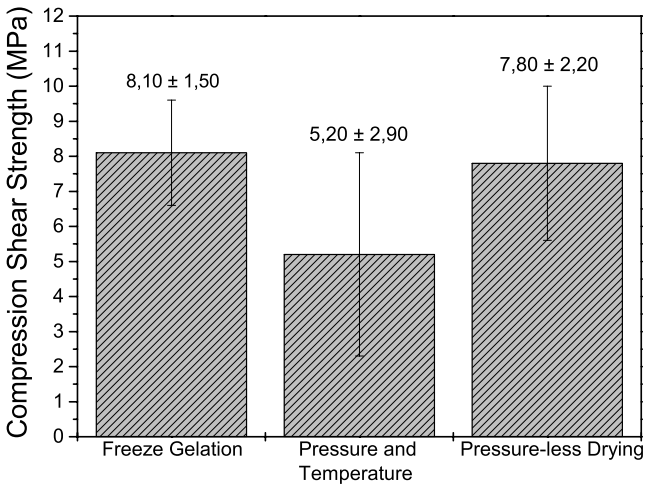

Figure 4-17 – Compression shear strength of sintered composites manufactured with Nextel^{TM} 610 fibers, 3000 denier and sol gel matrix MF_B via filament winding and different consolidation techniques.

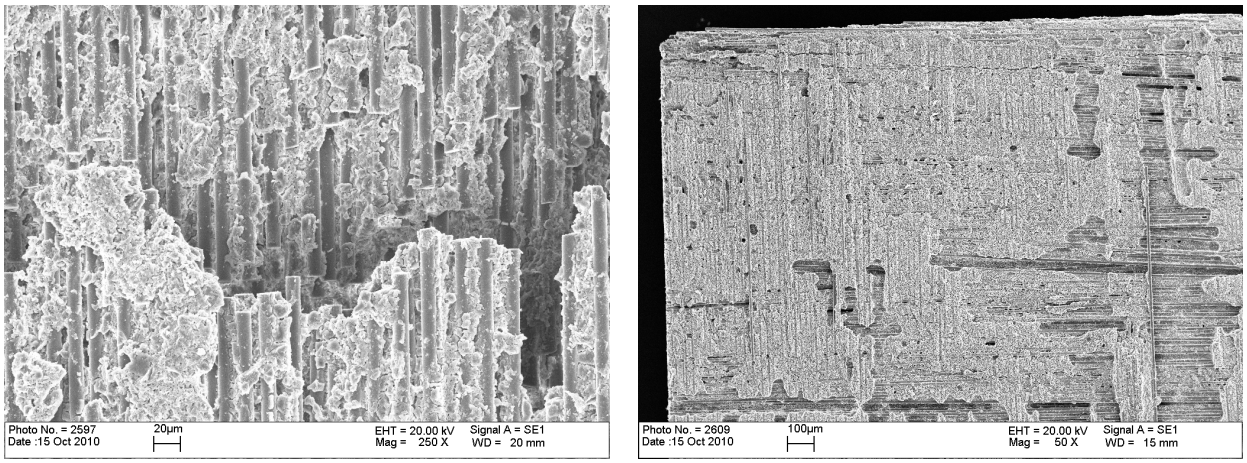

Figure 4-18 - Fracture surfaces of composites manufactured with Nextel^{TM} 610 fibers, 3000 denier and sol gel mullite matrix MF_B via filament winding and consolidated via freeze gelation (left) and pressure-less drying (right) after compressive shear test.

In Figure 4-19 results from transversal tensile tests are shown. The highest strength (2,32 ± 0,15 MPa) is measured on the samples manufactured via freeze gelation. In these samples energy dissipates from one layer to the following one, characterizing an interlaminar fracture. The CMC manufactured via autoclave process showed low transversal tensile strength (0,23 ± 0,04 MPa), all samples failed

intralaminar. The dried composites have transversal tensile strength of 1,10 ± 0,42 MPa, fracture surfaces indicate that failure occurred along one layer (intralaminar fracture) indicating low bonding strength between composite layers (Figure 4-20). These results can, once more, be correlated to the distribution of the porosity through the composite layers.

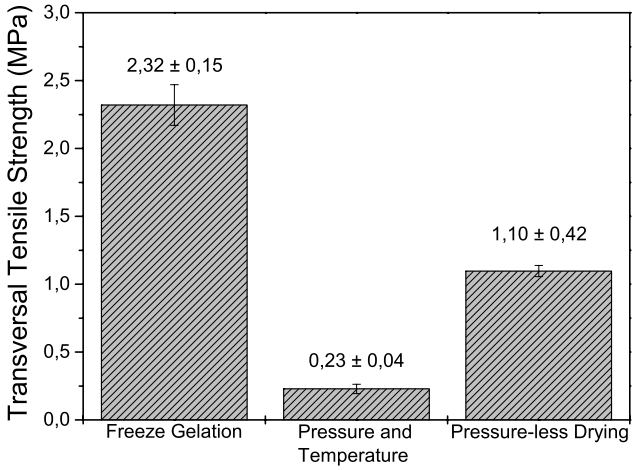

Figure 4-19 - Transversal tensile strength of sintered CMCs made with Nextel^{TM} 610 fibers, 3000 denier and sol gel matrix MF_B via filament winding and different consolidation techniques.

(a) (b) (c)

Figure 4-20 - Fracture surfaces of CMCs manufactured with Nextel^{TM} 610 fibers, 3000 denier and sol gel matrix MF_B via filament winding combined with freeze gelation (a), pressure and temperature (b) and pressure-less drying (c) after transversal tensile test.

Chapter Summary

Oxide ceramic matrix composites are manufactured using three different consolidation routes. Freeze gelation process is chosen to consolidate sol gel based

suspensions. The method is compared to other consolidation methods such as autoclave process in which pressure and temperature are applied, and pressure-less drying at ambient temperature.

All samples are fabricated using filament winding technique with the result of an excellent and homogeneous impregnation of the sol gel matrix within the fiber filaments. The use of different consolidation routes influenced the pore distribution and consequently the interlaminar properties of the composites. The average pore size is found to be larger in the samples fabricated under pressure and temperature. The autoclave process itself explains the larger pores, once the pressure applied forced the deposition of water, future composite porosity, to the bottom of the material before the component is dried. The microstructure of the composite explains its lower interlaminar strength. The composites manufactured via freeze gelation show porosity influenced by the growth of ice crystals during freezing. Pores are homogeneous distributed along all composite layers. Pressure-less drying consolidation does not induce such oriented pores. Pores are not distributed equally throughout the matrix and this lead to weaker fracture behavior and higher deviation of results.

The use of the freeze gelation route proved to be the most suitable route to consolidate oxide ceramic matrix composites when sol gel technique and fiber bundle impregnation via filament winding is used.

4.1.3 Development of Ceramic Composites with Mullite Matrix – Sintering Temperature

Further process optimization such as investigation of sintering parameters and their influence in the fiber-matrix interface is conducted to determine the optimum sintering temperature for the composite. The sintering temperature for ceramic matrix composites using oxide fibers is limited to approximately 1200°C due to fiber degradation (3M™ Ceramic Textiles and Composites) and to avoid reaction or adhesion between the fiber and the matrix, since no fiber coating is used. The sintering parameters chosen for oxide composites must be designed to avoid fiber damage and reactions and/ or adhesion between fiber-matrix, but still achieve matrix densification.

In this chapter, composite samples are sintered with different temperatures and their fracture toughness is investigated. Fracture toughness is chosen because it expresses the material resistance to fracture when a crack is present and, through fracture analysis, presence of fiber pull-out can be identified.

Furthermore, possible reaction or adhesion of the matrix to the fiber surface under the different sintering temperatures is evaluated via fiber push-in. Transmission Electron Microscope (TEM) investigation is conducted in one chosen sintering program.

Experimental Results

Materials fracture toughness is investigated via single edge notched bending test (SENB). Figure 4-21 shows the reduction of fracture toughness (K_{IC}) as the sintering temperature is increased. The difference between the material sintered at 1000°C and at higher temperatures such as 1200°C is significantly as fracture toughness decreases from 7,41 ± 0,56 $MPam^{0,5}$ to 2,70 ± 0,27 $MPam^{0,5}$. This proves that, by increasing the sintering temperature, the adhesion from the matrix to the fiber surface is greater, reducing the composite $K_{IC,}$ this behavior has been previously mention in the literature (Wang et al. 2015). This effect can also be seen in the fracture surface images (Figure 4-22 to 4-25) by an evident reduction of the fiber pull-out effect as sintering temperature increased.

When the composite is sintered at 1000°C (Figure 4-22), the effect of the fiber pull-out can be observed and reaches a length of approximately 150 μm. When sintering at 1000°C and 1150°C (Figure 4-23), pull-out effect could still be seen although its length is reduced to 50 – 100 μm. Regions where fiber and matrix are clustered can be observed. Sintering for 3 hours at 1150°C reduced even more fiber pull-out effect as shown in Figure 4-23. When composites are sintered at 1200°C (Figure 4-24) fiber pull-out is sporadically observed and brittle fracture is predominant. At this sintering temperature regions where matrix and fiber are sintered can be noticed and are detailed shown by arrows in Figure 4-25. Evidence of fiber pull-out and matrix crack along the fibers is a typical fracture surface observed when Weak Matrix Composites (WMC) approach is used (Lange 2010).

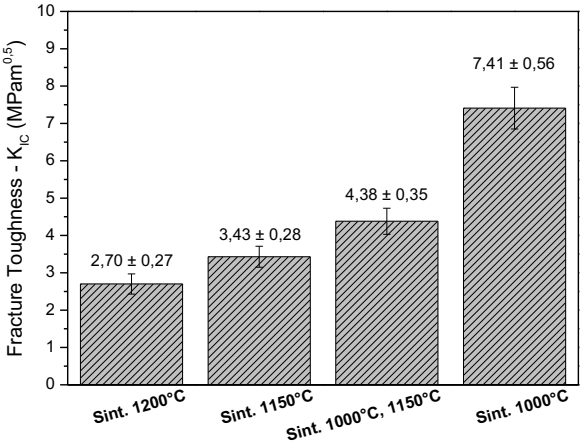

Figure 4-21 - Fracture toughness of CMCs made with Nextel™ 610 fibers and sol gel matrix MF_B via filament winding and freeze gelation technique sintered with different temperatures.

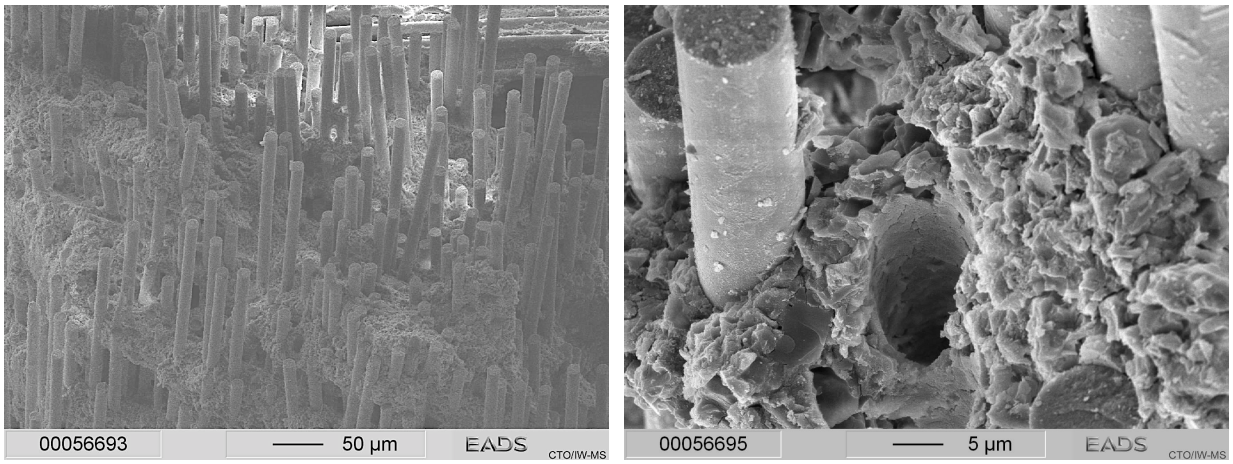

Figure 4-22 - Fracture surface after single edge notched bending test from sintered CMC manufactured with Nextel™ 610 fibers, 3000 denier via filament winding and freeze gelation. Sintering temperature of 1000°C for 3 hours.

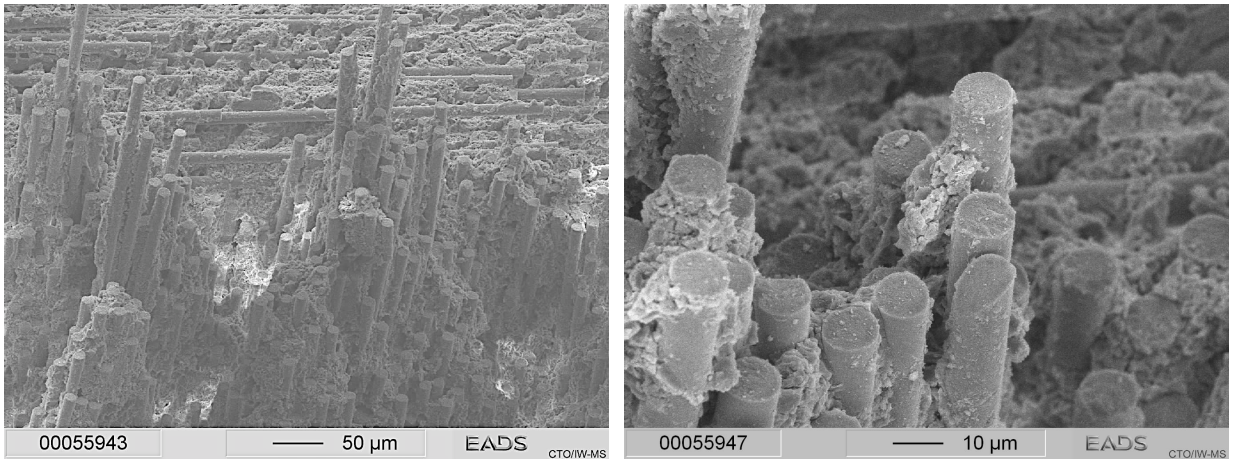

Figure 4-23 - Fracture surface after single edge notched bending test from sintered CMC manufactured with Nextel™ 610 fibers, 3000 denier via filament winding and freeze gelation. Sintering temperature of 1000°C for 3 hours and 1150°C for 1 hour.

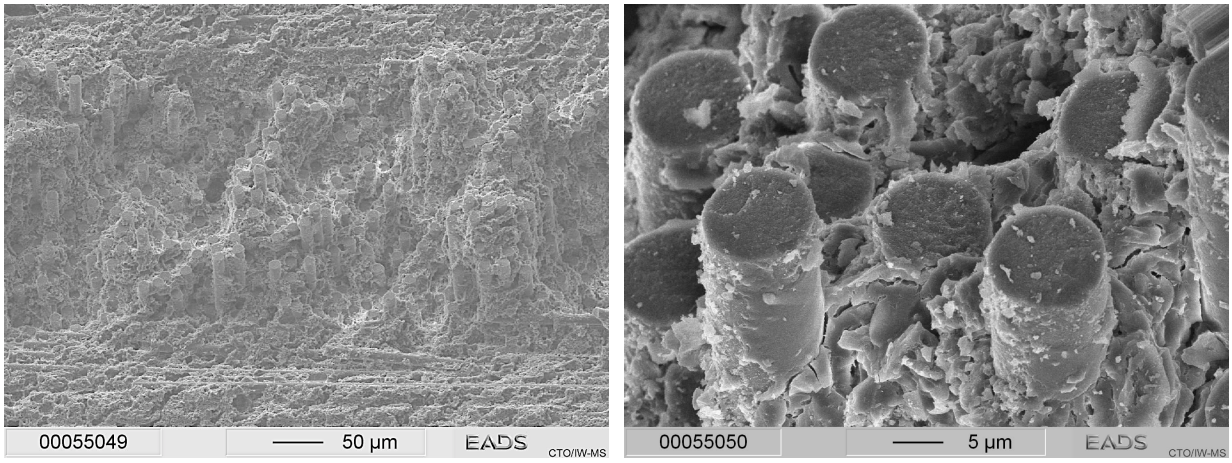

Figure 4-24 - Fracture surface after single edge notched bending test from sintered CMC manufactured with Nextel^{TM} 610 fibers, 3000 denier via filament winding and freeze gelation. Sintering temperature of 1150°C for 3 hours.

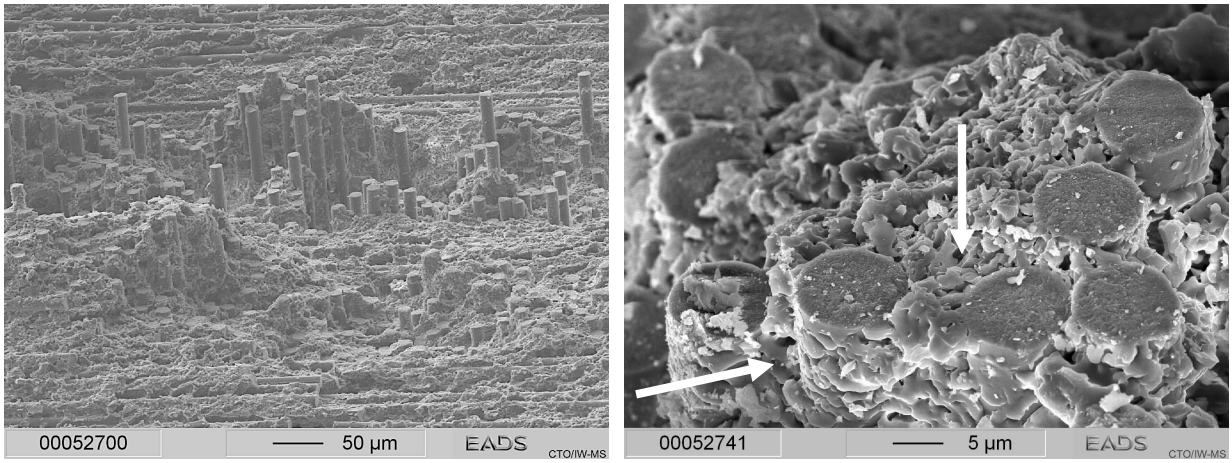

Figure 4-25 - Fracture surface after single edge notched bending test from sintered CMC manufactured with Nextel^{TM} 610 fibers, 3000 denier via filament winding and freeze gelation. Sintering temperature of 1200°C for 3 hours.

In order to understand the fracture toughness results and to measure the adhesion strength between the fiber and the matrix of the composites sintered with different temperatures, fiber push-in tests are performed.

Since sintering at 1000°C is not a viable temperature for mullite densification and it is used to have a clear influence of the fiber-matrix adhesion in the composite fracture toughness, fiber push-in is not investigated. This way, fiber push-in is performed in composites sintered with the following sintering parameters:

- Heating with 2°C/ min until 1200°C, dwelling time of 3h,
- Heating with 2°C/ min until 1150°C, dwelling time of 3h,

- Heating with 2°C/ min until 1000°C, dwelling time of 3h, heating with 5°C/min until 1150°C, dwelling time of 1 hour.

The results obtained from the push-in test are presented in Table 4-5 and a representative force vs. displacement curve of each is shown in Figure 4-26. In the composite sintered with two ramps, first 1000°C for 3 hours and then 1150°C for 1 hour, the force measured to push the fiber is 0,26 ± 0,03 N. In the force vs. displacement curve, the first break is identified by a first buckle in the curve, indicated with an arrow in Figure 4-26b. Additionally, hysteresis is observed, indicating a weaker bond between fiber and matrix, the effect of the hysteresis has been reported in the literature by Ferber et al. 2011.

For the composite sintered at 1150°C the force necessary to displace the fiber filament is 0,31 ± 0,06 N. No hysteresis is observed in its curve (Figure 4-26a), indicating stronger bond in the fiber-matrix interface. As the sintering temperature increases to 1200°C, the force necessary to displace the fiber filament from the composite matrix increases to 0,32 ± 0,02 N. Hysteresis is also not observed (Figure 4-26c).

Table 4-5 - Push-in displacement force from composites manufactured with Nextel™ 610, 3000 denier and matrix MF_B via filament winding and consolidated via freeze gelation after sintering with different temperatures.

Sintering Temperature (°C)	Average Force (N)
1000°C, 3h/ 1150°C, 1h	0,26 ± 0,03
1150°C, 3h	0,31 ± 0,06
1200°C, 3h	0,32 ± 0,02

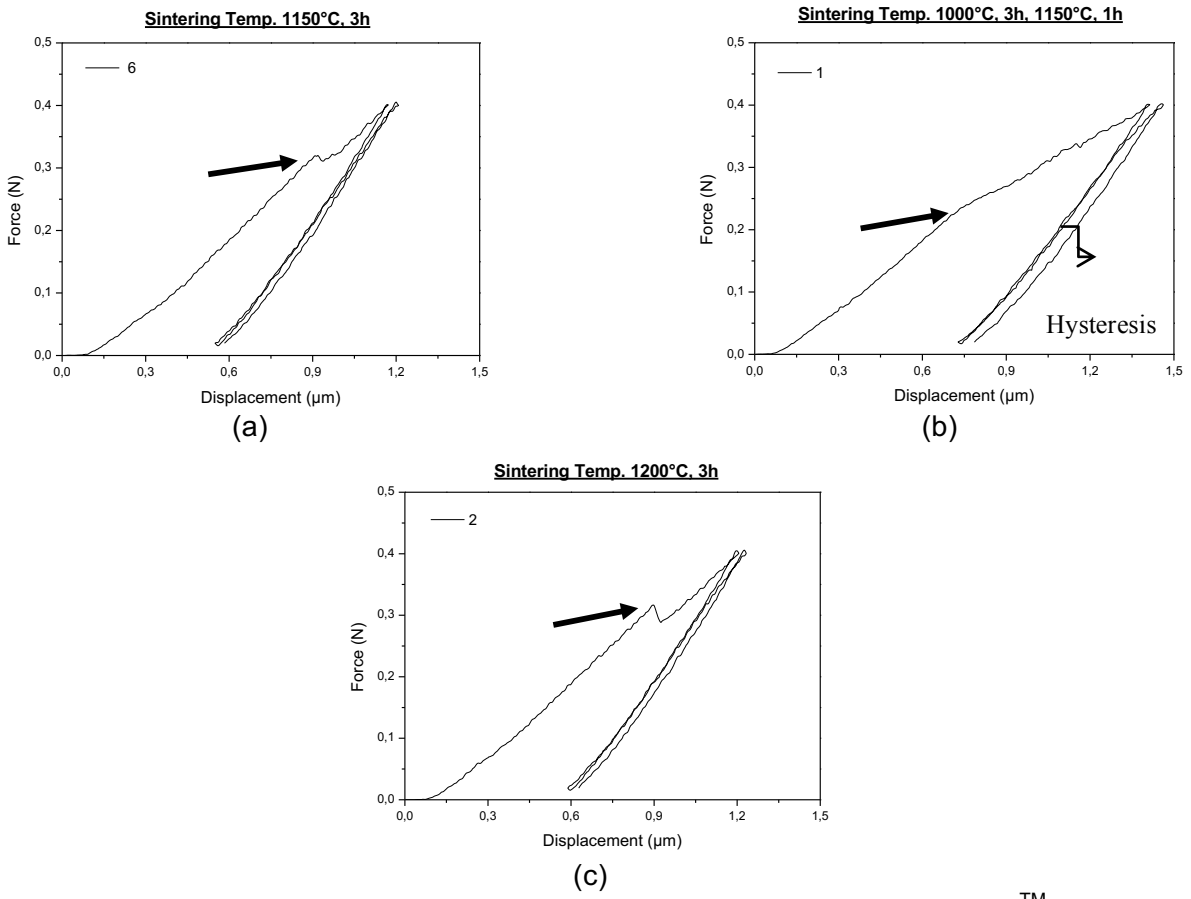

Figure 4-26 – Representative curves from push-in measurement from Nextel^{TM} 610 fiber, 3000 denier infiltrated with matrix MF_B and consolidated via freeze gelation sintered at (a) 1150°C, 3h; (b) 1000°C, 3h, 1150°C, 1h; (c) 1200°C, 3h.

The composite sintered first at 1000°C for 3 hours and then at 1150°C for 1 hour is analyzed under TEM due to its higher fracture toughness and lower fiber displacement strength.

Figure 4-27 shows an image of the lamella prepared for TEM measurement with the matrix with its mullite grains in the middle of two fiber filaments. It Figure 4-28, TEM image of fiber-matrix interface is shown together with its element mapping. The color pink represents Al (aluminum), green Si (silicon), blue O (oxygen) and yellow C (carbon) from the epoxy resin used for sample embedding. The fiber-matrix interface is well defined and no evidence of adhesion and/ or reaction is observed. EDX measurement is conducted in two different regions of the sample and, in none of them, adhesion in the fiber-matrix interface is recognized.

Adhesion between fiber and matrix is not desired as the fracture mode expected from WMC dictates that a crack, when initiated in the composite, shall propagate through the porous matrix and not be deflected into the fibers, causing failure at lower

strengths (Lang 2010). When fiber and matrix are sintered together, as shown in Figure 4-25, the crack could find its way into the fiber, causing the composite to fail at lower mechanical strengths.

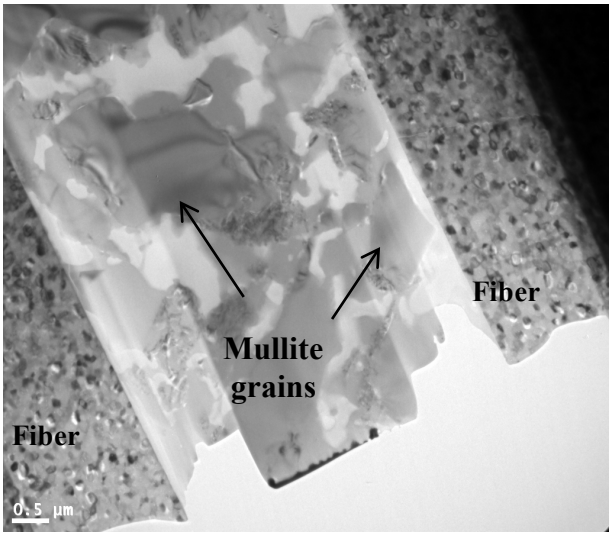

Figure 4-27 - Lamella for TEM investigation from a CMC manufactured with Nextel™ 610, 3000 denier and sol gel matrix MF_B sintered at 1000°C, 3hours, 1150°C, 1 hour.

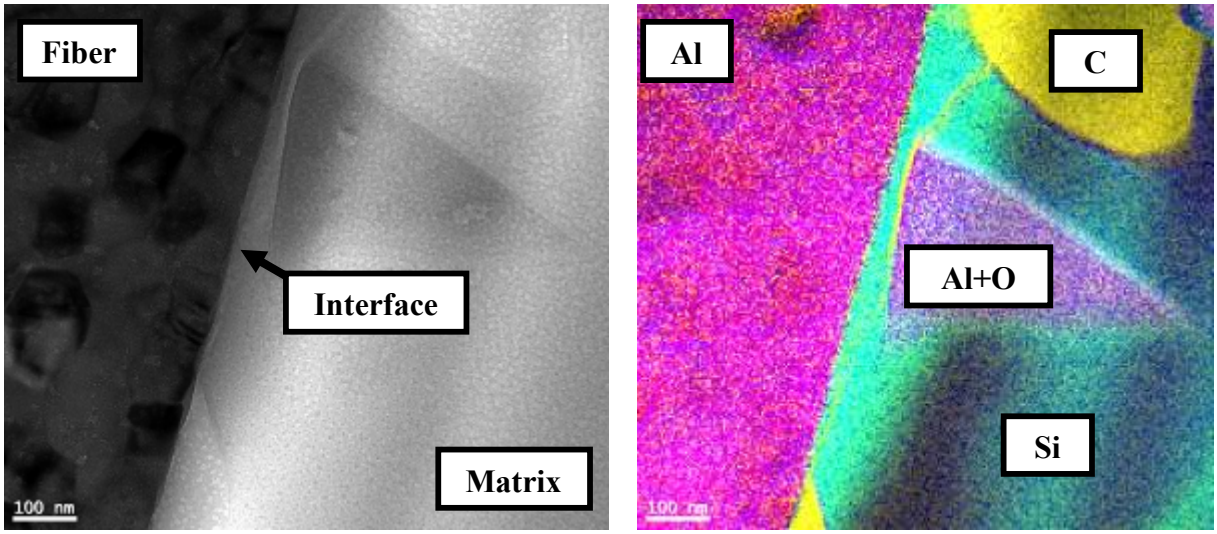

Figure 4-28 – TEM image (left) and element mapping (right) from a CMC manufactured with Nextel™ 610, 3000 denier and sol gel matrix MF_B sintered at 1000°C, 3hours, 1150°C, 1 hour. Legend: pink - Al; green – Si; blue – O and yellow – epoxy resin.

Chapter Summary

The influence of different sintering temperatures is analyzed in oxide based CMC with Nextel™ 610 fiber, 3000 denier, organic (PVA) sized, and sol gel based

ceramic slurry with mullite as filler (MF_B) via the combination of filament winding with freeze gelation.

In this chapter, it is proven that the sintering temperature influences in the composite fracture toughness once higher temperatures and sintering times induce adhesion of the ceramic matrix to the fiber surface, reducing composite fracture toughness.

The results obtained from the fracture toughness and fiber push-in tests, demonstrate that sintering at 1200°C with a dwelling time of 3 hours lowers the composite fracture toughness. This is due to a higher probability of adhesion or sintering of the ceramic matrix to the fiber surface, as observed in the SEM images from the specimen fracture toughness.

When two sintering ramps are used, first heating until 1000°C for 3 hours and then until 1150°C for 1 hour, fracture toughness increases from 2,70 ± 0,27 $MPam^{0,5}$ to 4,38 ± 0,35 $MPam^{0,5}$ (in comparison with sintering temp. of 1200°C) and fiber pull-out can be observed. Fiber displacement force is reduced from 0,32 ± 0,02 to 0,26 ± 0,03 (comparing with sintering temp. of 1200°C). TEM analysis from the composite sintered until 1000°C for 3 hours and then until 1150°C for 1 hour showed no evidence of matrix adhesion or reaction between fiber and matrix could be observed. Explaining the higher fracture toughness of this composite.

Therefore, the sintering parameter (heating with 2°C/ min until 1000°C, dwelling time of 3h, heating with 5°C/min until 1150°C and dwelling time of 1 hour) is chosen to be in the further development of the ceramic matrix composites in this work.

4.1.4 Development of Ceramic Composites with Mullite Matrix – Fiber Volume Content

In this chapter, composites are manufactured with fiber content of approximately 30 vol. %, 40 vol. % and 50 vol. % and characterized regarding their physical and mechanical properties such as interlaminar strength, fracture toughness and bending strength.

The composites are manufactured via the combination of filament winding with freeze gelation process as described in Chapter 3.2. The composite with 28,3 vol. % fiber content is referred as MF_B_30 and corresponds to the composite described in Chapter 4.1. Composite with 41,8 vol. % is referred as MF_B_40 and with 49,1 vol. %

as MF_B_50. The presented fiber volume contents are calculated based on image analysis (see Appendix A.1).

In order to increase the fiber percentage in the composites the amount of matrix infiltrated in the fiber bundle is reduced in the filament winding infiltration baths. Measuring the weight of one meter of fiber before and after infiltration controls this parameter. Knowing the weight of fiber and the weight of fiber plus matrix it is possible to calculate the amount of infiltrated matrix.

Composites are manufactured with 0°/90° fiber architecture disposed in 8 asymmetric layers in the case of MF_B_30 and MF_B_40, and 8 symmetric layers in MF_B_50. Composites with symmetric fiber lay-up are expected to have better mechanical performance as a consequence of equal thermal expansion throughout the layers during sintering. Freezing and drying parameters are kept constant in the three variations. MF_B_30 is sintered with heating rate of 2°C/min until 1200°C for 3 hours, the results correspondent to this composite were presented in Chapter 4.1 and are, therefore, partially repeated. MF_B_40 and MF_B_50 are sintered with 2°C/ min until 1000°C, dwelling time of 3h, heating with 5°C/min until 1150°C for 1 hour.

Microstructure of the composite MF_B_40 (Figure 4-29a and 4-29c) and MF_B_50 (Figure 4-29b and 4-29d) are shown. Composite layers disposed in fiber architecture of 0°/90° are indicated in Figure 4-29a. No sign of delamination between composite layers is observed in MF_B_40. Black regions correspond to pores. In MF_B_40, impregnation of the ceramic matrix among fiber filaments is successfully achieved and no regions with agglomerated fiber filaments is seen (Figure 4-29c). MF_B_30 microstructure (Figure 4-13a and 4-14a) also reveals a microstructure with homogeneous fiber infiltration and no signs of delamination.

In order to manufacture composite MF_B_50 less amount of matrix is used during composite manufacture. As a consequence, not enough matrix infiltrated the inner fiber filaments and delamination between composite layers (arrow a, Figure 4-29b) is observed, as well as regions without ceramic matrix (arrow b, Figure 4-29b). Since the amount of matrix used to achieve a higher fiber volume content is not enough to infiltrate all fiber filaments, during grinding and polishing of the sample some matrix pieces are removed (exemplarily circulated in Figure 4-29b) and fiber filaments are damaged (Figure 4-29d).

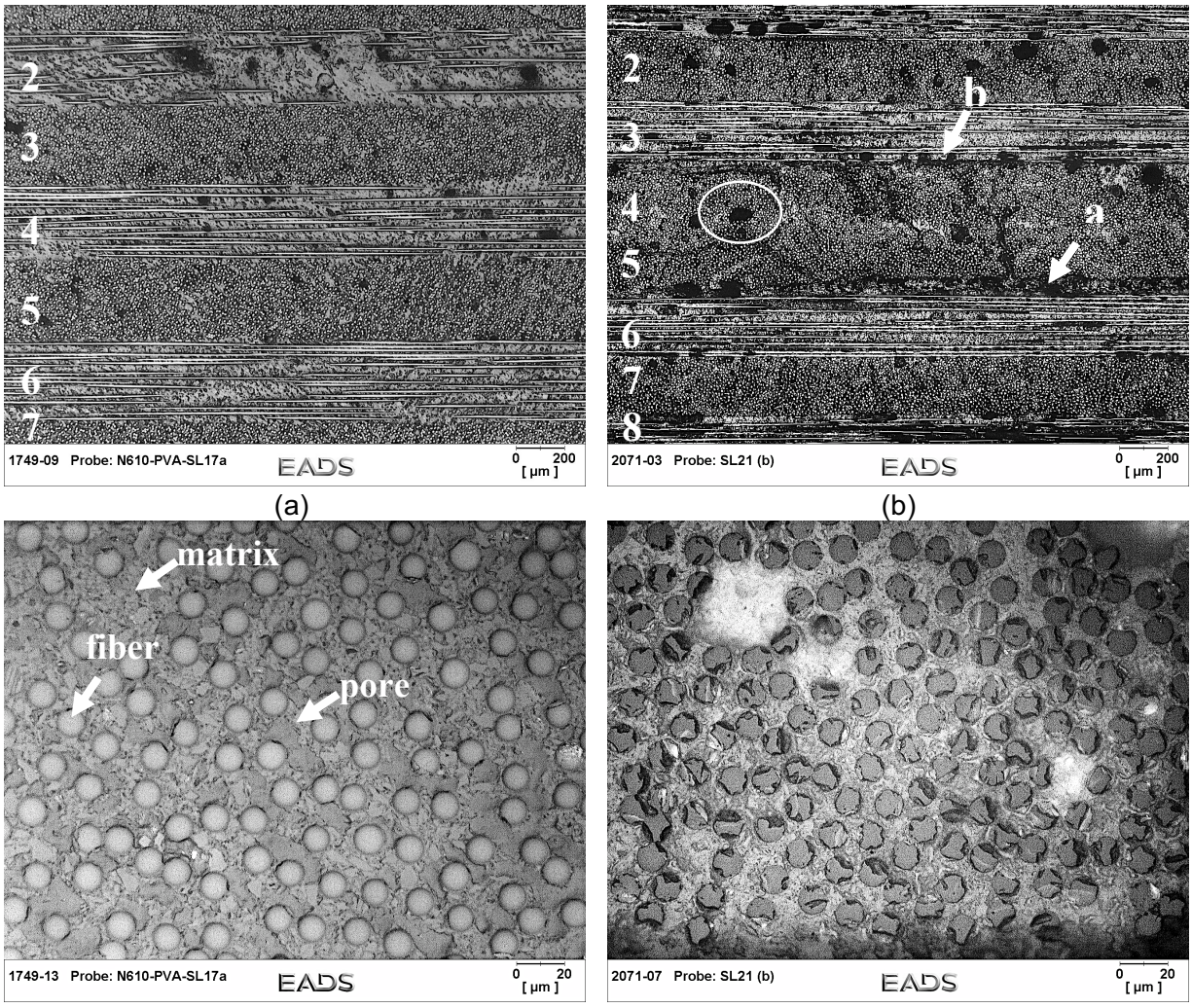

Figure 4-29 - Microstructure of sintered CMCs manufactured by impregnation of Nextel^{TM} 610 fibers, 3000 denier with mullite matrix via filament winding with (a, c) 40 fiber vol. % and (b, d) 50 fiber vol. %.

Porosity of composite MF_B_30 is greater than MF_B_40 and MF_B_50 (Figure 4-30, Table 4-6), fact that can be directly correlated to the higher amount of matrix in MF_B_30 leading to nucleation of more ice crystals in the freezing step. Total porosity of MF_B_50 is lower once less matrix is used during its manufacturing (Table 4-6). Likewise, composite density is inversely proportional to the amount of porosity in the composites.

MF_B_30 and MF_B_40 show mono-modal pore size distribution with the majority of the pores ranging 1μm to 10μm as shown in Figure 4-31. The bi-modal pore distribution from MF_B_50 with a peak of pores ranging approximately 10 μm can be attributed to the delamination observed in this composite microstructure.

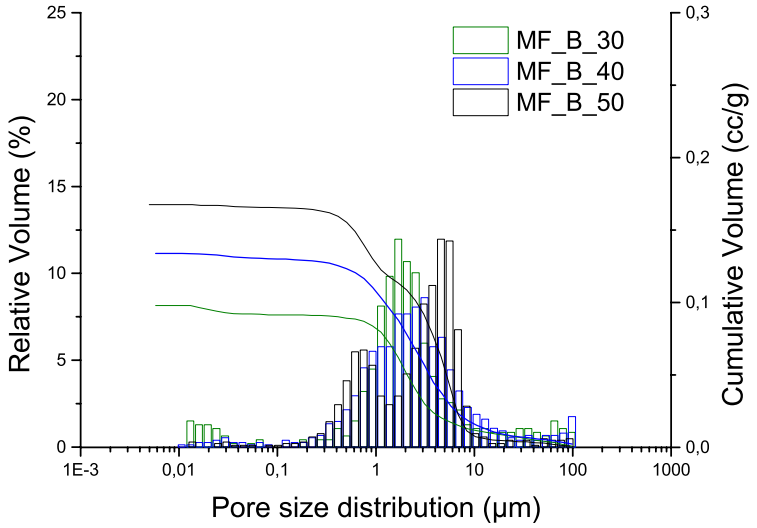

Figure 4-30 - Pore size distribution measured via Hg-Intrusion for sintered oxide based CMCs manufactured by impregnation of Nextel™ 610 fibers, 3000 denier with mullite matrix via filament winding with 30 vol. %, 40 vol. % and 50 vol. % fiber.

Table 4-6 - Density and porosity of sintered CMCs manufactured by impregnation of Nextel™ 610 fibers, 3000 denier with mullite matrix via filament winding with approximately 30 vol. %, 40 vol. % and 50 vol. % fiber content.

Composite	Fiber Content %	Porosity (vol. %) Archimedes	Bulk Density (g/cm³) Archimedes	Apparent Density (g/cm³) Archimedes
MF_B_30	30	33,88 ± 0,71	2,14 ± 0,02	3,24 ± 0,00
MF_B_40	40	32,57 ± 1,03	2,18 ± 0,04	3,23 ± 0,02
MF_B_50	50	27,86 ± 1,21	2,42 ± 0,03	3,35 ± 0,02

Interlaminar properties of the composites manufactured are assessed with compressive shear and transversal tensile test. In Figure 4-31a representative strength vs. displacement curve of each composite is shown. MF_B_30 has compression shear strength of 8,10 ± 1,50 MPa and interlaminar failure mode (Figure 4-18). Compression shear strength of 8,87 ± 1,76 MPa is achieved in MF_B_40. Its fracture is characterized mainly by interlaminar behavior once fracture energy is dissipated through more than one layer (Figure 4-32a).

MF_B_50 shows high standard deviation and intralaminar fracture in all samples (Figure 4-32b). Compression shear strength is 1,74 ± 0,78 MPa. These results correspond to the materials microstructure where delaminated areas are observed. Intralaminar fracture occurred in all samples between the 3rd and 4th layer, same layer where delamination is observed (Figure 4-29b).

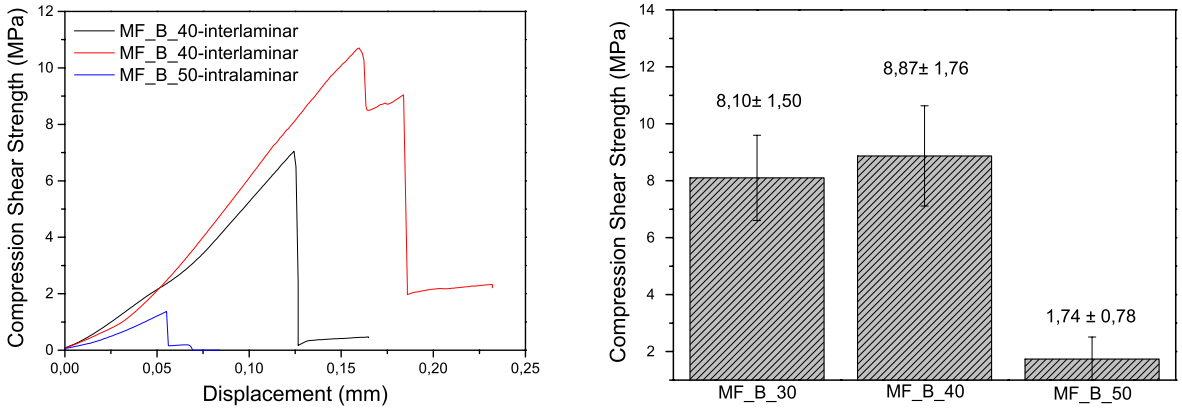

(a) (b)

Figure 4-31- Representative curves (a) and comparison of the compression shear strength (b) from sintered CMCs manufactured by impregnation of Nextel™ 610 fibers, 3000 denier with mullite matrix via filament winding with 30 fiber vol. % (MF_B_30), 40 fiber vol. % (MF_B_40) and 50 fiber vol. % (MF_B_50).

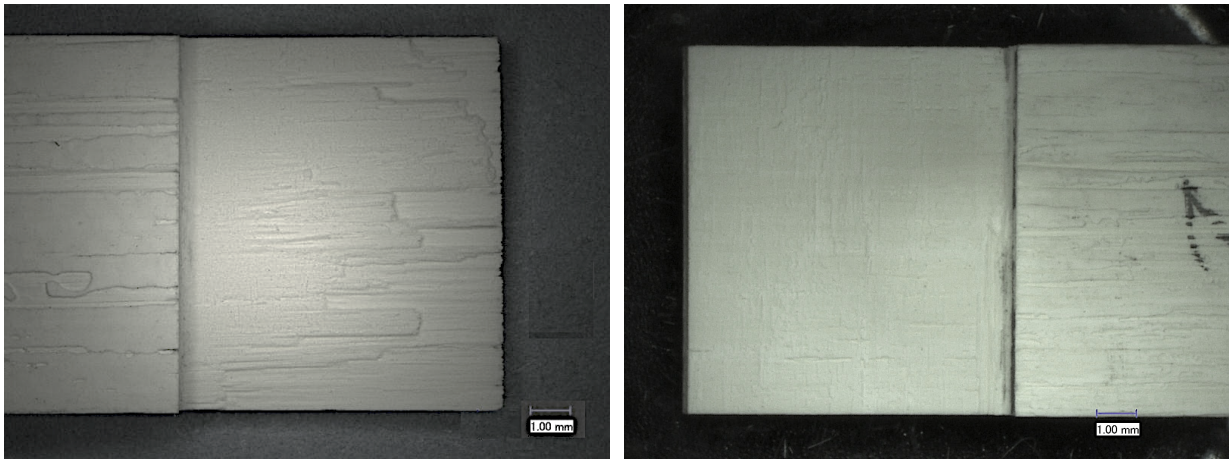

(a) (b)

Figure 4-32 - Fracture surface of sample showing interlaminar failure (a) of MF_B_40 and intralaminar failure (b) of MF_B_50 tested in compression shear. Scale bars indicate 1 mm.

It can be concluded that, as the fiber content is increased from 30 to 40 vol. %, compression shear strength does not change as this test is focused on characterizing the strength of the matrix. When the fiber content is increased to 50 vol. %, compression shear strength is significantly reduced. The amount of matrix necessary to manufacture a composite with fiber content of approximately 30 vol.% and 40 vol. % is enough to guarantee matrix infiltration and binding between layers. The amount of matrix necessary to manufacture the composite with 50 vol. % of fiber is not sufficient to infiltrate the composite fiber filaments and to promote binding between the composite layers, leading to lower composite interlaminar strength.

Furthermore, since MF_B_30 and MF_B_40 are sintered using different temperatures it is, again, shown that sintering using 1150°C results in higher matrix strength as demonstrated in Chapter 4.1.3.

Under transversal tensile load, MF_B_40 present high deviation characterizing an inhomogeneous material. Figure 4-33a shows representative strength vs. displacement curve of the materials. Transversal tensile strength achieved from MF_B_30 is 2,32 ± 0,15 MPa and 2,33 ± 1,76 MPa from MF_B_40. In all samples from both composites fracture dissipated from one layer to another characterizing an interlaminar failure (Figure 4-20a and 4-34a). MF_B_50 shows dispersed results and strength of 1,48 ± 0,48 MPa. Intralaminar and interlaminar fracture behavior is observed (Figure 4-34b).

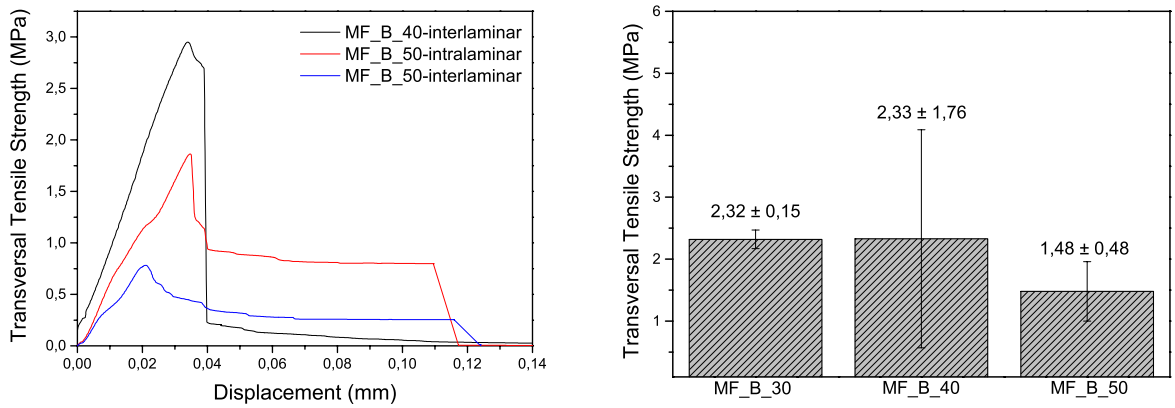

Figure 4-33 – Representative curves (a) and comparison of the transversal tensile strength (b) from sintered CMCs manufactured by impregnation of Nextel™ 610 fibers, 3000 denier with mullite matrix via filament winding with 30 fiber vol. % (MF_B_30), 40 fiber vol. % (MF_B_40) and 50 fiber vol. % (MF_B_50).

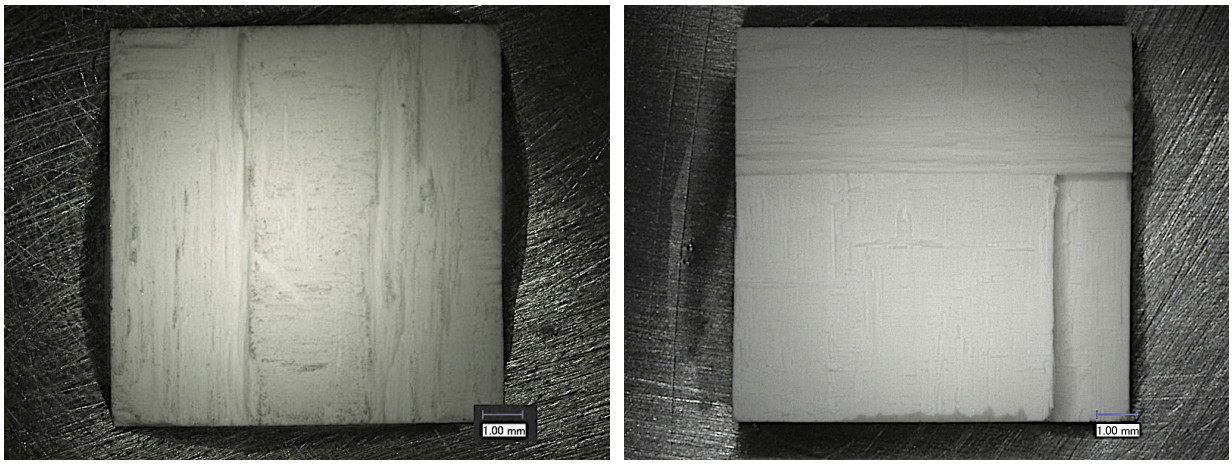

(a) (b)

Figure 4-34 - Fracture surface of sintered CMC with 40 fiber vol. % (a) and with 50 fiber vol. % (b) tested in transversal tensile both showing interlaminar failure. Scale bar indicates 1 mm.

Figure 4-33b shows that transversal tensile strength remains unchanged in the composites with 30 and 40 vol. % of fiber content. When the fiber content is increased to 50 vol. %, transversal tensile strength weakens. The fact that MF_B_50 showed lower strength values indicates, once again, that the amount of ceramic slurry used to achieve this fiber volume is not enough to promote binding between layers and also to infiltrate completely the composite; leading to delamination at low strengths. Under transversal tensile load the influence of using different sintering temperatures in MF_B_30 and MF_B_40 could not be seen since interlaminar strength can be considered to be the same.

The fracture toughness of these materials is evaluated via single edge notched bending (SENB) test. In the test, failure is induced through the introduction of a thin crack in the sample (Figure 4-35b). A representative curve of the strength vs. displacement from MF_B_40 is presented in Figure 4-34a. For MF_B_40 K_{IC} of 3,33 ± 0,19 $MPam^{0,5}$ is calculated. According to SEM analysis, fracture surface of the samples shows evidence of matrix fracture (Figure 4-36). Samples from MF_B_50 could not be successfully tested because once force is applied the composite delaminated as shown in Figure 4-37. The fracture did not grow from the induced thin crack and the measurement is, therefore, not valid. Delamination of MF_B_50 layers before the crack starts to dissipate shows that the amount of matrix needed to manufacture composites with a fiber content of 50 vol.% is not sufficient to bind the single composite layers.

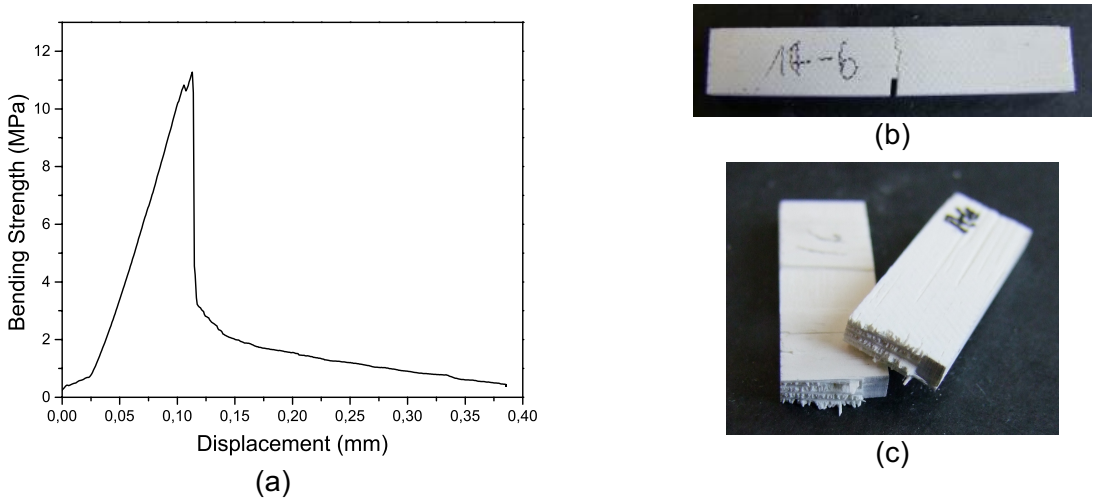

Figure 4-35 – Representative strength vs. displacement curve (a), image showing crack dissipation path (b) and fracture surface (c) of sintered MF_B_40 manufactured with Nextel^{TM} 610 fibers, 3000 denier with mullite matrix via filament winding and freeze gelation.

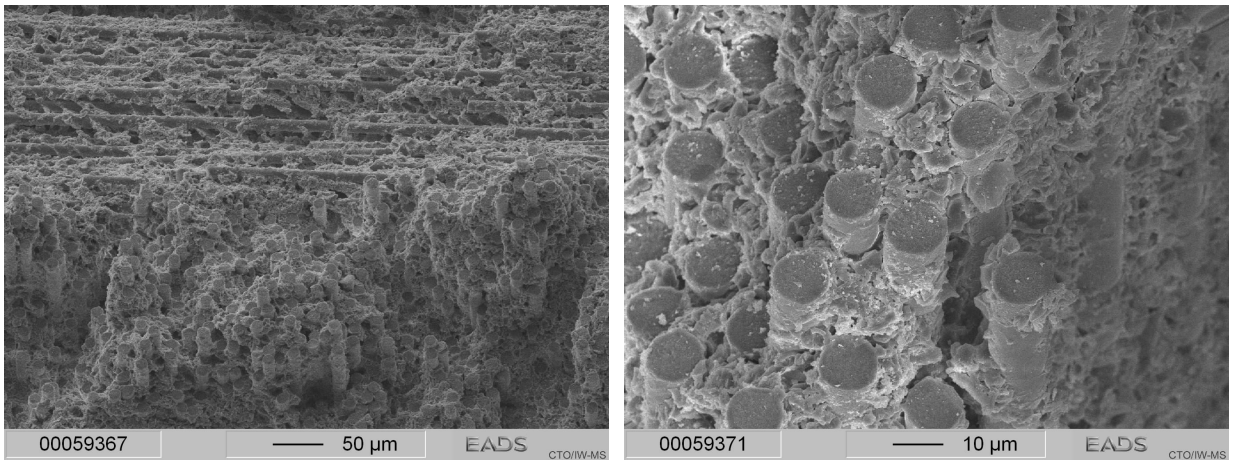

Figure 4-36 - Fracture surface of MF_B_40 manufactured with Nextel^{TM} 610 fibers, 3000 denier with mullite matrix via filament winding and freeze gelation after single edge notched bending test.

A comparison of K_{IC} from composite MF_B_30 and MF_B_40 is given in Figure 4-38. Besides the different fiber volume content these composites are also sintered at different temperatures, what influences in the fracture toughness of the material (Chapter 4.1.3). Fracture toughness from MF_B_40 is slightly higher as a consequence of the lower sintering temperature.

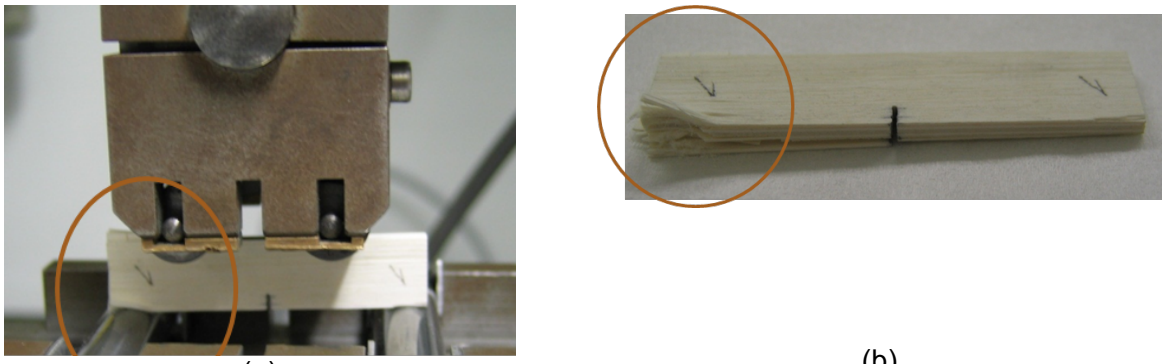

(a) (b)

Figure 4-37 - CMC sample manufactured by impregnation of Nextel™ 610 fibers, 3000 denier with mullite matrix via filament winding with 50 fiber vol. % during single edge notched bending test (a) and delaminated sample after test (b).

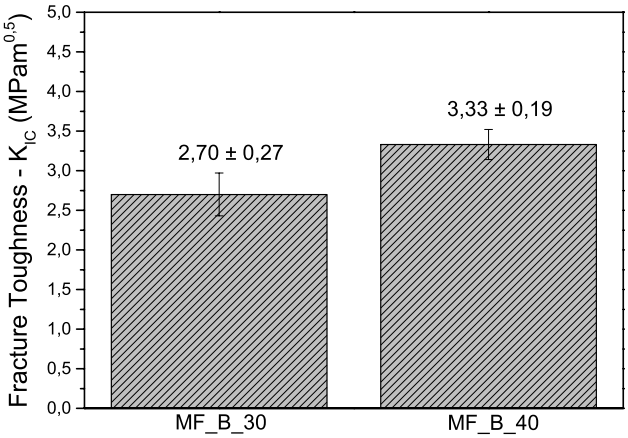

Figure 4-38 - K_{IC} from CMCs with ca. 30 fiber vol. % and 40 fiber vol. % manufactured with Nextel™ 610 fibers, 3000 denier with mullite matrix via filament winding.

Composite strength in fiber direction is measured under four-point bending test (Figure 4-39). Samples from MF_B_30 failed in tensile and showed an average bending strength of 78,11 ± 22,06 MPa. In MF_B_40 only one sample failed in tensile and a bending strength of 93,44 MPa is calculated. The other samples delaminated and their interlaminar shear strength is calculated to 1,13 ± 0,45 MPa. All MF_B_50 samples delaminated showing an interlaminar shear strength of 0,59 ± 0,12 MPa.

In MF_B_30 (Figure 4-40a) and one sample of MF_B_40 (Figure 4-40b) fracture started in the longitudinal fibers in the outer layer opposite to the loading bears. In MF_B_50, delamination between composite layers orientated in 0°/90° is observed (Figure 4-40c), in the composite symmetric layer delamination did not occur.

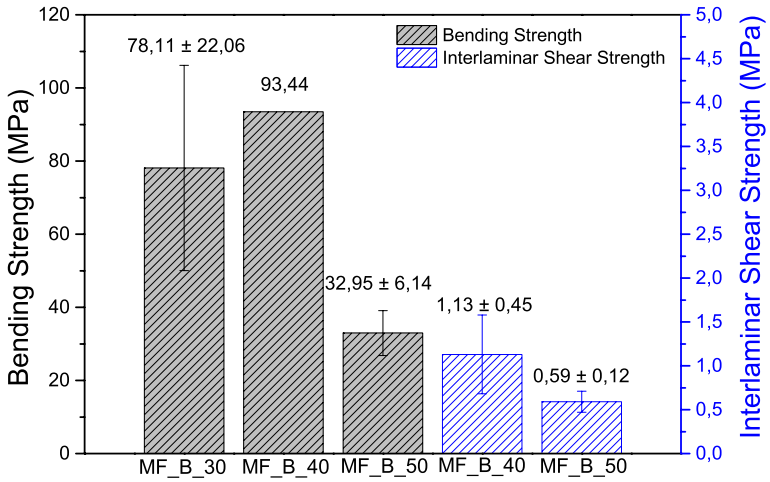

Figure 4-39 - Bending and interlaminar shear strength of CMCs manufactured with Nextel™ 610 fibers, 3000 denier with mullite matrix via filament winding and freeze gelation with 30 fiber vol. % (MF_B_30), 40 fiber vol. % (MF_B_40) and 50 fiber vol. % (MF_B_50) tested in four-point bending.

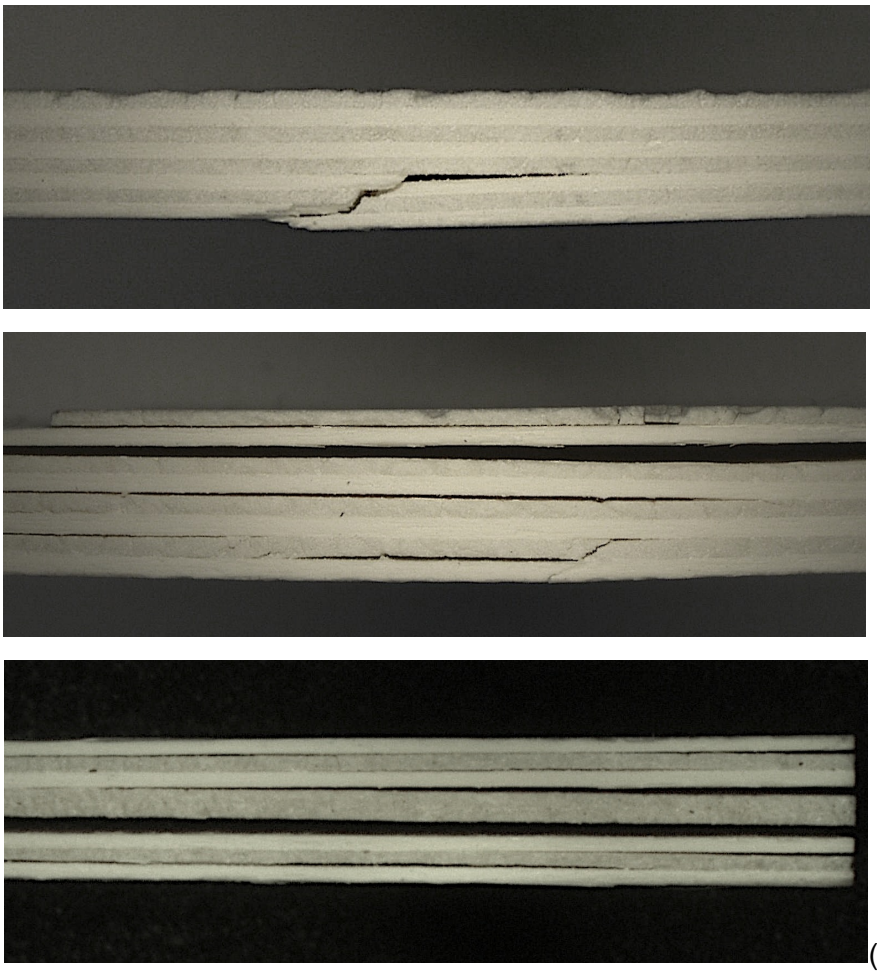

Figure 4-40 – CMC samples manufactured with Nextel™ 610 fibers, 3000 denier with mullite matrix via filament winding and freeze gelation with ca. 30 fiber vol. % (a), 40 fiber vol. % (b) and 50 fiber vol. % (c) after four point bending test.

Under compression shear and transversal tensile load, composite MF_B_30 and MF_B_40 presented nearly the same strength. In bending, it is expected that the composite with higher fiber volume content present higher resistance to bending loads. However, the composite with 30 vol. % fiber content (MF_B_30) failed in tensile mode while the composite with 40 vol. % (MF_B_40) of fiber delaminated. This might indicate that the strength given by matrix densification after sintering is lower than the strength of the fiber in tensile direction causing the material to delaminate before tensile fracture happened. This could be a sign that at the chosen sintering temperature (1000°C followed by 1150°C) diffusion of the mullite is too low and particles are not yet densified. This way, the ceramic matrix is not able to transfer its mechanical properties to the composite.

In order to investigate if the ceramic matrix manufactured with silica sol and mullite is densified after sintering up to 1150°C, thermal conductibility of the matrix is measured. The test result is shown in Figure 4-41. After the test, matrix MF_B thermal conductibility is 1,54 ± 0,04 mm²/s. From the literature (Schneider et al. 2005) the thermal conductibility of mullite at room temperature is 2,2 mm²/s and of silicon dioxide in the cristobalite phase is 0,9 mm²/s. The measurement indicates that densification of matrix B presented is mainly due to the beginning of silica crystallization observed above 900°C. Fact which is described in the thermal conductivity and thermal expansion measurements from this matrix (Chapter 4.1.1).

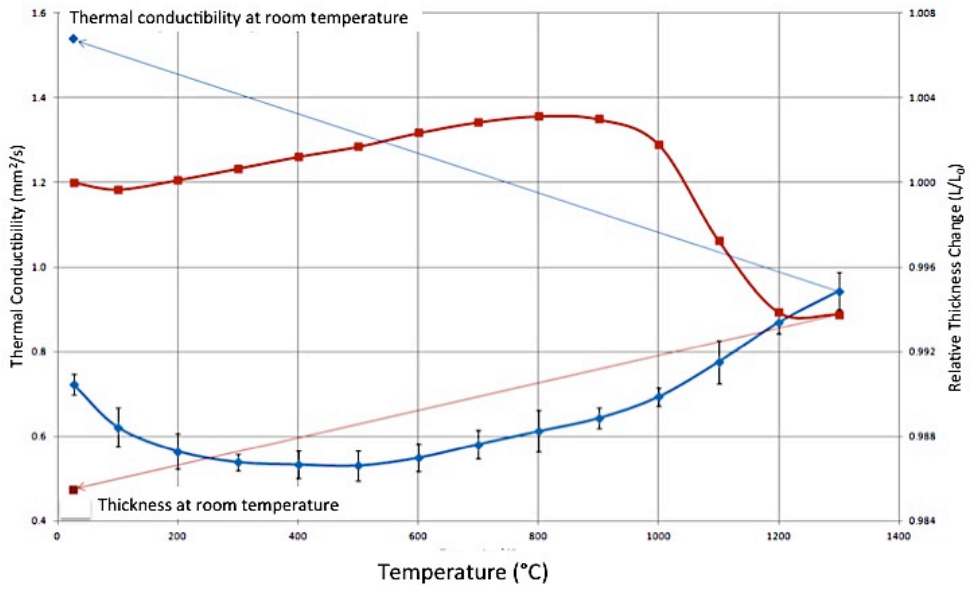

Figure 4-41 – Thermal conductibility (blue) and density (red) of the ceramic matrix manufactured with silica sol and mullite in relation to temperature.

Once silica corresponds to 17 wt. % of total matrix composition it is presupposed that sintered silica particles are distributed around bigger mullite particles (58 wt. %) that are not completely sintered. The amount of silica in the ceramic matrix composition corresponds to one third of silica. If sintering until 1150°C is enough only for silica densification, this amount of silica cannot strengthen the complete matrix resulting in lower properties from the matrix i.e. lower composite interlaminar strength.

A possibility to accelerate the diffusion of ceramic powders during sintering is the use of sintering additives. Magnesium oxide (MgO) is one of the sintering agents most commonly used to reduce the sintering temperature of mullite (Souto et al. 2009; Montanaro et al. 1997; Rani et al. 2001; Viswabaskaran et al. 2003).

Few studies have investigated the influence of sintering aids on the densification and sintering behavior of mullite bodies, and even fewer studies involved the use of commercial mullite powders. An example is the study from Souto et al. 2009, who investigated the influence of 0,1 wt. % to 0,5 wt. % MgO on the sintering of commercial mullite powder and showed that the use of 0,5 wt. % MgO reduced the sintering temperature of mullite in approximately 100°C.

Suspensions with 0,5 wt. % and 1,0 wt. % of MgO are manufactured, nevertheless both suspensions gelled right after the addition of MgO. This happens because the oxygen group from the sintering additive reacts with the H+ group from

the silica sol, causing the suspension to gel rapidly as explained in Figure 4-42 (Golshan et al. 2011). Consequently, use of sintering agent together with silica sol, when freeze gelation technique is aimed, is not possible.

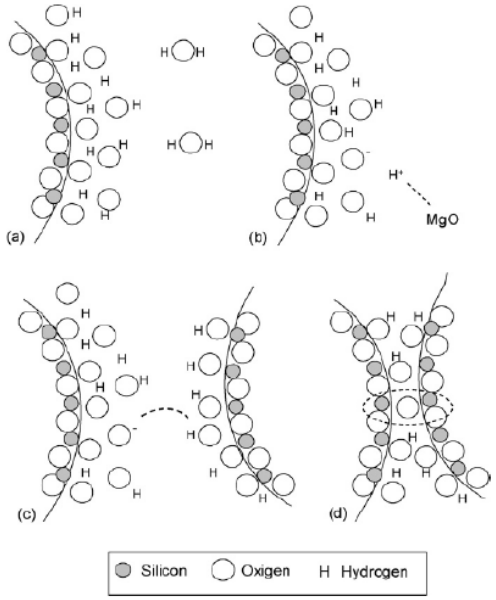

Figure 4-42 – Schematic representation of colloidal silica gelation in the presence of MgO. In (a) colloidal silica particle surface, (b) MgO addition, (c) siloxane bonds formation and (d) siloxane bonding (Si-O-Si) (Golshan et al. 2011).

Chapter Summary

Ceramic matrix composites manufactured with different fiber volume contents by combination of filament winding and freeze gelation are developed, manufactured and characterized. In order to increase the fiber volume content, the amount of the mullite matrix used to infiltrate the fiber bundle during filament winding is reduced.

From the materials microstructure images, it is possible to observe that the amount of matrix necessary to manufacture a composite with 50 vol. % fiber content (MF_B_50) is not enough to bind the composite layers and to infiltrate the fiber filaments. This is reflected in the composite low interlaminar properties, fracture toughness and bending strength (Table 4-7).

The distribution of fiber filaments among the ceramic matrix in the composites MF_B_30 and MF_B_40 are homogeneous. The pore size distribution indicates higher porosity of MF_B_30 as a consequence to its higher matrix content. The increase in fiber volume content showed that the amount of fibers under bending load enhances the composite strength. Nevertheless, lower matrix volume content and

higher sintering temperature showed not to affect the composites MF_B_30 and MF_B_40 interlaminar properties. This suggests that at both sintering temperatures (1150°C or 1200°C) the mullite particles do not undergo enough diffusion for ceramic densification.

Table 4-7 – Results from mechanical test of CMCs manufactured with Nextel^{TM} 610 fibers, 3000 denier with mullite matrix via filament winding and freeze gelation with 30 fiber vol. % (MF_B_30), 40 fiber vol. % (MF_B_40) and 50 fiber vol. % (MF_B_50).

	Compression Shear Strength (MPa)	Transversal Tensile Strength (MPa)	Four-point Bending (MPa)	Fracture Toughness – K_{IC} ($MPam^{0,5}$)
MF_B_30	8,10 ± 1,50	2,32 ± 0,15	78,11 ± 22,06	2,70 ± 0,27
MF_B_40	8,87 ± 1,76	2,33 ± 1,76	93,40 ± 0,00	3,33 ± 0,19
MF_B_50	1,74 ± 0,78	1,48 ± 0,48	32,95 ± 6,14	-

Since it is shown with matrix conductibility and differential thermal analysis that diffusion of silica particles takes place approximately at 900°C, sintering of a matrix system with silica nanoparticles and mullite up to 1150°C or 1200°C is not enough to enhance mullite density. Consequently, sintered silica particles corresponding to one third of the matrix volume content are surrounded by bigger mullite particles that are not fully sintered. This manner, the low interlaminar properties from the composites can be related to the fact that sintering at 1150°C is not enough to promote mullite densification and, hence, binding between composite single layers.

Use of mullite filler to manufacture oxide ceramic composites via filament winding and freeze gelation is limited. The fiber content is limited to 40 vol. %, above this the matrix content is not enough to infiltrate the fiber filaments and delamination between composite layers is observed. Sintering temperature is restricted to 1200°C due to fiber grain growth and consequent degradation of the fiber properties (3M^{TM} Ceramic Textiles and Composites) and due to adhesion from the matrix to the fiber surface above (chapter 4.1), reducing the composite fracture toughness. Therefore, enhancing the sintering temperature of the composite in order to improve matrix strength and composite interlaminar properties is not possible. Additionally, use of sintering additive to accelerate diffusion of ceramic particles is not viable in sol gel systems once these additives cause the sol to gel rapidly leaving no time for

composite processing. Increase of interlaminar properties in such composites still using sintering temperatures of up to 1200°C could be achieved only by the use of alternative ceramic fillers with higher diffusion rates, such as alumina.

4.2 Development of Oxide Ceramic Matrix Composites with Alumina Matrix

4.2.1 Development of Ceramic Matrix with Alumina Filler

Alumina (aluminum oxide) is used as filler once particle diffusion takes place at temperatures lower than in mullite particles, beginning at approximately 1150°C (Atanga 2013). It is expected, this way, an increase in the properties of the composite between fiber layers.

For the manufacture of the sol gel based ceramic matrix with alumina as filler, silica sol (Nexsil 20) is used. Four different alumina fillers are analyzed regarding their viscosity in suspension, thermal and mechanical properties as monolithic ceramic and as matrix from ceramic composites. The IEP point of alumina is found in the literature to be pH 9 and the use of dispersant agent reduces the pH to approximately 6.5 (Manjula et al 2005, Singh et al 2005, Singh at al 2004). The suspensions are, therefore manufactured with dispersant agent (Dolapix 0,5 wt. %) aiming a pH between 9 and 10 to avoid precipitation of the particles.

Suspensions manufactured and characterized are called AF_A, AF_B, AF_C and AF_D. Alumina fillers used in these suspensions and the matrices properties are described in Table 4-8.

Before freezing, viscosity of the suspensions is measured. Figure 4-43 resumes the viscosities measured. A thixotropic effect in the suspensions can be observed as their viscosity decreases with the increase of the shear rate. AF_A and AF_D alumina fillers have higher particle size (0,5 μm) than AF_B and AF_C (0,1 μm and 0,3 μm, respectively). As the number of particles increases when particle size decreases, surface area and the number of interactions between particles increases leading to an overall increase in viscosity. Static behavior between 25 and 40 RPM (velocity used for filament winding) is more evident in suspensions AF_A and AF_C, although also present in AF_B and AF_D.

Table 4-8 - Alumina based ceramic matrices manufactured using the freeze gelation route and its properties.

	AF_A	AF_B	AF_C	AF_D
Alumina	A16 SG	TM-DAR	CT3000 SG	APA-0.5
Particle Size - d_{50} (µm)	0,5	0,1	0,5	0,3
Surface Area (m^2/g)	8,9	14,5	7,5	8,0
Density (g/cm^3)	2,04	1,67	1,78	1,87
Porosity (%)	37,5	50,3	46,6	43,8
BoR Strength (MPa)	2,27	3,18	9,18	2,49
On-Set Temperature (°C)	1086	1110	978	1020
Shrinkage until 1000 °C (%)	0,51	0,34	1,93	0,79
Shrinkage until 1150 °C (%)	3,48	2,54	4,71	3,29
Crystal phase	Cristobalite + corundum	Corundum	Cristobalite (high amount) + corundum	Corundum

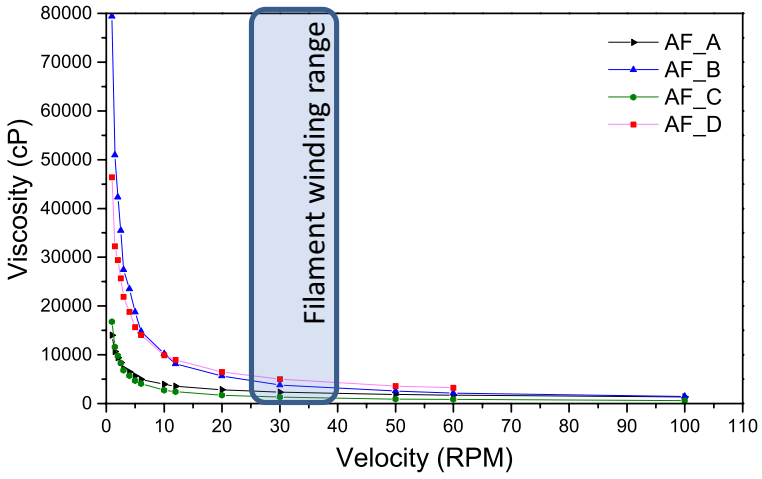

Figure 4-43 - Viscosity of the four matrices manufactured with silica sol and different alumina powders.

After suspension homogenization, molds measuring 100x100 mm (Figure 3-5a) are filled with the suspensions, frozen, dried and sintered with the parameters described above. Once both sides of the mold are made of aluminum and are in direct contact with the suspension and submitted to -18°C, growth of ice crystals starts from both sides of the mold.

Materials pore size distribution is evaluated. Figure 4-44 shows bimodal distribution of the pores of the four different ceramic slurries. AF_C (Figure 4-44a)

present a peak of pores measuring approximately 100 µm, and higher amount of nano-scaled pores than the other suspensions. In Figure 4-44b it is observed that AF_B has a peak in the pore size distribution graph around 100 µm and presents the highest amount of cumulative pore volume. Density of AF_B and AF_C is consequently reduced due to higher porosity (Table 4-8). Porosity found from 10 to 100 µm is attributed to the bigger pores found in the middle of the ceramic sample when the ice crystals which start growing from both walls of the mold meet each other in the middle of the sample (Figure 4-45). Pores from 0,01 to 0,1 µm corresponds to the residual porosity found in the particle interstices due to the nano-metric particle size as described in Scotti, Dunand 2018.

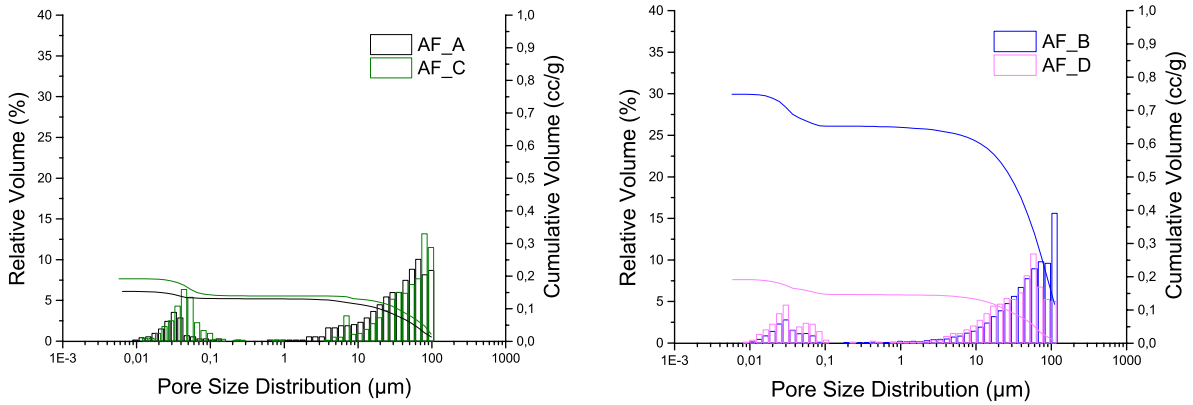

(a) (b)

Figure 4-44 – Pore size distribution of monolithic ceramics manufactured with sol gel-alumina matrix via freeze gelation of AF_A and AF_C (a) and AF_B and AF_D (b).

Figure 4-45 shows how the pore growth and formation differs from matrix to matrix:

- ⇨ AF_A shows lamellar oriented, elongated, continuous and fine pores. As pores grow inside the material its thickness is increased (Figure 4-45a). Transversal cracks, acting as bridges between the pores, are observed (exemplarily circled in Figure 4-45a).
- ⇨ AF_B shows the same characteristics observed in AF_A. Ice crystals growing from both ceramic boarders meet each other in the middle of the material forming pores in the range of 1mm (Figure 4-45b).
- ⇨ In AF_C pores grow randomly across the sample. Long lamellar and shorter pores are observed. Pores are thinner close to the freezing mold where pore growth starts (phenomenon described in Waschkies et al. 2009). The pores

become wider and not oriented as they grow into the ceramic. Less cracks between pores are seen in comparison to AF_A and AF_B.

⇨ AF_D shows random pore growth and formation of dendritic pores. Thermal cracks acting as bridge between longitudinal pores are noticed especially in the middle of the material. High porosity is formed in the middle of the ceramic plate when ice crystals growing from both materials extremities meet each other.

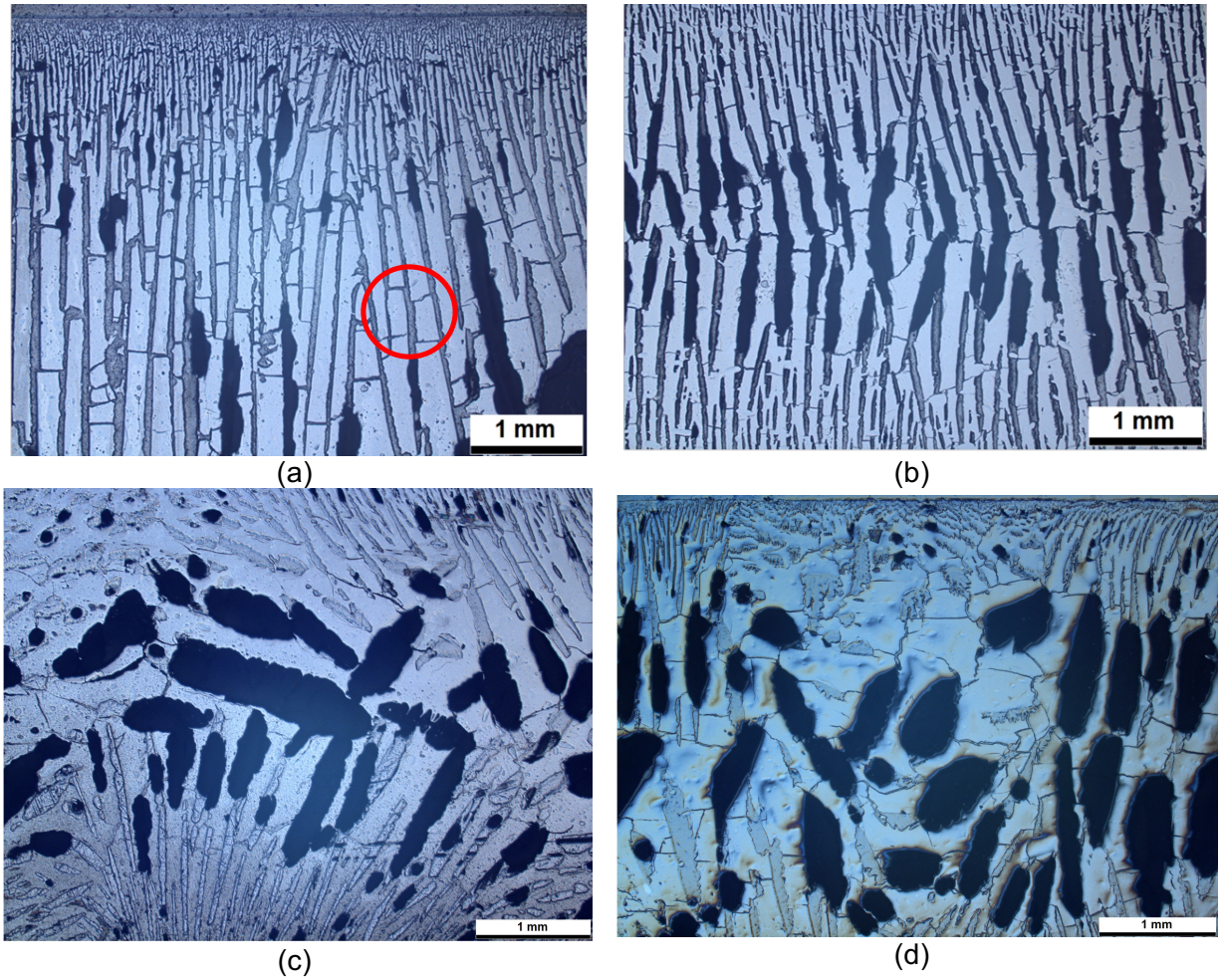

Figure 4-45 - Microstructure of monolithic ceramics manufactured with sol gel matrix (a) AF_A, (b) AF_B, (c) AF_C and (d) AF_D via freeze gelation. Red circle shows thermal cracks.

Formation of lamellar and dentritic pores are the most commonly reported types of porosity generated on freeze-casting; lamellar walls often exhibit dendritic features such as the ones observed in matrix AF_D (Scotti, Dunand 2018).

The strength of the ceramics is evaluated using the Ball on Ring (BoR) test (Table 4-8). AF_C shows higher mechanical strength than the other ceramic matrices

as a consequence of its lower on-set temperature, contributing to a higher matrix densification.

The on-set temperature and shrinkage of the ceramics up to 1000°C and 1150°C is conducted with the same sintering parameters used in the materials. The on-set temperature is the temperature at which the material begins to shrink; as a consequence of atom diffusion and neck formation between particles. As presented in Table 4-8, the on-set temperature is lower for matrix AF_C and AF_D (978°C and 1020°C respectively). This way, these matrices are denser than AF_B since its on-set temperature is 1110°C.

Thermogravimetry (TG) and Differential Thermal Analysis (DTA) of the ceramic matrices are conducted with the same parameters used to sinter the ceramic and composites materials.

In a sole silica system, transformation of silica into β-quartz takes place between 570-870°C, β-quartz is transformed into β-tridymite from 870-1470°C and β-tridymite is transformed into β-cristobalite from 1470-1705°C, these transformations are resulting in contractions in the material (Antaga 2013, Kim et al. 2016) which can explain the cracks observed in the matrices microstructure.

Since the system presented contain alumina and silica, the transformations are influenced by the presence of the fillers, their particle sizes and distribution among the silica particles. Differential Thermal analysis (Figure 4-46a) show similar behavior for all matrices up to approximately 900°C. It is believed that after 900°C, crystallization of silica in the cristobalite phase starts to happen and slightly differences between the matrices are observed. In AF_A and AF_C, from 900°C to 950°C small increase followed by a decrease in DTA signal is detected. This corresponds probably to the first silica crystallization into cristobalite phase, which can be seen in these two samples XRD spectrum (Figure 4-47). During the cooling phase, no evidence of reactions is observed.

Thermogravimetry (Figure 4-46b) shows loss of water corresponding to desorption of physically adsorbed water and from chemically bonded water and, additionally, to the beginning of silica phase transformations.

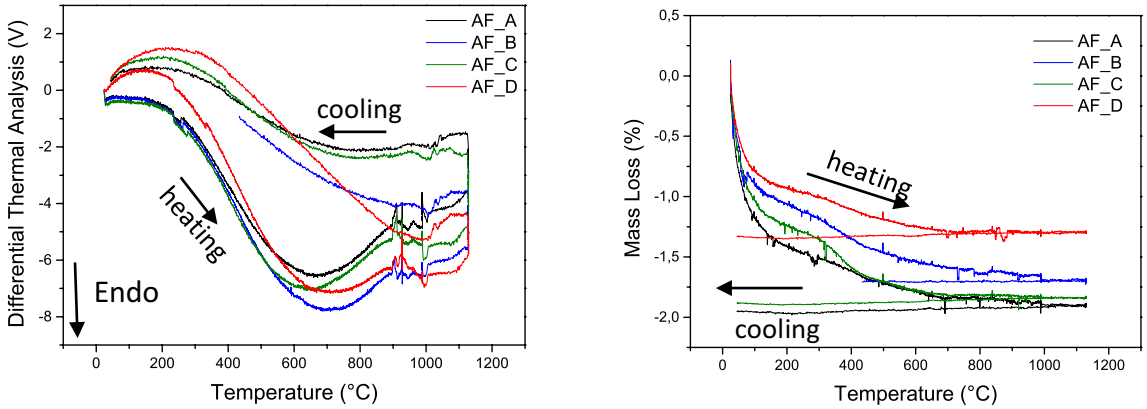

Figure 4-46 –Differential Thermal Analysis (a) and Thermogravimetry (b) of monolithic ceramics manufactured with sol gel-alumina matrix via freeze gelation with AF_A, AF_B, AF_C and AF_D.

The crystal structure of all materials in green state is the same since amorphous silica and alumina in form of corundum are used for the matrices manufacture. After heating until 1400°C with 10°C/min rate, cristobalite is observed in AF_A and AF_C (Figure 4-47). Matrix B and D do not show formation of cristobalite in their XRD spectrum, the even thinner particles (0,1 and 0,3 μm) of the alumina fillers used in these matrices distributed amongst the silica particles in these matrices probably lead to less nucleation sites for silica-silica particles to diffuse and form a different crystal phase.

X-Ray diffraction cards used to identify corundum and cristobalite are 00-046-1212 and 01-076-0941, respectively.

Temperatures where mullite is formed is reported to be higher than 1400°C when quartz particles below 2 μm and alumina particles ranging from 0,3-0,5 μm are used (Schneider et al. 1994) and after 1300°C (Liang et al. 2017). Even though nano-sized silica particles are used, which present higher activity than quartz with 2 μm due to higher surface area, formation of mullite is not observed in none of the matrices.

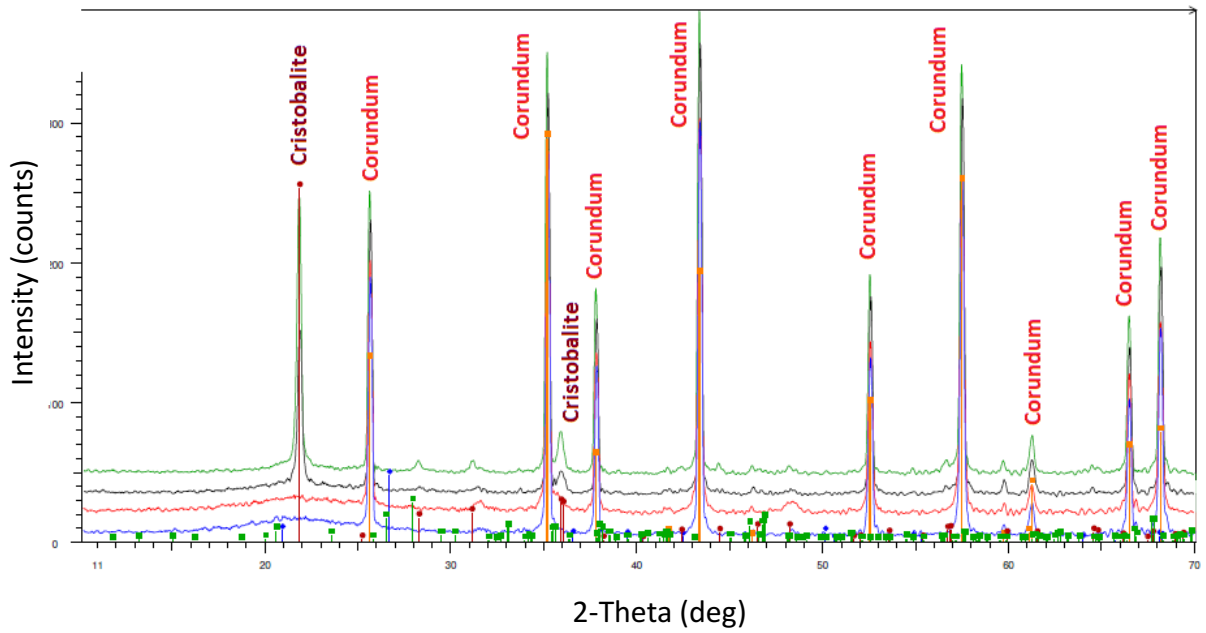

Figure 4-47 - X-Ray diffraction pattern from alumina matrices after heating with 10°C/min until 1400°C. Black line corresponds to AF_A, blue to AF_B, green to AF_C and red to AF_D.

Chapter Summary

Four different alumina powders are chosen and characterized. An influence of the particle size of the different alumina fillers in the pore size distribution and formation can be observed. The ceramic matrix composition AF_C presented higher strength amongst the compositions created which can be attributed to its lower on-set temperature and no formation of a cristobalite phase. However, this matrix present higher shrinkage which may lead to thermal mismatch when in conjunction with the fibers.

All compositions are chosen to manufacture oxide CMCs once no suspension alone could be identified with a higher potential of success when infiltrated with ceramic fibers. A more comprehensive conclusion on this topic is given at the end of Chapter 4.2.2.

4.2.2 Development of Ceramic Matrix Composites with Alumina Matrix

Manufacturing ceramic matrix composites via the combination of filament winding and freeze gelation technique using oxide fibers and sol gel based suspensions with alumina as ceramic filler is investigated in this chapter.

Table 4-9 shows density, total porosity (measured using Archimedes principle) and fiber volume content (measured according to Appendix A.1) of composites with alumina as ceramic filler. Composites are called AF for alumina filler followed by A, B, C or D.

Table 4-9 - Properties of ceramic matrix composites manufactured with Nextel^{TM} 610 fibers, 3000 denier and alumina matrix AF_A, AF_B, AF_C and AF_D via filament winding and freeze gelation.

Composites:	AF_A	AF_B	AF_C	AF_D
Alumina	A16 SG	TM-DAR	CT3000 SG	APA-0.5
CMC Density (g/cm³)	2,47	2,44	2,40	2,48
CMC Porosity (%)	31,5	31,2	33,2	31,4
Fiber Volume % (vol. %)	40,9	49,1	45,7	42,6

Pore size distribution is presented at Figure 4-48. Pores from 1 to 10 µm, observed in all matrices, are the pores correspondent to ice crystals growth (Deville 2008; Scotti, Dunand 2018). Bi-modal pore distribution is observed in the composites in exception of AF_B. AF_B shows high amount of pores with sizes ranging from 10 to 100 µm, correlated to delamination between composite single layers (Figure 4-49b). Porosity at 0,01 µm is related to the residual porosity found in the particle interstices due to the nano-metric particle size (Scotti, Dunand 2018).

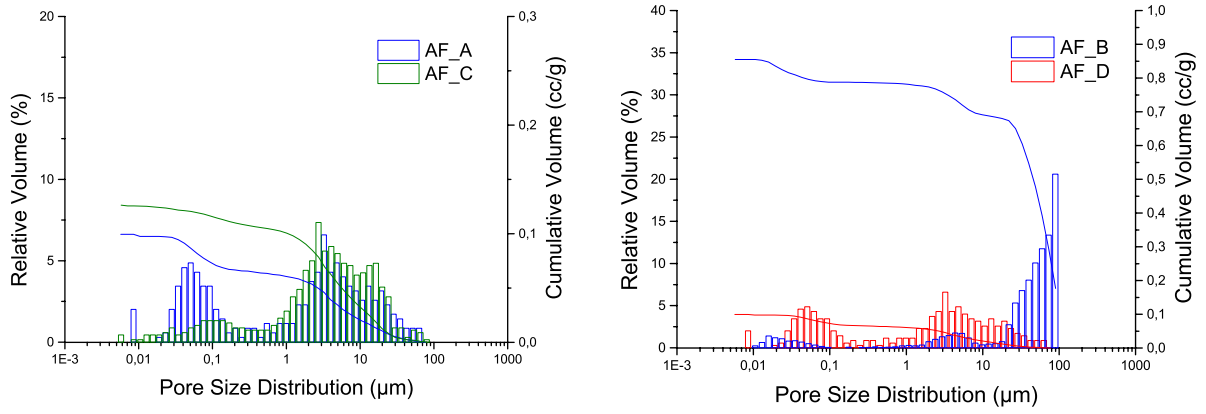

Figure 4-48 - Pore size distribution of CMCs manufactured with Nextel™ 610 fibers, 3000 denier with sol gel alumina AF_A and AF_C (a) and AF_6 and AF_D (b) matrices via filament winding and freeze gelation.

Microstructure of the composite shown in Figure 4-49 is described below:

- ⇨ AF_A slurry infiltrated homogeneously the inner fiber filaments (Figure 4-49a). High amount of cracks due to thermal shrinkage throughout all layers is observed. Due to the excessive amount of cracks it is difficult to identify pores from ice crystals with pores from cracks.
- ⇨ In AF_B, probably due to higher suspension viscosity, infiltration of the inner fiber filaments is not achieved. Instead, several areas with matrix between composite layers can be seen. Delamination between composite layers is observed (pointed by arrows in Figure 4-49b).
- ⇨ In AF_C homogeneous infiltration of the fiber filaments is achieved. Pores in the symmetric layer and regions with higher amount of matrix are indicated in Figure 4-49c with an arrow. In the regions where higher amount of matrix is accumulated cracks are observed. As mentioned in Kim et al. 2016, formation of cristobalite is accompanied by shrinkage, explaining the cracks observed in this matrix.
- ⇨ In AF_D cracks are not observed. Pores from ice crystals are evident in the sample and are found to be thinner and shorter than in other samples. In Figure 4-49d it can be clearly seen that ice crystal grows until it encounters a fiber. Few longer pores could be seen in the symmetric layer in the regions where concentrations of matrix are found (arrow in Figure 4-49d). Ceramic matrix infiltrated homogeneously fiber filaments.

The use of alumina filler to build composites shows different properties and results found when only monolithic ceramics are examined. This is because the fibers act as barrier for ice crystals growth during freezing. When the ice crystal growing in the ceramic matrix meets a fiber it stops growing. Therefore, the final pore structure, formation, geometry and size of the pores are different in composites and in monolithic ceramics. Additionally, monolithic ceramic plates are frozen with two freezing fronts, differently from the CMC plates, which are frozen with only one freezing front (Figure 3-5b).

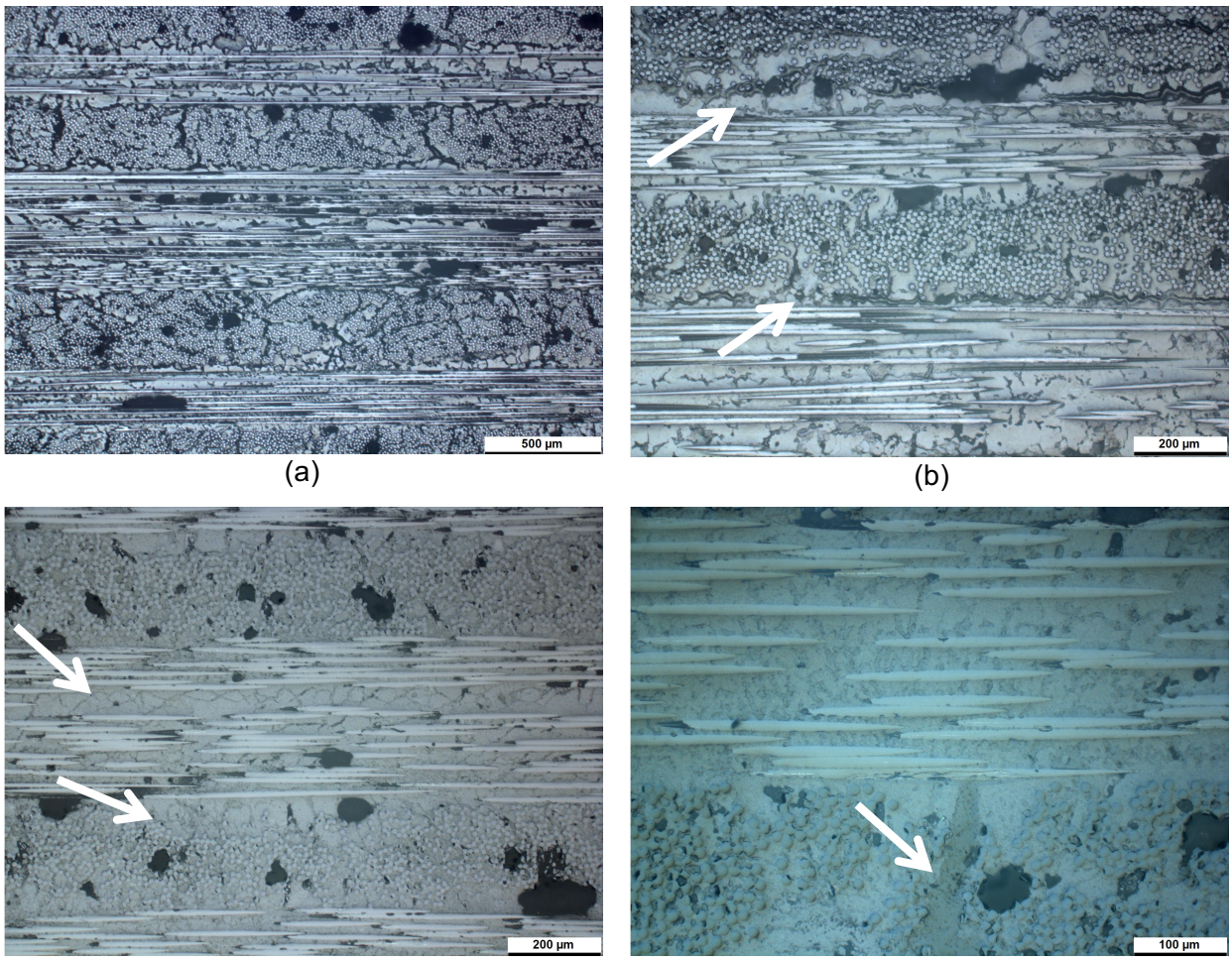

(a) (b)

(c) (d)

Figure 4-49 - Microstructure of CMCs manufactured with Nextel^{TM} 610 fibers, 3000 denier with sol gel- (a) AF_A, (b) AF_B, (c) AF_C and (d) AF_D matrices via filament winding and freeze gelation.

Composites are tested in compression shear, transversal tensile and short bending. Within the CMCs with alumina matrix, Figure 4-50 indicates a higher compression shear strength of 11,22 ± 1,43 MPa from AF_D. All samples failed

interlaminar in the symmetric layer (Figure 4-51d). Composite AF_C presents compression shear strength of 9,10 ± 3,18 MPa. Failure from these composites occurred mainly across the symmetric layers (Figure 4-51c). AF_A showed strength of 4,40 ± 1,51 MPa, interlaminar failure from the 3rd to the 4th layer is observed (Figure 4-51a). Its relative low strength can be correlated to the presence of cracks in the matrix structure. AF_B presents low interlaminar strength (1,19 ± 0,62 MPa) with mostly intralaminar failure from the 3rd to the 4th layer (Figure 4-51b). Failure of oxide ceramic composites through a single composite layer have been reported in Parthasarathy, Kerans 2016 and characterize materials with a weaker matrix strength between the composite layers. Composites strength vs. displacement curve shows high deformation, a consequence from the delamination observed in the material interlayers.

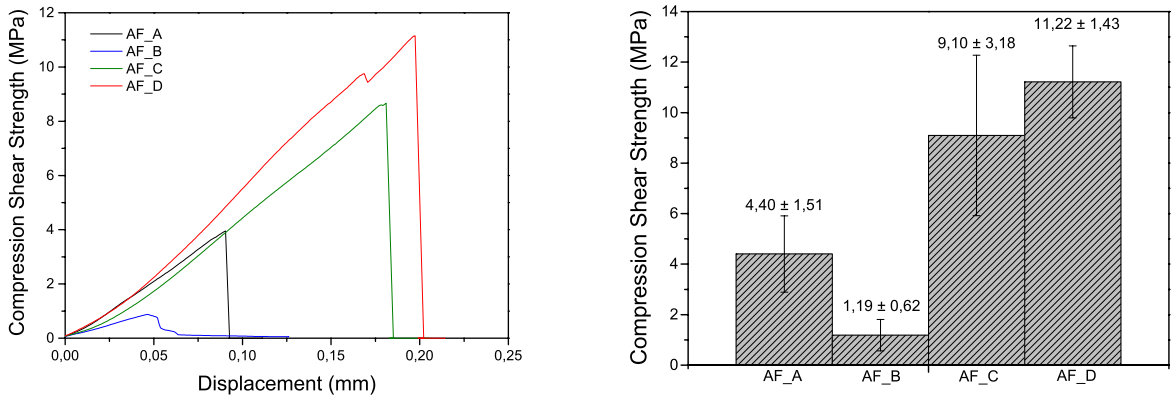

(a) (b)

Figure 4-50 – Representative curves (a) and compression shear strength (b) of sintered CMCs manufactured with Nextel™ 610 fibers, 3000 denier with sol gel alumina matrices (AF_A, AF_B, AF_C and AF_D).

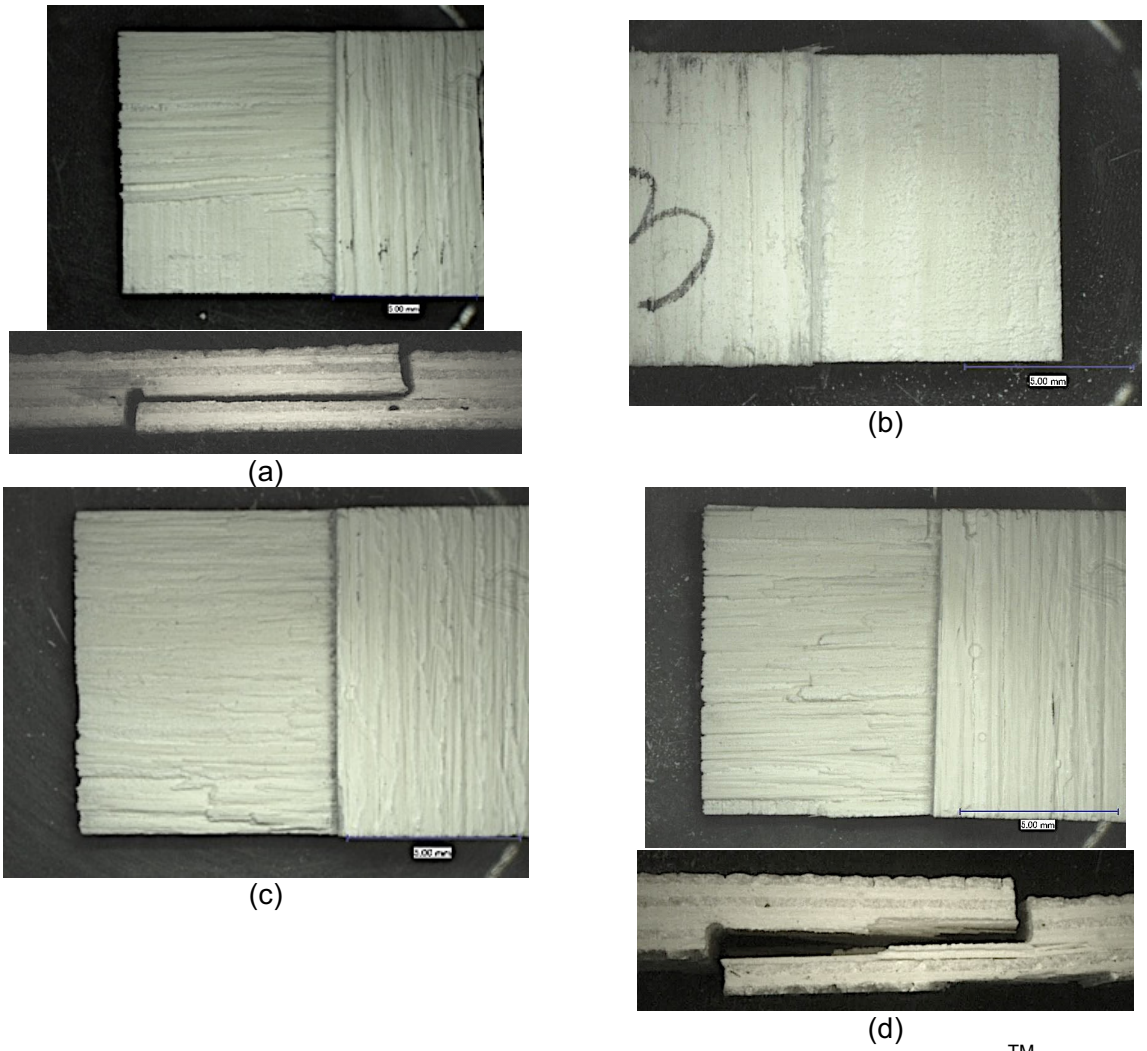

Figure 4-51 – Fracture surfaces from sintered CMCs manufactured with Nextel™ 610 fibers, 3000 denier and AF_A (a), AF_B (b), AF_C (c) and AF_D (d) matrices after compression shear test. Scale bars indicate 5 mm.

Under transversal tensile test (Figure 4-52) AF_D showed strength of 10,25 ± 2,23 MPa, interlaminar fracture from 3rd to 4th layer (0°/90° oriented) is observed in all samples (Figure 4-53d). AF_C presented transversal tensile strength of 1,84 ± 0,73 MPa with interlaminar fracture on all samples (Figure 4-53c). AF_A showed 1,24 ± 0,47 MPa transversal tensile strength with intra and interlaminar fracture behavior (Figure 4-53a); this can be explained by the presence of crack in the matrix, leading to an earlier failure of the matrix. AF_B exhibited once again the lowest strength with high variation of results, 0,53 ± 0,32 MPa, and intralaminar failure (Figure 4-53b). The high deformation of AF_B (Figure 4-52a) is attributed to delamination previously observed between composite layers.

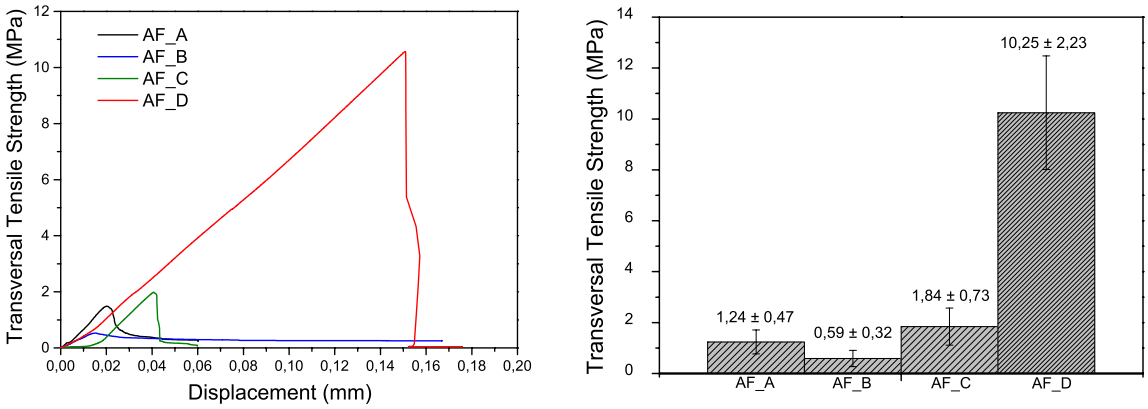

(a) (b)

Figure 4-52 - Representative curves (a) and transversal tensile strength (b) of sintered CMCs manufactured with Nextel™ 610 fibers, 3000 denier, with AF_A, AF_B, AF_C and AF_D matrices.

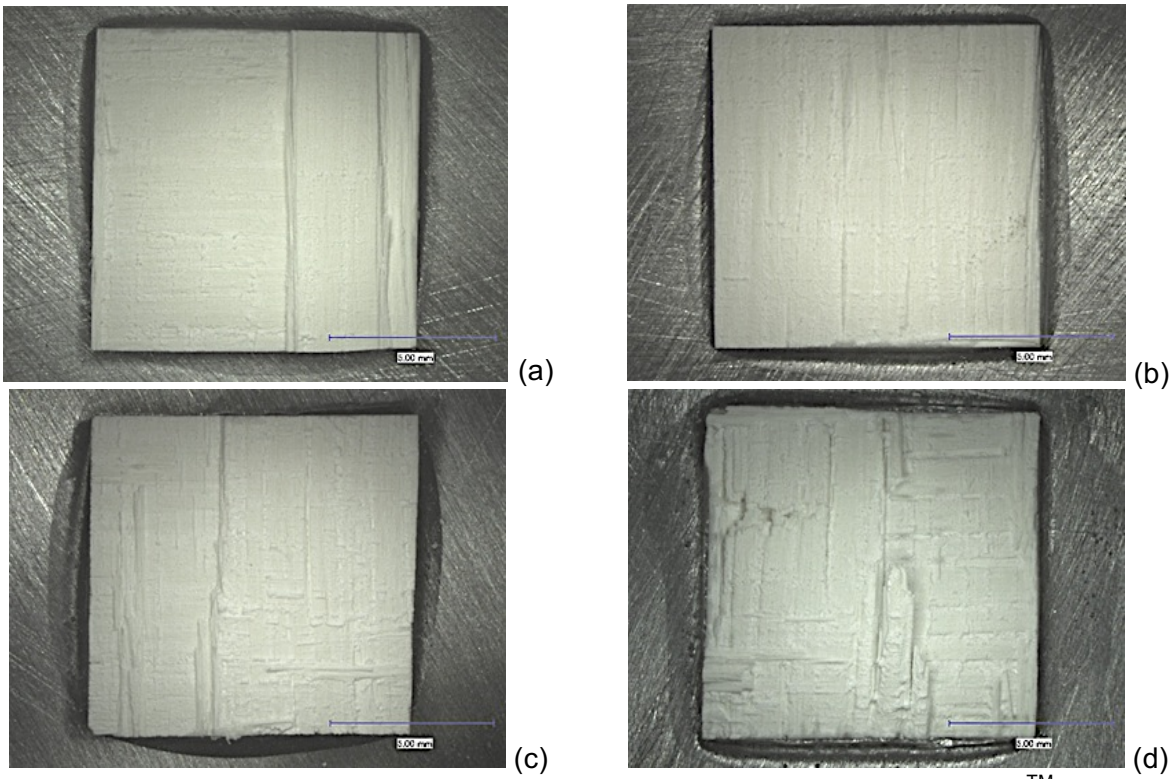

(a) (b) (c) (d)

Figure 4-53 - Fracture surfaces from sintered CMCs manufactured with Nextel™ 610 fibers and AF_A (a), AF_B (b), AF_C (c) and AF_D (d) matrices after transversal tensile test. Scale bars indicate 5 mm.

Under short bending all materials delaminated during test. Their ILSS and representative strength vs. displacement curve is displayed in Figure 4-54. AF_A and AF_B showed low strength values of 1,16 ± 0,19 MPa and 1,68 ± 0,25 MPa. All composite layers delaminated inclusive the symmetric ones (Figure 4-55a and 4-55b). Interlaminar strength of 2,47 ± 1,10 MPa and delamination only in the 0°/90°

oriented layers (Figure 4-55c) is observed in AF_C. Interlaminar shear strength of 6,90 ± 0,40 MPa is calculated for AF_D. In this composite only 0°/90° oriented layers delaminated (Figure 4-55d).

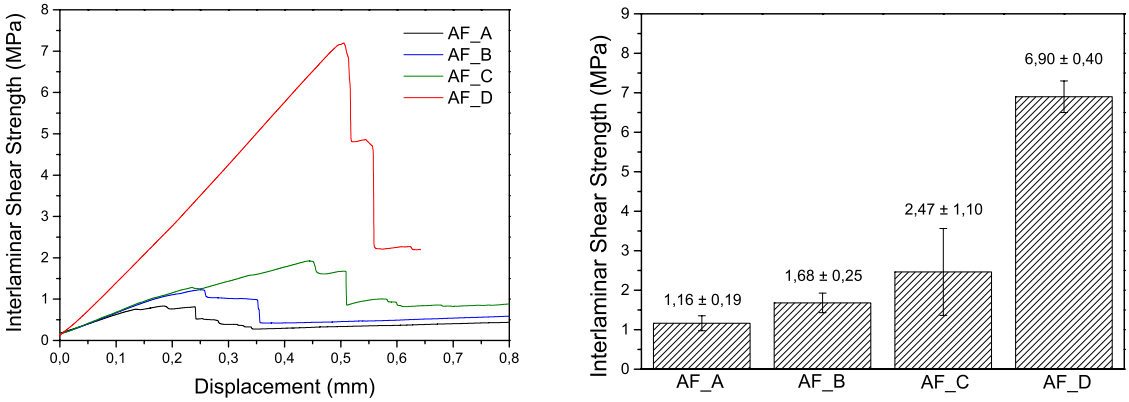

(a) (b)

Figure 4-54 - Representative curves (a) and interlaminar shear strength (b) of sintered CMCs manufactured with Nextel™ 610 fibers and AF_A, AF_B, AF_C and AF_D matrices.

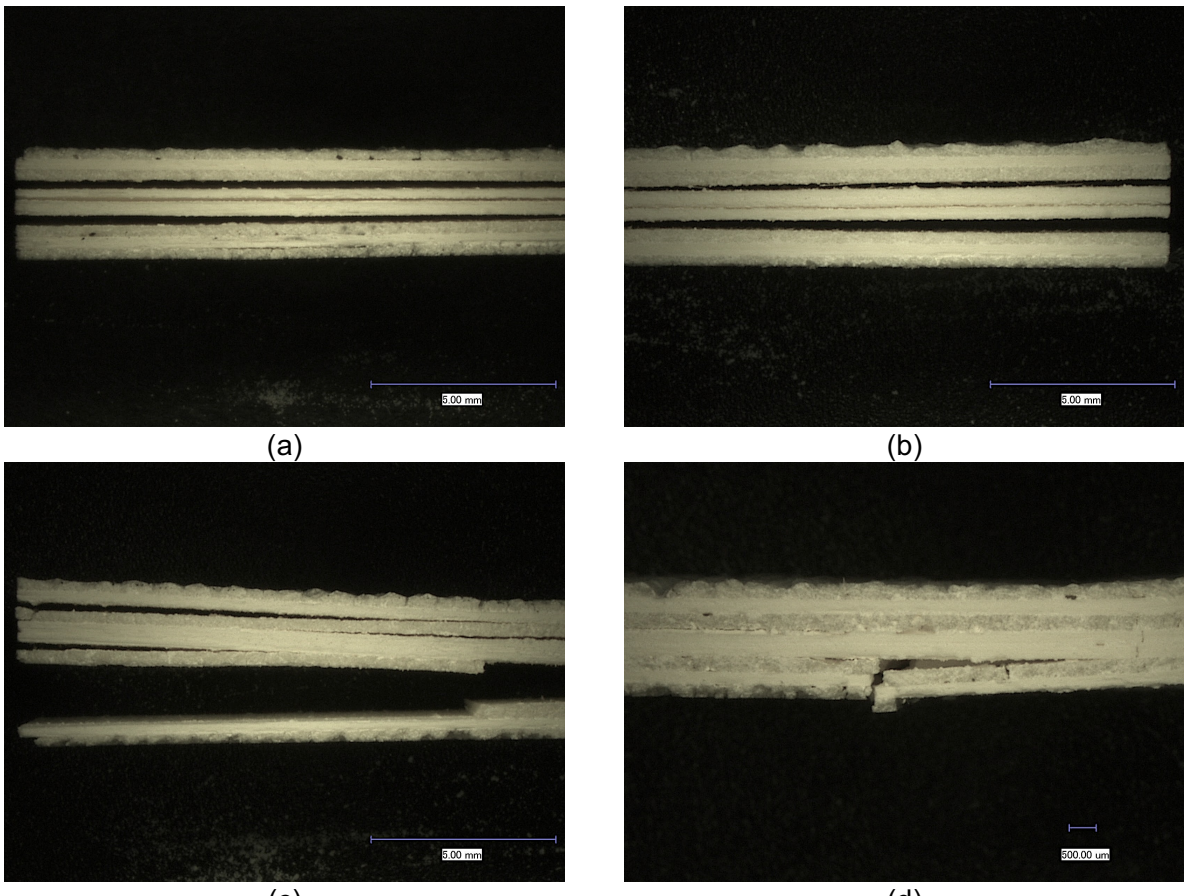

(a) (b)

(c) (d)

Figure 4-55 – Samples from CMCs manufactured with Nextel™ 610 fibers, 3000 denier with AF_A (a), AF_B (b), AF_C (c) and AF_D (d) matrices after short bending test. Scale bars indicate 5 mm for (a), (b) and (c) and 500 μm for (d).

Due to the better interlaminar properties of AF_D other properties such as fracture toughness, bending and tensile strength are investigated only in this composite.

Fracture toughness measured with Single Edge Notched Bending (SENB) showed a K_{IC} of 4,45 ± 0,61 $MPam^{0,5}$. An analysis of the fracture surfaces indicates presence of short fiber pull-out (Figure 4-56a) and evidence of matrix fracture (Figure 4-56b). These effects have been reported in the literature as typical fracture modes from oxide ceramic composites that use weak matrices as a way to promote crack dissipation (Lange 2010).

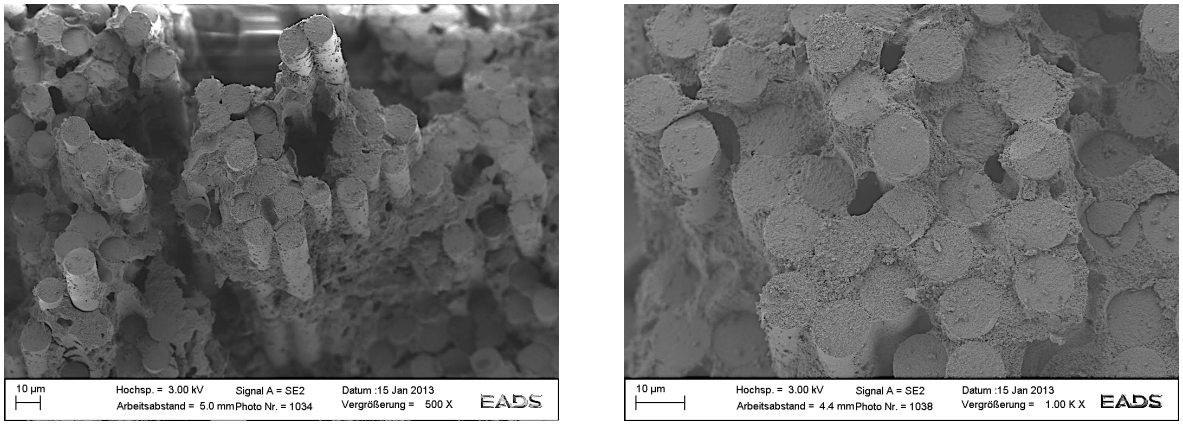

(a) (b)

Figure 4-56 - Fracture surfaces from sintered CMC manufactured with Nextel™ 610 fibers, 3000 denier with AF_D matrix after single edge notched bending test. Scale bars indicate 10µm.

Under four-point bending load, bending strength of 176,56 ± 12,40 MPa is achieved in the composite AF_D. Representative test curve is shown in Figure 4-57a. All samples failed in the fiber direction. Figure 4-57 shows the crack initiation in the material last layer which penetrates through five composite layers and finally delaminates throughout the sample between two layers oriented in 0°/90°.

Tensile strength of 70,77 ± 12,57 MPa and Young's modulus of 582,82 ± 12,37 MPa is calculated in composite AF_D. Representative strength vs. elongation is presented in Figure 4-58a. Failure happened in the samples radius outside of the gauge length. In the fractured area delamination of the composite layers is observed (Figure 4-58b).

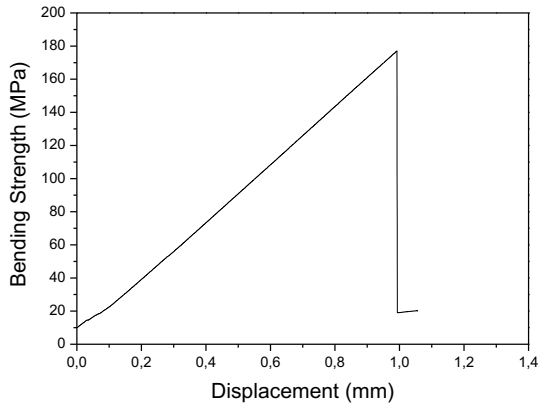

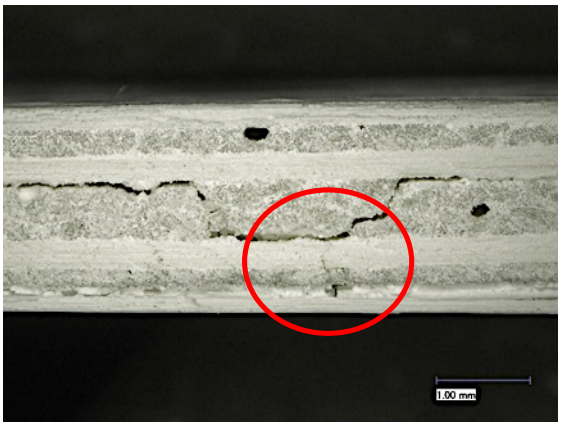

(a) (b)

Figure 4-57- Representative bending strength vs. displacement curve (a) and sample after fracture (b) of CMC manufactured with Nextel™ 610 fibers, 3000 denier with AF_D matrix after four-point bending test. Scale bar indicates 1 mm.

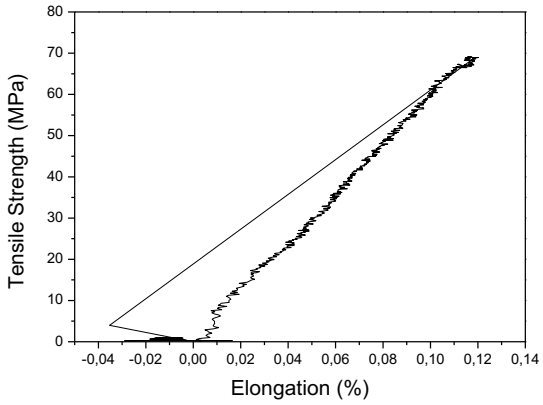

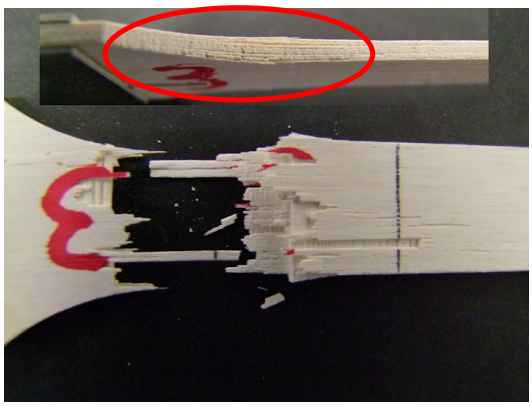

(a) (b)

Figure 4-58- Representative tensile strength vs. displacement curve (a) and sample after fracture (b) of CMC manufactured with Nextel™ 610 fibers, 3000 denier with AF_D matrix after tensile test.

Chapter Summary

The knowledge and experience acquired for the combination of filament winding using Nextel™ fibers with freeze gelation process using sol gel based suspensions with mullite as ceramic filler could be transferred to manufacture suspensions using alumina instead of mullite as filler. Aspects from suspension manufacturing pH range to freeze gelation are kept the same for mullite and alumina suspensions. Filament winding velocity, fiber gap, composite fiber volume content

and sintering temperature could be directly transferred from the studies conducted with mullite matrix composites to the development of alumina matrix composites.

The alumina A16SG from Almatis used to manufacture AF_A showed weak strength (ball-on-ring test) in monolithic ceramics. High shrinkage of 3,48% of this matrix reflected in a microstructure full of thermal cracks. In composites, the higher matrix shrinkage contributed to lower interlaminar strength (Table 4-10). Normally, layers in 0°/90° fiber direction present lower adhesion between each other than the layers laid-up in the same direction (symmetric layer). After short bending test AF_A composite delaminated even on its symmetric layer, evidencing the weakness of this composite.

TM-DAR alumina powder from Krahn-Chemie is used in AF_B and resulted in high thixotropic slurry. Infiltration of the inner fiber filaments from fiber bundle is not achieved and delamination between composite layers could be observed before composite is tested. Consequently, AF_B presented low interlaminar properties (Table 4-10). Additionally, higher on-set temperature of 1110°C measured in AF_B monolithic ceramic lead to lower matrix densification in comparison to the other matrices.

In AF_C, alumina CT3000 SG from Almatis is used. Monolithic ceramic tested with AF_C under ball on ring test showed higher strength (9,18 MPa) in comparison to other ceramics. This strength is, however, not reflected in the CMC. This is because pore growth and morphology is influenced by the presence of fibers. In composites, AF_C microstructure showed high amount of pores situated between composite layers, where a thick matrix layer is observed. These cracks contributed to the variation of results seen in all mechanical tests (Table 4-10).

In AF_D alumina APA-0,5 from Sasol is used, this alumina resulted in a monolithic ceramic with long fine and dendritic pores and a total porosity of 43,8 vol. %, responsible for a fragile ceramic with low strengths (Ball on Ring test). However, this slurry when combined with oxide fibers showed a microstructure with thinner and shorter pores, with a homogeneous distribution of the matrix among inner fiber filaments, no delamination and no shrinkage cracks. Additionally, its lower on-set temperature of 1020°C contributes to better matrix densification by the end of the sintering process. All these factors contributed to the achievement of better interlaminar strength of this composite in the different tests it is evaluated: compression shear, transversal tensile and short bending (Table 4-10).

Table 4-10 – Results from mechanical test of CMCs manufactured with Nextel™ 610 fibers, 3000 denier with AF_A, AF_B, AF_C and AF_D matrix via filament winding and freeze gelation.

	Compression Shear Strength (MPa)	Transversal Tensile Strength (MPa)	Interlaminar Shear Strength (MPa)
AF_A	4,40 ± 1,51	1,24 ± 0,47	1,16 ± 0,19
AF_B	1,19 ± 0,62	0,59 ± 0,32	1,68 ± 0,25
AF_C	9,10 ± 3,18	1,84 ± 0,73	2,47 ± 1,10
AF_D	11,22 ± 3,18	10,25 ± 2,33	6,90 ± 0,40

The fact that the mechanical properties measured in monolithic ceramics are not transferred to composite can be explained by the different pore formation (growth, length and geometry). When fibers are involved they act as barrier to crystal growth, stopping their growth and causing higher ice crystals nucleation points. In Figure 4-59 the microstructure of a frozen monolithic ceramic and the same ceramic in a composite is shown (AF_D). The difference in the pore formation such as geometry and size is noticeable. Large and thick pores observed in the ceramic matrix have a very different aspect than the short and thinner ones observed in the CMC. Besides, the pore gradient observed in monolithic ceramics from the freezing front to the middle of the material is not observed in the CMC because the fibers stop ice crystal growth and, as a consequence, nucleation of ice crystal takes place in multiple sites of the composite. This effect has not been previously reported in the composites developments using colloidal systems (Simon 2005, Chant et al. 1995a, Chant et al. 1995b).

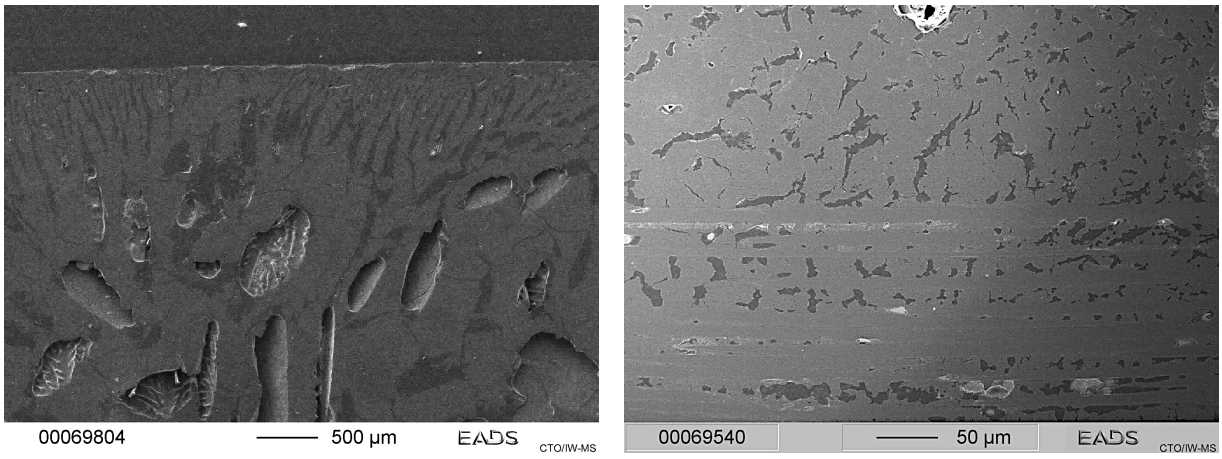

(a) (b)

Figure 4-59 - Porosity of monolithic ceramic (a) matrix AF_D shown in comparison to the porosity observed in the CMC (b) using the same matrix in the freezing conditions.

4.3 Comparison of Composites Manufactured with Mullite and Aluminum Oxide Matrix

The combination of filament winding and freeze gelation has been developed for the manufacture of oxide based ceramic matrix composites. In this chapter, the results achieved for ceramic composites using mullite (MF_B) and alumina (AF_D) as fillers in the ceramic matrix are compared. This comparison aims the better understanding of the properties achieved during the development of each composite.

For the manufacture of the suspensions, the method used to homogenize matrices with mullite (d_{50}=3 µm) as filler had to be optimized. Alumina particles have smaller particle size (d_{50}=0,3 µm) and need higher dispersion energy to promote a stable and agglomerate free suspension (Appendix A.2). Mullite filler used in MF_B is Mullite 21113 from Reimbold & Strick and alumina filler is Ceralox APA0,5 from Sasol, properties of both fillers are described in Table 3-2. Both suspensions are manufactured containing the same solids content (75 wt. %) as well as same amount of silica from silica sol (17 wt. %), filler (58 wt. %) and water (25 wt. %).

The influence of the ceramic filler in the suspension is investigated by measuring the viscosity of the suspensions. Knowledge on the viscosity of suspensions is important to understand its behavior when infiltrating the ceramic fiber bundles in the filament winding process. If a suspension viscosity is too low the suspension passes through the fiber filaments and is not retained within the filaments. As a consequence, the composite might present lack of bonding between laid composite layers resulting in low interlaminar properties. If the viscosity is excessively high the ceramic suspension will not infiltrate the inner fiber filaments, leaving big voids among the fiber filaments that might work as crack initiator under loading, reducing the composite mechanical performance.

Figure 4-60 demonstrates that both suspensions have a non-Newtonian behavior, that is, with the increase of velocity or shear rate, the viscosity deceases. An increase in viscosity when alumina is used as filler is observed, this is due to the smaller particle sizes from alumina that lead, consequently, to a higher surface area. The velocity then provide the control of the suspension viscosity, and, this way, for filament winding a range from 25 – 40 RPM has been used as it coincides with a

static behavior of the suspensions, providing an optimum range to infiltrate the fiber bundles.

Even though the viscosity of AF_D is approximately 4 times higher than MF_B, in the velocity range used during filament winding (25 – 40 RPM) infiltration of the inner fiber filaments is achieved (Figure 4-61).

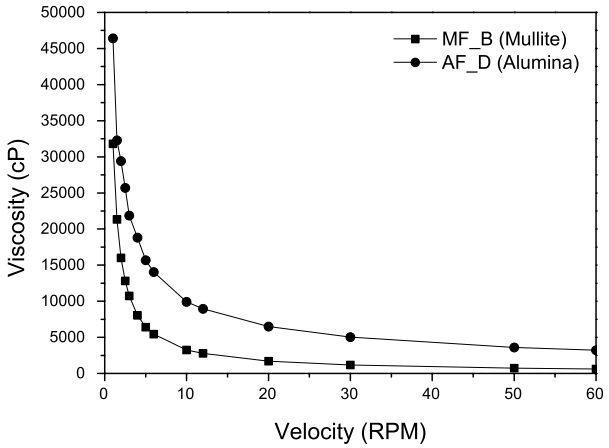

Figure 4-60 - Viscosity of sol gel suspension manufactured with mullite (MF_B) and alumina (AF_D) as filler measured using Brookfield Viscometer.

In mullite matrix composites, the winding procedure provides a uniform distribution of the filaments and a homogeneous infiltration of the ceramic slurry is achieved. The excellent infiltration of the slurry and the presence of the mullite grain sizes with 3 μm provide a constant spacing between the fiber filaments. No delamination between composite layers is observed (Figure 4-29a). Pores (from ice crystals) are found throughout the material ranging from 5 to 10μm (Figure 4-62a), these pores are not of a particular shape and are observed mostly between the fibers as indicated by arrows, figure 4-61a.

Microstructure images from alumina matrix composite attest that, even with a higher viscosity, infiltration of the fiber filaments is also sufficiently achieved (Figure 4-61b). Alumina powder is intrinsic mixture to the silica particles and, opposite than for mullite composites, the smaller particle size of the alumina and silica do not provide a constant spacing between the fiber filaments. Pore growth and pore distribution are different in comparison to the mullite matrix. Small and thin pores are formed (Figure 4-61b). Lamellar pores are observed in the regions where higher amount of matrix is present (Figure 4-61b).

Based on these results, a viscosity value between 1000 and 5700 cP at 25 to 40 RPM is indicated to manufacture well-infiltrated CMCs with homogeneous microstructures.

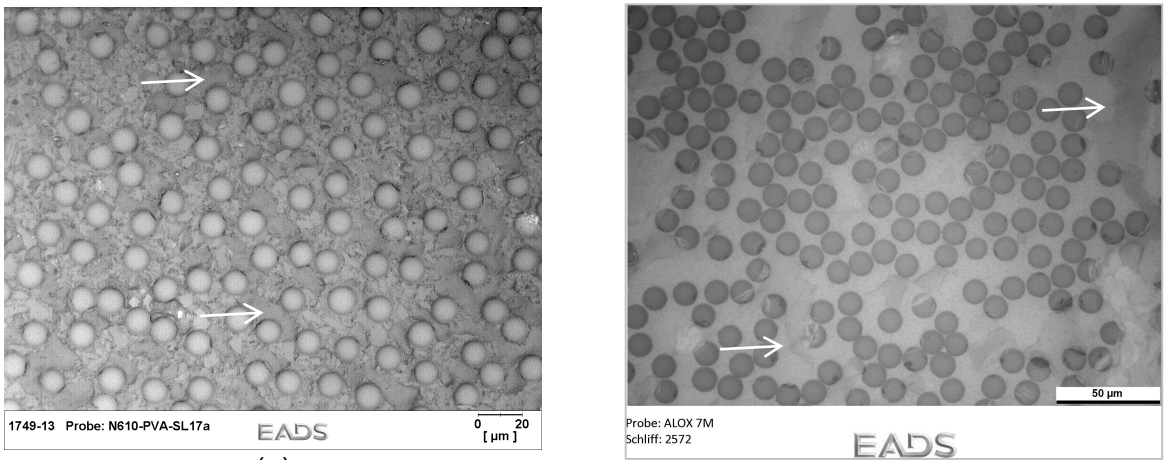

(a) (b)

Figure 4-61 – Microstructure of CMC manufactured via filament winding and freeze gelation with Nextel^{TM} 610 fibers, 3000 denier with (a) mullite and (b) alumina matrix.

Pore size distributions of the composites measured via Mercury Intrusion show higher fractions of nanopores when alumina is used as filler (Figure 4-62).

Mullite matrix presents higher cumulative volume of pores that can be related to its coarser particles and their looser packing. This effect has been previously explained in the literature (Deville 2008), bigger particles will leave a higher degree of porosity than thinner particles when mixed with sol gel suspensions.

Three different fractions of pores can be observed in the pore size distribution (Figure 4-62) from both materials. From 20 to 200 nm found only in alumina, from 200 nm to 4 μm higher porosity is observed in mullite matrix composite and pores larger than 4 μm are similarly found in mullite and alumina matrix composites. Alumina matrix presents higher nanoporosity than mullite. Once both matrices are manufactured using the same amount of silica sol (water and silica nanoparticles), the higher content of nanoporosity and lower fraction of pores ranging from 200 nm to 4 μm in alumina composites is a consequence of the fillers particle size. The homogeneity of the porous structure is lost when the particle size become too similar to the size of the ice crystals and morphological features cannot be well replicated into the final structure (Deville 2008). This means that, micron-sized particles will result in s structure with pores in the same micrometric range.

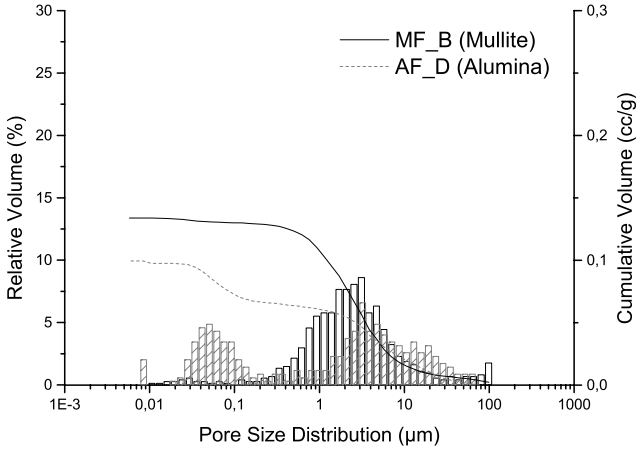

Figure 4-62 - Pore size distribution manufactured via filament winding and freeze gelation with Nextel™ 610 fibers, 3000 denier and MF_B (mullite) and AF_D (alumina) matrix.

The total porosity and fiber volume content from both samples are similar (Table 4-11) once the same slurry composition (wt. % of filler, silica and water) and same filament winding parameters are used for the manufacture of both composites. Density and total CMC porosity shown is measured using He pycnometry. Fiber volume content is calculated according to the method described in Appendix A.1.

Table 4-11 - Properties of CMC manufactured via filament winding and freeze gelation with Nextel™ 610 fibers, 3000 denier with MF_B (mullite) and AF_D (alumina) matrix.

	Particle Size (µm)	CMC Density (g/cm³)	CMC Porosity (%)	Fiber Volume Content (%)
MF_B (mullite)	3,0	2,18	32,57	41,8
AF_D (alumina)	0,3	2,48	31,40	42,6

A summary of the results achieved for the interlaminar strength of both composites (measured with compression shear, transversal tensile and four-point short bending test) is presented in Figure 4-63.

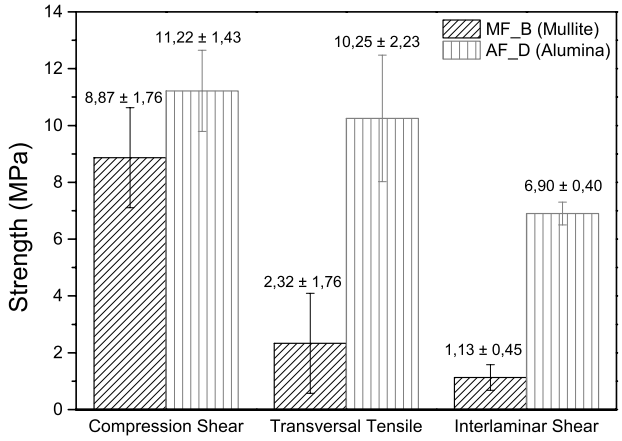

Figure 4-63 – Interlaminar properties of ceramic matrix composites manufactured via filament winding and freeze gelation with Nextel^{TM} 610 fibers, 3000 denier and MF_B (mullite) and AF_D (alumina) matrix.

Under compression shear load the stress of the composite with mullite filler (8,87 ± 1,76 MPa) is lower than from the composite with alumina filler (11,22 ± 1,43 MPa). Representative curves from both materials under compression shear test indicate similar behavior (Figure 4-64a).

All samples from both composites present interlaminar failure, i.e., fracture energy dissipates from one layer to the following one, as observed in Figure 4-65. In the alumina composites failure occurred in the symmetric layer. Generally, when fibers layers are orientated in 0°/0°, the fiber filaments from both layers mix and bond with each other better than in 0°/90° orientation. Failure in the symmetric layer is an indicative that the matrix strength between composite layers is achieved (Parthasarathy, Kerans 2016).

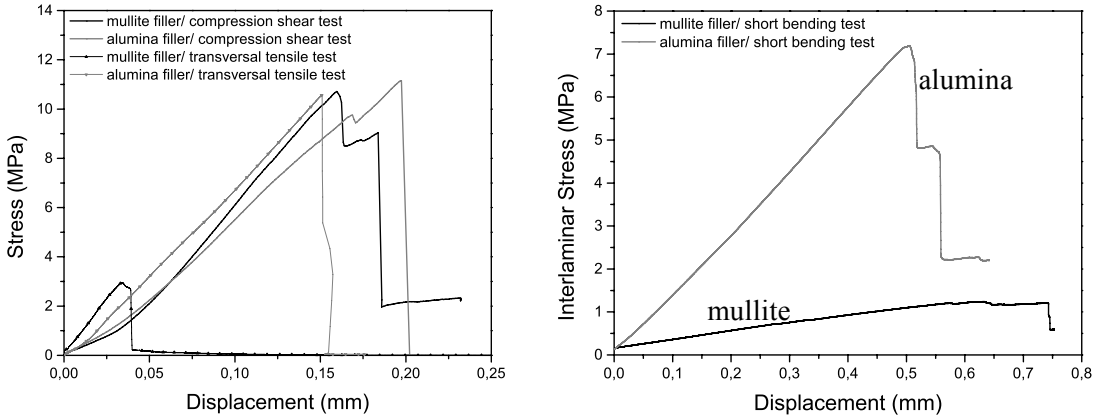

(a) (b)

Figure 4-64 – Representative curves of ceramic matrix composites manufactured with mullite and alumina as filler from transversal tensile test, compression shear test (a) and short bending test (b).

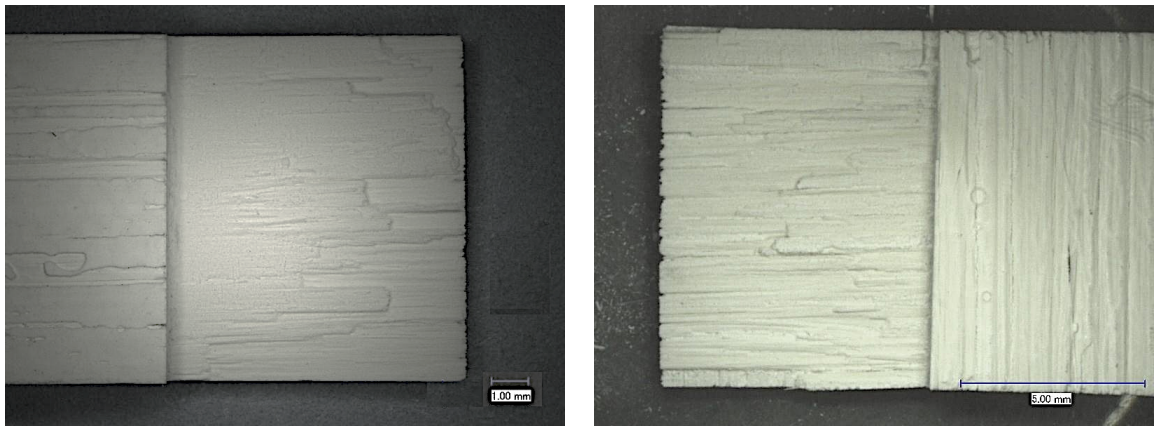

(a) (b)

Figure 4-65 - Fracture surfaces of ceramic matrix composites with (a) mullite filler and with (b) alumina filler after compression shear test. Scale bars indicate in (a) 1 mm and in (b) 5 mm.

In contrast to the results from the compression shear test, both composites respond to transversal tensile test and the short bending test with significant difference. Lower strength of mullite matrix composite (2,32 ± 1,76 MPa) in comparison to alumina (10,25 ± 2,23 MPa) is observed on transversal tensile test.

The fracture energy in mullite samples dissipated from one layer to another, characterizing an interlaminar failure (Figure 4-66a). In the alumina composite fracture from 0° to 90° oriented layers is observed in different regions from the sample (Figure 4-66b). The arrows show the orientation of the fibers on the fracture surface changing from 0° to 90°.

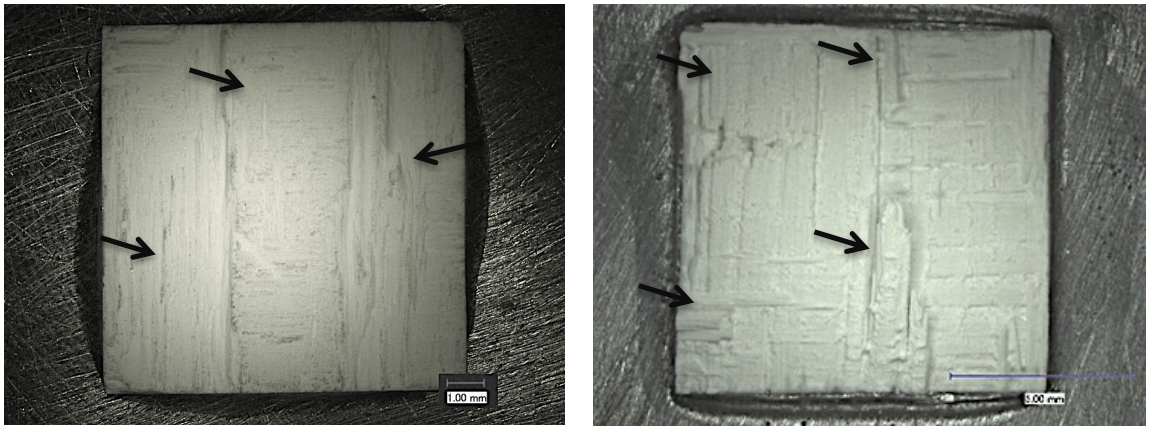

(a) (b)

Figure 4-66 - Fracture surfaces of ceramic matrix composites with (a) mullite filler and with (b) alumina filler after transversal tensile test. Scale bars indicate in 1 mm (a) and 5 mm (b).

Mathematical models for pure isotropic materials exist to predict the maximum shear stress at the material neutral axis (Al-Qureshi, 1988; Khurmi, 2005). Equation 4-1 shows the formula after derivation; where τ is the transversal shear stress, V is the shear force carried by the section and A is the area. Since the composite developed in this work is a bidirectional symmetrical and, therefore, an anisotropic material, it is necessary to apply a correction factor to Equation 4-1. It is generally known that the main difference between theoretical and the experimental values vary from 5 to 7; depending on the composite material used (Al-Qureshi, 1988; Khurmi, 2005). Table 4-12 summarizes the theoretical with and without correction factor and experimental shear stresses.

$$\tau = 1{,}5\frac{V}{A} \qquad \text{Equation 4-1}$$

Table 4-12 - Comparison between experimental and theoretical transversal shear strength of composites.

Composite	Experimental Shear Stress (MPa)	Theoretical Shear Stress without correction factor (MPa)	Theoretical Shear Stress with correction factor (MPa)
Mullite_TT_01	2,95	17,84	2,97
Mullite_TT_02	1,16	7,21	1,20
Mullite_TT_03	1,32	7,98	1,33
Mullite_TT_04	1,07	6,53	1,09
Mullite_TT_05	5,17	30,64	5,11
Alumina_TT_01	8,06	56,63	9,44
Alumina_TT_02	10,57	76,81	12,80
Alumina_TT_03	13,22	93,14	15,52
Alumina_TT_04	9,13	66,86	11,14

Interlaminar strength of mullite composite (1,13 ± 0,45 MPa) is calculated with the results obtained from four-point short bending test. From alumina composites the presented ILSS strength of 6,90 ± 0,40 MPa is calculated from the results achieved under short bending test. Samples from this material delaminated. Use of alumina as ceramic filler for sol gel based suspensions for the manufacture of composite materials indicated, once again, better interlaminar properties than mullite filler.

Failure in composites occurs in different ways depending on the matrix and fiber combination; occasionally fiber may break under short-bending load and, in this case, the bending load is considered for comparison purposes. Bending strength of mullite composite is 93,44 MPa. Figure 4-67 shows the representative curves from both materials and the strength achieved. Ceramic composites with alumina filler achieved a strength of 176,56 ± 12,40 MPa.

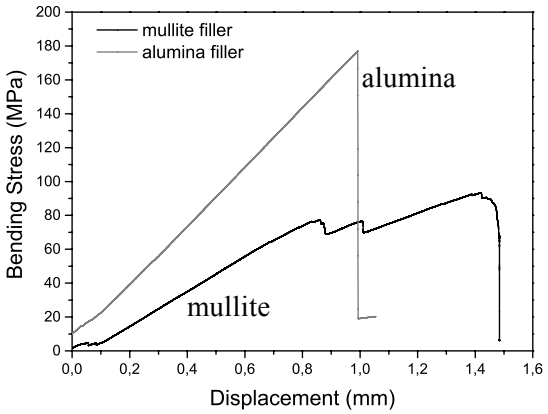

Figure 4-67 – Bending stress representative curve of ceramic matrix composites manufactured with mullite and alumina filler.

Fracture toughness of 4,38 ± 0,35 $MPam^{0,5}$ and 4,45 ± 0,61 $MPam^{0,5}$ is calculated respectively for composite with mullite and with alumina matrix. Figure 4-68 brings a representative curve for each composite showing similar brittle behavior and steady crack growth; at the top of the curve serrated pattern indicate resistance to failure. Fracture analysis (Figure 4-69) indicates regions in which short fiber pull out is observed (arrow 1) identified more clearly in alumina matrix composites. It is observed, mainly in mullite composites, regions where fibers and matrix show characteristic brittle failure. According to the literature (Lange, 2010), in porous ceramic composites fiber pull out is normally not seen, what is observed is that most of the matrix between the fibers are missing or still attached to the fiber, demonstrating that the matrix have fragmented during loading. This effect is also revealed on both composites fracture surfaces (arrow 2), however more evidently in alumina matrix composites.

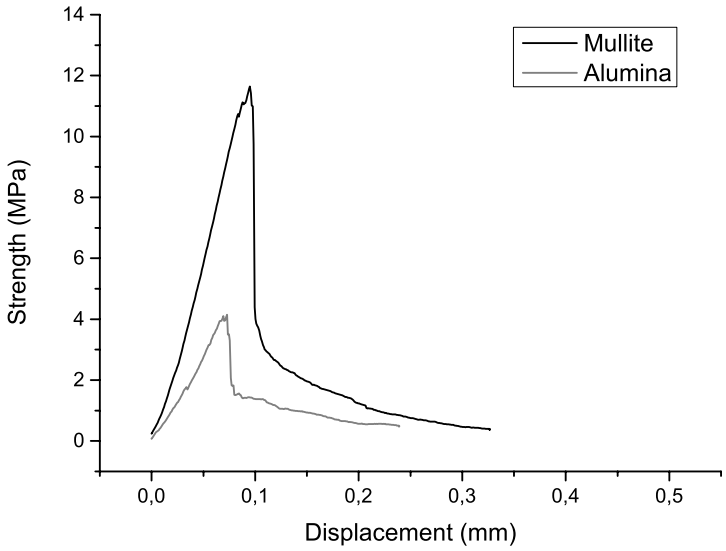

Figure 4-68 - SENB representative curves from Mullite matrix and Alumina matrix composite.

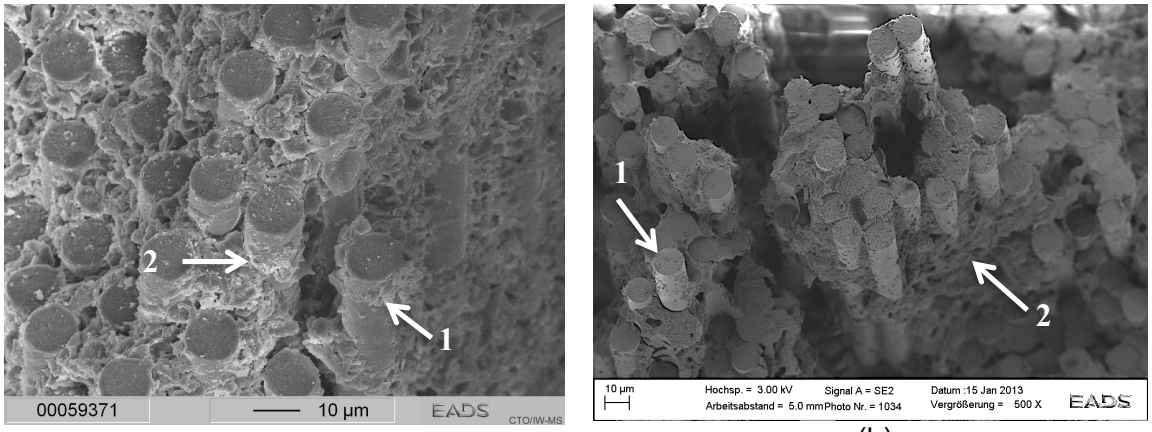

(a) (b)

Figure 4-69 - Scanning Electron Microscope (SEM) images from the fracture surface of mullite (a) and alumina (b) composites after Single Edge Notched Bending (SENB) test.

Chapter Summary

An important part of the work showed that using the same silica sol but different ceramic fillers (alumina and mullite) influenced significantly the suspension homogenization, viscosity and pore formation in the matrix. These matrix characteristics are mainly influenced by the filler particle size. Combined to this, is the fact that the ice crystals, in general, when they nucleate and start growing they do not have enough energy to surpass a fiber filament or a big mullite particle. As a consequence, both microstructures show the formation of numerous ice crystals in different places and with different sizes.

Composites with mullite present a good distribution of fiber filaments amongst the matrix due to the constant spacing provided by the 3μm mullite filler, however, these particles and the fibers provided a barrier for ice crystals to grow through the matrix, fact that lead to multiple and relatively big pores in between fibers and matrix. Furthermore, the porosity combined with the crystal structure formed due to crystallization of silica resulted in a composite with less shrinkage and higher total amount of porosity.

On the other hand, the microstructure formed in the composites with alumina provided regions in which a higher amount of matrix is present and pores need less energy to grow and regions where fibers are closer to each other still presenting a small amount of matrix between then. In these regions, smaller porosity and possibly nanoporosity are observed as the ice crystals are prevented to grow and so multiple ice crystals initiate in the matrix but do not have energy to grow and surpass fibers.

The higher state of dispersion of the silica nanoparticles amongst the alumina nanoparticles is believed to have led to less nucleation points for the silica particles to diffuse between them and so, after sintering, formation of cristobalite could not be observed in the X-Ray pattern. On the mullite based matrix, however, silica changed from amorphous into a polymorph phase (β-cristobalite) indicating an initial phase of sintering. Mullite crystal phase is not transformed during sintering process as the sintering temperature used is not enough to promote densification of the mullite particles.

Because the mullite particles are 10 orders of magnitude bigger than the alumina particles it is believed that, added to the lower sintering kinetics from the mullite, the silica nanoparticles are clustered together crystalized, however surrounded by these bigger mullite particles that are not able to give the material enough strength, especially between the composite layers (schematic illustrated in Figure 4-70).

Consequently, it is observed in the mechanical testing, that indeed the alumina composite performs better than the mullite and presents higher strength both in the ceramic matrix (interlaminar shear strength) and in fiber direction (bending strength).

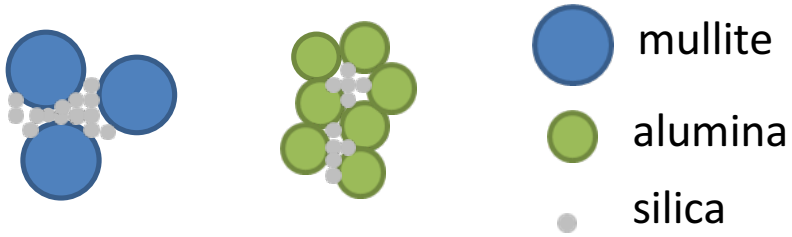

Figure 4-70 - Schema showing particle packing in suspensions made with silica sol/ mullite filler and silica sol/ alumina filler.

4.4 Process Verification to Manufacture Rotation Symmetric Structures

The process developed during this work is verified to manufacture rotation symmetric and complex structures. For this, the geometry of a gas turbine prototype is chosen.

The first prototype manufactured is shown in Figure 4-71a. The prototype is manufactured with the ceramic slurry AF_D (alumina matrix) reinforced with Nextel^{TM} 610, 3000 denier (PVA organic sizing). Ceramic fiber Nextel^{TM} 610, 3000 denier (organic sizing) showed to be stable to winding conditions once fiber break during processing did not occur and maximum velocity of the winding machine could be used.

A composite with 2 layers could be manufactured in 4 hours. Problems encountered during manufacturing are related to long winding time and, as a consequence to matrix drying since the suspension is water based and dries out with the time. During filament winding it is necessary to apply small pressure on the fibers so that the bundles could spread out and give a better tool coverage. This must be done constantly while the fiber is being laid-up and still wet in order to avoid regions where a gap between fiber bundles can be observed, as indicated by an arrow in Figure 4-71a.

(a) (b)

Figure 4-71 – Rotation symmetric component after filament winding, freeze gelation and sintering of sol gel based matrix (AF_D) infiltrated in (a) Nextel™ 610, 3000 denier fiber and (b) Nextel™ 610, 10000 denier fiber.

To increase tool coverage and consequently reduce winding time a fiber with higher filament denier is used (Nextel™ 610 fiber, 10000 denier). The 10000 denier fiber has 2550 filaments in one bundle while the fiber with 3000 denier has 800 filaments. Using 10000 denier fiber allowed a better coverage of the tool and the manufacture of a prototype with 6 layers in 5 hours (Figure 4-71b). Maximum winding velocity during manufacture could be used with no fiber break.

Another possible solution to decrease winding times is to wind with fiber Nextel™ 610 3000 denier storing the composite overnight in a humid chamber in order to keep it still wet. This possibility is investigated, firstly, in a composite plate. A 4 layers composite with fiber architecture of 0°/90° is manufacture in one day. The composite is kept in a humid chamber with 80% humidity and temperature of 25°C. After 24 hours, further 4 layers with fiber architecture of 0°/90° are winded to the composite. The final composite with 8 layers is then frozen, dried and sintered with the same parameters used for composite AF_D (Chapter 4.2).

Microstructure of the composite after sintering (Figure 4-72) indicate that storing the composite overnight in a humid chamber is not enough to keep the material humid and to avoid the water from the matrix to dry out. Leading to delamination between the composite middle layers, as indicated by an arrow in Figure 4-72.

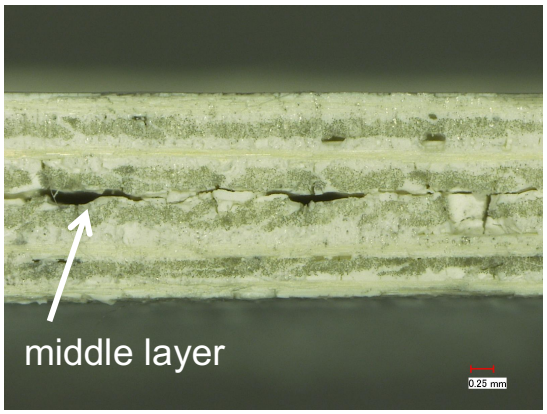

Figure 4-72 – Composite sample after winding, freezing and sintering manufactured in two-step winding and kept overnight in humid chamber. Composite manufactured with fiber Nextel^{TM} 610, 3000 denier and sol gel AF_D alumina matrix.

5 CONCLUSIONS

Within this work the manufacture of ceramic matrix composites by the combination of filament winding with freeze gelation process are developed and the composites materials characterized.

Throughout the work, composites are manufactured using mullite or alumina as ceramic filler. In the development of mullite matrix and alumina matrix composites the following aspects and associated conclusions are summarized.

- Mullite Matrix and Mullite Matrix Composite:

Different particle sizes from the mullite fillers influences in the suspension viscosity, pore formation and in the thermal behavior of ceramic matrices. Smaller particles sizes lead to formation of pores with different geometries, cracks in the monolithic matrix and consequently to lower mechanical properties. Monolithic ceramic denominated MF_B (Silica sol Nexsil 20 and mullite filler 21113) showed higher mechanical strength in comparison to the other matrices. Its mechanical performance is attributed to homogeneous growth of ice crystals throughout the matrix and crystal phase formation.

In weak matrix systems, the fracture energy is dissipated through a porous matrix. During sintering, matrix and fiber are in constant contact and matrix can sinter with the fiber surface reducing the material fracture toughness. Composites materials are sintered with different temperatures and their fracture toughness is evaluated. The composite heated with 2°C/ min until 1000°C for 3 hours and then heated again with 5°C/ min until 1150°C with a dwelling time of 1 hour showed higher fracture toughness and no evidence of bonding between fiber and matrix.

By adjusting the amount of matrix to be infiltrated in the fibers, composites with 30 vol. % (MF_B_30), 40 vol. % (MF_B_40) and 50 vol. % (MF_B_50) fiber content are manufactured. The amount of matrix necessary to infiltrate fibers and to achieve fiber content of 50 vol. % is not enough to promote homogeneous fiber infiltration and binding between composite layers, leading to delamination and low mechanical properties.

Interlaminar strength measured are similar in the composites MF_B_30 and MF_B_40. Delamination of the composite with 40 vol. % of fiber under bending loads and the relative low interlaminar strength of the composites MF_B_30 and MF_B_40 indicated that the sintering temperature used is not enough to promote particle

diffusion and matrix densification. From thermal analysis and thermal conductivity tests it is seen that diffusion of silica particles starts after 900°C by the formation of cristobalite. Mullite particles presents lower diffusion rates and need temperatures of up to 1500°C for complete diffusion. In the matrix, 17wt. % of densified silica particles are surrounded by 58 wt.% of not dense mullite particles. The silica particles are, therefore, not able to transfer their strength to the matrix and to the composite interlaminar properties.

Once, sintering temperatures of composites using Nextel^{TM} fiber is limited due to fiber grain growth after 1200°C. Use of sintering additives to accelerate diffusion of mulite particles is not possible due to rapid gelation of the silica sol. Therefore, the properties of oxide based ceramic matrix composites manufactured with sol gel suspension and mullite filler is limited.

In order to enhance the composite properties, the ceramic filler used in combination with silica sol is replaced by alumina due to its higher strength and lower sintering temperatures (starting from 1150°C).

- Alumina Matrix and Alumina Matrix Composites:

In monolithic ceramics, the matrix in contact with the freezing front is cooled rapidly and a uniform microstructure with ultra-fine crystals is formed. As the distance from the surface increases the velocity of the liquid front decreases rapidly until it reaches a steady state with an approximate constant value, forming a porosity gradient throughout the sample (Deville 2008). In composites, the presence of homogeneously distributed fibers among the ceramic matrix act as barrier to ice crystal growth. Nucleation of ice crystals starts in several regions of the composite leading to a homogeneous pore distribution. This explains the different mechanical strengths seen as monolithic ceramic and composite matrix are tested.

Amongst four different alumina fillers studied, higher interlaminar properties (compression shear strength of 11,22 ± 1,43 MPa, transversal tensile strength of 10,25 ± 2,23 MPa and short bending strength of 6,90 ± 0,40 MPa) are achieved in the composite manufactured with an alumina with particle diameter of 0,3 µm (AF_D). The suspension stability, homogeneous infiltration among fiber filaments, pore formation throughout the composite, crystal structure and on-set temperature of 1020°C contributed to the better mechanical performance of this composite.

When comparing the composites developed, use of alumina showed to be more suitable than mullite as ceramic filler for sol gel suspensions to be used as ceramic matrix from composites. Higher interlaminar strength is achieved, especially under transversal tensile test and short bending test when interlaminar strength increases in 440% and 611%, respectively. Fiber infiltration and pore formation from both composites is successfully achieved.

- Overall Conclusions

Up-scaling of the developed process is demonstrated to be viable using the developed manufacturing route by the manufacture of a component with the geometry of a gas turbine. For the prototype manufacture a fiber with higher filament count (Nextel^{TM} 610 with 10000 denier instead of Nextel^{TM} 610 with 3000 denier) is used to reduce processing times and winding of the component to one day.

The composite developed is given the name WITA-OX^{TM}. The main advantages from this process are its cost-efficiency and versatility. From slurry preparation up to final sintering, composites components can be manufactured within 5 days. This is an immense advantage when compared to other available composites as, for example, UMOX^{TM} which manufacturing route can take up to 3 months. Allied to the low production time of the developed composite is the absence of fiber coating or re-infiltration cycles followed by extra sintering steps and the possibility of sintering the composites under air other than under inert atmosphere. All these facts contribute to an extreme cost reduction in the manufacturing of composites via filament winding and freeze gelation technique.

The main drawback from the process is its sensibility to some process conditions. The use of water based suspension limit the processing time of components in areas without control of ambient temperature and humidity. The suspension homogeneity and the freezing step are fundamental to pore formation and influence directly in the mechanical properties of the composites. All process steps must be well controlled to guarantee reproducibility and quality of the final composite.

The graph shown in Figure 2-34 is presented once again in Figure 5-1 with the addition of composite AF_D. Composite AF_D is called in the graphic WITA-OX^{TM}. The interlaminar strength of the developed composite still needs to be improved.

The combination of filament winding with the freeze gelation process to manufacture composites is a promising technique, offering several advantages over other manufacturing techniques, in especial its low cost and production times. The

mechanical performance of the composites must be, nevertheless, further developed. Suggestions for further developments of this composite are given in Chapter 6.

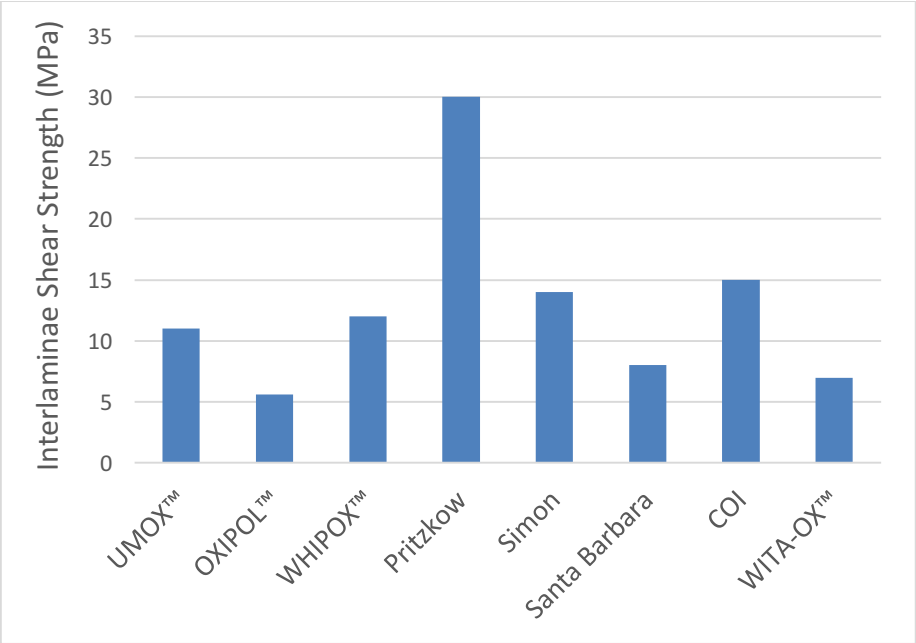

Figure 5-1 – Comparison of the interlaminar strength from ceramic matrix composites and the composite WITA-OX™.

6 OUTLOOK

For the further development of oxide ceramic matrix composites using filament winding and freeze gelation, the following optimizations for further investigations are suggested:

- ⇨ Development of the ceramic suspension by addition of zirconium oxide or yttrium stabilized zirconium oxide as ceramic filler together with aluminum oxide. These two components have shown in other works (Pritzkow et al 2015) to improve the mechanical performance of oxide ceramic based composites. Here, it is also advised that along with the further development of the ceramic matrix, more attention is given to the thermal properties of the matrix.
- ⇨ Freezing from composites is conducted immediately after lay-up in a freezer where the filament winding mold is placed without application of pressure. Application of constant pressure to both sides of the mold while freezing takes place could enhance the interlaminar properties of the material. The development of such an apparatus must be also applicable when rotation symmetric composites are manufactured.
- ⇨ Control of humidity in the room where filament winding is conducted to avoid the ceramic matrix to dry improving the adhesion between composite layers.
- ⇨ It is shown during the adaptation of filament winding to sol gel based suspensions and the development of the freeze gelation process that several processing steps have a major influence in the CMC properties. Other parameters that could be investigated are, for example, the influence of winding velocity in fiber impregnation to investigate if suspensions with higher viscosity would, due to capillarity, infiltrate the inner fiber filaments when more time is given. Winding in a closed system with controlled humidity in order to avoid or to postpone drying of ceramic suspension. Influence of different freezing temperature and application of different freezing fronts to study the pore formation in composites and its influence in composite properties.
- ⇨ Also, when manufacturing bigger and thicker components the drying stage must be carefully controlled (time and temperature) in order to avoid formation of defects such as cracks or material distortion. Here it is suggested the implementation of the technique lyophilisation, also called freeze-drying. In this

technique, the frozen water is removed from the material direct from the solid to vapor state through sublimation.

- ⇨ Investigation of composite mechanical properties when higher sintering temperatures and longer dwelling times are applied. A compromise shall be found where mechanical properties from the fiber are not lost while still achieving sufficient matrix densification to enhance the composite interlaminar shear strength.
- ⇨ Automatize the adjustment of the amount of matrix being impregnated in the fiber and the rotation system of the rollers that conduct the fiber from the roving through the infiltration bath for better accuracy of the fiber volume content from the composite and improvement of the composite infiltration. The reproducibility of the developed process depends strongly on all processing steps, which must be always followed.
- ⇨ In order to manufacture rotation symmetric components with complex structures using Nextel^{TM} 610 fiber 3000 denier with reduced winding times and consequently matrix drying another possible solution could be winding with simultaneously 3 fiber roving. In the winding machine used for filament winding there is the possibility of winding with up to 3 fibers roving as shown in the scheme at Figure 2-10.

REFERENCES

3M™ Ceramic Textiles and Composites: 3M™ Nextel™ Technical Notebook.

Aksay, I.A (1991): Molecular and Colloidal Engineering of Ceramics. In *Ceramics International* 17, pp. 267–274.

Al-Qureshi, H. A. (1988): Composite Materials: Fabrication and Analysis. In *ITA*, 3rd Edition.

Antaga, V.K. (2013): Processing and properties of alumina reinforced mullite ceramics. PhD Thesis. University of Otto-von-Guericke Magdeburg.

Arnold, J.C (2007): Environmental effects on crack growth in composites. In *Comprehensive structural integrity*, pp. 428–470.

Asomoza, M.; Dominguez, M.P; Solis, S.; Lara, V.H; Bosch, P.; Lopez, T. (1998): Hydrolysis catalyst effect on sol-gel silica structure. In *Materials Letters* 36, pp. 249–253.

B. Heidenreich; W. Krenkel; M. Frieß (2004): Net shape manufacturing of Febric Reinforced Oxide/ Oxide Components via Resin Transfer Moulding and Pyrolysis. In *Proceedings of 28th International Cocoa Beach Comference on Advanced Ceramics and Composites*.

Bansal, N.P (Ed.) (2005): Handbook of Ceramic Composites: Kluwer Academic Publishers.

Behrens, S.; Müller, M. (2004): Technologies for thermal protection systems applied on reusable launcher. In *Acta Astronautica* 55 (3-9), pp. 529-536.

Bergström, L. (2001): Colloidal Processing of Ceramics. In K. Holmberg (Ed.): *Handbook of Applied Surface and Colloid Chemistry*, vol. 1. 1-2: John Wiley & Sons, Ltd, pp. 201–218.

Boakye, E. E.; Mogilevsky, P.; Hay, R. S.; Cinibulk, M. K. (2011): Rare-Earth Disilicates as Oxidation-Resistant Fiber Coatings for Silicon Carbide Ceramic-Matrix Composites. In *Journal of the American Ceramic Society*, pp. 1–9.

Braun, M; Weihs, H. (2012): Experiments on SHEFEX successful. In: *www.dlr.de*, accessed in Mai 2014.

Brinker, C.J; Scherer, G.W (1990): Sol-Gel Science. In: *The physics and Chemistry of Sol-Gel Processing*. United States of America: Academic Press.

Bunsell, A. R. (2005): Oxide fibers for high-temperature reinforcement and insulation. High Performance Fibers. In *JOM* 48, pp. 48–51.

Carelli, E.A.V; Fujita, H.; Yang, J.Y; Zok, F. W. (2002): Effects of Thermal Aging on the Mechanical Properties of a Porous-Matrix Ceramic Composite. In *Journal of American Ceramic Society* 3 (85), pp. 595–602.

Chant, J.M; Bleay, S.M; Harris, B.; Russel-Floyd, R.S; Cooke, R.G; Scott, V.D (1995a): Mechanical properties and microstructures of sol-gel derived ceramic-matrix composites. In *Journal of Materials Science* 30, pp. 2769–2784.

Chant, J.M; Cooke, R.G; Harris, B. (1995b): Freeze gelation: A Modified Sol-Gel Method for the Fabrication of Ceramic-Matrix Composites. In *Advances in Ceramic Matrix Composites II*, pp. 223–234.

Chawla, K. (1998): Composite Materials. In *Science and Engineering*, vol. 1. United States of America: Springer Science+Business Media.

Chawla, K. (2008): Interface Engineering in Mullite Fiber/Mullite Matrix Composites. In *Journal of the European Ceramic Society* 28 (2), pp. 447–453.

Chen, Z.; Duncan, S.; Chawla, K.K; Koopman, M.; Janowski, G.M (2002): Characterization of interfacial reaction products in alumina fiber/barium zirconate coating/alumina matrix composite. In *Materials Characterization* 48, pp. 305–314.

Clauß, B. (2008): Fibers for Ceramic Matrix Composites. In W. Krenkel (Ed.): *Ceramic Matrix Composites. Fiber Reinforced Ceramics and their Applications*, vol. 1: Wiley-VCH, pp. 1–20.

COI Ceramics, Inc: Oxide Ceramic Matrix Composites. In *http://www.coiceramics.com*, accessed in 2010.

Cox, B.N; Zok, F. W. (1996): Advances in ceramic composites reinforced by continuous fibers. In *Ceramics, composites and intergrowths*, pp. 666–672.

Davis, J.B; Kristoffersson, A.; Carlström, E.; Clegg, W.J (2000): Fabrication and Crack Deflection in Ceramic Laminates with Porous Interlayers. In *J American Ceramic Society* 83 (10), pp. 2369–2374.

Davis, J.B; Marshall, D.B; Morgan, P.E.D (2000): Monazite-containing oxide/ oxide composites. In *Journal of the European Ceramic Society* 20, pp. 583–587.

Department of Defense (2002): Composite Materials Handbook, vol. 5. United States of America: Department of Defense.

Deville, S. (2006): Freezing as a Path to Build Complex Composites. In *Science* 311 (5760), pp. 515–518.

Deville, S. (2008): Freeze-Casting of Porous Ceramics: A Review of Current Achievements and Issues. In *Adv. Eng. Mater* 10 (3), pp. 155–169.

Deville, S.; Maire, E.; Lasalle, A.; Bogner, A.; Gauthier, C.; Leloup, J.; Guizard, C. (2010): Influence of Particle Size on Ice Nucleation and Growth During the Ice-Templating Process. In *Journal of the American Ceramic Society* 93 (9), pp. 2507–2510.

Deville, S.; Saiz, E.; Tomsia, A. P. (2007): Ice-templated porous alumina structures. In *Acta Materialia* 55 (6), pp. 1965–1974.

DIN EN 658-3, November 2002: Mechanische Eigenschaften von keramischen Verbundwerkstoffen bei Raumtemperatur Teil 3: Bestimmung der Biegefestigkeit.

DIN EN 658-4, Mai 2003: Mechanische Eigenschaften von keramischen Verbundwerkstoffen bei Raumtemperatur Teil 4: Bestimmung der Scherfestigkeit von gekerbten Proben unter Druckbeanspruchung.

DIN EN 658-5, March 2003: Mechanische Eigenschaften von keramischen Verbundwerkstoffen bei Raumtemperatur Teil 5: Bestimmung der Scherfestigkeit im Drei-Punkt-Biegeversuch mit kurzem Auflagerabstand.

DIN EN ISO 15732, Dezember 2004: Prüfverfahren zur Bestimmung der Bruchzähigkeit monolithischer Keramik bei Raumtemperatur an einseitig gekerbten Biegeproben.

DIN V ENV 658, March 1993: Mechanische Eigenschaften von keramischen Verbundwerkstoffen bei Raumtemperatur Teil 1:Bestimmung der Zugfestigkeit.

Ferber, M.K.; Lara-Curzio, E.; Russ, S.E.; Chawla, K.K. (2011): Single Fiber Push-In vs Single Fiber Push-Out: A Comparison Between Two Test Methods to Determine the Interfacial Properties of Brittle Matrix Composites. In *www.cambridge.org/core/journals*. Accessed in 2017.

Fujita, H.; Jefferson, G.; McMeeking, R.M; Zok, F. W. (2004): Mullite/ Alumina Mixtures for Use as Porous Matrices in Oxide Fiber Composites. In *J American Ceramic Society* 2 (87), pp. 261–267.

Gerendas, M.; Cadoret, Y.; Wilhelmi, C.; Machry, T.; Knoche, R.; Behrendt, T. et al. (2011): Improvement of Oxide/Oxide CMC and Development of Combustor and Turbine Components in the HIPOC Program. In *Proceedings of ASME Turbo Expo*. ASME Turbo Expo 2011. Vancouver, Canada.

Gerendas, M.; Wilhelmi, C.; Machry, T.; Knoche, R.; Werth, E.; Behrendt, T. et al. (2013): Development and Validation of Oxide/Oxide CMC Combustors within the HIPOC Program. In *Proceedings of ASME Turbo Expo*. ASME Turbo Expo 2013. Texas, USA.

Glissen, R.; Erauw, J.P; Smolders, A.; Vanswijgenhoven, E.; Luyten, J. (2000): Gelcasting, a near net shape technique. In *Materials and Design* 21, pp. 251–257.

Glover, P. (2012): Porosity. Formation Evaluation. In *MSc Course Notes*. University of Aberdeen.

Golshan, N. H.; Sarpoolaky, H.; Souri, A. R. (2011): Microstructure and Properties of Colloidal Silica Bonded Magnedite Castable Refractories. In *Iranian Journal of Materials Science and Engineering* 8 (1), pp. 25–31.

Göring, J.; Flucht, F.; Schneider, H. (2001): Processing and Microstructure of WHIPOX. In W. Krenkel, R. Naslain, H. Schneider (Eds.): *High Temperature Ceramic Matrix Composites*. 4th International Conference on High Temperature Ceramic Matrix Composites. Munich, Germany, 01-03 October: Wiley-VCH Verlag GmbH, pp. 675–680.

Göring, J.; Hackermann, S.; Kanka, B. (2007): WHIPOX: Ein faserverstärker oxidkeramischer Werkstoff für Hochtemperatur Langzeitanwendungen. In *Materialwissenschaft und Werkstofftechnik* 38 (9), pp. 766–772.

Groß, R. (2008): Untersuchungen zu Optimierungsmöglichkeiten bei der textiltechnischen Verarbeitung von SiBN3C-Rovings. Diploma Thesis. Technical University Munich/ EADS Innovation Works, Munich.

Harris, B.; Cooke, R.G; Hammett, F.W; Russel-Floyd, R.S (1998): Sol-Gel Composites - A Low Cost Manufacturing Route. In *Industrial Ceramics* 18 (1), pp. 33–37.

Haslam, J.J; Berroth, K.E; Lange, F. F. (2000): Processing and properties of an all-oxide composite with a porous matrix. In *Journal of the European Ceramic Society* 20 (607-618).

He, M.; Hutchinson, J.W (1989): Kinking of a Crack Out of an Interface. In *Journal of Applied Mechanics* 56, pp. 270–278.

Heathcote, J.A; Gong, X.Y; Yang, J.Y; Ramamurty, U.; Zok, F. W. (1999): In-Plane Mechanical Properties of an All-Oxide Ceramic Composite. In *J American Ceramic Society* 82 (10), pp. 2721–2730.

Hench, Larry L.; West, Jon K. (1990): The sol-gel process. In *Chem. Rev* 90 (1), pp. 33–72.

Holmquist, M.; Lundberg, R.; Suder, O.; Razzel, A.G; Molliex, L.; Benoit, J.; Adlerborn, J. (2000): Alumina/alumina composite with a porous zirconia interphase - Processing, properties and component testing. In *Journal of the European Ceramic Society* 20, pp. 599–606.

Iler, R.K (1979): The Chemistry of Silica: solubility, polymerization, colloid and surface properties and biochemistry. University of California: Wiley-VCH.

Ismael, M.R; dos Anjos, R.D; Salomao, R.; Pandolfelli, V.C (2006): Colloidal Silica as a Nanostructured Binder for Refractory Castables. In *Refractories Applications and News* 11 (4), pp. 16–20.

Kanka, B.; Schmücker, M.; Luxem, W.; Schneider, H. (2001): Mechanical Behavior of WHIPOX Ceramic Matrix Composites. In W. Krenkel, R. Naslain, H. Schneider (Eds.): *High Temperature Ceramic Matrix Composites*. 4th International Conference on High Temperature Ceramic Matrix Composites. Munich, Germany, 01-03 October: Wiley-VCH Verlag GmbH, pp. 610–615.

Kanka, B.; Schneider, H. (2000): Aluminosilicate fiber/mullite matrix composites with favorable high-temperature properties. In *Journal of the European Ceramic Society* 20, pp. 619–623.

Kanzaki, S.; Tabata, H.; Kumazawa, T.; Ohta, S. (1985): Sintering and mechanical properties of stoichiometric mullite. In *J American Ceramic Society* 68, pp. C6-C7.

Keller, K.A; Jefferson, G.; Kerans R.J. (2005): Oxide-Oxide Composites. In N.P Bansal (Ed.): Hanbook of Ceramic Composites: Kluwer Academic Publishers, pp. 377–394.

Keller, K.A; Mah, T.; Parthasarathy, T. A.; Cooke, C.M (2000): Fugitive Interfacial Carbon Coatings for Oxide/Oxide Composites. In *J American Ceramic Society* 83 (2), pp. 329–336.

Keller, K.A; Mah, T.; Parthasarathy, T.A; Boakye, E. E.; Mogilevsky, P.; Cinibulk, M. K. (2003): Effectiveness of Monazite Coatings in Oxide/Oxide Composites after Long-Term Exposure at High Temperature. In *J American Ceramic Society* 86 (2), pp. 325–332.

Kerans R.J.; Hay, R.S; Parthasarathy, T.A (1999): Structural ceramic composites. In *Solid State & Materials Science* 4, pp. 445–451.

Khurmi, R. S. (2005): Applied Mechanics and Strength of Materials. In: S Chand & Co Ltd, 13th edition.

Kim, Y.; Yeo, J.; Choi, S. (2016): Shrinkage and flexural strength improvement of silica-based composites for ceramic cores by colloidal alumina infiltration. In *Ceramics International* 42, pp. 8878-8883.

Knoche, R. (2010): The Response of C/SiC Ceramic Matrix Composites Exposed to Severe Thermo-mechanical Load Conditions for Hot Structures and Thermal Protection Systems in Reusable Launch Vehicles. PhD Thesis. University of Bremen, Bremen. Advanced Ceramics Institute.

Koch, D. (2008): Microstructural Modeling and Thermomechanical Properties. In W. Krenkel (Ed.): *Ceramic Matrix Composites*. Fiber Reinforced Ceramics and their Applications: Wiley-VCH, pp. 231–259.

Koch, D.; Andresen, L.; Schmedders, T.; Grathwohl, G. (2003): Evolution of Porosity by Freeze Casting and Sintering of Sol-Gel Derived Ceramics. In *Journal of Sol-Gel Science and Technology* 26, pp. 149–152.

Koch, D.; Knoche, R.; Grathwohl, G. (2008a): Ceramics Science and Technology. Multiphase Fiber Composite. In W. Krenkel (Ed.): *Ceramic Matrix Composites*. Fiber Reinforced Ceramics and their Applications, vol. 1: Wiley-VCH, pp. 511–582.

Koch, D.; Tushtev, K.; Gaab, L.; Horvath, J.; Grathwohl, G. (2008b): Evaluation of Mechanical Properties of Ceramic Matrix Composites. In *VDI Berichte* 2028.

Koch, D.; Tushtev, K.; Grathwohl, G. (2008c): Ceramic fiber composites: Experimental analysis and modeling of mechanical properties. In *Composites Science and Technology* 68 (5), pp. 1165–1172.

Kopeliovich, D. (2010): Fabrication of Ceramic Matrix Composites by Chemical Vapor Infiltration (CVI). In *www.substech.com*, accessed in February 2012.

Kopeliovich, D. (2018): Advances in manufacture of ceramic matrix composites by infiltration techniques. In *Advances in Ceramic Matrix Composites*, vol. 2: Woodland Publishing, pp. 93-119.

Koussios, S.; Bergsma, O.K; Beukers, A. (2006): Filament winding: kinematics, collision control and process optimisation through application of dynamic programming. In *Composites Part A: Applied Science and Manufacturing* 37 (11), pp. 2088–2104.

Lange, F. F. (2010): Oxide/Oxide Composites: Control of Microstructure and Properties. In W. Krenkel, J. Lamon (Eds.): *High Temperature Ceramic Materials and Composites*. 7th International Conference on High Temperature Ceramic Matrix Composite. Bayreuth, Germany. Germany: AVISO Verlagsgesellschaft mbH, pp. 587–599.

Lange, F.; Tu, W.C; Evans, A.G (1995): Processing of damage-tolerant, oxidation-resistant ceramic matrix composites by a precursor infiltration and pyrolysis method. In *Materials Science and Engineering: A* 195, pp. 145–150.

Laurie, J.; Bagnall, C.M; Harris, B.; Jones, R. W.; Cooke, R.G; Russel-Floyd, R.S et al. (1992): Colloidal suspensions for the preparation of ceramics by a freeze casting route. In *Journal of Non-Crystalline Solids* 147&148, pp. 320–325.

Levi, C.G; Zok, F. W.; Yang, J.Y; Mattoni, M.; Löfvander, J.P.A (1999): Microstructural design of stable porous matrices for all-oxide ceramic composites. In *Zeitschrift für Metallkunde* 12 (90), pp. 1037–1047.

Levi, G.; Yang, J.Y; Dalgleish, B.J; Zok, F. W.; Evans, A.G (1998): Processing and Performance of an All-Oxide Ceramic Composite. In *J American Ceramic Society* 81 (8), pp. 2077–2086.

Lewis, J.A (2001): Colloidal Processing of Ceramics. In *Journal of the American Ceramic Society* 83 (10), pp. 2341–2359.

Lewis, M.H; York, S.; Freeman, C.; Alexander, I.C; Al-Dawery, I.; Doleman, P.A (2000): Oxide CMCs: Novel fibres, coatings, and fabrication procedures. In *Ceram. Eng. Sci. Proc.* 21, pp. 535–548.

Liang, J.; Lin, Q.H; Zhang, X.; Jin, T.; Zhou, Y.Z.; Sun, X.F.; Choi, B.G.; Kim, I.S.; Do, J.H.; Jo, C.Y. (2017): Effects of Alumina on Cristobalite Crystallization and Properties of Silica-Based Ceramic Cores. In *Journal of Materials Science & Technology* 33, pp. 204-209.

Liang, Y.; Hilal, N.; Langston, P.; Starov, V. (2007): Interaction forces between colloidal particles in liquid: Theory and experiment. In *Advances in Colloid and Interface Science* 134-135, pp. 151–166.

Lima, L. (2001): Characterization of an oxide based CMC. Internship Report IV. University of Bremen, Bremen. Advanced Ceramics Institute.

Liu, R.; Xu, T.; Wang, C. (2016): A review of fabrication strategies and applications of porous ceramics prepared by freeze-casting method. In *Ceramics International* 42, pp. 2907-2925.

M. Frieß; B. Heidenreich; W. Krenkel (2003): Langfaserverstärke oxidkeramische Verbundwerkstoffe nach dem LPI-Verfahren. In *14. Symposium: Verbundwerkstoffe und Werkstoffeverbunde*.

Machry, T. (2008): Processing of Ceramic Matrix Composites via Freeze Gelation. Diploma Thesis. University of Bremen, Bremen. Advanced Ceramics.

Machry, T.; Koch, D.; Wilhelmi, C. (2010): Development of a New Oxide Ceramic Matrix Composite. In W. Krenkel, J. Lamon (Eds.): *High Temperature Ceramic Materials and Composites*. 7th International Conference on High Temperature Ceramic Matrix Composite. Bayreuth, Germany. Germany: AVISO Verlagsgesellschaft mbH, pp. 435–445.

Machry, T.; Wilhelmi, C.; Koch, D. (2011): Novel High Temperature Wound Oxide Ceramic Matrix Composites Manufactured via Freeze Gelation. In S. Widjaja, D. Singh (Eds.): *Proceedings of the conference on Advanced Ceramics and Composites*. 35th International Conference on Advanced Ceramics and Composites. Daytona Beach, Florida: John Wiley & Sons, Ltd.

Manjula, S; Kumar, S.; Raichur, A.; Madhu, G.; Suresh, R.; Raj, M. (2005): A sedimentation study to optimize the dispersion of alumina nanoparticles in water. In *Ceramica* 51, pp. 121-127.

Mattoni, M.; Yang, J.Y; Levi, C.G; Zok, F. W. (2001): Effects of Matrix Porosity on the Mechanical Properties of a Porous-Matrix, All-Oxide Ceramic Composite. In *J American Ceramic Society* 11 (84), pp. 2594–2602.

Mello, M.D; Florentine, R.A (1993): 3-D Braided Continuous Fiber Ceramic Matrix Composites Produced by Chemical Vapor Infiltration. In *SBIR-Report. US Army Research Laboratory*.

Meyer, P.; Waas A.M. (2018): Experimental results on the elevated temperature tensile response of SiC/SiC ceramic matrix notched composites. In *Composites Part B* 143, pp. 269-281.

Montanaro, L.; Tulliani, J. M.; Perrot, C.; Negro, A. (1997): Sintering of Industrial Mullites. In *Journal of the European Ceramic Society* 17, pp. 1715–1723.

Motz, G.; Schmidt, S.; Beyer, S. (2008): The PIP-process: Precursor Properties and Applications. In W. Krenkel (Ed.): *Ceramic Matrix Composites*. Fiber Reinforced Ceramics and their Applications: Wiley-VCH, pp. 166–186.

Munro, M. (1988): Review of manufacturing of fiber composites components by filament winding. In *Polymer Composites* 9 (5), pp. 352–359.

Naskar, M.; Chatterjee, M.; Dey, A.; Basu, K. (2004): Effects of processing parameters on the fabrication of near-net-shape fibre reinforced oxide ceramic matrix composites via sol–gel route. In *Ceramics International* 30 (2), pp. 257–265.

Naskar, Milan Kanti; Basu, Kunal; Chatterjee, Minati (2009): Sol–gel approach to near-net-shape oxide–oxide composites reinforced with short alumina fibres - The effect of crystallization. In *Ceramics International* 35 (8), pp. 3073–3079.

Naslain, R.R; Pailler, R.; Bourrat, X.; Bertrand, S.; Heurtevent, F.; Dupel, P.; Lamouroux, F. (2001): Synthesis of highly tailored ceramic matrix composites by pressure-pulsed CVI. In *Solid State Ionics* 141/142, pp. 541–548.

Newman, B.N (2002): The effect of fibre coatings in oxide-oxide ceramic matrix composites. PhD Thesis. Manchester Materials Science Centre. EADS Innovation Works.

Newman, B.N; Schäfer, W. (2001): Processing and Properties of Oxide/Oxide Composites for Industrial Applications. In W. Krenkel, J. Lamon (Eds.): High Temperature Ceramic Materials and Composites. 7th International Conference on High Temperature Ceramic Matrix Composite. Bayreuth, Germany. Germany: AVISO Verlagsgesellschaft mbH, pp. 600–609.

Nubian, K.; Saruhan, B.; Kanka, B.; Schmücker, M.; Wahl, G. (2000): Chemical vapor deposition of ZrO_2 and C/ZrO_2 on mullite fibers for interfaces in mullite/aluminosilicate fiber-reinforced composites. In *Journal of the European Ceramic Society* 20 (537-544).

Parthasarathy, T.A.; Kerans, R.J. (2016): Failure of Ceramic Composites. In *Reference Module in Materials Science and Materials Engineering*, Elsevier Inc.

Peng, L.; Qisui, W.; Xi, L.; Chaocan, Z. (2009): Investigation of the states of water and OH groups on the surface of silica. In *Colloids and Surfaces A: Physicochemical and Engineering Aspects* 334 (1-3), pp. 112–115.

Peng, P.; Li, X.D; Yuan, G.F; She, W.Q; Cao, F.; Yang, D.M et al. (2001): Aluminium Oxide/ Amorphous Carbon Coating on Carbon Fibers. In *Procedings ACUN-3 Technology Convergence in Composites Applications*, pp. 339–343.

Petzold, S.; Morche, M.; Taesler, J.: Oxide-ceramic continuous fibres and ceramic fibre reinforced composites – innovative materials for the firing process. In *www.cerafib.de*, accessed in 2013.

Pierre, A.C (1998): Introduction to sol-gel processing. In: *Boston: Kluwer Academic Publishers*.

Pritzkow, W.E.C (2001): "Keramikblech" Properties and Applications. In *High Temperature Ceramic Matrix Composites*, pp. 681–685.

Pritzkow, W.E.C (2008): Oxide-Fibre-Reinforced Oxide Ceramics. In *Process Engineering* 85 (12), pp. 31–35.

Pritzkow, W.E.C. (2018): Abgehoben: Schubdüsen aus Keramikblech im Testflug eines unbemannten Luftfahrzeugs (UVA). In *https://www.keramikblech.com/news/*. Accessed in 2018.

Pritzkow, W.E.C; Rüdinger, A.; Glaubitt, W. (2005): Mullitische Matrices aus Sol-Gel-Vorstufen für die Herstellung oxidkeramischer Faserverbundwerkstoffe. In *Verbundwerkstoffe und Werkstoffverbunde*, pp. 163–168.

Pritzkow, W.; Nöth, A.; Rüdinger, A. (2015): Oxide Ceramic Matrix Composites – Manufacturing, Machining, Properties and Industrial Applications. In Ceramic Applications, 3, pp. 48-54.

Ramdane, C.B; Julian-Jankowiak, A.; Valle, R.; Renollet, Y.; Parlier, M.; Martin, E.; Diss, P. (2017): Microstructure and mechanical behaviour of a Nextel™610/alumina weak matrix composite subjected to tensile and compressive loadings. In *Journal of the European Ceramic Society* 37, pp. 2919-2932.

Rani, D. A.; Jayaseelan, D. D.; Gnanam, F. D. (2001): Densification behaviour and microstructure of gel-derived phase-pure mullite in the presence of sinter additives. In *Journal of the European Ceramic Society* 21, pp. 2253–2257.

Razzell, A.G (2008): Potential and Challenges of Fibre Reinforced Ceramics in Gas Turbines. In *VDI Berichte* 2028.

Rezwan, K. (2009): Unterlagen zum Keramiklabor. Dichtebestimmung in porösen keramischen Werkstoffen. University of Bremen.

Rice, R.W (1999): Effects of amount, location, and character of porosity on stiffness and strength of ceramic fiber composites via different processing. In *Journal of Materials Science* 34, pp. 2769–2772.

Roberts; A.P.; Garboczi, E.J (2000): Elastic properties of model porous ceramics. In *Journal of the American Ceramic Society* 12 (83), pp. 3041–3048.

Rodeghiero, E.D; Moore, B.C; Wolkenberg, B.S; Wuthenow, M.; Tse, O.K; Giannelis, E.P (1998): Sol-gel synthesis of ceramic matrix composite. In *Materials Science and Engineering: A* (A244), pp. 11–21.

Roode, M.; Price, J.; Miriyala, N.; Leroux, D.; Fahme, A.; Smith, K. (2005): Ceramic matrix composite combustor liners: a summary of field evaluations. In *Proceedings of GT2005*, vol. 1. ASME Turbo Expo 2005: Power for Land, Sea and Air. 3041-3048, June 6-9: ASME, pp. 283–292.

Rüdinger, A.; Pritzkow, W.E.C (2012): Aqueous slurries for oxide ceramic composites. Correlation between mechanical properties of the composite and composition of the Al_2O_3/ZrO_2 powder. Presentation In *EUCOMAS*, Hamburg.

Russel-Floyd, R.S; Cooke, R.G; Harris, B. (1994): Low cost ceramic-matrix composites. In I. Birkby (Ed.): *Ceramic Technology International*. The International Review of Ceramic Production and Manufacturing Technology: Sterling Publications, pp. 62–65.

Russel-Floyd, R.S; Harris, B.; Cooke, R.G; Laurie, J.; Hammett, F.W (1993a): Application of Sol-Gel Processing Techniques for the Manufacture of Fiber-Reinforced Ceramics. In *Journal of American Ceramic Society* 76 (10), pp. 1635–1643.

Russel-Floyd, R.S; Cooke, R.G; Harris, B.; Laurie, J.; Jones, R. W.; Wang, T.H; Hammett, F.W (1993b): Sol-Gel Fabrication of CMCs. In *Engineering Ceramics: Fabrication Science & Technology* 50, pp. 101–104.

Russel-Floyd, R.S; Harris, B.; Jones, R. W.; Cooke, R.G; Wang, T.W; Laurie, J.; Hammett, F.W (1990): Sol-Gel Processing of Fibre-Reinforced Ceramic Shapes. In *British Ceramic Transactions* 92 (1), pp. 685–690.

Schmidt, S.; Bayer, S.; Immich, H.; Knabe, H.; Meistring, R.; Gessler, A. (2005): Ceramic matrix composites: a challenge in space-propulsion technology applications. In *International Journal of Applied Ceramic Technology* 2 (2), pp. 85–96.

Schmidt, S.; Bayer, S.; Knabe, H.; Immich, H.; Meistring, R.; Gessler, A. (2004): Advanced ceramic matrix composite materials for current and future propulsion technology applications. In *Acta Astronautica* 3-9 (55), pp. 409–420.

Schmidt, S.; Bayer, S.; Mittmann, S.; Wilhelmi, C. (2008): High Performance LPI-C/SiC Combustion Chamber and Nozzle Extension for Next Generation Satellite Engines. In *VDI Berichte* 2028, pp. 477–478.

Schmücker, M,; Mechnich, P. (2008): The PIP-process: Precursor Properties and Applications. In W. Krenkel (Ed.): *Ceramic Matrix Composites*. Fiber Reinforced Ceramics and their Applications: Wiley-VCH, pp. 205-229.

Schneider, H.; Göring, J.; Schmücker, M.; Hackermann, S.: Oxidkeramischer Faserverbundwerkstoff mit hochporöser Matrix. In *Ingenieur Werkstoffe*.

Schneider, H.; Okada, K.; Pask, J.A (1994): Mullite and Mullite Ceramics. 1st Ed.: John Wiley & Sons, Ltd.

Schneider, H.; Schmücker, M.; MacKenzie, K.J.D (2005): Basic Properties of Mullite. In H. Schneider, S. Komarneni (Eds.): *Mullite*. Weinheim: Wiley-VCH Verlag GmbH & Co, pp. 141–191.

Schneider, H.; Schreuer, J.; Hildmann, B. (2008): Structure and properties of mullite - A review. In *Journal of the European Ceramic Society* 28 (2), pp. 329–344.

Scotti, K.L.; Dunand, D.C. (2018): Freeze casting – A review of processing, microstructure and properties via the open data repository, FreezeCasting.net. In *Progress in Materials Science* 94, pp. 243-305.

Sharma, P.K; Varadan, V.V; Varadan, V.K (2003): A critical role of pH in the colloidal synthesis and phase transformation of nano size a-Al_2O_3 with high surface area. In *Journal of the European Ceramic Society* 23, pp. 659-666.

Shaw, D.J (1992): Introduction to Colloid & Surface Chemistry. 4th Ed. Burlington, MA: Butterworth-Heinemann.

Shen, F.C (1995): A filament-wound structure technology overview. In *Materials Chemistry and Physics* 42, pp. 96–100.

Shi, Y.; Hönig, S.; Frieß, M.; Rüdinger, A.; Pritzkow, W.; Koch, D. (2018): Manufacture and characterization of oxide ceramic matrix composites out of commercial pre-impregnated fabrics. In *Ceramics International* 44, pp. 2320-2327.

Sigmund, W.M; Bell, N.S; Bergström, L. (2000): Novel Powder-Processing Methods for Advanced Ceramics. In *Journal of American Ceramic Society* 83 (7), pp. 1557–1574.

Silva, D.F (2011): Optimization of the Mechanical Properties of a Ceramic Matrix Composite via Modification of Sol-Gel Matrix and Re-Infiltration Technique. Diploma Thesis. Federal University of Santa Catarina, Florianópolis. EADS Innovation Works.

Simon, R.A (2004): Entwicklung und kolloidale Herstellung eines neuen Oxid/Oxid-Verbundwerkstoffes. PhD Thesis. Montan Universität Leoben, Leoben. DaimlerChrysler Forschung und Technologie.

Simon, R.A (2005): Progress in Processing and Performance of Porous Matrix-Oxide Oxide Composites.pdf. In *International Journal of Applied Ceramic Technology* 2 (2), pp. 141–149.

Simon, R.A; Danzer, R. (2006): Oxide fiber composites with promising properties for high-temperature structural applications. In *Advanced Engineering Materials* 8 (11), pp. 1129–1134.

Singh, B. P.; Bhattacharjee, S.; Besra, L.; Sengupta, D. K. (2004): Evaluation of dispersability of aqueous alumina suspension in presence of Darvan C. In *Ceramics International* 30, pp. 939-946.

Singh, B. P.; Menchavez, R.; Takai,C.; Fuji, M.; Takahashi, M. (2005): Stability of dispersions of colloidal alumina particles in aqueous suspensions. In *Journal of Colloid and Interface Science* 291, pp. 181-186.

Souto, P. M.; Menezes, R. R.; Kiminami, R. H. G. A. (2009): Sintering of Commercial Mullite Powder: Effect of MgO Dopant. In *Journal of Materials Processing Technology* 209, pp. 548–553.

Statham, M.J; Hammett, F.W; Harris, B.; Cooke, R.G; Jordan, R.M; Roche, A. (1998): Net-Shape Manufacture of Low-Cost Ceramic Shapes by Freeze-Gelation. In *Journal of Sol-Gel Science and Technology* 13 (171-175).

Stobbe, M. (2010): Entwicklung eines Verfahrens zur Herstellung von oxidkeramischen Verbundwerkstoffen (CMCs) über die Flechttechnik. Diploma Thesis. Technische Universität Darmstadt, Darmstadt.

Tari, G. (2003): Gelcasting Ceramics: A review. In *American Ceramic Society Bulletin* 82 (4), pp. 43–46.

Trabandt, U.; Esser, B.; Knoche, R.; Koch, D.; Tumino, G. (2005): Ceramic Matrix Composites Life Cycle Testing under Reusable Launcher Environmental Conditions. In *Journal of Applied Ceramic Technology* 2(2), pp. 150-161.

Thustev, K; Hovarth, J; Rezwan, K. (2015): Study on the mechanical behavior of FW12 at room and elevated temperatures. In *www.ceramics.uni-bremen.de*, accessed in 2016.

Türk, F. (2011): Optimierung eines Verfahrens zur Herstellung von oxidkeramischen Verbundwerkstoffen (CMCs) über die Flechttechnik. Diploma Thesis. Karlsruhe Institute of Technology, Karlsruhe. Institute of Applied Materials - Ceramics in Mechanical Engineering.

Twitty, A.; Russel-Floyd, R.S; Cooke, R.G; Harris, B. (1995): Thermal Shock Resistance of Nextel/ Silica-Zirconia Ceramic-Matrix Composites Manufactured by Freeze Gelation. In *Journal of the European Ceramic Society* 15, pp. 455–461.

Vaseschko, V.; Flucht, T. (2018): Mechanical investigation of weak regions in a wound oxide-oxide ceramic matrix composite. In *Journal of the European Ceramic Society*, http://doi.org/10.1016/j.jeurceramsoc.2018.05.009.

Venkatesh, R. (2002): Interphase effects on the bend strength and toughness of an oxide fibre/oxide matrix composite. In *Ceramics International* 28, pp. 565–573.

Viswabaskaran, V.; Gnanam, F. D.; Balasubramanian, M. (2003): Effect of MgO, Y_2O_3 and boehmite additives on the sintering behaviour of mullite formed from kaolinite-reactive alumina. In *Journal of Materials Processing Technology* 142 (1), pp. 275–281.

Vogel, W.D; Spelz, U. (1995): Cost effective production techniques for continuous fibre reinforced ceramic matrix composites. In *Ceramic Processing Science and Technology* 51, pp. 225–259.

Volkmann, E., Tushtev, K., Koch, D., Wilhelmi, C., Gratwohl, G., Rezwan, K. (2014): Influence of fiber orientation and matrix processing on the tensile and creep performance of Nextel 610 reinforced polymer derived ceramic matrix composites. In: *Materials Science & Engineering A* 614, pp. 171-179.

Volkmann, E., Tushtev, K., Koch, D., Wilhelmi, C., Göring, J., Rezwan, K. (2015): Assessment of three oxide/oxide ceramic matrix composites: Mechanical performance and effects of heat treatments. In: *Composites: Part A* 68, pp. 19-28.

Wahl, F.M; Grim, R.E; Graf, R.B (1961): Phase transformations in silica as examined by continuous X-Ray diffraction. In *The American Mineralogist* 46, pp. 193–208.

Wang, Y; Liu, H.; Cheng, H.; Wang, J. (2015): Fabrication and properties of 3D oxide fiber-reinforced Al_2O_3-SiO_2-SiOC composites by a hybrid technique based on sol-gel and PIP process. In *Ceramics International* 41, pp. 1065-1071.

Wang. W.; Shi, Z.; Wang, Z.; Wang, S. (2018): Phase transformation and properties of high-quality mullite ceramics synthesized using desert drift sands as raw materials. In *Materials Letters* 221, pp. 271-274.

Waschkies, T.; Oberacker, R.; Hoffmann, M. J. (2009): Control of Lamellae Spacing During Freeze Casting of Ceramics Using Double-Side Cooling as a Novel Processing Route. In *Journal of the American Ceramic Society* 92, pp. 79–84.

Weaver, J. H.; Rannou, J.; Mattoni, M. A.; Zok, F. W. (2006): Interface Properties in a Porous-Matrix Oxide Composite. In *Journal of American Ceramic Society* 9 (89), pp. 2869–2873.

Weaver, J.H; Yang, J.; Zok, F.W (2008): Control of Interface Properties in Oxide Composites Via Fugitive Coatings. In *Journal of the American Ceramic Society* 12 (91), pp. 4003–4008.

Wilhelmi, C.; Machry, T.; Knoche, R.; Koch, D. (2011): Processing of Oxide/ Oxide Composites for Gas Turbine Applicatios Based on Braiding Technique (OXITEX^{TM}). In S. Widjaja, D. Singh (Eds.): *Proceedings of the conference on Advanced Ceramics and Composites*. 35th International Conference on Advanced Ceramics and Composites. Daytona Beach, Florida: John Wiley & Sons, Ltd.

Wilson, D.M (2006): New High Temperature Oxide Fibers. In *www.3m.com,* accessed in 2009.

Wilson, D.M; Visser, L.R (2001): High Performance oxide fibers for metal and ceramic composites. In *Composites Part A: Applied Science and Manufacturing* 32, pp. 1143–1153.

With, G.; Wagemans, H.M (1989): Ball-on-Ring Test Revisited. In *J American Ceramic Society* 72 (8), pp. 1538–1541.

WPX Faserkeramik GmbH (2016): Whipox Re-entry Kapsel. In https://www.wpx-faserkeramik.de/aktuelles/. Accessed in 2017.

Zok, F. W. (2006): Developments in Oxide Fiber Composites. In *J American Ceramic Society* 11 (89), pp. 3309–3324.

Zok, F. W.; Levi, G. (2001): Mechanical Properties of Porous-Matrix Ceramic Composites. In *Adv. Eng. Mater* 3 (1-2), pp. 15–23.

APPENDIX

A.1 Measurement of the Fiber Volume Content Using Image Program

For the composite fiber volume content estimation using image analysis two programs are used: Gimp 2.4 and Image J. Since in the composite microstructure image fiber and matrix are represented in different grey scales (Figure A-1a) it is necessary to identify in a binary color system what is fiber and what is matrix. Therefore, with Gimp program, the fibers are painted in black and the background in white (Figure A-1c). Afterwards, the binary color image is opened in the program Image J. With this program the ratio of the black color in relation to the background is calculated. Once the black points correspond to fibers, the fiber volume percentage in the image is obtained.

For each material in this work this image analysis is made in three different places of the sample and the results presented correspond to an average.

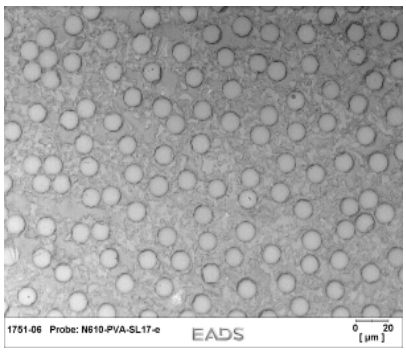

(a)

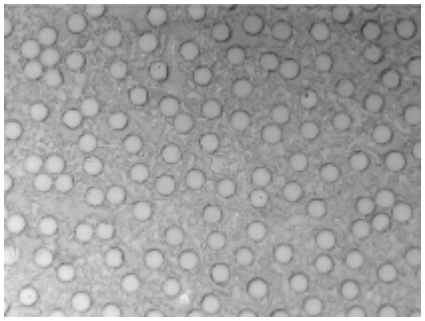

(b)

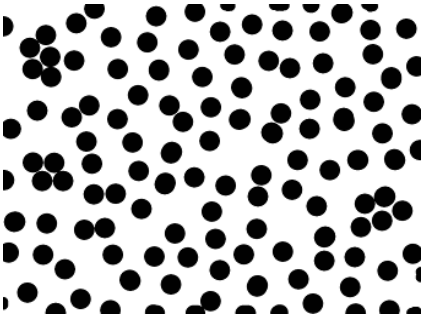

(c)

Figure A-1 – Original microstructure image (a), microstructure image after removing label and scale bar (b), black and white image after painting the fibers (c).

Step-by-step instruction for the image analysis:

➔ Gimp Program

- Open the image to be analyzed with Microsoft Office and remove label and scale bar of the image so that only the microstructure from the material is left (Figure A-1a to b), save the image,

- Open Gimp program and the image to be analyzed (Figure A-1b),
- In the layer settings select: create a new layer, transparent and give it a name,
- Select the created layer to work,
- Select the spherical brush and adjust its size to the size of the fiber filaments, paint all fiber filaments in black,
- After painting the fibers, go again in the layers settings: select the layer background and delete it with the icon of a bin,
- Paint the image background with white and save the image (Figure A-1c).

➔ Image J

- Open program and the image saved in the Gimp program,
- Select: image/ adjust/ threshold/ red/ auto/ set
- Open the original picture with scale: select line cursor and draw a line above the scale bar,
- Select: analyze/ set scale/ write the distance in pixels (e.g. 20) and the unit of length of the original picture scale (e.g. µm)/ select global/ Ok
- Select: analyze/ analyze particles/ display results/ clear results/ summarize/ Ok
- Then a window with the percentage of black pixels in relation to the white ones will appear, this will correspond to the composite fiber volume %.

A.2 Homogenizing sol gel suspensions

Composites using aluminum oxide as filler are manufactured using the parameters from AF_D with only one difference: the mixer used for suspension preparation. These composites are called AF_D_2. For preparation of AF_D_2 slurry, a mechanical mixer with velocities up to 600 RPM is used. Composite AF_D (named here AF_D_1) is homogenized with a high-energy mixer named Ultra-TURRAX in which velocities up to 24.000 RPM are achieved. Measurement of both suspensions viscosity indicates no difference (Figure A-2).

AF_D_2 composites plates measuring 140x140 mm and 230x230 mm are manufactured via filament winding and freeze gelation. Composites density and porosity are measured using He Pycnometer (Table A-1) and pore size distribution is evaluated with mercury intrusion (Figure A-3). Fiber volume content iss calculated based on image analysis (Appendix A.1).

ALOX 07-2 shows higher amount of bigger pores than ALOX 07-1. Higher pore size ranging 10 μm to 100 μm is observed in composite AF_D_2.

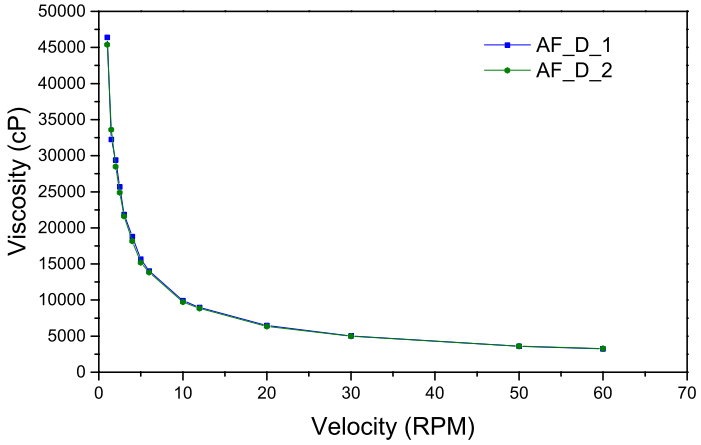

Figure A-2 - Viscosity of ceramic suspensions AF_D_1 and AF_D_2 measured using Brookfield Viscometer.

Table A-1 - Density and porosity of composite AF_D_1 and AF_D_2 manufactured with Nextel™ 610 fibers, 3000 denier with alumina filler measured using He-Pycnometer and fiber volume content measured via image analysis.

	AF_D_1	AF_D_2
CMC Density (g/cm³)	3,59	3,63
CMC Porosity (%)	31,6	34,4
Average Pore Size (μm)	3,25	8,26
Fiber Content (Vol. %)	42,6	44,9

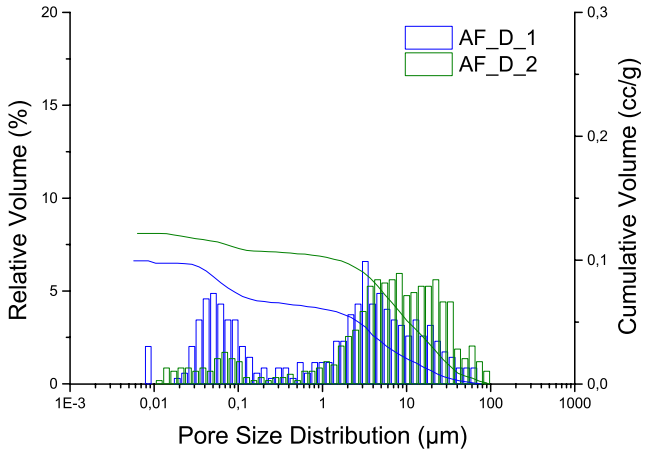

Figure A-3 - Pore size distribution of AF_D_1 and AF_D_2 manufactured with Nextel™ 610 fibers, 3000 denier with alumina filler via filament winding and freeze gelation.

Microstructure of AF_D_2 shows that this matrix did not infiltrate the fiber filaments, staying mostly as ceramic blocks between the composite layers and also among fiber bundles. In regions with high amount of matrix thermal cracks are formed after sintering (Figure A-4).

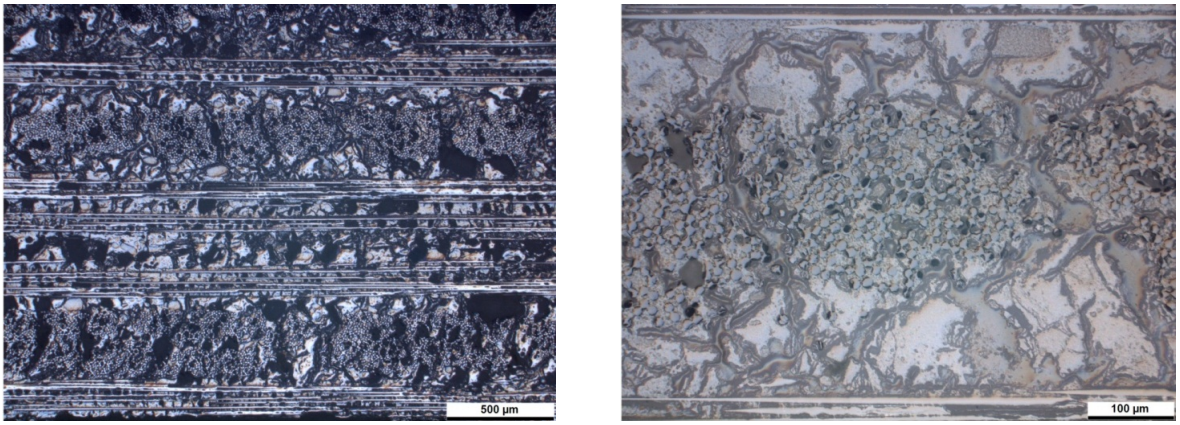

(a) (b)

Figure A-4 - Microstructure of AF_D_2 manufactured with Nextel™ 610 fibers, 3000 denier with alumina filler via filament winding and freeze gelation (from plate with 230x230 mm).

Interlaminar shear strength measured with short bending test shows delamination in the layers where fibers are oriented in 0°/90°. Interlaminar shear strength of 1,97 ± 0,39 MPa is calculated for AF_D_2 (Figure A-5) and 6,90 ± 0,40 MPa for AF_D_1. Although both composites are manufactured with the same components, interlaminar shear strength is drastically reduced when lower mixing velocities are used during suspension homogenization. Samples tested in short bending are prepared from composite plate measuring 230x230 mm.

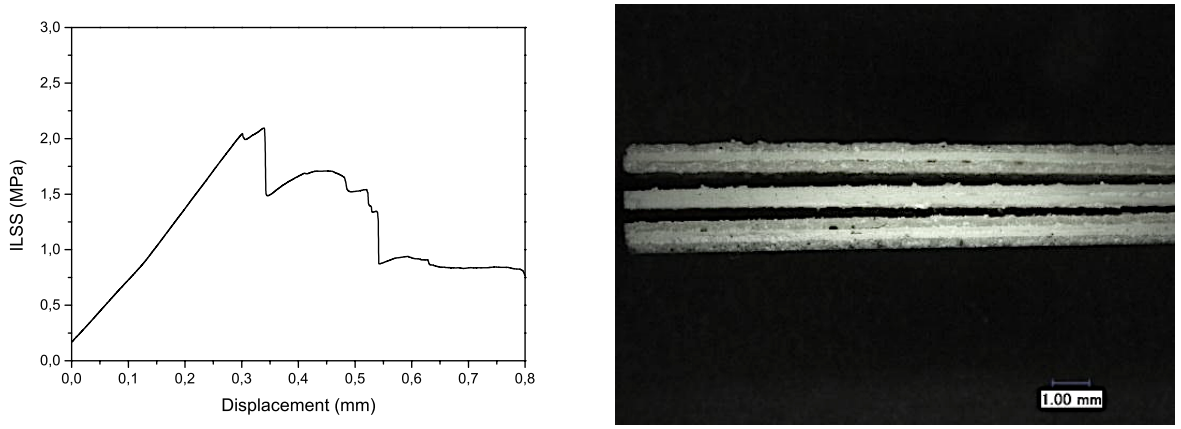

(a) (b)

Figure A-5 - Representative short bending strength vs. displacement curve (a) and tested sample (b) of AF_D_2 manufactured with Nextel™ 610 fibers, 3000 denier with alumina filler via filament winding and freeze gelation. Scale bar indicates 1 mm.

Transversal tensile test shows low interlaminar properties from AF_D_2, with a transversal tensile strength of 2,45 ± 0,13 MPa. Fracture is dominated by intralaminar behavior (Figure A-6). These samples are prepared from the plate with 230x230 mm. Since the samples tested in AF_D_1 are from a plate with 140x140 mm, two extra samples of AF_D_2 are prepared from the plate with 140x140 mm in order to verify if the lower transversal tensile strength measured in AF_D_2 could have been influenced by the geometry of the winding tool used.

Transversal tensile properties of two new samples are even lower (0,73 ± 0,06 MPa) and higher deformation is observed. In the microstructure from AF_D_2 (Figure A-7) pre-delamination between the 5° and 6° layer in addition to inhomogeneous matrix infiltration within fiber filaments and consequent accumulation of matrix between composite layers explains the lowest strength of these two samples.

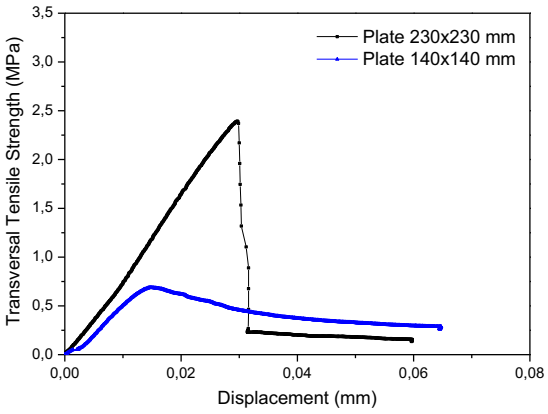

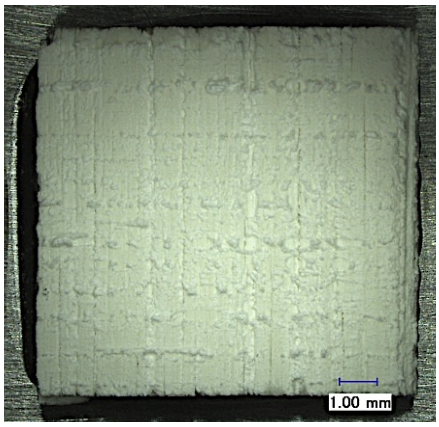

(a) (b)

Figure A-6 - Representative transversal tensile strength vs. displacement curve (a) and fracture surface (b) of AF_D_2 manufactured with Nextel^{TM} 610 fibers, 3000 denier with alumina filler via filament winding and freeze gelation after transversal tensile test. Scale bar indicates 1 mm.

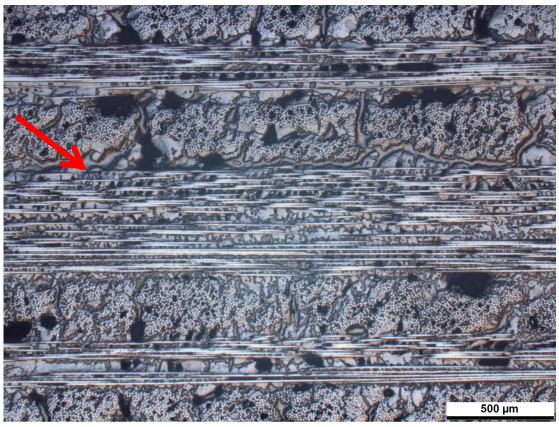

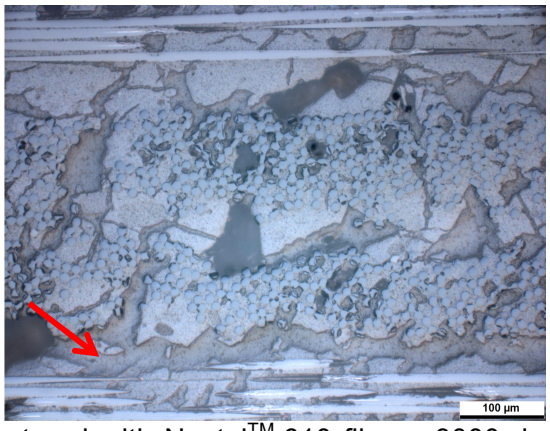

Figure A-7 - Microstructure of AF_D_2 manufactured with Nextel^{TM} 610 fibers, 3000 denier with alumina filler via filament winding and freeze gelation (from plate with 140x140 mm).

Monolithic ceramics from both materials are analyzed under scanning microscope. The difference in the microstructure from both matrices can be seen in Figure A-8. When homogenized with a high-energy mixer (AF_D_1), alumina particle agglomerates are destroyed. With a suspension free of agglomerates, ice crystals are able to grow during freezing as observed by the path lead from the ice crystals in Figure A-8a. Single alumina particles surrounded by the sol gel suspension are shown in Figure A-8b. Using lower mixing velocities (AF_D_2), particle agglomerates cannot be destroyed. Hence, ice crystals do not grow uniformly among the agglomerates because they do not have sufficient energy to overcome this barrier. The final material microstructure is reflected by nearly no signs of ice crystals growth

and by several agglomerates from the alumina powder evolved by the silica sol (Figure A-8c and A-8d).

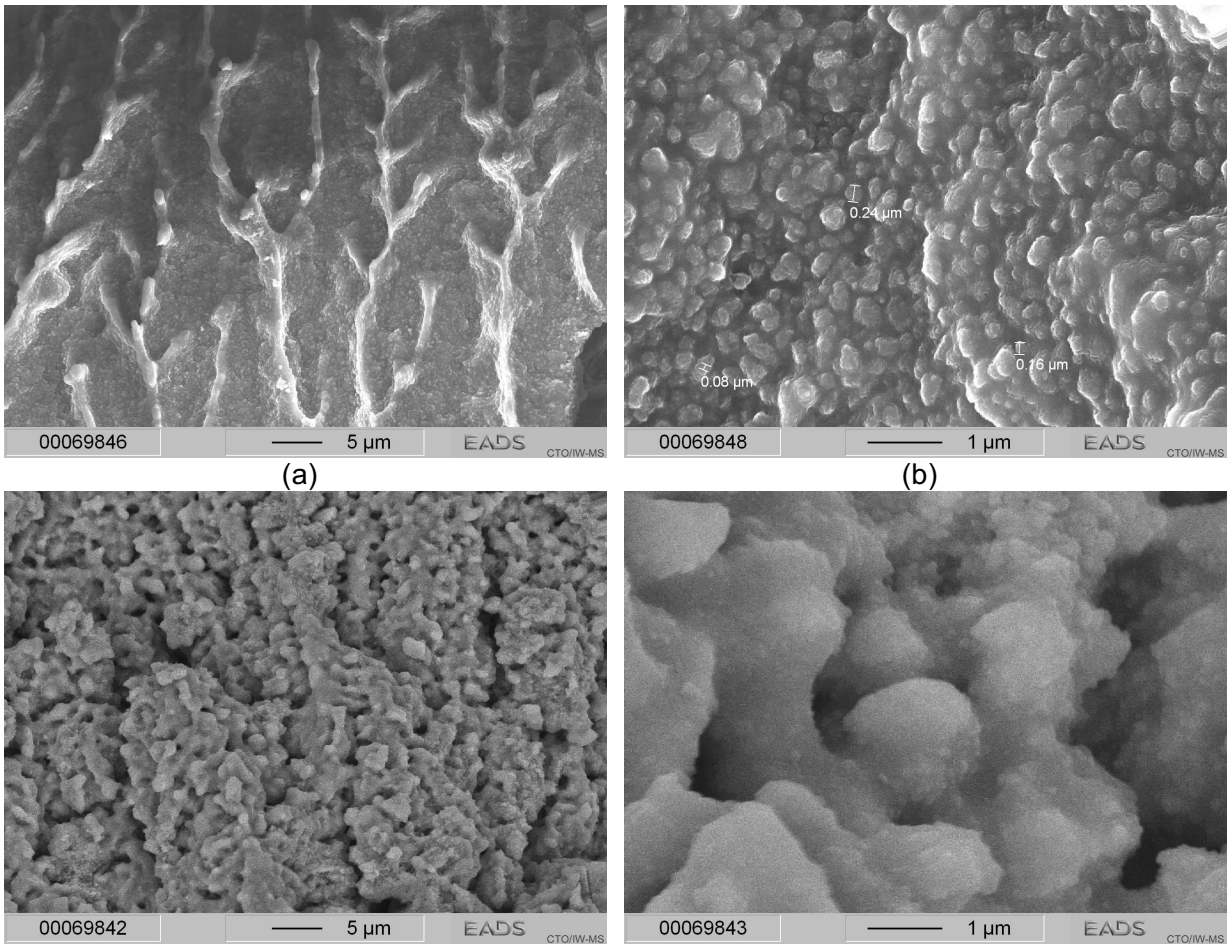

Figure A-8 - Fracture surface images of a monolithic sample manufactured with AF_D_1 (a,b) and AF_D_2 after freeze gelation (c,d).